Optical Parametric Oscillators: Noncollinear Phase Matching and Linewidth Studies in Beta Barium Borate

By Lawrence A.W. Gloster

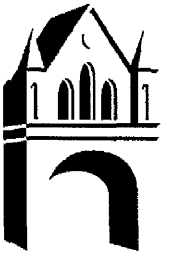

THE UNIVERSITY
of MANCHESTER

Department of Physics and Astronomy
University of Manchester

1995

A thesis submitted to the University of Manchester for the degree of Doctor of Philosophy in the Faculty of Science

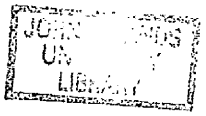

Contents

Abstract

Noncollinear phase matching and line narrowing has been explored in detail in beta barium borate (β-BaB_2O_4, BBO) optical parametric oscillators (OPOs) in the nanosecond time domain, with a view to increasing the efficiency of OPOs and assessing their potential as spectrally narrow spectroscopic sources.

Using the harmonics of a flashlamp-pumped Nd:YAG laser as the pump source for these devices, type I noncollinear phase matching has been investigated in BBO pumped at both 355 nm and 532 nm. Excellent agreement has been shown with respect to the tuning profiles and the oscillation threshold of the OPOs with developed theoretical models, as a function of their noncollinearity. Significant improvements were observed in the efficiency of the noncollinear OPOs and the threshold as a result of countering Poynting vector walk-off of the extraordinary wave in the medium. All the noncollinear phase matched oscillators have been characterised and compared with respect to their threshold, inherent linewidth, efficiency, tuning capability and the extent to which walk-off has been compensated.

A grazing incidence BBO OPO was constructed and pumped at 10 Hz by a frequency-tripled Nd:YAG laser. By varying the spectral bandwidth of the pump laser, the dependence of the linewidth of the resonant signal wave of the OPO has been studied. It was observed that single-longitudinal mode (SLM) operation of the OPO was not possible with a broad pump bandwidth (~30 GHz). SLM operation was seen in the OPO when an injection-seeded, single-mode pump source was used. The stability of the mode was poor, however, and subject to mode-hopping and dual-mode action. The grazing incidence OPO has been optimised with respect to linewidth, efficiency and wide range tunability.

Using a novel coupled cavity configuration, which incorporated the grazing incidence design, single-mode operation has been observed in the OPO for several minutes with no active cavity control. The coupled cavity design secured SLM in the OPO with a seven-fold increase in the external efficiency and a 20 % fall in the threshold of the device. The (mirror-limited) tuning range of the OPO was 580 nm to 690 nm and the time-averaged linewidth was 210±70 MHz.

Declaration

The work reported in this thesis has been carried out under the supervision of Professor T.A. King at the University of Manchester.

No portion of the work referred to in this thesis has been submitted in support of an application for another degree or qualification of this or any university or other institute of learning.

Publications Resulting from this Work

"Highly efficient optical parametric oscillator" L. A. W. Gloster, Z. X. Jiang and T. A. King, 11th UK National Quantum Electronics Conference, Belfast (1993)

"Characterisation of a Nd:YAG-pumped β-BaB_2O_4 optical parametric oscillator in collinear and noncollinear phase matched configurations" L. A. W. Gloster, Z. X. Jiang and T. A. King, IEEE J. Quantum Electron., 30, 2961, (1994)

"Noncollinear phase matching in a type I barium borate optical parametric oscillator" L. A. W. Gloster, I. T. McKinnie and T. A. King, Opt. Commun., 112, 328-332, (1994)

"Type I and type II noncollinear phase matching in barium borate OPOs" L. A. W. Gloster, Z. X. Jiang and T. A. King, Conference on Lasers and Electro-Optics, CWM1 (1994)

"Bandwidth studies of a grazing incidence BBO OPO" L. A. W. Gloster, I. T. McKinnie, Z. X. Jiang and T. A. King, J. M. Boon-Engering, W. E. van der Veer and W. Hogervorst, Conference on Lasers and Electro-Optics, CTul31 (1995)

"A narrowband β-BaB_2O_4 OPO in a grazing incidence configuration" L. A. W. Gloster, I. T. McKinnie, Z. X. Jiang and T. A. King, J.M. Boon-Engering, W. E. van der Veer and W. Hogervorst, submitted to J. Opt. Soc. Am. B., Special Issue on Parametric Devices, March 1995

"A highly efficient, single-longitudinal mode β-BaB_2O_4 optical parametric oscillator with a new cavity design" J. M. Boon-Engering, L. A. W. Gloster, W. E. van der Veer, I. T. McKinnie, W. Hogervorst and T. A. King, submitted to Opt. Lett. May 1995

"Single-longitudinal mode in a grazing incidence BBO optical parametric oscillator " L. A. W. Gloster, I. T. McKinnie, T. A. King, J. M. Boon-Engering, W. E. van der Veer and W. Hogervorst, submitted to Conference on Quantum Electronics 12, University of Southampton, September, (1995)

Other Publications

"Chromium doped forsterite: the influence of crystal characteristics on laser performance" I. T. McKinnie, L. A. W. Gloster and T. A. King, to be published

"Tunable Cr:forsterite laser with Ti:sapphire excitation" Z. X. Jiang, L. A. W. Gloster and T. A. King, European Conference on Lasers and Electro-Optics, LDFr2, (1993)

"Line narrowing and tuning in chromium doped forsterite" I. T. McKinnie, L. A. W. Gloster, Z. X. Jiang and T. A. King, IOP Congress on Advanced Solid State Lasers (1994)

"Laser excitation sources for chromium doped forsterite: a comparative study" I. T. McKinnie, L. A. W. Gloster, Z. X. Jiang and T. A. King, Conference on Lasers and Electro-Optics, CTuE4, (1994)

"Laser excitation sources for chromium doped forsterite: a comparative study" I. T. McKinnie, L. A. W. Gloster, Z. X. Jiang and T. A. King, European Conference on Lasers and Electro-Optics, CTuK58, (1994)

"Titanium-doped sapphire: the potential for the new generation of high dopant level laser crystals" I. T. McKinnie, L. A. W. Gloster and T. A. King, OSA Annual Meeting, WL2, (1994)

"Laser characteristics of chromium doped forsterite with Ti:sapphire laser excitation" Z. X. Jiang, L. A. W. Gloster and T. A. King, J. Mod. Opt., 1411, (1993)

Glossary of Terms

BBO	Barium borate
LBO	Lithium triborate
KTP	Potassium titanyl phosphate
$LiNbO_3$	Lithium niobate
d-LAP	Deuterated L-arginine phosphate
NPP	N-(4-nitrophenyl)-(L)-propinol
POM	3-methyl-4-nitropyridine-1-oxide
OPO	Optical parametric oscillator
GIOPO	Grazing incidence optical parametric oscillator
NCPM	Noncritical phase matching
CPM	Critical phase matching
SLM	Single-longitudinal mode
NLO	Non-linear optics/optical
OMA	Optical multi-channel analyser
PZT	Piezoelectric transducer
LIS	Laser isotope separation
FOM	Figure of merit
CW	Continuous wave
PLSA	(Burleigh) pulsed laser spectrum analyser
AVLIS	Atomic vapour laser isotope separation
MLIS	Molecular laser isotope separation

The Author

The author graduated from the University of Manchester in July 1990 with a Bachelor of Science Degree in Physics. He went on to join the Laser Photonics Group in the Physics and Astronomy Department at the University of Manchester in October 1991, under the supervision of Professor TA King where he has spent three years working on pulsed optical parametric oscillators, diode pumped solid state lasers and tunable solid state lasers.

Acknowledgements

I gratefully acknowledge the support of my supervisor Professor Terry King for providing me with the opportunity to carry out this work in the Laser Photonics Group and for his help and encouragement during the course of this thesis. Thanks and respect are due to Dr. Iain McKinnie for tireless help over the years and for proof-reading this thesis and for correcting my English(ness), and to Dr. Zhi-Xing Jiang for his drive in the middle years. I have thoroughly enjoyed working alongside Joke Boon-Engering and hope that this will continue and I, therefore, thank Professor Wim Hogervorst for allowing that to happen. I thank John Hobdell for his assistance with Fortran programming, and I am grateful to Dr. Walt Bosenberg for his inspiration and helpful discussions: I feel sure that he will never have to turn to this thesis for reference.

The apparatus was drawn by John Rowcroft, built by the staff of the Mechanical Workshop and photographed by Ian Callaghan. My sincere thanks go to all of them. The research was funded by the EPSRC under the Total Technology Scheme and by Urenco (Capenhurst) Plc, and I thank Richard Dutton for his generosity and for many helpful discussions over the years.

I am eternally grateful to my parents who have supported and encouraged me throughout my first degree and this work, despite claiming to understand nothing of what I do. Finally, it is to Lucy to whom I dedicate this thesis. Without her, it may never have been written.

Chapter 1

Introduction

The presence of the optical parametric oscillator (OPO) in the laboratory has grown tremendously in the last few years, and has become the choice of many research workers because of its versatility and its potential for large tunability. The motivation behind this work was to explore the OPO's potential as a source of pulsed, efficient, narrow-linewidth, tunable radiation for spectroscopic applications and, in particular, laser isotope separation (LIS). To this end, the objectives of the work are principally two fold; first, to demonstrate that the OPO can be a source of highly efficient, tunable radiation and, second, that significant line-narrowing and single-mode operation can be attained in the visible spectral region whilst maintaining its tunability.

In order to generate efficient radiation from the OPO, the approach adopted here is a process of noncollinear phase matching in the crystal to compensate for the spatial walk-off of the extraordinary ray in the OPO interaction. This technique is shown to be highly effective, with a factor of four increase observed in the external efficiency, whilst still maintaining a large tuning range. The strategy for line-narrowing the OPO involves a series of pump lasers with different bandwidths, and frequency-selective cavities. The importance of the pump bandwidth is explored, and using the combination of a single-axial mode pump source and a grazing incidence cavity, single-axial mode operation in the OPO is successfully demonstrated.

The basic principles of the OPO are introduced in this chapter with some of the milestone discoveries and devices highlighted. A brief summary of the history of the parametric oscillator and non-linear optics is presented and then a short comparison with other tunable sources is discussed, followed by a review of modern OPOs. The work contained in this thesis was funded by the Engineering and Physical Science Research Council (EPSRC) and by Urenco (Capenhurst) plc. The process of laser

isotope separation is a principal interest to Urenco (Capenhurst) plc, and a basic description of laser isotope separation is given towards the end of the chapter.

1.1 An Historical Review of Optical Parametric Oscillators

Since the invention of the first laser in 1960, using ruby as the gain medium [1], there has been a great deal of interest in the development of coherent radiation at optical frequencies, as such devices would have many applications in the broad fields of industry, medicine and research. Alongside the discovery of the laser was some pioneering work by Franken *et al* [2] in 1961, who demonstrated optical non-linearity in a piece of crystalline quartz. They were able to produce the second harmonic of ruby at 347 nm using the intense optical field generated by the laser at 694 nm to probe the small non-linear response in the quartz. Quartz has a non-linear coefficient of ~0.3 pm/V and the device was not phase matched leading to a very small second harmonic signal corresponding to an efficiency of 10^{-6} %. Nevertheless, the field of non-linear optics was born, and in 1962 Giordmaine [3] was able to demonstrate efficient second harmonic generation (SHG) in a birefringent material. Phase matching, a technique devised to exploit the birefringence of a non-linear material so that the fundamental wave travels at the same speed as the generated second harmonic wave in the crystal, was used in Giordmaine's experiment to enhanced the SHG efficiency. Then, in the same year, a landmark publication by Armstrong *et al* [4] detailed the interaction of three waves in non-linear interactions coupled by the $\chi^{(2)}$ parameter of the non-linear crystal. The experiments discussed in the paper involved two waves providing amplification to a third wave, via the $\chi^{(2)}$ coefficient such as the two pump waves in SHG and the pump and signal waves in sum- and difference-frequency mixing. In the same year, Kroll [5] published a paper postulating that it would be possible to generate broadly tunable radiation in the visible and near infrared by optically pumping a non-linear media. Hence, the theoretical birth of the optical

parametric oscillator. Amplification in the OPO takes place at both the generated signal and idler frequencies, with only the pump wave present initially. The parametric process begins from a fluctuation in the zero point energy of a single photon per mode from which the amplification of the signal and idler occurs [6].

It was not until 1965 that Giordmaine and Miller demonstrated the first OPO at the Bell Telephone Laboratories [7]. Using a Q-switched, Nd:$CaWO_4$ laser at 1.058 μm and doubled to 529 nm to pump a ~0.5 cm lithium niobate ($LiNbO_3$) crystal to generate tunable radiation from 970 nm to 1.15 nm. For the next twenty years, research into OPOs progressed steadily and there followed an intense effort to develop the OPO into a practical device. However, the progress was encumbered by a lack of suitable non-linear optical materials and, to some extent, by a small choice of pump sources. Undeterred by this, a group of specialists continued to advance the OPO, and a diversity of theoretical and experimental papers was published [8]-[11].

Experimental OPOs during this period tended to be confined to the infrared region of the spectrum and $LiNbO_3$ was widely used as the non-linear crystal, in both singly and doubly resonant cavities [12], and its versatility meant that it could be both angle-tuned [13]-[14] and temperature-tuned [15]. Other crystals were regularly used during this early period and in 1971, Yarborough and Massey [16] achieved a tuning range of 420 nm to 730 nm by pumping ammonium dihydrogen phosphate (ADP) with the fourth harmonic of a Nd:YAG laser. Other materials were popular also, including cadmium selenide (CdSe) for the generation of light in the near and middle infrared [17]. All of these devices were pumped by pulsed lasers and it was Smith *et al* who claimed the first CW pumped OPO using barium-sodium niobate ($Ba_2NaNb_5O_{15}$) pumped by 532 nm radiation [18], rapidly followed by Byer *et al* who demonstrated a CW OPO based on $LiNbO_3$ pumped with an argon laser at 514.5 nm [19]-[20]. Another material used was deuterated rubidium dihydrogen arsenate (RD*A) and in

1975, Kato [21] pumped such a crystal with the third harmonic of a Nd:YAG laser to produce tunable radiation from 647 nm to 785 nm.

The first single-mode OPO was demonstrated by Kreuzer in 1969 [22] using a single-longitudinal mode, Q-switched ruby laser to pump a $LiNbO_3$ crystal. Using a tilted etalon in the OPO cavity with a free spectral range greater than the gain bandwidth of the OPO, a single-mode was observed with a linewidth limited to the spectrometer resolution. This began to break new ground for the OPO as a potential source for spectroscopic applications. In the same year, Falk and Murray [23] noncollinearly phase matched a $LiNbO_3$ OPO using a ruby laser. Using this type of phase matching, they were able to counter Poynting vector walk-off in the crystal, and secure singly resonant oscillation.

1.2 Basic Concepts of the OPO

The optical parametric process is a second order non-linear interaction in which a pump photon, propagating in a non-linear material, breaks down into two photons of lower frequency, such that $\omega_p=\omega_s+\omega_i$ where subscripts s and i denote the "signal" and "idler" waves. The conversion of the pump photon to the simultaneous production of the signal and idler photons is by a stimulated emission process and the parametric gain is based upon the action of stimulated emission. That is, the rate of emission of signal and idler photons depends upon the number of these photons present and the larger this number is, the greater the chance of more being produced.

The break-down of the pump photon to the signal and idler photons is not uniquely determined by the conservation of energy, since this would result in a wide and continuous spread of lower frequencies. A further constraint of momentum conservation is also obeyed such that, $\mathbf{k_p}=\mathbf{k_s}+\mathbf{k_i}$ which is also known as the phase

matching condition. A schematic diagram of a simple cavity OPO is shown in figure 1.1.

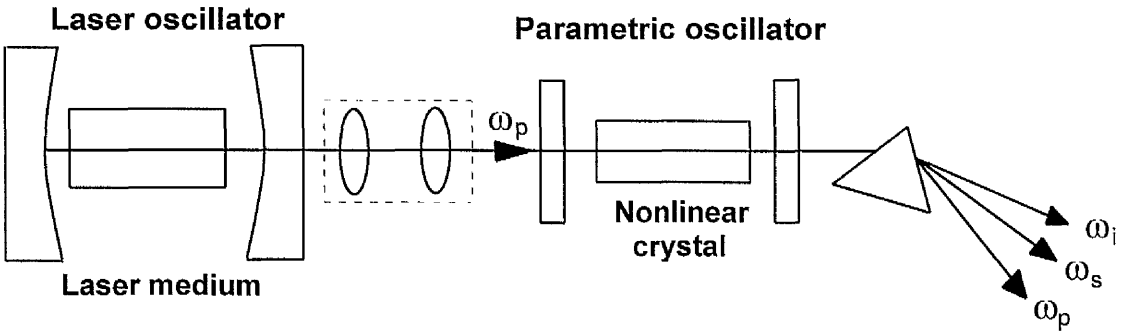

Figure 1.1. Schematic diagram of a simple cavity OPO pumped at a frequency ω_p from a laser. The lower frequencies ω_s and ω_i are generated.

The most common approach to satisfy the phase matching condition is to take advantage of the birefringence in an anisotropic medium to compensate for the dispersion in the material by reducing the momentum of the pump photon with respect to the signal and idler photons. In an anisotropic medium, the refractive index of the extraordinary wave varies continuously and smoothly with the direction of propagation. As the crystal is rotated, therefore, the magnitude of the k-vector of the extraordinary ray will change, thus changing the frequency of the two generated photons. This is discussed in greater depth in chapter two. Throughout this thesis, the signal always refers to the generated wave of the higher of the two frequencies.

Reaching threshold in an OPO depends, among other things, upon the magnitude of the second order non-linear susceptibility $\chi^{(2)}$ of the crystal, the available pump power, the crystal length and the cavity losses. The magnitude of $\chi^{(2)}$ for a typical inorganic non-linear crystal is ~1 pm/V. For a crystal length of ~1 cm, threshold is usually reached with optical powers of a few tens of MW/cm^2 of pulsed pump power, whilst the tuning range depends upon the pump frequency, the transparency range of the material and its birefringence.

Modern OPOs are routinely constructed to generate pulse outputs whose durations can span six orders of magnitude from nanosecond pulses to a few tens of femtoseconds [24]-[25], with each time domain often being a field of study in itself. For pulsed operation, it is usually sufficient for only one wave (the signal or the idler) to be resonant in the cavity because of the high peak powers involved, and this is known as a singly resonant oscillator (SRO). For continuous wave OPOs, however, reaching threshold is not so easy. Although this thesis is concerned only with the nanosecond time domain, a few words about CW OPOs will follow.

To reduce the threshold of the CW OPO, it is usually necessary to resonate both the signal and the idler in the cavity. This is known as a doubly resonant oscillator (DRO) and it poses a particularly severe problem [11]. As a result of dispersion, the axial mode spacing of the signal and idler frequencies is slightly different and simultaneous oscillation of a signal and idler mode (whose frequencies sum to the pump frequency) can only occur for certain mode pairs. Fluctuations in the pump frequency, crystal temperature or crystal angle can cause severe mode-hopping to occur. Further reduction in threshold can be attained by weakly resonating the pump as well as the two generated waves. Such a cavity is known as a triply resonant oscillator (TRO). TROs present an additional problem which requires the pump field also to be held resonant in the cavity. However, low thresholds can be observed with such devices and using a single-frequency argon laser, Colville *et al* [26] demonstrated a threshold of 50 mW in LBO. To stabilise the cavity modes and prevent mode-hopping, active cavity-length control is required to keep both (or all three) waves resonant. In addition, to keep the threshold low, CW OPOs tend to rely on noncritical phase matching (to remove the effects of Poynting vector walk-off) and require temperature tuning which limits the available tuning range.

1.3 Tunable Sources and Pump Sources

With ever improving crystal quality, greater transparency ranges, the drive for higher non-linear coefficients and higher damage thresholds, the OPO is becoming a serious competitor to other tunable sources. Increasingly, OPOs are replacing other, more conventional, laser sources in many areas of spectroscopy [27]-[30] and they are reaching the level where they are being considered for applications such as atmospheric spectroscopy and lidar [31]. In fact, the OPO has a broader tuning range than any laser known.

Two recently developed laser materials are titanium-doped Al_2O_3 (Ti:sapphire) and chromium-doped $LiSrAlF_6$ (Cr:LiSAF). Ti:sapphire has the broadest tuning range of any laser, from 650 nm up to 1.1 μm [32], and can be frequency doubled to generate light in the UV and blue [33]. Absorption occurs strongly at ~500 nm and cannot, therefore, be diode-pumped until a diode laser with such a wavelength exists. Cr:LiSAF was developed in 1989 and can be flashlamp pumped [34], or diode-pumped [35]-[36] and has a tuning range of 780 nm to 1.01 μm. The tuning ranges of these materials and others are shown in figure 1.2.

In the figure, the tuning ranges of a variety of metal ion- and rare earth-doped solid state laser materials are shown. The OPO tuning range shown is for barium borate pumped with the third harmonic of a Nd:YAG laser. To include the tuning range of other OPOs would be superfluous; however, tuning ranges are attainable to down to the UV [44] and into the mid-infrared [45]. Clearly, the OPO has the largest tuning range of any laser material currently available.

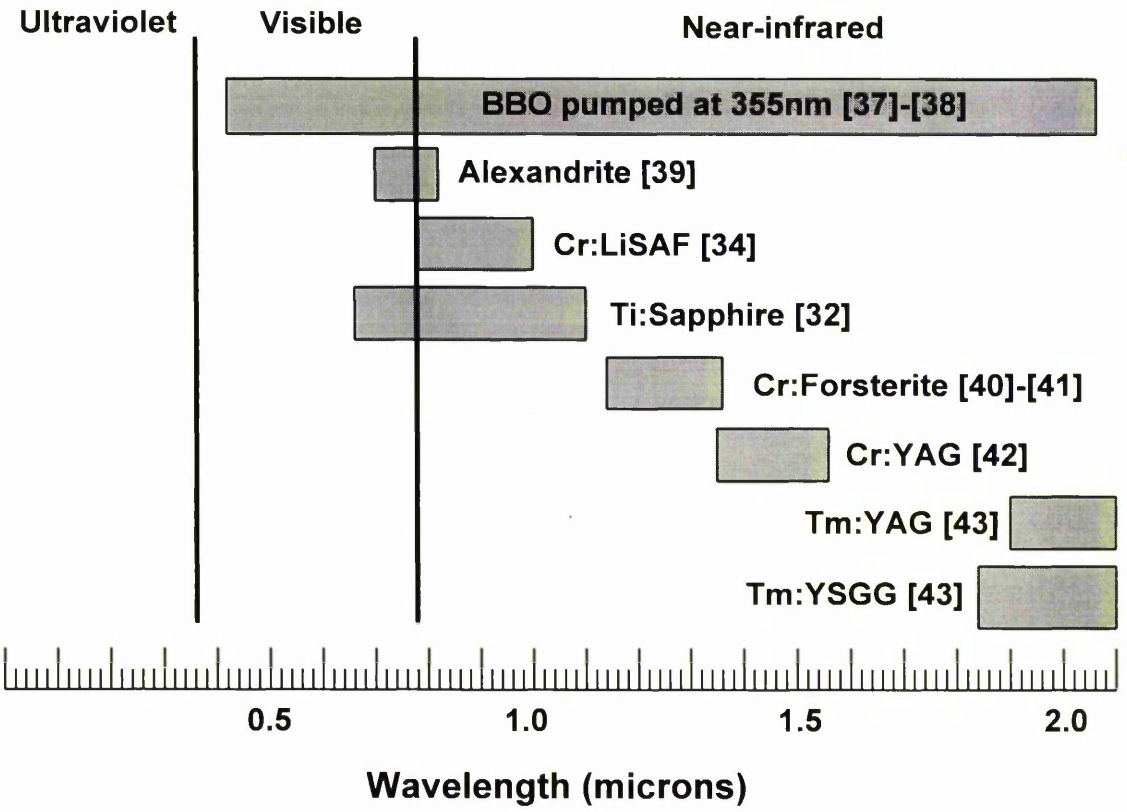

Figure 1.2. A comparison of solid state laser tuning ranges compared with that of a BBO OPO pumped at 355 nm. Each tuning range is referenced after the material name.

These solid state laser sources can also be used successfully as pump sources for the OPO. The combined tuning capability of the OPO with that of the pump source can create an impressive composite tuning range. Ti:sapphire is a popular choice of pump source for an OPO for the generation of short pulses at wavelengths longer than the Ti:sapphire tuning range. Using lithium triborate (LiB_3O_5, LBO) as the OPO gain medium, pulse durations of a few hundred femtoseconds have been produced at wavelengths of 1.374 μm to 1.530 μm pumped with a self-mode-locked Ti:sapphire laser at 800 nm [46]. By varying the pump wavelength, the phase matching temperature and the tuning profile changes. Other researchers have worked on similar systems using potassium titanyl phosphate ($KTiOPO_4$, KTP) as the OPO medium to extend this tuning range into the 1 μm to 3 μm region [47]-[48].

Non-tunable sources are the most common choice for pumping the OPO. In the last 30 years, the field has moved steadily away from the use of the ruby laser to many varied sources covering a wide range of wavelengths. Materials like BBO and LBO, which are transparent down to ~200 nm, have provided access to the visible and blue spectral regions as well as the infrared. In order to reach the blue/green spectral region, the OPO requires a higher frequency pump wave, which falls in the UV region. To this end, the excimer laser has proved to be an excellent UV pump source for the OPO, initially with urea as the OPO gain medium [49]-[51], and later with BBO [52]-[54] and LBO [44]. The advantage with the excimer laser is that the UV region is reached without the need for frequency conversion.

Neodymium ion-doped laser hosts have provided the bulk of the pump sources for OPOs in recent times. The Nd:YAG laser has been used extensively to produce Q-switched pulses at 1064 nm which can be frequency-doubled to 532 nm, and sum-frequency mixed to 354.7 nm in the UV (henceforth, this shall be written as 355 nm). The fourth harmonic, generated by frequency-doubling the second harmonic or sum-frequency mixing the fundamental with the third harmonic to produce 266 nm [55], is also available in commercial Nd:YAG systems. The development of efficient UV generation from the Nd:YAG laser has been instrumental in the resurgence of interest in the OPO. In particular, the third harmonic of the Nd:YAG laser has been used extensively to pump OPOs. The first urea OPO was demonstrated using the third harmonic of a Nd:YAG laser [56] to generate light in the visible and near-infrared. From then on, as new materials became available, the harmonics of the Nd:YAG laser were often the first pump sources to successfully demonstrate oscillation in the new crystal [57].

Other Nd-doped hosts which have been used as pump sources for the OPO include YLF [58] and YAP (or $YAlO_3$) [59]. Both have fundamental wavelengths in the 1 μm region, can be readily frequency-converted to the visible and UV and, like YAG, can

be diode-pumped [60]-[62]. It is particularly this last feature of these laser materials which have enabled them to progress with the development of the OPO, improving the efficiency of the OPO and making it a more compact device. Ultimately, as the cost/Watt of laser diodes fall, diode-pumped Nd-doped lasers will replace flashlamps for many applications and become the common pump source for the OPO.

Indeed, the diode laser has progressed to such an extent recently that a direct-diode-pumped OPO has been demonstrated by two research groups. Past attempts have failed because of the stringent constraints imposed on the spatio-spectral structure of the pump beam by the OPO crystal. However, in the first ever demonstration of its kind, a doubly resonant KTP OPO was pumped with a 210 mW diode to produce 12 mW of signal [63]. A few months later, a diode-pumped, degenerate, periodically poled [64] $LiNbO_3$ OPO pumped with a 977 nm master oscillator/power amplifier at 370 mW was reported with a threshold of 98 mW and peak output powers of 64 mW of signal/idler radiation at 1.96 μm [65].

1.4 A Review of Contemporary OPOs

It is the development of new non-linear crystals which has led to the resurgence of interest in the OPO in recent years. In this section, the review of contemporary OPOs begins in the mid-1980's, with the development of BBO by a group of Chinese investigators under the supervision of Professor Chuangtian Chen at Fujian Institute of Research on the Structure of Matter. Discussions on LBO and BBO will make up the bulk of the review, since these materials are capable of parametric generation into the visible, and BBO is covered in greater depth again, since it is this material with which this thesis is concerned.

Since its development, BBO has been reviewed extensively [66]-[69] and has proved to be an excellent material for the generation of widely tunable light in the UV, visible and the near infrared. The most versatile BBO OPO pumping scheme is currently the 355 nm pumped oscillator. This OPO can generate continuously tunable radiation from 412 nm to 2.55 μm [70] with a total conversion efficiency of 24 %, and by double passing the pump in the cavity, efficiencies of 41 % have been observed [71]. Similar external efficiencies of 40 % have been seen using noncollinear phase matching to counter the effects of Poynting vector walk-off within the crystal [38] and, using two crystals in the cavity, conversion efficiencies of 32 % have been demonstrated [72]. The efficiency of this OPO is currently limited to the pulse duration of the pump light which limits the number of round-trip passes the resonant signal (or idler) photons can undergo in the cavity. With pump pulses of typically 10 ns in duration, the number of round-trips of the resonant wave is less than that needed to fully saturate the pump to reach the upper efficiency limit of over 60 % [66].

Tuning down to the UV is well within the capability of BBO with a sufficiently short pump wavelength. The fourth harmonic of a Nd:YAG laser at 266 nm has successfully been used to generate a wavelength range of 330 nm to 1.370 μm [73] and, although problems may arise from mirror-coating damage at this pump wavelength, intracavity steering optics can largely eliminate this risk.

Without line-narrowing, the BBO OPO spectral width can vary between 1.5 nm and 10 nm or more as it is tuned from 450 nm towards degeneracy. By phase matching the BBO OPO in the type II scheme, the overall linewidth variation over the same tuning range is 0.05 nm to 0.3 nm [74]. Clearly, for medium to high resolution spectroscopy, the linewidth needs to be significantly less than that produced by the free-running OPO. Noticeable progress has been made in this area, and the BBO OPO is now challenging other laser systems, such as the dye laser, as a laboratory spectroscopic tool. Single-longitudinal mode operation of the BBO OPO has been reported with

linewidths as low as 400 MHz by injection-seeding the cavity [27]-[28] and single-mode operation has been observed using a grazing incidence configuration [75]-[76] with similar products now available on the market [77]. Table 1.1 summarises some of the significant BBO parametric oscillators developed with respect to their characterised parameters.

It is clear from the table that 355 nm has proved to be the most popular and versatile pump wavelength for the BBO OPO over several orders of magnitude of pump pulse duration. The table also compares the performances of the ultra-narrow linewidth OPOs (<0.017 cm^{-1} or ~500 MHz), and indicates the method used to narrow the line. It is apparent that injection seeding the parametric oscillator ("In. seed" in the column entitled "Cavity type") can produce a single-longitudinal mode with relatively high external efficiency, but has a tuning range limited to that of the seed of ~10 nm (in the case of a SLM laser diode).

The coupled cavity ("Couple" in the "Cavity type" column), on the other hand, has an external efficiency which is an order of magnitude less than the seeded OPOs, but is capable of generating a single-mode over an impressive tuning range. This coupled cavity is discussed in greater depth in chapter seven.

Pump nm	**Pulse length**	**Tuning μm**	**Xtal length mm**	**Con eff %**	**Line-width**	**Cavity type**	**Ref**
527	190 fs	0.7-1.8	5.8	3	~10 nm	Synch	[78]
308	17 ns	0.37-0.42	20	50*	/	SRO	[79]
308	12 ns	0.422-0.477	7.0	5.4	/	SRO	[52]
308	17 ns	0.36-0.62	20	9*	SLM	Etalon	[54]
308	10 ns	0.35-2.37	12	10	2-10 nm	SRO	[53]

Table 1.1 continued.....

Pump nm	Pulse length	Tuning range μm	Xtal length mm	Con .eff %	Line-width	Cavity type	Ref
360	30 ps	0.4-3.17	12	8.5	0.24 nm	Grating	[59]
532	85 ps	0.68-2.4	7.2	30	~10 nm	Synch	[80]
532	25 ps	0.65-1.02	10	30	0.35 nm	Synch	[81]
532	12 ns	0.94-1.22	9	10	/	SRO	[57]
532	20 ns	0.7-2.2	12	40*	8-12 nm	SRO	[82]
355	65 ps	0.59-0.89	11.8	0.05	2.4 cm^{-1}	Grating	[83]
355	9 ns	0.67-0.69	5	20	0.017 cm^{-1}	In. seed	[28]
355	5 ns	0.61-0.62	12	17	0.013 cm^{-1}	In.seed	[27]
355†	8 ns	0.48-0.63	17, 12	12	2 cm^{-1}	SRO	[74]
355	8 ns	0.48-0.63	11.5	9.4	/	SRO	[37]
355	6 ns	0.41-2.5	12	24	<0.1 cm^{-1}	SRO	[70]
355	10 ns	0.41-2.4	10	41	0.2-5 nm	P. refl.	[71]
355	8 ns	0.42-2.3	11.5, 9.5	9	1.2 cm^{-1}	Grating	[72]
355	5 ns	/	12	32	0.1 cm^{-1}	In. seed	[29]
355	6 ns	0.46-1.5	12	25	5 nm	SRO	[38]
355	6 ns	0.57-0.94	14	1.3	0.007 cm^{-1}	Couple	[76]
355	19 ns	0.47-1.4	14, 14	1.9	0.3 cm^{-1}	Grating	[75]
266	9 ns	0.33-1.37	20.5	/	/	SRO	[73]

*Table 1.1. A summary of some BBO OPOs pumped with various sources and optimised for certain parameters indicated in the table. KEY: * = internal efficiency, synch = synchronous pumping, P.refl = with pump reflection, couple = cavity described in chapter seven. All are type I phase matched, except for †.*

In many respects, lithium triborate (LBO) corrected many of the problems associated with BBO; namely, it is non-hygroscopic, has a smaller walk-off angle and a higher

damage threshold [84]-[85]. However, its smaller non-linear coefficient means it is less suited to high power, high threshold cavities and its smaller birefringence tends to limit its phase matching spectral range. LBO, a biaxial crystal, has the advantage that it can be phase matched in a number of different ways; type I and type II noncritical phase matching (NCPM) are possible and tuning is accomplished by changing the temperature of the crystal. NCPM allows for large crystal acceptance angles for frequency conversion to the visible and infrared [86] and zero walk-off in the crystal. In addition to NCPM, type I critical phase matching is also possible.

The first demonstration of the LBO OPO involved type II NCPM using a frequency-doubled Nd:YAG laser as the pump source to generate tunable light from 950 nm to 1.006 μm [87]. Since then, the LBO OPO has developed into a sophisticated device capable of generating CW radiation by noncritical type I [26] and type II [88] phase matching producing tunable radiation in the near-infrared with a 514.5 nm argon-ion laser, and in the blue/green when pumped with an argon-ion laser at 364 nm [89]. Pulsed devices have also generated blue light in NCPM schemes, such as 355 nm pumping a type II phase matched LBO OPO to produce tunable radiation from 457 nm to 481 nm with an external efficiency of 27 % [90]. Further pumping into the UV, at 266 nm, has produced a wavelength of 310 nm with an external efficiency of 10 % [91]. Other researchers have combined the high efficiency associated with NCPM with the faster tuning type I phase matching to generate tunable radiation from 652 nm to 2.65 μm with pump radiation at 523.5 nm and depletions of 20 % [58].

Although NCPM LBO OPOs tend to have rather limited tuning ranges, critical phase matching can also take place in the crystal to generate tuning ranges comparable to that of BBO. Type I critical phase matching of LBO pumped at 355 nm can generate a wavelength range from 435 nm to 1.922 μm, with a respectable conversion efficiency of 22 % in a 16 mm long crystal [92].

LBO has also been used extensively as a frequency converter of short-pulse lasers. Owing to its favourable NCPM capability, LBO can be tuned in a synchronously-pumped cavity without tilting the crystal, an act which requires the cavity to be readjusted [93]. Efficient generation of 33 ps pulses has been seen from a picosecond-pumped type I NCPM LBO OPO tunable from 0.909 μm -1.235 μm using a frequency-doubled, Q-switched diode-laser pumped Nd:YLF laser [94]. Critical phase matching has also been demonstrated in similar cavities, producing considerably larger tuning ranges but being encumbered by angle-tuning [95]-[96].

Finally, organic materials have played a small, but significant, role in the development of the modern OPO. Urea, which has been mentioned earlier, awoke the field in the 1980's and recently deuterated L-arginine phosphate (d-LAP) has been reported which has the potential of being a high efficiency, high damage threshold frequency converter and it can be grown in large sizes [97]-[98]. Its phase matching properties have been assessed in terms of second harmonic generation of 1.064 μm, and these have proved promising [99]. In fact, in 1993, Robertson *et al* reported optical parametric oscillation in d-LAP for the first time [100]. Unfortunately, organic materials are often characterised as being hygroscopic, which requires more elaborate crystal housing to prevent crystal-contact with moist air. However, they also tend to have high non-linear coefficients. Meta-nitroaniline (m-NA), for example, has a type I effective non-linear coefficient for SHG of 1.064 μm of 10 pm/V [101] and N-(4-nitrophenyl)-(L)-prolinol (NPP) has one of the highest non-linear coefficients of any material transparent in the range 510 nm to 1.65 μm, with d_{21} = 56.5 pm/V [102]-[103]. In fact, near-infrared optical parametric oscillation has been demonstrated in NPP, tunable from 900 nm to 1.7 μm [104]. If the problems of chemical instability are overcome, organic crystals could play a much greater role in the future.

1.5 Laser Isotope Separation

By combining the properties of tunability and narrow linewidth in an intense laser beam, isotopes of a particular element can be selectively excited or ionised. In this way, the abundance of a rare isotope can be increased. The enrichment of rare isotopes has applications in the medical field as well as the nuclear industry, and it is with the latter case that this work is predominately associated.

The ^{235}U isotope has an odd-even nucleus and, as a result, is much less stable than the naturally dominant ^{238}U isotope. It is, therefore, ^{235}U that undergoes fission in the nuclear reactor process. Most reactors require enrichment from the naturally occurring 0.7 % abundance to around 3 % [105]. Currently, around 90 % of the enriched uranium world-wide is produced by gaseous diffusion. This technique is, however, inefficient and requires around 1000 stages of preparation to reach the required separation. Separation by the method of gaseous centrifuse can increase the efficiency and has up to ten times the production capacity of diffusion.

However, it has been predicted that laser isotope separation (LIS) could increase the production by a further factor of 100 [106]. Two methods of enrichment using lasers exist. These are Atomic Vapour Laser Isotope Separation (AVLIS) using atoms of uranium metal and Molecular Laser Isotope Separation (MLIS) of the UF_6 molecule. Recently, however, the uranium LIS programmes both in Britain and the United States have undergone a 'stop-start' process as the need for enriched uranium is assessed on the world market. Currently, the expertise gained during the AVLIS program at Urenco (Capenhurst) plc is being applied to other isotopes such as strontium for medical applications.

1.5.1 The Isotope Shift

The difference in the nuclear size of the ^{235}U and ^{238}U isotopes causes small variations in their transition energies, called the isotope shift (IS). The AVLIS technique makes use of the IS. Calculating the magnitude of the IS for the lightest elements is possible, but for higher atomic numbers the problem becomes too complex. An estimate of the shift cam be made by considering the following parameters and their effects.

The nuclear mass has an effect on the reduced mass of the atomic electrons causing a mass dependence on the atomic level energies, or "mass effect" [107]. The mass effect is proportional to $1/M^2$, for a nuclear mass M, and the contribution to IS falls off rapidly with increasing atomic number Z. However, for values of Z>100, the magnitude of the IS begins to increase due to a "volume shift" which is proportional to the volume occupied by the atom. In the case of uranium, the IS is dominated by the volume shift.

In addition to this shift, the energy levels of the isotope may split as a result of the orientational potential energy of its nuclear magnetic dipole moment associated with the nucleus in the magnetic field associated with the motion of the electrons. Splitting may also occur from the interaction of the electric quadrupole moment Q of the nucleus in the atomic electric field. This splitting of the atomic energy levels is referred to as hyperfine structure. The energy shift, ΔE_μ, arising from the interaction of the nuclear magnetic dipole moment μ_I with the magnetic field B_{ele}, caused by the motion of the charged electrons, is

$$\Delta E_\mu = -\langle \mu_I \cdot B_{ele} \rangle \qquad (1.1)$$

Clearly, hyperfine structure caused by this interaction only exists if the nucleus exhibits a net magnetic dipole moment μ_I.

For nuclei whose charge distribution departs from spherical symmetry, the electric quadrupole moments Q≠0 and the nucleus will have an orientational potential in the atomic field which is not spherically symmetrical. The energy level splitting ΔE_Q associated with the interaction of the electric quadrupole moment with the electric field dV_e/dz of the orbiting electrons is given by

$$\Delta E_Q \propto eQ\left\langle \frac{d^2V_e}{dz^2} \right\rangle \tag{1.2}$$

In the case of uranium, the energy levels of ^{235}U are split by both the interactions described above, and hyperfine structure is observed, whereas ^{238}U exhibits no hyperfine structure. The lack of hyperfine structure in ^{238}U results from the fact that it is an even-even nucleus, that is, the atomic number Z and the mass number A are both even (Z=92, A=238) giving a resultant nuclear spin of I=0 and, therefore, $Q=\mu_I=0$ leading to a single spectral line. The ^{235}U isotope, on the other hand, is characterised by a "spectral signature" as a result of having an even-odd nucleus (Z=92, A=235) giving a resultant spin of I=7/2, and both Q and μ_I are non-zero, leading to (2I+1)=8 energy levels.

1.5.2 Laser Enrichment of Isotopes

An ideal laser isotope process may involve a spectrally narrow laser source tuned to excite the electrons in one of the isotopes but not in the other. A beam of mixed-isotope neutral atoms pass through a laser beam which excites the electrons of one of the isotopes to a particular excited state or ionised state. The rare ions may then be separated from the unwanted species.

The isotope shift of the atomic line between ^{235}U and ^{238}U is 7 to 10 GHz, so a laser linewidth of typically less than one GHz is required. Moreover, the laser linewidth

must be able to resolve the hyperfine structure of ^{235}U. The separation of the hyperfine structure splitting in ^{235}U is ~100 MHz [105] and the radiation must be spectrally pure (single-longitudinal mode). The two ionisation routes of most interest in the ^{235}U isotope are the two-photon process and the three-photon process. The two photon route falls in the blue region of the spectrum and the three photon route requires orange radiation.

1.6 Thesis Outline

In this thesis, chapter two details the basic theory of the optical parametric interaction and this forms the basis from which other ideas are drawn throughout the work. Chapter three compares LBO and BBO in terms of their suitability for line narrowed operation, by attempting to predict their performance in such a cavity. Chapter four details the ideas and theory of noncollinear phase matching, while the following chapter sets out the experimental results of noncollinear phase matching in BBO at two pump wavelengths. Chapters six and seven are concerned with the grazing incidence OPO and the requirements of attaining single mode in the OPO and, in chapter seven, the coupled cavity grazing incidence OPO is demonstrated. Finally, chapter eight concludes the thesis and a discussion on future work is given.

References

[1] T. H. Maiman "Stimulated optical radiation in ruby" Nature, 187, 493, (1960)

[2] P. A. Franken, A. E. Hill, C. W. Peters and G. Weinreich "Generation of optical harmonics" Phys. Rev. Lett., 7, 118, (1961)

[3] J. A. Giordmaine "Mixing of light beams in crystals" Phys. Rev. Lett., 8,19, (1962)

[4] J. A. Armstrong, N. Bloembergen, J. Ducuing and P. S. Pershan "Interactions between light waves in a non-linear dielectric" Phys. Rev., 127, 1918, (1962)

[5] N. M. Kroll "Parametric amplification in spatially extended media and application to the design of tunable oscillators at optical frequencies" Phys. Rev., 127, 1207, (1962)

[6] W. H. Louisell, A. Yariv and A. E. Siegman "Quantum fluctuations and noise in parametric processes I" Phys. Rev., 124, 1645, (1961)

[7] J. A. Giordmaine and R. C. Miller "Tunable coherent parametric oscillation in $LiNbO_3$ at optical frequencies" Phys. Rev. Lett., 14, 973, (1965)

[8] R. L. Byer "Quantum electronics: A Treatise" Non-linear optics I, part B, Academic Press, New York, (1975)

[9] S. E. Harris "Tunable optical parametric oscillators" Proc. IEEE, 57, 2096, (1969)

[10] S. J. Brosnan and R. L. Byer "Optical parametric oscillator threshold and linewidth studies" J. Quantum Electron., 15, 415, (1979)

[11] J. E. Bjorkholm "Some spectral properties of doubly and singly resonant pulsed optical parametric oscillators" Appl. Phys. Lett., 13, 399, (1968)

[12] J. E. Bjorkholm "Efficient optical parametric oscillation using doubly and singly resonant cavities" Appl. Phys. Lett., 13, 53, (1968)

[13] R. L. Herbst, R. N. Fleming and R. L. Byer "A 1.4-4 μm high-energy angle-tuned $LiNbO_3$ parametric oscillator" Appl. Phys. Lett., 25, 520, (1974)

[14] R. C. Miller and W. A. Nordland "Tunable $LiNbO_3$ optical oscillator with external mirrors" Appl. Phys. Lett., 10, 53, (1967)

[15] R. W. Wallace "Stable, efficient, optical parametric oscillators pumped with doubled Nd:YAG" Appl. Phys. Lett., 17, 497, (1970)

[16] J. M. Yarborough and G. A. Massey "Efficient high-gain parametric generation in ADP continuously tunable across the visible spectrum" Appl. Phys. Lett., 18, 438, (1971)

[17] R. L. Herbert and R. L. Byer "Singly resonant CdSe infrared parametric oscillator" Appl. Phys. Lett., 21, 189, (1972)

[18] R. G. Smith, J. E. Geusic, H. J. Levinstein, J. J. Rubin, S. Singh and L. G. Van Uitert "Continuous optical parametric oscillation in $Ba_2NaNb_5O_{15}$" Appl. Phys. Lett., 12, 308, (1968)

[19] R. L. Byer, M. K. Oshman, J. F. Young and S. E. Harris "Visible CW parametric oscillator" Appl. Phys. Lett., 13, 109, (1968)

[20] R. L. Byer, A. Kovrigin and J. F. Young "A CW ring-cavity parametric oscillator" Appl. Phys. Lett., 15, 136, (1969)

[21] K. Kato "3547-Å pumped parametric oscillator in RD*A" IEEE J. Quantum Electron., 12, 939, (1975)

[22] L. B. Kreuzer "Single-mode oscillation of a pulsed singly resonant optical parametric oscillator" Appl. Phys. Lett., 15, 263, (1969)

[23] J. Falk and J. E. Murray "Single-cavity noncollinear optical parametric oscillation" Appl. Phys. Lett., 14, 245, (1969)

[24] J. D. Kafka, M. L. Watts and J. W. Pieterse "A synchronously pumped optical parametric oscillator producing 40 fs pulses" Conference on Lasers and Electro-Optics Post-deadline, CPD-32, (1993)

[25] J. M. Dudley, D. T. Reid, M. Ebrahimzadeh and W. Sibbett "Characteristics of a noncritically phasematched Ti:sapphire pumped femtosecond optical parametric oscillator" Opt. Commun., 104, 419, (1994)

[26] F. G. Colville, A. J. Henderson, M. S. Padgett, J. Zhang and M. H. Dunn "Continuous-wave parametric oscillation in lithium borate" Opt. Lett., 18, 205, (1993)

[27] J. M. Boon-Engering, W. E. van der Veer and J. W. Gerritsen "Bandwidth studies of an injection-seeded β-barium borate optical parametric oscillator" Opt. Lett., 20, 380, (1995)

[28] P. Bourdeon, M. Péalat and U. I. Fabelinsky "Continuous-wave diode-laser injection-seeded β-barium borate optical parametric oscillator: a reliable source for spectroscopic studies" Opt. Lett., 20, 474, (1995)

[29] J. G. Haub, M. J. Johnson and B. J. Orr "Continuously tunable, injection-seeded β -barium borate optical parametric oscillator: spectroscopic applications" Appl. Phys. Lett., 56, 1718, (1991)

[30] J. G. Haub, R. M. Heutschel, M. J. Johnson and B. J. Orr "Controlling the performance of a pulsed optical parametric oscillator to suit the spectroscopic

application" Submitted to J. Opt. Soc. Am. B., Special Issue on Parametric Devices April (1995)

[31] T. D. Gardiner, M. J. T. Milton and P. T. Woods "Injection seeding of an infrared optical parametric oscillator with a tunable diode laser" Conference on Quantum Electronics 11, Tech. Digest 112, Belfast, (1993)

[32] W. R. Rapoport and C. P. Khattak "Titanium sapphire laser characteristics" Appl. Opt., 27, 2677, (1988)

[33] D-W. Chen and J. T. Lin "Temperature-tuned phase-matching properties of $LiNbO_3$ for Ti:sapphire laser frequency doubling" IEEE J. Quantum Electron., 29, 307, (1993)

[34] M. Stalder, B. H. T. Chai and M. Bass "Flashlamp pumped Cr:$LiSrAlF_6$ laser" Appl. Phys. Lett., 58, 216, (1991)

[35] F. Balembois, F. Faloz, P. Georges and A. Brun "Efficient diode-pumped LiSAF laser in a continuous wave and actively mode locked regime" Opt. Soc. Am. Proc. on Advanced Solid State Lasers, 20, 236, (1994)

[36] R. Mellish, P. M. W. French, J. R. Taylor, P. J. Delfyett and L. T. Florez "All-solid-state femtosecond diode-pumped Cr:LiSAF laser" Opt. Soc. Am. Proc. on Advanced Solid State Lasers, 20, 239, (1994)

[37] L. K. Cheng, W. R. Bosenberg and C. L. Tang "Broadly tunable optical parametric oscillator in β-BaB_2O_4" Appl. Phys. Lett., 53, 175, (1988)

[38] L. A. W. Gloster, Z. X. Jiang and T. A. King "Characterisation of a Nd:YAG-pumped β-BaB_2O_4 optical parametric oscillator in collinear and noncollinear phasematched configurations" IEEE J. Quantum Electron., 30, 2961, (1994)

[39] J. S. Krasinski and D. F. Heller "Alexandrite laser pumped by semiconductor lasers" Appl. Phys. Lett., 56, 2288, (1990)

[40] V. Petricevic, A. Seas and R. R. Alfano, Laser Focus World, November, 109, (1990)

[41] Z. X. Jiang, L. A. W. Gloster, H. Ahmad and T. A. King "Laser characteristics of chromium doped forsterite with Ti:sapphire laser excitation" J. Mod. Opt., 40, 1411, (1993)

[42] P. M. W. French, N. H. Rizvi, R. J. Taylor and A. V. Shestakov "Continuous-wave mode-locked Cr^{4+}:YAG laser" Opt. Lett., 18, 39, (1993)

[43] R. C. Stoneman and L. Esterowitz "Efficient, broadly tunable, laser-pumped Tm:YAG and Tm:YSGG CW lasers" Opt. Lett., 15, 486, (1990)

[44] M. Ebrahimzadeh, G. Robertson and M. H. Dunn "Efficient ultraviolet LiB_3O_5 optical parametric oscillator" Opt. Lett., 16, 767, (1991)

[45] P. E. Power, C. L. Tang and L. K. Cheng "High-repetition-rate femtosecond optical parametric oscillator based on $CsTiOAsO_4$" Opt. Lett., 19, 37, (1994)

[46] M. Ebrahimzadeh, S. French, W. Sibbett and A. Miller "Picosecond Ti:sapphire-pumped optical parametric oscillator based on LiB_3O_5" Opt. Lett., 20, 166, (1995)

[47] A. Nebel, C. Fallnich, T. H. Herrman, C. H. Gräβer, D. Wang, R. Beigang and R. Wallenstein "Synchronously pumped continuous wave mode-locked picosecond and femtosecond optical parametric oscillator" Opt. Soc. Am. Proc. on Advanced Solid State Lasers, 20, 410 (1994)

[48] G. R. Holtom, R. A. Crowell and X. S. Xie "Non-critically phasematched femtosecond optical parametric oscillator near 3 microns" Opt. Soc. Am. Proc. on Advanced Solid State Lasers, 20, 407, (1994)

[49] M. Ebrahimzadeh and M. H. Dunn "Optical parametric fluorescence and oscillation in urea using an excimer laser" Opt. Commun., 69, 161, (1989)

[50] A. J. Henderson, M. Ebrahimzadeh and M. H. Dunn "Characterisation of urea optical parametric oscillators pumped by excimer lasers" J. Opt. Soc. Am. B, 7, 1402, (1990)

[51] M. Ebrahimzadeh, M. H. Dunn and F. Akerboom "Highly efficient visible urea optical parametric oscillator pumped by a XeCl excimer laser" Opt. Lett., 14, 560, (1989)

[52] H. Komine "Optical parametric oscillation in a beta-barium borate crystal pumped by a XeCl excimer laser" Opt. Lett., 13, 643, (1988)

[53] M. Ebrahimzadeh, A. J. Henderson and M. H. Dunn "An excimer-pumped β-BaB_2O_4 optical parametric oscillator tunable from 354 nm to 2.370 μm" IEEE J. Quantum Electron., 26, 1241, (1990)

[54] G. Robertson, A. J. Henderson and M. H. Dunn "Efficient, single-axial mode oscillation of a beta barium borate optical parametric oscillator pumped by an excimer laser" Appl. Phys. Lett., 62, 123, (1993)

[55] R. Wu, J. D. Myers and S. J. Hamlin "Intracavity fourth harmonic generation using three pieces of LBO in a Nd:YAG laser" Opt. Soc. Am. Proc. on Advanced Solid State Lasers, 20, 377, (1994)

[56] W. R. Donaldson and C. L. Tang "Urea optical parametric oscillator" Appl. Phys. Lett., 44, 25, (1984)

[57] Y. X. Fan, R. C. Eckardt, R. L. Byer, C. Chen and A. D. Jiang "Barium borate optical parametric oscillator" IEEE J. Quantum Electron., 25, 1196, (1989)

[58] M. Ebrahimzadeh, G. J. Hall and A. L. Ferguson "Singly resonant, all-solid-state, mode-locked LiB_3O_5 optical parametric oscillator tunable from 652 nm to 2.65 μm" Opt. Lett., 17, 652, (1992)

[59] S. Burdalis, R. Grigonis, A. Piskarskas, G. Sinkevicius, V. Sirutkaitis, A. Fix, J. Nolting and R. Wallenstein "Visible optical parametric oscillation in synchronously pumped beta-barium borate" Opt. Commun., 74, 398, (1990)

[60] R. J. Shine, A. J. Alfrey, R. L. Byer "Conduction-cooled, continuous wave, diode-pumped Nd:YAG mini-slab laser" Opt. Soc. Am. Proc. on Advanced Solid State Lasers, 20, 6, (1994)

[61] M. D. Selker, R. S. Afzal and P. Reicher "Automatically TEM_{00} mode selected side pumped Nd:YLF laser" Opt. Soc. Am. Proc. on Advanced Solid State Lasers, 20, 11 (1994)

[62] G. A. Rines, R. A. Schwark and P. F. Moulton "Diode-laser-pumped, continuous wave, intracavity-doubled Nd:YLF laser" Opt. Soc. Am. Proc. on Advanced Solid State Lasers, 20, 336, (1994)

[63] Reported by R. Wallenstein "Diode laser pumped NCPM CW KTP optical parametric oscillator" in place of scheduled paper, Conference on Lasers and Electro-Optics-Europe, CWA7, (1994)

[64] L. E. Myers, G. D. Miller, R. C. Eckardt, M. M. Fejer, R. L. Byer, and W. R. Bosenberg "Quasi-phase-matched 1.064μm pumped optical parametric oscillator in bulk periodically poled $LiNbO_3$" Opt. Lett., 20, 52, (1995)

[65] L. E. Myers, R. C. Eckardt, M. M. Fejer, R. L. Byer, J. W. Pierce and R. G. Beausoleil "CW diode pumped optical parametric oscillator in bulk periodically poled $LiNbO_3$" Opt. Soc. Am. Proc. on Advanced Solid State Lasers, PD9-1, (1995)

[66] C. L. Tang, W. R. Bosenberg, T. U. Kachi, R. J. Lane and L. K. Chen "Optical parametric oscillators" Proc. IEEE, 80, 365, (1992)

[67] A. Borsutzky, R. Brünger, C. L. Huang and R. Wallenstein "Harmonic and sum-frequency generation of pulsed laser radiation in BBO, LBO and KD*P" Appl. Phys. B, 52, 55, (1992)

[68] D. Eimerl, L. Davis, S. Velsko, E. K. Graham and A. Zalkin "Optical, mechanical and thermal properties of barium borate" J. Appl. Phys., 62, 1968, (1987)

[69] D. N. Nikogosyan "Beta barium borate (BBO): a review of its properties and applications" Appl. Phys., A, 52, 359, (1991)

[70] Y. X. Fan, R. C. Eckardt, R. L. Byer, J. Nolting and R. Wallenstein "Visible BaB_2O_4 optical parametric oscillator pumped at 355 nm by a single-axial-mode pulsed source" Appl. Phys. Lett., 53, 2014, (1988)

[71] Y. Wang, Z. Xu, D. Deng, W. Zheng, X. Liu, B. Wu and C. Chen "Highly efficient, visible β-BaB_2O_4 optical parametric oscillator with pump reflection" Appl. Phys. Lett., 58, 1461, (1991)

[72] W. R. Bosenberg, W. S. Pelouch and C. L. Tang "High-efficiency and narrow-linewidth operation of a two-crystal β-BaB_2O_4 optical parametric oscillator" Appl. Phys. Lett., 55, 1952, (1989)

[73] W. R. Bosenberg, L. K. Cheng and C. L. Tang "Ultraviolet optical parametric oscillation in β-BaB_2O_4" Appl. Phys. Lett., 54, 13, (1989)

[74] W. R. Bosenberg and C. L. Tang "Type II phasematching in a β-barium borate optical parametric oscillator" Appl. Phys. Lett., 56, 1819, (1990)

[75] L. A. W. Gloster, I. T. McKinnie, Z. X. Jiang, T. A. King, J. M. Boon-Engering, W. E. van der Veer and W. Hogervorst "A narrow band β-BaB_2O_4 optical parametric oscillator in a grazing incidence configuration" Submitted to J. Opt. Soc. Am B. Special Issue on Parametric Devices, March, (1995)

[76] J. M. Boon-Engering, L. A. W. Gloster, W. E. van der Veer, I. T. McKinnie, W. Hogervorst and T. A. King, "A highly efficient, single-longitudinal mode β-BaB_2O_4 optical parametric oscillator with a new cavity design" Submitted to Opt. Lett., May, (1995)

[77] see, for example, Quanta-Ray MOPO-700 series Optical Parametric Oscillators, Spectra-Physics Lasers, Mountain View, CA

[78] R. Laenen, H. Greaner and A. Laubereau "Broadly tunable femtosecond pulses generated by optical parametric oscillation" Opt. Lett., 15, 971, (1990)

[79] G. Robertson, A. Henderson, and M. H. Dunn "Attainment of high efficiencies in optical parametric oscillators" Opt. Lett., 16, 1584, (1991)

[80] L. J. Bromley, A. Guy and D. C. Hanna "Synchronously pumped optical parametric oscillation in beta barium borate" Opt. Commun., 67, 316, (1988)

[81] G. P. Banfi, M. Ghigliazza and P. Di. Trapani "Bandwidth and beam quality of barium borate parametric oscillator synchronously pumped by active-passive mode-locked Nd:YAG laser " Opt. Commun., 89, 63, (1992)

[82] L. A. W. Gloster, I. T. McKinnie and T. A. King, "Noncollinear phase matching in a type I barium borate optical parametric oscillator" Opt. Commun., 112, 328, (1994)

[83] A. Piskarskas, V. Smilgevicius, A. Umbrasas, A. Fix and R. Wallenstein "Parametric oscillation in beta-barium borate synchronously pumped by the third harmonic of a continuously excited mode-locked and Q-switched Nd:YAG laser " Opt. Commun., 77, 335, (1990)

[84] S. Lin, Z. Sun, B. Wu and C. Chen "The non-linear optical properties of a LiB_3O_5 crystal" J. Appl. Phys., 67, 634, (1990)

[85] C. Chen, Y. Wu, A. Jiang, B. Wu, G. You, R. Li and S. Lin "New non-linear-optical crystal: LiB_3O_5" J. Opt. Soc. Am. B. 6, 616, (1989)

[86] J. T. Lin, J. L. Montgomery and K. Kato "Temperature-tuned noncritically phase-matched frequency conversion in a LiB_3O_5 crystal" Opt. Commun., 80, 159, (1990)

[87] K. Kato "Parametric oscillation in LiB_3O_5 pumped at 0.532 μm" IEEE J. Quantum Electron., 26, 2043, (1990)

[88] G. Robertson, M. J. Padgett and M. H. Dunn "Continuous-wave singly resonant pump-enhanced type II LiB_3O_5 optical parametric oscillator" Opt. Lett., 19, 1735, (1994)

[89] F. G. Colville, M. J. Padgett, A. J. Henderson, J. Zhang and M. H. Dunn "Continuous-wave parametric oscillator pumped in the ultraviolet" Opt. Lett., 18, 1065, (1993)

[90] Y. Cui, M. H. Dunn, C. J. Norrie, W. Sibbett, B. D. Sinclair, Y. Tang and J. A. C. Terry "All-solid-state optical parametric oscillator for the visible" Opt. Lett., 17, 646, (1992)

[91] Y. Tang, Y. Cui and M. H. Dunn "Lithium triborate optical parametric oscillator pumped at 266 nm" Opt. Lett., 17, 192, (1992)

[92] Y. Wang, Z. Xu, D. Deng W. Zheng, B. Wu and C. Chen "Visible optical parametric oscillation in LiB_3O_5" Appl. Phys. Lett., 59, 531, (1991)

[93] S. D. Butterworth, M. J. McCarthy and D. C. Hanna "Widely tunable synchronously pumped optical parametric oscillator" Opt. Lett., 18, 1429, (1993)

[94] M. Ebrahimzadeh, G. J. Hall and A. I. Ferguson "Temperature-tuned noncritically phase-matched LiB_3O_5 optical parametric oscillator" Appl. Phys. Lett., 60, 1421, (1992)

[95] J. Y. Zhang, J. Y. Huang, Y. R. Shen, C. Chen and B. Wu "Picosecond optical parametric amplification in lithium triborate" Appl. Phys. Lett., 58, 213, (1991)

[96] V. Kubecek, Y. Takagi, K. Yoshihara and G. C. Reali "Lithium triborate picosecond optical parametric oscillator" Opt. Commun., 91, 93, (1992)

[97] D. Eimerl, S. Velsko, L. Davis, F. Wang, G. Loiacono and G. Kennedy "Deuterated L-arginine phosphate: A new efficient non-linear crystal" IEEE J. Quantum Electron., 25, 179, (1989)

[98] A. Yokotani, T. Sasaki, K. Yoshida and S. Nakai "Extremely high damage threshold of a new non-linear crystal L-arginine phosphate and its deuterium compound" Appl. Phys. Lett., 55, 2692, (1989)

[99] C. E. Barker, D. Eimerl and S. Velsko "Temperature-insensitive phase matching for second harmonic generation in deuterated l-arginine phosphate" J. Opt. Soc. Am. B., 8, 2481, (1991)

[100] G. Robertson and M. H. Dunn "Deuterated L-arginine phosphate optical parametric oscillator" Conference on Lasers and Electro-Optics, CThS27, 508, (1993)

[101] G-F. Haung, J. T. Lin, G. Su, R. Jiang and S. Xie "Characterisation of the non-linear crystal meta-nitraniline (m-NA)" Opt. Commun., 89, 205, (1992)

[102] I. Ledoux, C. Lepers, A. Périgaud, J. Badan and J. Zyss "Linear and non-linear optical properties of N-4-nitrophenyl L-prolinol single crystals" Opt. Commun., 80, 2, (1990)

[103] P. Andreazza, D. Josse, F. Lefaucheux, M. C. Robert and J. Zyss "Structural investigations and optical properties of chiral N-(4-nitrophenyl)-(L)-propinol gel-grown crystals" Phys. Rev. B., 45, 7640, (1992)

[104] D. Josse, S. X. Dou, J. Zyss, P. Andreazza and A. Périgaud "Near-infrared optical parametric oscillation in a N-(4-nitrophenyl)-(L)-propinol molecular crystal" Appl. Phys. Lett., 61, 121, (1992)

[105] M. Clere and P. Plurien "Advanced uranium enrichment processes" Commission of the European Communities, June (1986)

[106] D. Massignon "Cycle du combustible et enrichissement de l'uranium" in Les Technique de l'Ingenieur B-3600-1 (1982)

[107] K. S. Krane "Introductory nuclear physics" John Wiley and Sons, New York, (1988)

Chapter 2

Theory of the Parametric Interaction

This chapter presents an overview of the basic theory of the optical parametric oscillator (OPO). The material in the following sections will be drawn on throughout the thesis. It documents the nature of the three wave interaction of the OPO, the non-linear coefficient and phase matching in both uniaxial and biaxial crystals. The principles of momentum mis-match and Poynting vector walk-off are also discussed.

Unless otherwise stated, SI units are used throughout this analysis. The unit of the non-linear coefficient is metres per volt. In the cgs system, the coefficient is measured in centimetres per statvolt. The conversion between the two unit systems is $d(SI) = 4\pi/3 \cdot 10^4 d(esu)$.

2.1 Three Wave Interaction

Provided that the intensity of the electric field is low, the polarisation response of the electrons in a optically transparent material can be considered to depend linearly on the electric field. That is, the electron polarisation P is linearly dependent upon the electric field E whose frequency is ω_1, such that

$$P(\omega_1) = \varepsilon_o \chi^{(1)} E(\omega_1) \tag{2.1}$$

where ε_0 is the permittivity of free space and $\chi^{(1)}$ is the dimensionless linear susceptibility. However, the linear dependence of the polarisation on the driving electric field is an approximation valid for low electric field intensities only. When the linear dependence breaks down in the presence of an intense electric field, other, higher

order terms, must be included for the electron polarisation to be described. Under such conditions, we write

$$P(\omega_1) = \varepsilon_o \chi^{(1)} E(\omega_1) + \varepsilon_o \chi^{(2)} E(\omega_2) E(\omega_3) + \varepsilon_o \chi^{(3)} E(\omega_4) E(\omega_5) E(\omega_6) \quad (2.2)$$
$$+ \text{higher order terms}$$

where $\omega_1 = \omega_2 + \omega_3 = \omega_4 + \omega_5 + \omega_6$. The coefficients $\chi^{(2)}$ and $\chi^{(3)}$ are the second and third order non-linear susceptibilities of the material. The concept of optical non-linearity has long been known, but it is only since the advent of the laser in 1960 that the high field intensities required to investigate the non-linear terms have become available. The particular interest here is with the second order susceptibility, since this is required for the parametric generation process and, incidently, the second harmonic and sum-frequency mixing processes too. A lack of inversion symmetry in the medium is necessary for all these interactions, since this ensures a non-zero second order susceptibility.

For a more complete analysis of the three wave interaction coupling waves of frequency ω_1, ω_2 and ω_3 it is necessary to invoke Maxwell's equations, and to include in them a term for the non-linear polarisation. Neglecting terms of third order and higher in equation 2.2, we obtain

$$P(\omega_1) = \varepsilon_o \chi^{(1)} E(\omega_1) + \varepsilon_o \chi^{(2)} E(\omega_2) E(\omega_3) \quad (2.3)$$

When equation 2.3 is substituted into Maxwell's equations [1] the wave equation of the E field in the non-linear medium is derived. In one dimension, this is shown to be

$$\frac{d^2 E}{dz^2} = \mu_o \varepsilon \frac{d^2 E}{dt^2} + \mu_o \frac{d^2 P}{dt^2} \quad (2.4)$$

With the interaction limited to the three frequencies ω_1, ω_2 and ω_3, the corresponding fields can be described in the form of travelling plane waves, in the form

$$E_i(z,t) = E_i(z)e^{i(\omega_i t - k_i z)} \tag{2.5}$$

where the subscript i is used to denote the three waves 1, 2 and 3, k_i is the wave vector for the waves and $E_i(z)$ is the slowly varying amplitude associated with the electric field $E_i(z,t)$. The solution to equation 2.4 has been described in detail by Armstrong *et al* [2] and several other authors [1] and [3] resulting in the coupled differential equations shown below in equations 2.6. Each equation gives the rate of change of amplitude at one frequency with distance as a function of the amplitudes of the other two frequencies, and of the phase difference between the polarisation wave and the electromagnetic wave.

$$\begin{aligned}
\frac{dE_1}{dz} &= -i\omega_1\sqrt{\frac{\mu_o}{\varepsilon_1}}\varepsilon_o\chi^{(2)}E_3E_2^*e^{-i(k_1-k_2-k_3)z} \\
\frac{dE_2^*}{dz} &= +i\omega_2\sqrt{\frac{\mu_o}{\varepsilon_2}}\varepsilon_o\chi^{(2)}E_1E_3^*e^{-i(k_1+k_2-k_3)z} \\
\frac{dE_3}{dz} &= -i\omega_3\sqrt{\frac{\mu_o}{\varepsilon_3}}\varepsilon_o\chi^{(2)}E_1E_2e^{-i(k_1+k_2-k_3)z}
\end{aligned} \tag{2.6}$$

where ε_1, ε_2 and ε_3 are the relative electric susceptibilities. The phase difference can be written as $\Delta k = k_3 - k_2 - k_1$. In the case of an OPO, the field denoted by the subscript 3 is referred to as the 'pump', and the two generated fields, E_1 and E_2, are called the 'signal' and the 'idler' waves. These terms are derived from the parametric amplifier and, as such, are a little confusing when applied to the oscillator. In the parametric amplifier, a weak signal and an intense pump are coincident on a non-linear medium, and the amplification of the signal is accompanied by the generation of the idler, such that $\omega_i = \omega_p - \omega_s$, where the subscripts i, s and p refer to the idler, signal and

pump waves. In the case of an OPO, both the signal and idler fields are generated simultaneously at the expense of the pump, in accordance with the conservation of energy $\omega_p = \omega_s + \omega_i$ and the concept of a 'signal' is accordingly somewhat redundant. This nomenclature is, however, frequently applied to the OPO and the convention adopted in this thesis is the signal and idler refer to the generated waves of higher and lower frequency, respectively.

Equations 2.6 contain a great deal of information concerning the nature of the three wave interaction in the OPO. If the pump depletion is considered to be small, then $dE_p/dz \approx 0$ and $E_p(0)=E_p(z)$. The first two equations can be rewritten to include a coupling constant κ for the signal and the idler, giving

$$\begin{aligned} \frac{dE_s}{dz} &= -i\kappa_s E_i^* E_p e^{-i\Delta kz} \\ \frac{dE_i^*}{dz} &= i\kappa_i E_p^* E_s e^{i\Delta kz} \end{aligned} \tag{2.7}$$

where $\kappa_s = \omega_s \sqrt{\mu_o \varepsilon_o}\chi^{(2)} E_p / n_s$ and a similar expression exists for the idler coupling coefficient κ_i. The single pass gain of the OPO, γ, is defined as

$$\gamma^2 = \gamma_o^2 - \left(\frac{\Delta k}{2}\right)^2$$

where $$\gamma_o^2 = \kappa_s \kappa_i = K I_p \tag{2.8}$$

and $$K = \frac{2\omega_i \omega_s \chi^2}{n_i n_s n_p \varepsilon_o c^3}$$

where I_p is the pump intensity in Wm^{-2}. The signal power can be expressed as a function of the single pass gain and the length of the gain medium by finding the solution to the coupled differential equations in 2.7. This has been carried out by several authors, for example [1], [3]-[4] and yields the signal intensity I_s from a crystal length l as

$$G = \left(\frac{I_s}{I_o}\right) = \gamma_o^2 l^2 \frac{\sinh^2\left\{\left[\gamma_o^2 - \left(\frac{\Delta k}{2}\right)^2\right]^{\frac{1}{2}} l\right\}}{\left[\gamma_o^2 - \left(\frac{\Delta k}{2}\right)^2\right] l^2} \tag{2.9}$$

where $$\gamma_o^2 = \frac{2\omega_s \omega_i \chi^2 I_p}{n_i n_s n_p \varepsilon_o c^3}$$

with the superscript (2) of the second order susceptibility dropped for clarity. The centre of the parametric gain profile occurs at $\Delta k=0$. At line centre, the signal power gain is

$$G = \sinh^2(l \cdot \gamma_o) \tag{2.10}$$

Thus, the single pass power gain G is given as the ratio of the signal intensity I_s to the initial intensity I_o. As an example, a typical value for γ_o^2 is $4\text{x}10^{-8}$ I_p (Wm^{-2}). If I_p is taken to be 60MWcm^{-2}, for a 12 mm long crystal, the single pass gain is

$$G = \left(\frac{I_s}{I_o}\right) \approx 11 \tag{2.11}$$

The single pass gain of the OPO gives some insight into the cavity length and necessary pump pulse duration, since it is possible to estimate the number of cavity round trips required for the oscillator to reach threshold. By arbitrarily defining the oscillation threshold as a signal energy of 100 μJ [5] and by allowing one idler photon to be present to begin the parametric process [6], we can state that the total gain required to reach threshold is approximately 150 dB. Therefore, for a single pass gain of G, n cavity passes are required to reach threshold, where

$$G^n \approx 150dB \approx 11^{14} \tag{2.12}$$

giving n=14 passes. For a 30 mm cavity length, the duration of 14 passes is approximately 2 ns. For an OPO pumped by a 6 ns pulse, the build-up time to threshold is 1/3 of the pulse duration and threshold is easily attained.

For non-ideal phase matching, Δk is not equal to zero and the parametric gain becomes sensitively dependent upon the degree of phase mis-match. We can rewrite the single pass power gain of equation 2.9 using a small gain approximation of $\Delta k^2 l^2/4 >> \gamma_o^2 l^2$ which yields

$$G_{small} = \gamma_o^2 l^2 \,\mathrm{sinc}^2\left(\tfrac{\Delta k \cdot l}{2}\right) \tag{2.13}$$

From equation 2.13, it is seen that the gain depends critically upon the phase mis-match of the three waves. In section 2.3, a technique to match the phase of the waves is discussed.

Further examination of the coupled equations (2.6) shows that when each equation is multiplied by its complex conjugate, the expressions are related by

$$\frac{1}{\kappa_s}\frac{d}{dz}\left(E_s E_s^*\right) = \frac{1}{\kappa_i}\frac{d}{dz}\left(E_i E_i^*\right) = -\frac{1}{\kappa_p}\frac{d}{dz}\left(E_p E_p^*\right) \tag{2.14}$$

where the phase mis-match Δk in equation (2.6) is taken to be zero. This expression can be simplified to describe the power exchange at each frequency to give

$$\frac{\Delta P_s}{\omega_s} = \frac{\Delta P_i}{\omega_i} = -\frac{\Delta P_p}{\omega_p} \tag{2.15}$$

where ΔP_s is the change in power of the signal and similar expressions are shown for the idler and the pump. This relation was first formulated by Manley and Rowe [7].

Although the analysis of the three wave interaction has been carried out with reference to the OPO, the Manley-Rowe relation has been derived from the coupled amplitude equations without specifying the nature of the three wave interaction. The result is, therefore, also relevant to both sum-frequency generation and difference-frequency generation. For example, in sum-frequency generation (where two laser beams at frequency ω_s and ω_i are mixed in a non-linear medium to generate a third frequency ω_p, such that $\omega_p=\omega_s+\omega_i$), the Manley-Rowe relation states that both the sources at ω_s and ω_i will lose power to the generated frequency at ω_p. But in difference-frequency generation, $\omega_p-\omega_s=\omega_i$, the same relation predicts that loss at ω_p is accompanied by gain at both ω_s and ω_i. This is the same as saying the pump photon is split in two to form two new, lower frequency, photons. If a weak signal source is passed through the non-linear medium repeatedly it will gain power at every pass at the expense of the pump photons. In the case of the OPO, rather than injecting the signal from an external source, it can be a frequency component in the noise [6]. If the non-linear medium is placed within a resonator, repeated passes of the signal can occur and providing the gain exceeds the loss, such a system will oscillate. This is the essence of the optical parametric oscillator.

2.2 Effective Non-linear Coefficient

The energy conversion efficiency of the parametric process is not only affected by the phase mis-match Δk, but it is also strongly dependent upon the magnitude of the second order non-linear susceptibility $\chi^{(2)}$ in the presence of three electric fields conforming to $\omega_p = \omega_s + \omega_i$. From the previous section, the polarisation vector $P(\omega_p)$, induced by the interactions of the two electric fields $E(\omega_s)$ and $E(\omega_i)$ can be expressed using the third rank tensor d_{ijk}. Using the subscripts *l, m, n* for the three waves to avoid confusion in the nomenclature, we get

$$P_i(\omega_l) = 2\varepsilon_o d_{ijk} E_j(\omega_m) E_k(\omega_n) \qquad (2.16)$$

where a summation takes place over repeated indices. d_{ijk} is the second order polarisation tensor of the non-linear crystal and is related to χ_{ijk} by $\chi_{ijk}=2\cdot d_{ijk}$. The tensor d_{ijk} is of rank three having 27 components, where the subscripts i, j, k denote the X, Y, Z axes. Fortunately, in most materials, many of the individual tensor components vanish and do not contribute to d_{ijk}. The fact that we can attach no physical significance to the ordering of the two fields E_j and E_k means that d_{ijk} is symmetrical in j and k, such that, for example, $d_{123}E_2E_3=d_{132}E_3E_2$. This can only be true if $d_{123}=d_{132}$. The consequence of this is to reduce the number of components of the tensor to 18. An even more sweeping symmetry condition applies to non-linear processes in which the lossless region of the crystal includes all the interacting frequencies. This condition, first formulated by Kleinman [8], states that the elements of the tensor d_{ijk} formed by freely permuting i, j, k are all equal. This is equivalent to stating that the susceptibility is not dependent upon dispersion. A more concise notation known as *matrix notation* is often used in place of tensor notation as a result of the reduction in the number of tensor elements.

In tensor notation, a component of d_{ijk} would be written as, for example, d_{211}. In matrix notation, this is rewritten as d_{21} and the general tensor is denoted $d_{i\mu}$. The subscript μ maps on to the subscripts jk in the following way

Tensor notation	11	22	33	23,32	31,13	12,21
Matrix notation	1	2	3	4	5	6

Re-expressing equation 2.16 in terms of the matrix notation gives

$$\begin{bmatrix} P_x(\omega_l) \\ P_y(\omega_l) \\ P_z(\omega_l) \end{bmatrix} = 2\varepsilon_o \begin{bmatrix} d_{11} & d_{12} & d_{13} & d_{14} & d_{15} & d_{16} \\ d_{21} & d_{22} & d_{23} & d_{24} & d_{25} & d_{26} \\ d_{31} & d_{32} & d_{33} & d_{34} & d_{35} & d_{36} \end{bmatrix} \begin{bmatrix} E_x(\omega_m)E_x(\omega_n) \\ E_y(\omega_m)E_y(\omega_n) \\ E_z(\omega_m)E_z(\omega_n) \\ E_y(\omega_m)E_z(\omega_n)+E_z(\omega_m)E_y(\omega_n) \\ E_x(\omega_m)E_z(\omega_n)+E_z(\omega_m)E_x(\omega_n) \\ E_x(\omega_m)E_y(\omega_n)+E_y(\omega_m)E_x(\omega_n) \end{bmatrix}$$

As a result of the similarity in symmetry between the piezoelectric coefficients and the non-linear optical coefficients, it has been the tradition to write both sets of coefficients in the tensor reporting frame of the piezoelectric coefficients, XYZ. The relationship between the two frames depends on the crystal class in question. The optical xyz frame and the XYZ frame are spatially coincident with the principal dielectric axes of the crystal in the cases of uniaxial and orthorhombic crystal classes, although they are not necessarily oriented so that x maps on to X etc. In the case of other crystal classes, a rotation of one of the axes with respect to the other may be necessary to reconcile the two frames. In the uniaxial crystal class, there is an *a priori* relationship between the axes of the two frames, namely, x=Z in a negative uniaxial and z=Z in a positive uniaxial, where Z is usually taken to be the polar axis. This is dealt with in more detail later.

Although the number of tensor components has been reduced to 18, the description of the polarisation still involves a summation over the non-zero matrix elements and the direction of polarisation of the interacting waves. Returning to the subscripts applied to the parametric oscillator, the equation describing the polarisation can be simplified by writing

$$P(\omega_p) = 2\varepsilon_o d_{eff} E(\omega_s) E(\omega_i)$$

where the summation has been carried out already for the particular interaction being described. Here, a new term is defined known as the effective non-linear coefficient d_{eff} and is defined as

$$d_{eff} = \mathbf{a}_i d_{ijk} \mathbf{a}_j \mathbf{a}_k \tag{2.17}$$

where $\mathbf{a}_i, \mathbf{a}_j$ and $\mathbf{a}_k$ are the unit vectors of $P(\omega_p)$, $E(\omega_s)$ and $E(\omega_i)$, respectively. All further derivations are made using this effective optical non-linearity, which yields a simple expression for the description of the strength of the coupling between the three waves. A more detailed description of the effective non-linearity is now carried out after Yao and Sheng [9], with relevant alterations made to conform to the convention discussed by Roberts [10].

An optical wave propagating in an anisotropic crystal with a wave vector **k** will decompose into two mutually orthogonal polarisation directions perpendicular to **k** denoted by $\mathbf{e_1}$ and $\mathbf{e_2}$. The projection on the co-ordinate axis system xyz of the two electric displacement vectors $\mathbf{D}^{e}{}_1$ and $\mathbf{D}^{e}{}_2$ for the two polarisation directions is given by

$$\mathbf{D}_j^{e_1}(\omega_i) = \mathbf{b}_j^{e_1}\left|D^{e_1}(\omega_i)\right| \qquad \text{and} \qquad \mathbf{D}_j^{e_2}(\omega_i) = \mathbf{b}_j^{e_2}\left|D^{e_2}(\omega_i)\right| \tag{2.18}$$

where subscripts j=1, 2, 3 represent the x, y, z axes system, $\mathbf{b}^{e_1}$ and $\mathbf{b}^{e_2}$ are the direction cosine unit vectors given by [9]

$$\mathbf{b}^{e_1} = \begin{pmatrix} \cos\theta\cos\phi\cos\delta_i - \sin\phi\sin\delta_i \\ \cos\theta\sin\phi\cos\delta_i + \cos\phi\sin\delta_i \\ -\sin\theta\cos\delta_i \end{pmatrix}$$

$$\mathbf{b}^{e_2} = \begin{pmatrix} -\cos\theta\cos\phi\cos\delta_i - \sin\phi\cos\delta_i \\ -\cos\theta\sin\phi\sin\delta_i + \cos\phi\cos\delta_i \\ \sin\theta\sin\delta_i \end{pmatrix} \tag{2.19}$$

θ is measured from the k vector to the z axis and ϕ is the azimuthal angle subtending the x axis and the projection of the k vector in the xy plane. δ is the polarisation angle and is defined later in section 2.3.2.

Owing to the phenomenon of double refraction of the extraordinary ray in an anisotropic medium, the displacement vector **D** is not necessarily parallel to the electric field vector **E**. This is discussed in more detail in section 2.7. Failure to make this correction in the calculation for d_{eff} can result in a 0-20 % error in the calculation of d_{eff} (max) and even larger for non-maximum values [10].

The vectors **D** and **E** are related by a second rank tensor in ε and by suitable rotation of the co-ordinate axis system the cross-product terms can be made to vanish to leave

$$\begin{pmatrix} E_x \\ E_y \\ E_z \end{pmatrix} = \begin{pmatrix} 1/n_x^2 & 0 & 0 \\ 0 & 1/n_y^2 & 0 \\ 0 & 0 & 1/n_z^2 \end{pmatrix} \begin{pmatrix} D_x \\ D_y \\ D_z \end{pmatrix} \tag{2.20}$$

This new co-ordinate axis system is called the principal dielectric axis. Equation 2.20 shows how the refractive index n depends upon the direction of propagation of the waves in the crystal and is the basis of the index ellipsoid or optical indicatrix of the anisotropic medium.

From equations 2.18 and 2.20 we can write the electric field vectors (perpendicular to the Poynting vector) of the two polarisation states, $\mathbf{E}^{e}{}_1$ and $\mathbf{E}^{e}{}_2$ as

$$\begin{aligned} \mathbf{E}^{e_1} &= \left[\frac{\left(b_1^{e_1}\right)^2}{n_1^4} + \frac{\left(b_2^{e_1}\right)^2}{n_2^4} + \frac{\left(b_3^{e_1}\right)^2}{n_3^4} \right]^{\frac{1}{2}} \cdot \mathbf{D}^{e_1} \\ &= R \cdot \mathbf{D}^{e_1} \end{aligned}$$

$$\mathbf{E}^{e_2} = \left[\frac{\left(b_1^{e_2}\right)^2}{n_1^4} + \frac{\left(b_2^{e_2}\right)^2}{n_2^4} + \frac{\left(b_3^{e_2}\right)^2}{n_3^4} \right]^{\frac{1}{2}} \cdot \mathbf{D}^{e_2} \qquad (2.21)$$
$$= S \cdot \mathbf{D}^{e_2}$$

Since the electric field can be projected on to the co-ordinate axis system in much the same way as the displacement vector was in equation 2.18, we can write

$$\mathbf{a}^{e_1} = \frac{1}{\left|\mathbf{E}^{e_1}\right|} \begin{pmatrix} E_1^{e_1} \\ E_2^{e_1} \\ E_3^{e_1} \end{pmatrix} \qquad (2.22)$$

and a similar expression for the unit vector electric field associated with $\mathbf{e_2}$. By considering equations 2.21, 2.22 and 2.18, we finally generate an expression for the terms a_i, a_j and a_k used in equation 2.17. These are

$$\mathbf{a}^{e_1} = \frac{1}{R} \begin{pmatrix} n_1^{-2} b_1^{e_1} \\ n_2^{-2} b_2^{e_1} \\ n_3^{-2} b_3^{e_1} \end{pmatrix} \quad \text{and} \quad \mathbf{a}^{e_2} = \frac{1}{S} \begin{pmatrix} n_1^{-2} b_1^{e_2} \\ n_2^{-2} b_2^{e_2} \\ n_3^{-2} b_3^{e_2} \end{pmatrix} \qquad (2.23)$$

To conform to the convention of Roberts [10], $\mathbf{e_1}$ is the slow ray and $\mathbf{e_2}$ is the fast ray in the "positive NLO frame" but are reversed for the "negative NLO frame", where the positive and negative frames are reserved for the positive/negative crystals. This convention ensures that $\mathbf{e_1}$ and $\mathbf{e_2}$ conform to the traditional idea of an "e" and "o" ray in the uniaxial limit. Thus, the effective non-linear coefficient can be determined for each type of interaction by using the relevant polarisations in equation 2.17 and setting δ to zero in equation 2.19. The general forms of d_{eff} are shown in table 2.1, below.

In biaxial crystals, the distinction between positive and negative is less clear since there is not necessarily a sudden change in the non-linear optical behaviour at the optic axis. However, Roberts [10] recommends a convention which is discussed in section 2.3.2.

	Positive	Negative
Type I phase matching	$d_{eff} = \begin{pmatrix} a_1^{e_2} \\ a_2^{e_2} \\ a_3^{e_3} \end{pmatrix} d_{ijk} \begin{pmatrix} (a_1^{e_1})^2 \\ (a_2^{e_1})^2 \\ (a_3^{e_1})^2 \\ 2a_2^{e_1}a_3^{e_1} \\ 2a_1^{e_1}a_3^{e_1} \\ 2a_1^{e_1}a_2^{e_1} \end{pmatrix}$	$d_{eff} = \begin{pmatrix} a_1^{e_1} \\ a_2^{e_1} \\ a_3^{e_1} \end{pmatrix} d_{ijk} \begin{pmatrix} (a_1^{e_2})^2 \\ (a_2^{e_2})^2 \\ (a_3^{e_2})^2 \\ 2a_2^{e_2}a_3^{e_2} \\ 2a_1^{e_2}a_3^{e_2} \\ 2a_1^{e_2}a_2^{e_2} \end{pmatrix}$
Type II phase matching	$d_{eff} = \begin{pmatrix} a_1^{e_2} \\ a_2^{e_2} \\ a_3^{e_3} \end{pmatrix} d_{ijk} \begin{pmatrix} a_1^{e_1}a_1^{e_2} \\ a_2^{e_1}a_2^{e_2} \\ a_3^{e_1}a_3^{e_2} \\ a_2^{e_1}a_3^{e_2} + a_3^{e_1}a_2^{e_2} \\ a_1^{e_1}a_3^{e_2} + a_3^{e_1}a_1^{e_2} \\ a_1^{e_1}a_2^{e_2} + a_2^{e_1}a_1^{e_2} \end{pmatrix}$	$d_{eff} = \begin{pmatrix} a_1^{e_1} \\ a_2^{e_1} \\ a_3^{e_1} \end{pmatrix} d_{ijk} \begin{pmatrix} a_1^{e_1}a_1^{e_2} \\ a_2^{e_1}a_2^{e_2} \\ a_3^{e_1}a_3^{e_2} \\ a_2^{e_1}a_3^{e_2} + a_3^{e_1}a_2^{e_2} \\ a_1^{e_1}a_3^{e_2} + a_3^{e_1}a_1^{e_2} \\ a_1^{e_1}a_2^{e_2} + a_2^{e_1}a_1^{e_2} \end{pmatrix}$

Table 2.1 *General form of the effective non-linear coefficient for type I and type II phase matching in both positive and negative crystals.*

2.3 Phase-matched Interactions and Frequency Tuning

The consequence of three waves propagating through a medium with different frequencies is that their relative phase changes. That is, a mis-match occurs between the polarisation wave and the generated electromagnetic waves because of colour dispersion. The birefringence of an anisotropic material can, however, be exploited to force the waves to travel through the medium at a single phase velocity, c/n. This phenomenon is called phase matching and is most simply illustrated in a uniaxial crystal.

2.3.1 Uniaxial Crystals

We found in the previous section that, for a given direction in the crystal, two linearly polarised modes exist which are the rays of propagation. Each mode possesses a unique direction of polarisation (direction of **D**) and velocity of propagation (the corresponding index of refraction). The polarisation directions and indices of the two rays are found from the general form of the index ellipsoid in the principal axis system, x, y, z given by

$$\frac{x^2}{n_x^2}+\frac{y^2}{n_y^2}+\frac{z^2}{n_z^2}=1 \qquad (2.24)$$

The two eigenvectors, in general, experience different refractive indices and can be found by solving the quadratic in n of the Fresnel equation [11]. Using n' and n" to represent the two eigen refractive indices, we have

$$n'=\left[\frac{2}{-B+\sqrt{B^2-4C}}\right]^{1/2} \quad \text{and} \quad n''=\left[\frac{2}{-B-\sqrt{B^2-4C}}\right]^{1/2} \qquad (2.25)$$

where

$$B=\left[-k_x^2\left(n_y^{-2}-n_z^{-2}\right)-k_y^2\left(n_x^{-2}-n_z^{-2}\right)-k_z^2\left(n_x^{-2}-n_y^{-2}\right)\right]$$

$$C=\left[k_x^2n_y^{-2}n_z^{-2}+k_y^2n_x^{-2}n_z^{-2}+k_z^2n_x^{-2}n_y^{-2}\right]$$

and k_x, k_y and k_Z are the spherical polar co-ordinates of the k vector in the principal axis system, given by $k_x=\sin\theta\cos\phi$, $k_y=\sin\theta\sin\phi$ and $k_z=\cos\theta$.

A uniaxial crystal has a single optic axis. That is, a single direction exists in the crystal where the two eigen refractive indices are equal. In general, however, the eigenvalues are not equal since it is found that one depends on the polar angle θ. A positive uniaxial has $n_x=n_y=n_o$ and $n_Z=n_e$ whereas a negative uniaxial has $n_y=n_z=n_o$ and $n_x=n_e$

where n_o and n_e are referred to as the ordinary and extraordinary refractive index, respectively. The relative magnitudes of the ordinary and extraordinary refractive indices determine whether the crystal is of a "negative" or "positive" uniaxial class. For $n_e-n_o>0$, the crystal is considered to be positive and for $n_e-n_o<0$, the crystal is negative. When the refractive indices are substituted into equation 2.24, the generated surface for both crystal classes is an ellipsoid. For a positive uniaxial, the ellipsoid resembles the shape of a "rugby ball" whilst a negative uniaxial indicatrix is like the shape of a "Smartie". Both have their optic axes along the axis of rotational symmetry. Figure 2.1 illustrates the index ellipsoid for both classes of crystal.

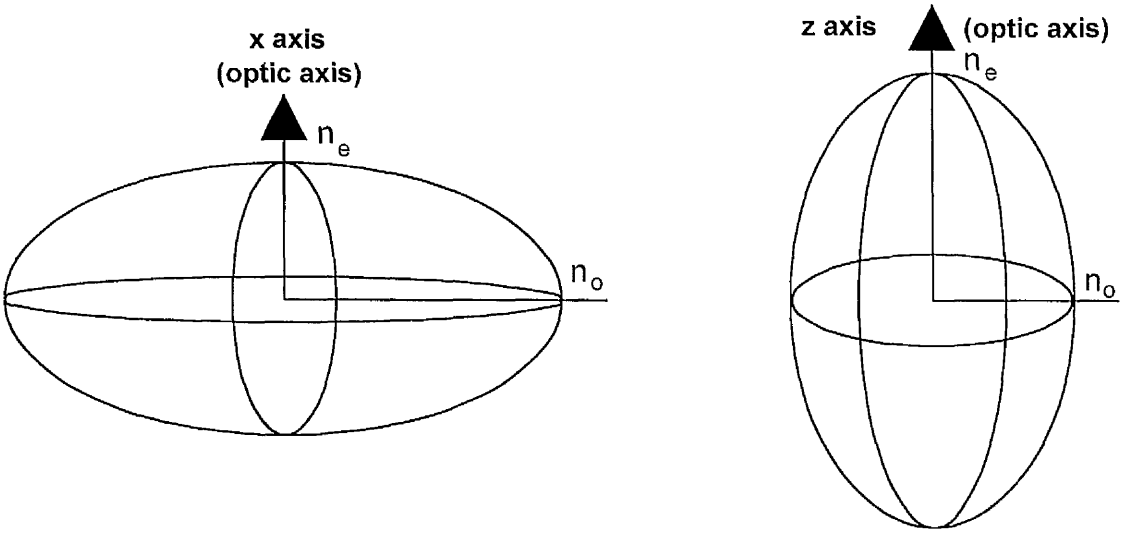

Negative uniaxial Positive uniaxial

Figure 2.1. Index ellipsoid (or optical indicatrix) of a negative and a positive uniaxial crystal.

The cross section of the normal to the optic axis in both ellipsoids in figure 2.1 is a circle, indicating that $n_o=n_e$. Therefore, the orthogonal $\mathbf{D_o}$ and $\mathbf{D_e}$ vectors perpendicular to a wave travelling along the optic axis experience the same refractive indices. This defines the optic axis. In general, however, for a wave vector at an angle θ to the optic axis, $\mathbf{D_o}$ experiences a different refractive index to $\mathbf{D_e}$. This is illustrated

in figure 2.2(a) for a positive uniaxial crystal, where $\mathbf{D_o}$ and $\mathbf{D_e}$ point in the direction of the minor and major axis of the elliptical cross section of the indicatrix. It is clear from the figure that as the k vector angle of propagation θ varies, the direction of the polarisation of the ordinary ray ($\mathbf{D_o}$) remains the same whilst that for the extraordinary ray changes. In fact, the extraordinary refractive index changes from $n_e(\theta=0°)= n_o$ to $n_e(\theta=90°)= n_e$.

The generated three-dimensional surface of n_o and n_e as functions of both θ and ϕ is called the *normal surface* of the crystal. Its construction is derived from the index ellipsoid and is shown in figure 2.2(b).

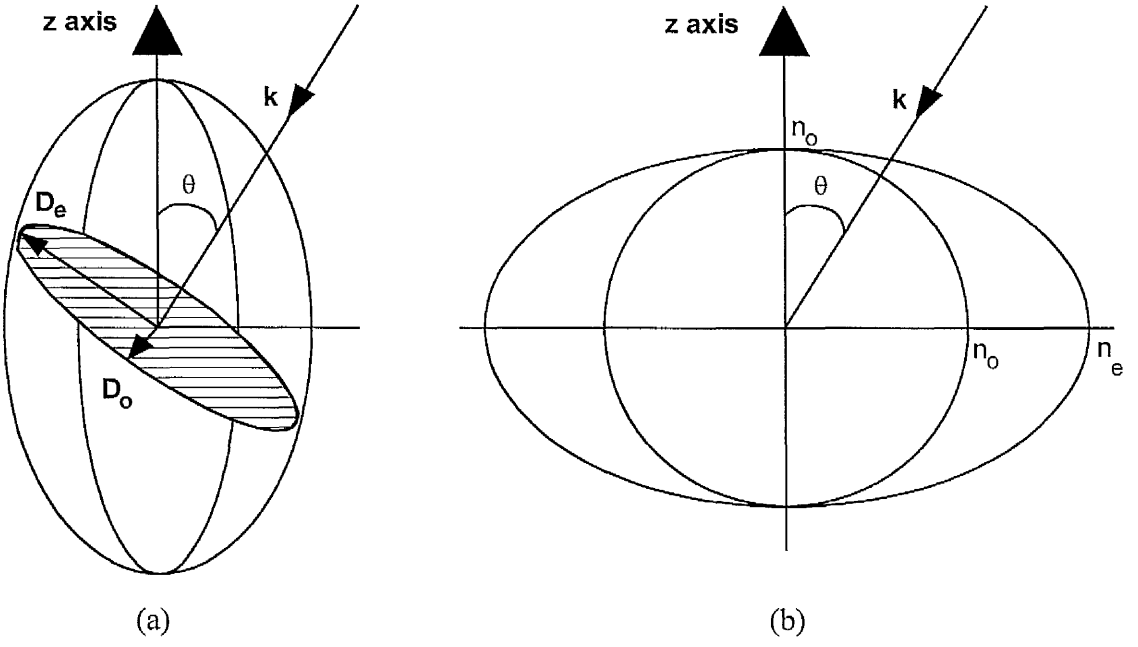

Figure 2.2 (a) shows the construction of the directions of the displacement vectors for a given wave normal propagation in a positive uniaxial and (b) the subsequent development of the normal surfaces

In a uniaxial crystal, the ellipsoid of revolution is symmetrical about the optic axis which allows the refractive index to be described in terms of θ only without loss of generality.

A prerequisite for efficient parametric generation is that the three waves are phase matched so that $\Delta k=0$ and momentum and energy are conserved according to $k_p = k_s + k_i$, (for collinear phase matching) and $\omega_p = \omega_s + \omega_i$ respectively.

Taking the phase matching requirement, and using the expression $k^{(\omega)} = \omega n^{(\omega)}/c$, we can derive the phase matching requirement for the collinear phase matching regime as

$$n^{(\omega_p)}\omega_p = n^{(\omega_s)}\omega_s + n^{(\omega_i)}\omega_i \qquad (2.26)$$

In normal dispersive materials, the index of the ordinary wave or the extraordinary wave increase with ω, making equation 2.26 impossible to satisfy if all three waves are of the same polarisation. However, under certain circumstances, if one of the waves is ordinary, or extraordinary, the equation can be satisfied. Two types of phase matching in birefringent crystals are possible in principle; type I has the signal and idler of the same polarisation (either both ordinary or both extraordinary), and type II has orthogonal signal and idler polarisations. Whether the waves propagate as o-rays or e-rays in type I phase matching is determined by the crystal class, that is, whether it is a positive or negative uniaxial.

The general form of the phase matching types, given in terms of the eigen refractive indices are

$$\begin{aligned} n_p'\omega_p &= n_s''\omega_s + n_i''\omega_i && \text{type I phase matching} \\ n_p'\omega_p &= n_s''\omega_s + n_i'\omega_i && \text{type II phase matching} \end{aligned} \qquad (2.27)$$

where n'' is the larger of the two eigenvalues.

Table 2.2 shows the eigenvalues for both type I and type II phase matching for each uniaxial crystal class and includes the concise nomenclature borrowed from second harmonic generation where 'e' and 'o' denote extraordinary and ordinary polarisations.

	n'	n''
Negative uniaxial	$\left[\frac{\sin^2\theta}{n_e^2}+\frac{\cos^2\theta}{n_o^2}\right]^{-1/2}$	n_o
Positive uniaxial	n_o	$\left[\frac{\sin^2\theta}{n_e^2}+\frac{\cos^2\theta}{n_o^2}\right]^{-1/2}$

Table 2.2. Eigen refractive indices for uniaxial crystals.

For a fixed pump frequency, ω_p, it is apparent from the form of equation 2.26 and figure 2.2(b) that changing θ changes the refractive index of the e-ray and also causes the signal and idler frequencies to change, to preserve the phase matching condition. By rotation of the crystal with respect to the pump k vector, the signal and idler frequencies can be made to tune in accordance with the conservation of energy. This is know as angle tuning and is characterised by critical phase matching (CPM). Other forms of frequency tuning also exist. Fast tuning over relatively small ranges can result from electro-optic tuning [12]. Phase matching can be made to depend noncritically on the acceptance parameters of the crystal (see chapter 3 for detail on acceptance parameters) by directing the pump light normal to one of the axes of the index ellipse. Tuning is usually then accomplished by changing the temperature of the crystal, providing the refractive indices are sufficiently sensitive to changes in temperature. This is known as noncritical phase matching (NCPM) and has the additional advantage of zero walk-off of the extraordinary ray. Greater detail on both CPM and NCPM is provided in the next chapter.

2.3.2 Biaxial Crystals

The existence of two optic axes in biaxial crystals makes phase matching more complicated to analyse. The wave surfaces form a two-sheeted surface and neither of the two optic axes coincide with a principal axis. Although the phase matching directions still form a cone around each of the optic axes, the cone cross-section is not

necessarily circular. In principle, the two eigenvalues of refractive index can both be extraordinary in nature, but usually the phase matching is chosen to take place within a principle plane of the crystal. In this case, one eigenvector behaves as an ordinary ray and the other as an extraordinary ray.

Figure 2.3 shows the index ellipsoid for a positive biaxial crystal. With $n_x<n_y<n_z$, the optic axes lie in the xz plane of the principal axis system at an angle Ω to the z axis. The shaded areas represent only the planes of intersection that have a circular cross section. The normal to each plane is an optic axis (OA).

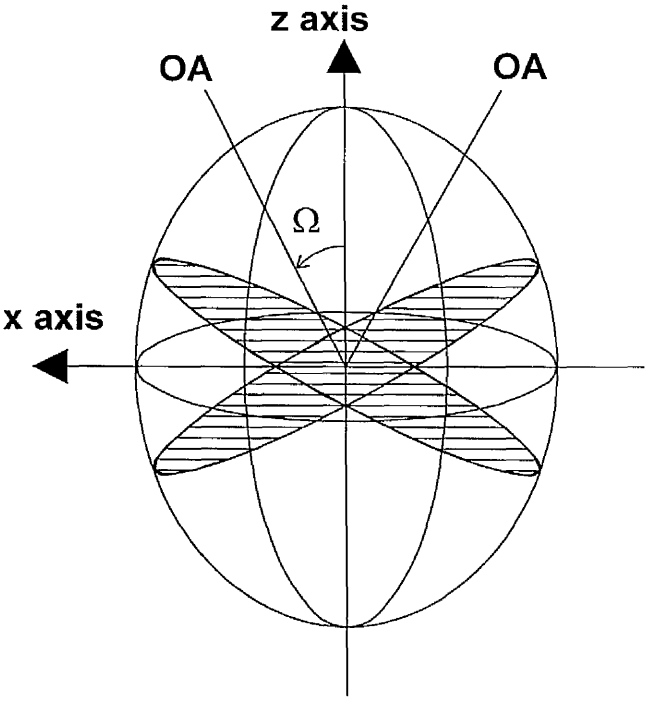

Figure 2.3 Index ellipsoid of a positive biaxial crystal. The optic axes lie in the xz plane at an angle Ω to the z axis when the axes of the ellipse are defined as $n_x<n_y<n_z$.

When phase matching takes place in a principal plane of the crystal, not only do the eigen vectors behave like an "o" and an "e" ray, but the polarisation angle δ is zero. This "uniaxial" behaviour results from the k vector always remaining at right angles to an axis of one of the three ellipses which make up the biaxial indicatrix. For example,

when phase matched interactions take place in the xy plane, **k** is always perpendicular to the z axis. The refractive index experienced by the eigenmode parallel to the electric displacement vector along this out-of-plane axis remains constant and equal to the length of the z-semi-axis. The other eigen mode experiences an index of refraction whose value varies from the semi-axis lengths of the two other ellipses as the tuning angle changes from 0° to 90°. Under the conditions of a general phase matched direction k(θ,ϕ), both the eigenvectors behave as e-rays and the polarisation angle is non-zero.

The polarisation angle δ is shown in figure 2.4 and subtends the $\mathbf{e}_1$ and the **k**-"3" plane.

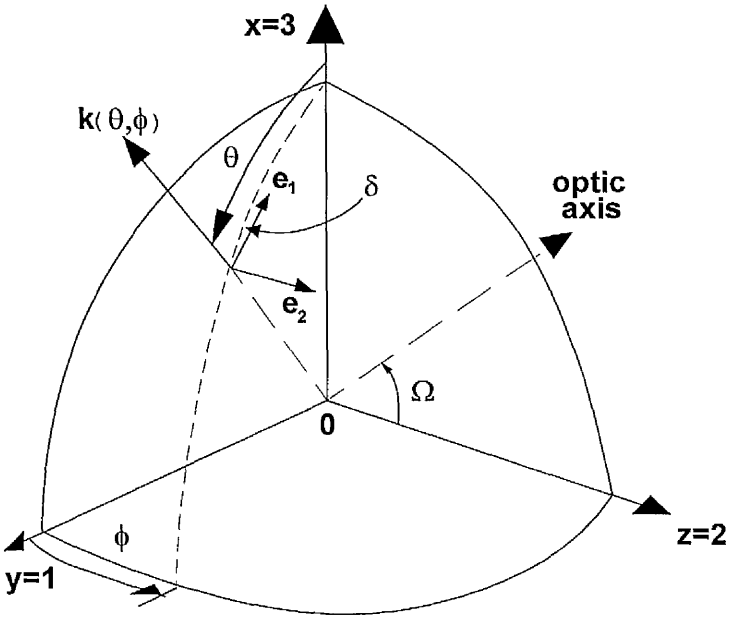

Figure 2.4 An octant of the index ellipsoid of a biaxial crystal. The displacement vector is decomposed along two orthogonal directions e_1 and e_2. When phase matching takes place away from a principal plane, the polarisation angle δ is non-zero. The optic axis lies at an angle Ω from the z axis in the xz plane. Its formulation is in the text. (Figure is based on [10])

The polarisation angle is defined as

$$\tan 2\delta_i^+ = \frac{\sin 2\phi \cos\theta}{\sin^2\phi - \cos^2\theta\cos^2\phi + \cot^2\Omega_i \sin^2\theta} \qquad (2.28)$$

for a positive biaxial, and

$$\tan 2\delta_i^- = \frac{-\sin 2\phi \cos\theta}{\cos^2\phi - \cos^2\theta \sin^2\phi + \tan^2\Omega_i \sin^2\theta} \tag{2.29}$$

for a negative biaxial crystal. The definition of negative and positive biaxiality is taken from the magnitude of the angle Ω which is the position of the optic axis from the z axis. The crystal is said to be negative for Ω>45° and positive for Ω≤45°. In a marginal case, the crystal can be considered to be both positive and negative. The definition of Ω is

$$\sin\Omega = \frac{n_z}{n_y}\left[\frac{n_y^2 - n_x^2}{n_z^2 - n_x^2}\right]^{\frac{1}{2}} \tag{2.30}$$

By considering the plane of interaction in the crystal, the eigen refractive indices n' and n'' can be found. These are tabulated below (table 2.3)

	n'	n''
k in xz plane (θ<Ω)	$\left[\frac{\sin^2\theta}{n_z^2} + \frac{\cos^2\theta}{n_x^2}\right]^{-½}$	n_y
k in xz plane (θ>Ω)	n_y	$\left[\frac{\sin^2\theta}{n_z^2} + \frac{\cos^2\theta}{n_x^2}\right]^{-½}$
k in xy plane	$\left[\frac{\sin^2\phi}{n_x^2} + \frac{\cos^2\phi}{n_y^2}\right]^{-½}$	n_z
k in yz plane	n_x	$\left[\frac{\sin^2\theta}{n_z^2} + \frac{\cos^2\theta}{n_y^2}\right]^{-½}$

Table 2.3. The eigen refractive indices for phase matching in the principal planes of a biaxial crystal.

2.4 Oscillation Threshold

When considering the threshold of an oscillator, we require that the single pass parametric gain of the resonant wave(s) is sufficient to offset the round-trip cavity losses. For a singly resonant oscillator (SRO), Brosnan and Byer [5] have derived a model for the threshold of a parametric oscillator. Using Gaussian wave forms to describe the pump and the resonant signal, the model considers a time independent gain profile whose width is determined by the time for which the oscillator has net gain greater than unity, which in practice is taken to be the pump pulse duration. Threshold is defined as a signal energy of 100 μJ generated at the expense of the pump. The pump threshold fluence for a collinear phase matched SRO is given by

$$J_o = \frac{2.25}{\mathrm{K} g_s L^2} \tau \left[\frac{l_o}{2\tau c} \ln \frac{p_n}{p_o} + 2\alpha_l l + \ln \frac{1}{\sqrt{R}} + \ln 2 \right]^2 \tag{2.31}$$

where K is defined in equation 2.8, g_s is the signal spatial mode coupling coefficient, 2 τ is the pump pulse duration, l_0 is the optical cavity length, α_l is crystal absorption and R is the mirror reflectivity. L is the effective crystal length after Poynting vector walk-off has been taken into account This is discussed in more detail later. For a threshold of 100 μJ, the signal to noise power ratio of $\ln(P_n/P_o) \approx 33$.

The approximation of a time independent gain profile predicts a higher theoretical threshold fluence than that observed by the authors of the model. Indeed, this trend has been found by other researchers [13]-[14]. In reference [14], the authors attribute the high predicted threshold value to the use, in their experiments, of a multi-mode pump source rather than the single-mode pump source assumed in the model. Others [15] attribute the discrepancy to erroneously low values of the effective non-linear coefficient. Generally, it should be noted that the gain of the oscillator is unlikely to

exceed the losses for the duration of the pump pulse, which makes τ in equation 2.31 large.

2.5 Momentum Mis-match

In practice, the phase matching in OPOs is often far from ideal, since the pump wave has a finite divergence and is non-monochromatic. In section 2.1, the gain equations for the OPO are critically dependent upon the magnitude of the phase mis-match. Therefore, it becomes necessary to calculate the degree to which the spectral and angular spread of the pump wave and the temperature changes of the crystal affect the gain of the interaction. In general terms, the mis-match of the three waves can be written as a Taylor series [16], in this case to first order, as

$$\Delta k \approx \Delta k(0) + \frac{\partial(\Delta k)}{\partial \theta} \cdot \Delta\theta + \frac{\partial(\Delta k)}{\partial \nu} \cdot \Delta\nu + \frac{\partial(\Delta k)}{\partial T} \cdot \Delta T \tag{2.32}$$

where $\Delta k(0)$ is the mis-match for perfect phase matching and is obviously zero. Each partial derivative can be evaluated by assuming the other two arguments are constant under the varying condition. The point at which the mis-match is defined to be intolerable is when it equals π/l where l is the crystal length [4].

The collinear phase mis-match can be written as

$$\Delta k = \left[n_p \omega_p - n_s \omega_s - n_i \omega_i \right] \cdot \frac{1}{c} \tag{2.33}$$

where p, s, i denote the pump, signal and idler. In order to calculate the acceptance angle of the crystal which is angle tuned, equation 2.33 is differentiated with respect to θ under the condition that the cavity is resonating the signal wave. With $\omega = 2\pi c/\lambda$, we obtain

$$\frac{d(\Delta k)}{d\theta} = 2\pi\left[\frac{dn_p}{d\theta_p}\cdot\frac{1}{\lambda_p} - \frac{dn_i}{d\theta_i}\cdot\frac{1}{\lambda_i}\right] \tag{2.34}$$

Since the acceptable limit of Δk is π/l, substituting this into equation 2.34 gives the maximum half angle divergence of the pump wave, according to

$$\Delta\theta_p = \frac{1}{2l}\left[\frac{dn_p}{d\theta_p}\cdot\frac{1}{\lambda_p} - \frac{dn_i}{d\theta_i}\cdot\frac{1}{\lambda_i}\right]^{-1} \tag{2.35}$$

In a type I interaction in a negative uniaxial (in simple nomenclature, the interaction can be described as e→o+o, where e and o are the polarisation states of the waves) the second term in the brackets is zero and the acceptance angle limit is dependent upon the variation of the extraordinary refractive index of the pump wave with respect to the phase matching angle θ_p, the pump wavelength and the crystal length.

In a similar way, the maximum allowable frequency bandwidth of the pump wave can be calculated by differentiating equation 2.33 with respect to frequency and setting $\Delta k = \pi/l$ once again. When the frequency is substituted for wavelength, this gives

$$\Delta\nu_p = \frac{c}{l}\left[\lambda_i\left(\frac{\partial n_i}{d\lambda_i}\right) - \lambda_p\left(\frac{\partial n_p}{d\lambda_p}\right) + \left(n_p - n_i\right)\right]^{-1} \tag{2.36}$$

in Hz. The temperature bandwidth of the OPO can be expressed in a similar method by differentiating the phase mis-match with respect to temperature. It is also useful to be able to calculate the temperature sensitivity of the OPO: the frequency change induced in the OPO per degree change in temperature. This parameter can be written as

$$\beta_T = \frac{\partial(\Delta k)}{\partial T} \tag{2.37}$$

A similar expression can also be sought for the angular sensitivity, as described elsewhere [17].

2.6 Inherent Oscillator Linewidth

A principal difference between a laser and an OPO is that a laser can absorb and store uncollimated energy of a broad frequency range, and re-emit radiation in accordance with the dominant energy transition of the gain material. The central wavelength and inherent bandwidth of a laser are generally not affected by the spectral and spatial distribution of the pump radiation. In contrast, the inherent linewidth of an OPO is influenced by the divergence and frequency of the pumping radiation, since phase coherence between the pump, signal and idler is important.

There are three contributing factors to the inherent linewidth of the OPO. The first, and most dominant, factor is the degree to which the signal frequency may depart from the ideal phase matching condition before which the fall in gain becomes intolerable, which has been previously defined as $\Delta k=\pi/l$. The calculation is similar to that carried out in the previous section, except that in this instance we assume that the pump frequency is fixed and the signal and idler frequencies are free to change. By differentiating the collinear phase matching equation 2.33 with respect to the signal frequency and noting that $d\omega_s = -d\omega_i$, we obtain

$$\Delta\nu_s^{(1)}(Hz) = \frac{c}{l}\left[(n_i - n_s) + \lambda_s \frac{dn_s}{d\lambda_s} - \lambda_i \frac{dn_i}{d\lambda_i}\right]^{-1} \tag{2.38}$$

In the type I phase matching regime, the term in the small brackets becomes large as n_i-$n_s \rightarrow 0$ close to the degenerate condition ($\omega_s=\omega_i$), causing the linewidth to increase sharply. Maximum signal (and idler) linewidths at degeneracy under such phase matching conditions are a common feature of OPOs and the result is the linewidth can

change by an order of magnitude or more across the tuning range. The two other contributing factors to the linewidth of the OPO are the angular and spectral spread of the pump beam. The linewidth component arising from the angular spread, or divergence, of the pump beam can be determined by considering the measured divergence as a fraction of the maximum allowable divergence (section 2.5) and multiplying this by the allowable variation of the signal $\Delta\nu_s^{(1)}$. This can be expressed as

$$\Delta\nu_s^{(2)} = \frac{c}{\lambda_p}\left(\frac{\partial n_p}{\partial\theta}\right)\cdot\Delta\theta_p\cdot\left[\left(n_i - n_s\right) + \lambda_s\frac{dn_s}{d\lambda_s} - \lambda_i\frac{dn_i}{d\lambda_i}\right]^{-1} \tag{2.39}$$

in Hertz, where $\Delta\theta_p$ is the full angle divergence of the pump beam. Finally, the contribution to the linewidth resulting from the finite bandwidth of the pump can be determined in a similar fashion. Referring to equation 2.36 in section 2.5, we can write

$$\Delta\nu_s^{(3)} = \Delta\nu_p\left[\left(n_p - n_i\right) + \lambda_i\frac{dn_i}{d\lambda_i} - \lambda_p\frac{dn_p}{d\lambda_p}\right]\cdot\left[\left(n_i - n_s\right) + \lambda_s\frac{dn_s}{d\lambda_s} - \lambda_i\frac{dn_i}{d\lambda_i}\right]^{-1} \tag{2.40}$$

in Hertz. The total linewidth of the OPO is the sum of the three components. $\Delta\nu_s^{(3)}$ is often considerably smaller than the other two contributions since the actual pump bandwidth $\Delta\nu_p$ is usually smaller than the restriction placed upon it by the crystal (equation 2.36), and for practical purposes can usually be excluded. However, as we shall see in chapters seven and eight, when $\Delta\nu_p \approx \Delta\nu_{opo}$, $\Delta\nu_s^{(3)}$ plays an important part in the overall linewidth of the OPO.

2.7 Poynting Vector Walk-off

In birefringent materials, **D**, the displacement vector and **E**, the electric field vector, do not always point in the same direction. Since **D** is perpendicular to the wave vector **k**

and **E** is perpendicular to the power flow **S**, the direction of power flow and the wave normal separate during their passage through the crystal. These vector pairs form an orthogonal set with **H** (figure 2.5 (a)), where **H** points in a direction perpendicular to the page. **S** is known as the Poynting vector and is equal to $\mathbf{E} \wedge \mathbf{H}$. The angle between the orthogonal sets is known as the walk-off angle, ρ.

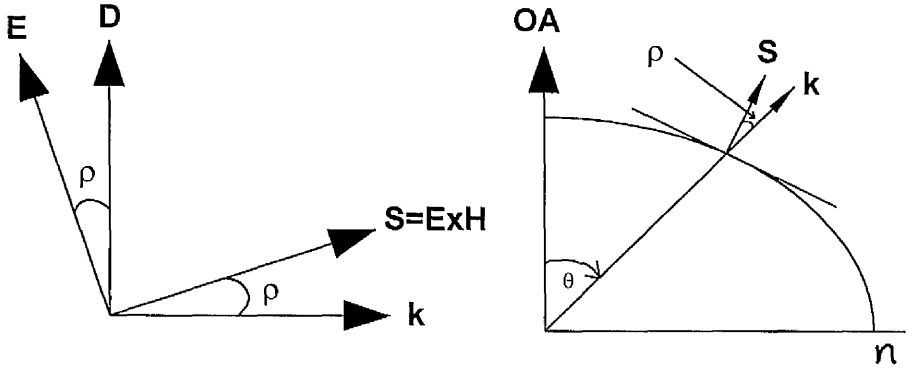

*Figure 2.5 (a) Vector construction showing the walk-off angle between the Poynting vector **S** and the wave vector **k** and (b) the wave surface of a negative uniaxial.*

Figure 2.5 (b) shows the wave surface of a negative uniaxial with **k** at an angle θ to the optic axis (OA). The Poynting vector of the extraordinary ray is constructed so that it lies normal to the surface of the wave. In an isotropic medium, the phenomenon of Poynting vector walk-off is not seen, since the octant of the ellipse drawn in figure 2.5 (b) would be a circle and the two vectors would lie parallel. This is also the case for ordinary rays. From the figure, it is clear that when θ=0° or 90°, the walk-off angle ρ is zero. Although phase matching cannot take place along the optic axis (θ=0°), in many materials it is possible to phase match at 90° to the optic axis. This is known as noncritical phase matching (NCPM).

A simple method of calculating the walk-off angle is to consider the angle the Poynting vector makes with the optic axis, say, β. Then, from geometry, we find

$$\tan\beta = \left(\frac{n_o}{n_e}\right)^2 \tan\theta \qquad (2.41)$$

The walk-off angle, ρ, for a uniaxial crystal is then the difference between β and θ. Providing the analysis is made in the principal axis system, equation 2.41 also applies to biaxial crystals since the behaviour of the refractive indices is analogous to that of "ordinary" and "extraordinary" waves.

Considering a phase matched interaction in the principal plane of a crystal (uniaxial or biaxial), one wave is necessarily polarised differently to the other two. The Poynting vector of the e-ray(s) will separate from its wave normal and, in so doing, will separate from the Poynting vectors of the o-ray(s). Consequently, Poynting vector walk-off can have a severely detrimental effect on the conversion efficiency of the OPO, since it ultimately limits the useful crystal length available in the interaction. It is interesting, in this respect, to talk about the walk-off length. That is, the useful length of the crystal in the interaction before the waves become too separated to interact. The walk-off length l_ρ can be defined as [5]

$$l_\rho = \frac{\sqrt{\pi}}{2}\frac{w_p}{\rho} \qquad (2.42)$$

where w_p is the electric field radii of the pump wave.

2.8 Conversion Efficiency

The optical conversion efficiency is a measure of the amount of pump light that is converted into signal and idler light. The analysis for the conversion efficiency of a singly resonant oscillator (SRO) has been carried out by a Kreuzer [18] using plane-wave assumptions. Bjorkholm [19], however, considers the implications of conversion efficiency using Gaussian waves. This analysis is summarised here.

If I_{in} is the input pump intensity, I_{th} is the threshold intensity, I_{tr} is the transmitted pump through the oscillator and I_s and I_i are the signal and idler intensities, respectively, then

for $I_{in} \geq I_{th,}$, the internal conversion efficiency is given by

$$\eta_{\text{int}} = \frac{P_s + P_i}{P_{in}} = 1 - \frac{I_{tr}}{I_{in}} \tag{2.43}$$

where P represents the power (in W) and the subscripts are defined above. Considering a perfectly phased matched interaction ($\Delta k=0$) the efficiency for the plane-wave assumption is given by

$$\eta_{\text{int}} = 1 - \cos^2 \gamma \tag{2.44}$$

where

$$\frac{I_{th}}{I_{in}} = \frac{\sin^2 \gamma}{\gamma^2}$$

By integrating (2.44) over the pump beam cross section, Bjorkholm found the Gaussian-beam solution to be

$$\frac{P_{tr}}{P_{in}} = \frac{P_{th}}{P_{in}} + \int_0^{\ln\left(P_{in}/P_{th}\right)} e^{-x} \cdot \cos^2 \gamma(x) dx \tag{2.45}$$

where

$$\frac{P_{th}}{P_{in}} \cdot e^x = \frac{\sin^2 \gamma(x)}{\gamma^2(x)}$$

Equation 2.45 has been numerically integrated by Bjorkholm and compared with the solutions to the plane-wave equations. The results show that full pump depletion is not possible with Gaussian waves. The maximum conversion efficiency is 71 % under the

pumping condition of $P_{in} \approx 6.5 \cdot P_{th}$. However, for a uniform plane-wave pump, 100 % conversion efficiency is possible when $P_{in} = (\pi/2)^2 P_{th}$ (or $P_{in} \approx 2.5 \cdot P_{th}$).

The external conversion efficiency of the OPO is simply a fraction of the internal efficiency, according to the losses experienced by the wave under study. For the non-resonant wave, or free wave, the efficiency is

$$\eta_{ext} = \eta_{\text{int}} \frac{\omega_{free}}{\omega_p} \tag{2.46}$$

For the resonant wave, or confined wave, the conversion efficiency is given by

$$\eta_{ext} = \frac{\omega_{confined}}{\omega_p} \cdot \frac{\varepsilon_c}{\varepsilon_c + \varepsilon_l} \cdot \eta_{\text{int}} \tag{2.47}$$

where ε_c is the loss coefficient which contributes to the output of the confined wave including the mirror coupling and losses resulting from mirror tilt. ε_l is the loss coefficient for non-contributory waste including Fresnel reflection from the crystal face and crystal absorption.

References

[1] A. Yariv, "Quantum Electronics" Wiley, 3rd edition, 389, (1989)

[2] J. A. Armstrong, N. Bloembergen, J. Ducuing and P. S. Pershan "Interactions between light waves in a non-linear dielectric" Phys. Rev., 127, 1918, (1962)

[3] F. Zernike and J. E. Midwinter, "Applied non-linear optics" Wiley, 41, (1973)

[4] S. E. Harris "Tunable optical parametric oscillators" Proc. IEEE 57, 2096, (1969)

[5] R. L. Byer and S. J. Brosnan "Optical parametric oscillator threshold and linewidth studies" IEEE J of Quantum Electron., 15, 415, (1979)

[6] R. L. Byer and S. E. Harris "Power and bandwidth of spontaneous parametric emission" Phys. Rev., 168, 1064, (1968)

[7] J. M. Manley and H. E. Rowe "General energy in non-linear reactances" Proc. IRE, 47, 2115, (1959)

[8] D. A. Kleinman "Non-linear dielectric polarization in optical media" Phys. Rev., 126, 1977, (1962)

[9] J. Yao, W. Sheng and W. Shi "Accurate calculation of the optimum phase-matching parameters in three-wave interactions with biaxial non-linear-optical crystals" J. Opt. Soc. Am. B. 9, 891, (1992)

[10] D. A. Roberts "Simplified characterization of uniaxial and biaxial non-linear optical crystals: A plea for standardization of nomenclature and conventions" IEEE J. Quantum Electron. 28, 2057, (1992)

[11] M. Born and E. Wolf "Principles of optics" chapter 14, Oxford, (1970)

[12] L. B. Kreuzer "Ruby-laser-pumped optical parametric oscillator with electro-optic tuning " Appl. Phys. Lett. 10, 336, (1967)

[13] W. R. Bosenberg, L. K. Cheng and C. L. Tang "Ultraviolet optical parametric oscillator in β-BaB_2O_4" Appl. Phys. Lett. 54, 13, (1988)

[14] M. Ebrahimzadeh, A. J. Henderson and M. H. Dunn "An excimer-pumped β-BaB_2O_4 optical parametric oscillator tunable from 354 nm to 2.370 μm" IEEE J. Quantum Electron., 26, 1241, (1990)

[15] Y. X. Fan, R. C. Eckardt, R. L. Byer, J. Nolting and R. Wallenstein "Visible BaB_2O_4 optical parametric oscillator pumped at 355 nm by a single-axial-mode pulsed source" Appl. Phys. Lett., 53, 2014, (1988)

[16] N. P. Barnes and V. J. Corcoran "Parametric generation processes: spectral bandwidth and acceptance angles" Appl. Opt., 15, 696, (1976)

[17] D. Eimerl, L. Davis, S. Velsko, E. K. Graham and A. Zalkin "Optical, mechanical and thermal properties of barium borate" J. Appl. Phys., 62, 1968, (1987)

[18] L. B. Kreuzer "Single and multimode oscillation of the singly resonant optical parametric oscillator" Proc. Joint Conference on Lasers and Optoelectronics, Univ. Southampton, IERE, London, 53, (1969)

[19] J. E. Bjorkholm "Some effects of spatially nonuniform pumping in pulsed optical parametric oscillators" IEEE J. Quantum Electron., 7, 109, (1971)

Chapter 3

Non-linear Materials

The matching of a non-linear material to a pump laser source for a specific OPO application is extremely important. Often, the choice of pump source has already been made by what is available in the laboratory, and the question lies only with the choice of crystal. In the case of this thesis, the harmonics of a Nd:YAG laser were available. For each application, the crystal transparency, tuning range, effective non-linear coefficient, acceptance parameters, double refraction angle and damage threshold must be considered carefully to ensure that the final device will operate efficiently over the desired tuning range. The particular interest here is with the generation of tunable, narrow linewidth radiation in the visible region of the spectrum, particularly in the orange/red and the blue regions. The two crystals under study are barium borate (BBO) and lithium triborate (LBO). Both exhibit respectable non-linear coefficients, high damage thresholds and can be phase matched across the visible region.

This chapter examines the figures of merit for BBO and LBO crystals initially to allow a comparison to be made. Further studies are then carried out on each of these crystals to determine which is best suited to narrow linewidth operation.

3.1 Figure of Merit

In an attempt to classify non-linear crystals by way of their performance, a figure of merit (FOM) can be calculated in each case and different crystals can then be directly compared. Defining the FOM, however, can be a troublesome matter. In trying to circumvent the cumbersome procedure of calculating all the parameters of a crystal, the FOM often fails to give a complete picture of the crystal performance. Each FOM must, therefore, be treated with a degree of caution for reasons which are explained below.

The most commonly used FOM is defined as

$$M_{com} = \frac{d_{eff}^2}{n_p n_s n_i} \tag{3.1}$$

which is taken from the equation of the gain coefficient (2.9). Using the third harmonic of a Nd:YAG laser at 355 nm as the pump source, both LBO and BBO can be phase matched to generate radiation across the visible spectrum. Comparing the common FOM for type I-BBO, type I-LBO and type II non-critically phase matched (NCPM) LBO all pumped by the third harmonic of a Nd:YAG laser (shown graphically in figure 3.1) we see that BBO has the highest FOM, almost a factor of two greater than LBO. However, this definition of the FOM fails to take into account the Poynting vector walk-off of the extraordinary rays in the crystal; an effect which is more detrimental in BBO than in LBO and non-existent in NCPM interactions.

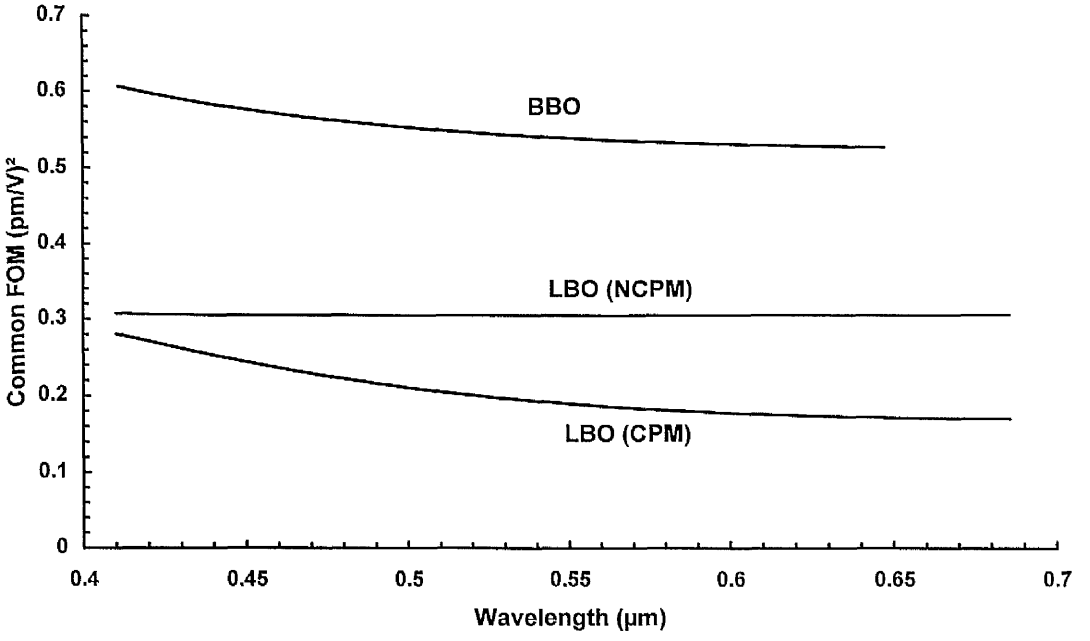

Figure 3.1 Common FOM of BBO, LBO and noncritically phase matched LBO over the tuning range of each oscillator pumped at 355 nm.

It should be noted that the tuning range of the NCPM LBO OPO is unlikely to extend across such a large range, as indicated in the figure, because of its relatively insensitive refractive index change with temperature.

In defining a FOM which allows for the effect of Poynting vector walk-off, we have returned to the idea of an effective length of the crystal. The separation of the waves in the crystal can be thought of as forming a cone or a truncated cone, depending upon the crystal length, as shown in figure 3.2.

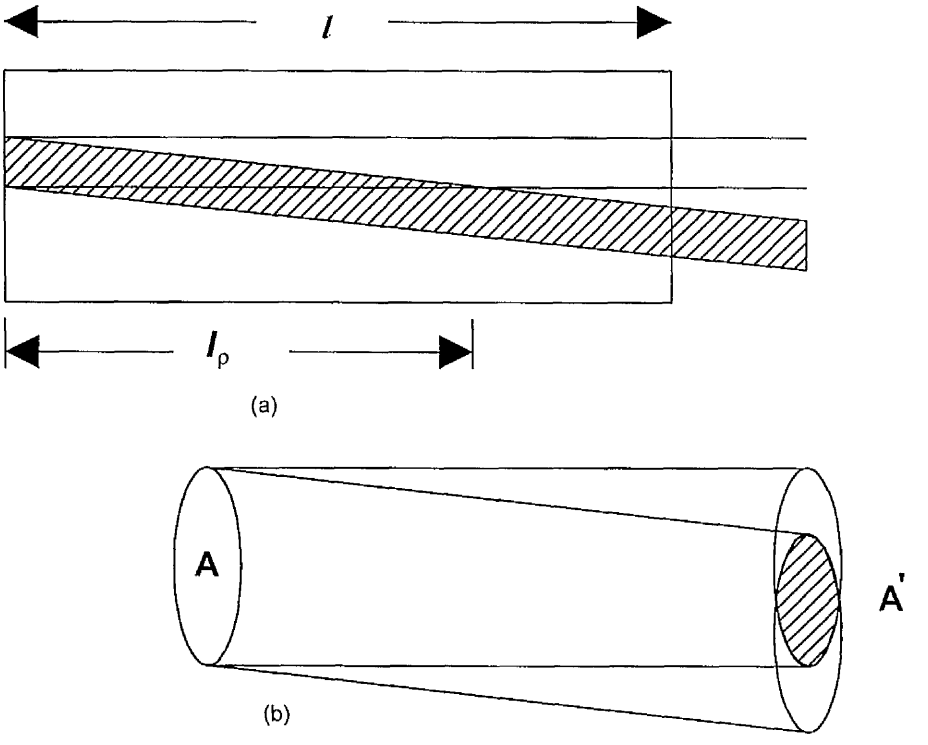

Figure 3.2 (a) depicts a schematic of the extraordinary ray departing from the ordinary ray, thus, defining a walk-off length l_ρ. (b) shows the generated "cone" of the interaction volume. The initial area of the beam is A and the area of interaction at any point in the crystal is A'.

This cone defines the volume of interaction of the waves. Any incremental crystal length beyond the interaction volume cannot contribute to the gain of the OPO. The

parametric gain coefficient can be expressed in terms of plane-waves for the case of perfect phase matching as

$$G = \gamma^2 \cdot l^2 = \left(\frac{8\pi^2}{\varepsilon_o c}\right)\left[\frac{d_{eff}^2}{n_p n_s n_i \lambda_s \lambda_i}\right] \cdot l^2 \frac{P_p}{A} \tag{3.2}$$

where γ is defined in equation 2.9, P_p is the pump intensity (W cm^{-2}) and A is the area of the pump beam. From equation 3.2, we can define a FOM M_w to encompass the effects of walk-off by defining the crystal length l as the effective length of the crystal l_{eff}. The conditions imposed on the effective length are

for $l < l_\rho$

$$l_{eff} = l$$

for $l > l_\rho$

$$l_{eff} = l_\rho$$

where the walk-off length, l_ρ, is defined as $w_p \approx \rho \cdot l_\rho$ where w_p is the pump radius and ρ is the double refraction angle. As the beams gradually separate within the crystal, the overlap, or pumping volume, can be calculated (assuming that the overlap is circular) and the calculated value of the power available for the interaction reduced accordingly. From equation 3.2, we can write

$$M_w = \frac{1}{2}\left[\frac{d_{eff}^2}{n_p n_s n_i \lambda_s \lambda_i}\right] \cdot \left(l_{eff}\right)^2 \cdot \frac{P_p}{A} \cdot \frac{\overline{A}}{A}$$

where $\overline{A}$ is the average interaction area of the beams, giving

$$M_w = \frac{1}{2}\left[\frac{d_{eff}^2}{n_p n_s n_i \lambda_s \lambda_i}\right] \cdot \left(l_{eff}\right)^2 \cdot \frac{P_p}{A} \cdot \left[\frac{2 \cdot l_\rho - l_{eff}}{l_\rho}\right] \tag{3.3}$$

Equation 3.3 for the FOM has units of W/V^2. Calculations based on equation 3.3 have been carried out again for the three cases used previously, with P_p set at 50 MW/cm^2 and a 2 mm diameter pump beam. The calculation was performed by summing over incremental crystal lengths to find M_w. The result is shown in figure 3.3. For any crystal length, the corresponding value of M_w can be found. We see that the value of M_w for BBO rises more rapidly than that for LBO, for crystal lengths up to 14 mm. With longer crystals the effects of Poynting vector walk-off become intolerable, and M_w falls with increasing length. NCPM LBO, on the other hand, experiences no walk-off and consequently has a greater FOM than LBO (CPM). The effects of walk-off do not seriously affect the performance of LBO (CPM) until crystal lengths of about 30 cm are reached.

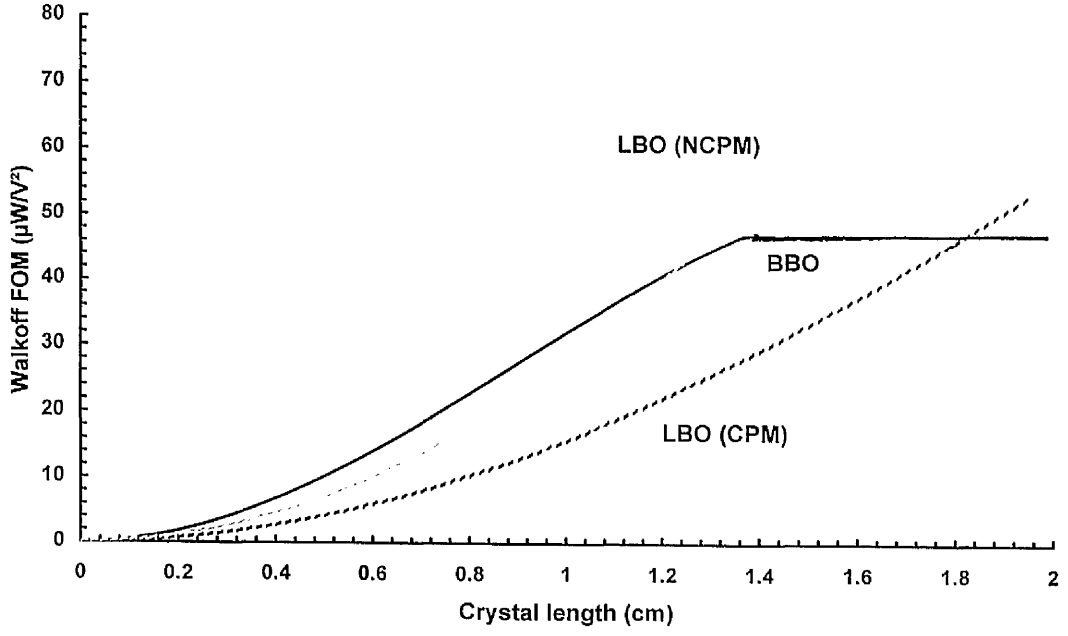

Figure 3.3 Walk-off FOM applied to BBO, LBO and LBO (NCPM) for pumping intensities of 50 MW/cm^2 and a 2 mm pump beam diameter, versus crystal length.

The results of a similar calculation are shown in figure 3.4 where the variation of M_w over the tuning ranges of the parametric oscillators for a fixed crystal length of 14 mm and a pump size of 2 mm diameter in each case.

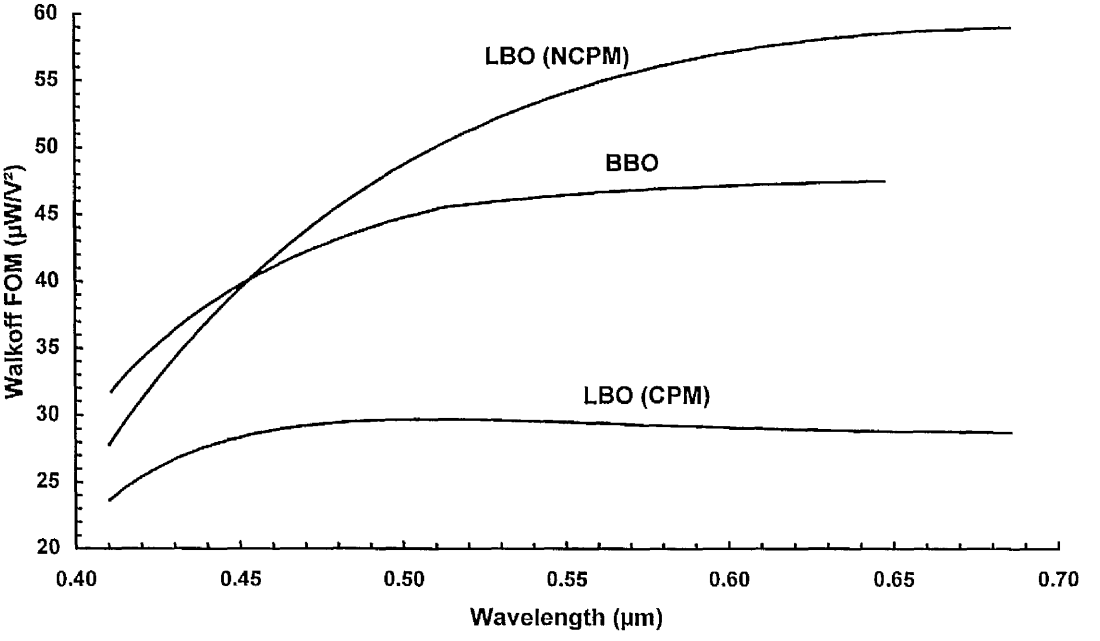

Figure 3.4 Variation of the walk-off FOM for a 14 mm crystal in BBO, LBO and (NCPM) LBO over the visible tuning range of each oscillator.

Here, M_W for BBO is ~1.5 times greater than LBO (CPM) but only exceeds LBO (NCPM) in the blue region of the spectrum. However, the tuning range of (NCPM) LBO is exaggerated in figure 3.4, since such a wavelength range would be impossible for the reasons given earlier.

In summary then, M_{com} shows clearly the superior behaviour of BBO over LBO, whereas M_W indicates an improved performance for LBO when walk-off is taken into account. Other FOMs can also be calculated to include different crystal parameters such as surface damage threshold. However, implicit from the variation of the two different FOM definitions shown here is that all FOM calculations must be used only as a crude guide to the overall crystal performance and not as a substitute for a more detailed crystal feature study. Such an analysis is now carried out for both BBO and LBO.

3.2 Barium Borate

Barium borate (BaB_2O_4, BBO) is an inorganic, negative uniaxial crystal which crystallises in two phases, α and β. The first phase has a square non-linearity tensor of zero, whilst the second lacks the inversion symmetry necessary for optical non-linear processes. Initially, BBO was assigned to the wrong crystal class which resulted in errors in the calculation of the effective non-linearity in early publications [1]-[2]. The crystal class was finally confirmed by Eimerl *et al* [3] and the effective non-linear coefficient for both type I and type II phase matching is given by

$$\begin{aligned} d_{eff}^{eoo} &= d_{15}\sin\theta - d_{22}\cos\theta\sin 3\phi \\ d_{eff}^{eoe} &= d_{22}\cos^2\theta\cos 3\phi \end{aligned} \tag{3.4}$$

The values of the coefficients are d_{22}=(1.78±0.09) pm/V and d_{15}=(0.12±0.06) pm/V [4], although some researches have found these to be low and have published d_{22}=(2.22±0.09) pm/V and d_{15}=(0.16±0.08) pm/V [5].

To maximise d_{eff} in the case of a type I (e→o+o) interaction, the azimuthal angle ϕ is set to 90° (or 30°) Both maxima are shown in figure 3.5(a), which depicts the topology of the square of the effective non-linear coefficient with θ and ϕ variations.

Type II (e→o+e) phase matching is also possible in BBO [6], but the interaction has a smaller effective non-linear coefficient. This is evident from figure 3.5(b) which shows the surface dropping away more quickly as θ is increased as a result of the cosine squared term in equation 3.4, despite the maxima for each type of interaction being the same.

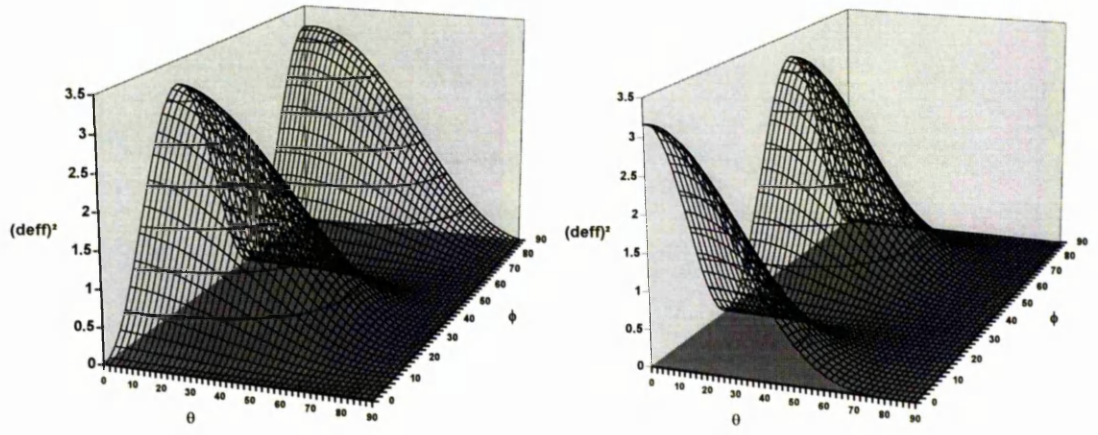

(a) *(b)*

Figure 3.5 (a) Topology of the square of the effective non-linear coefficient of BBO for a type I interaction, and (b) for a type II interaction as θ and ϕ are varied.

BBO has a transparency which extends from 189 nm to 3500 nm and, owing to its large birefringence (n_o-n_e = 0.12 at λ = 532 nm), phase matching can be carried out to generate radiation into the UV. For example, second harmonic generation of 410 nm has been demonstrated to produce UV light at 205 nm [1], [3]. Shorter wavelengths are obtainable by sum frequency mixing of UV and infrared light [7] to generate light at 190 nm. BBO also has a high damage threshold of ~13 GWcm^{-2} [3], making it a strong contender for high intensity pumping. For a more detailed overview of the phase matching properties of BBO, see reference [8].

The dispersion relations (Sellmeier equations) for BBO, given by a number of researchers, conform to the empirical equation

$$n^2 = a + \frac{b}{\lambda^2 - c} - d \cdot \lambda^2$$

The constants a, b, c, d and e (where necessary) are shown in Table 3.1

Reference		a	b	c	d	e
[1]	n_o	2.7359	0.01878	0.01822	0.01354	0
	n_e	2.3753	0.01224	0.01667	0.01516	0
[3]	n_o	2.7405	0.0184	0.0179	0.0155	0
	n_e	2.3730	0.0128	0.0156	0.0044	0
[9]†	n_o	1.46357	1.26172	0.01628	0.00166	30
	n_e	1.40567	0.95869	0.01431	0.01644	30

† conforms to $n^2 = a + \frac{b \cdot \lambda^2}{\lambda^2 - c} + \frac{d \cdot \lambda^2}{\lambda^2 - e}$

Table 3.1 Sellmeier data for BBO from three reference sources.

From the data given in table 3.1, the type I and type II phase matching curves for a BBO optical parametric oscillator can be calculated using equations 2.27 for a given pump wavelength of 355 nm. The tuning responses are shown below in figure 3.6.

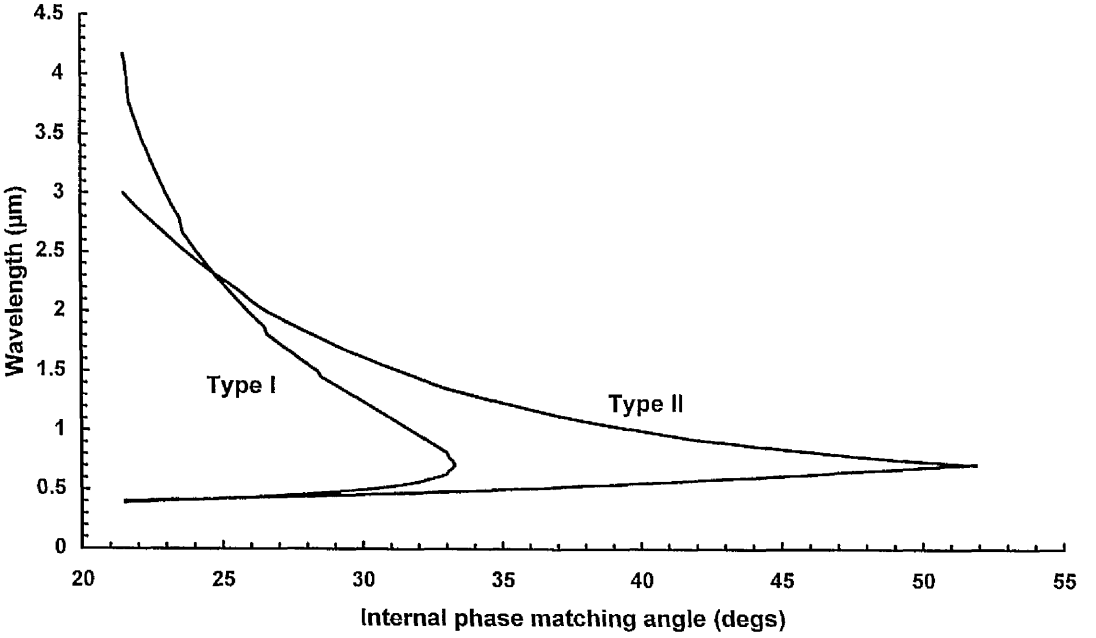

Figure 3.6. Tuning curves for type I and type II phase matching in BBO pumped at 355 nm.

The tuning curves span the visible part of the spectrum and extend into the near infrared to wavelengths near the infrared cut-off. The availability of such an extensive range of wavelengths for both types of phase matching has made BBO an extremely useful source of visible radiation. However, further investigations need to be made into the acceptance angles of the crystal and the extent of Poynting vector walk-off experienced by the e-ray(s), to fully assess the potential of the crystal for both type I and II phase matching. To this end, the angular, spectral and temperature bandwidths to the point where the gain falls by π/l from the perfectly phase matched condition can be calculated for both type I and type II interactions in BBO from equations 2.35-2.37. The maximum allowable pump bandwidth in GHz is shown in figure 3.7 over the tuning range of each type of interaction for a pump wavelength of 355 nm. In both cases, idler resonance places a less severe restriction on the spectral parameters of the pump, but even the signal resonance is much broader than the bandwidth of a free running Nd:YAG laser (~ 30 GHz).

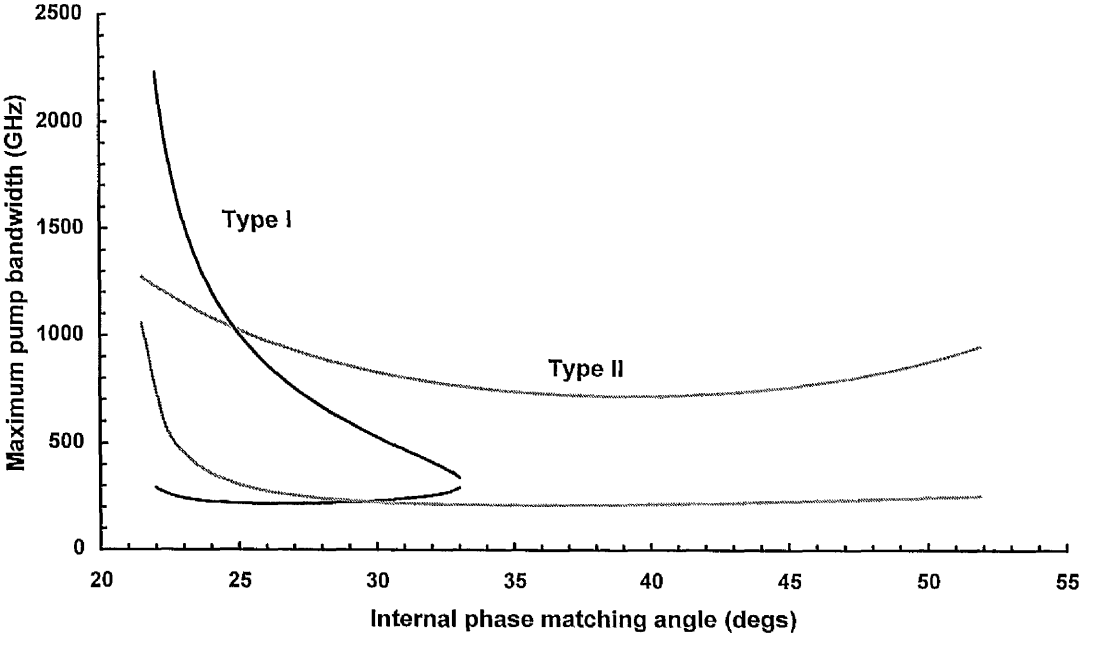

Figure 3.7. Maximum pump bandwidth for type I and II phase matching of BBO pumped at 355 nm using 12 mm crystal lengths.

The pump spectral width will not, therefore, adversely affect the performance of the OPO for the crystal lengths of 12 mm, used in this calculation.

The acceptance angle of the crystal limits the divergence of the incoming pump beam for a given crystal length. It is well known that the acceptance angle in BBO is strict; for modest crystal lengths the allowable divergence of the pump laser is small. Figure 3.8 shows the acceptance angles for type I and type II phase matching over the tuning range of the respective oscillators. For type I phase matching, the limit is shown to vary from 0.3 mrad to 0.24 mrad. A near diffraction-limited Nd:YAG laser beam at the fundamental wavelength has a typical divergence of 0.5 mrad (full angle), so this restriction can be expected to be a source of loss. In the type II regime, the restriction is again alleviated to some extent and is shown to increase to 0.55 mrad near degeneracy.

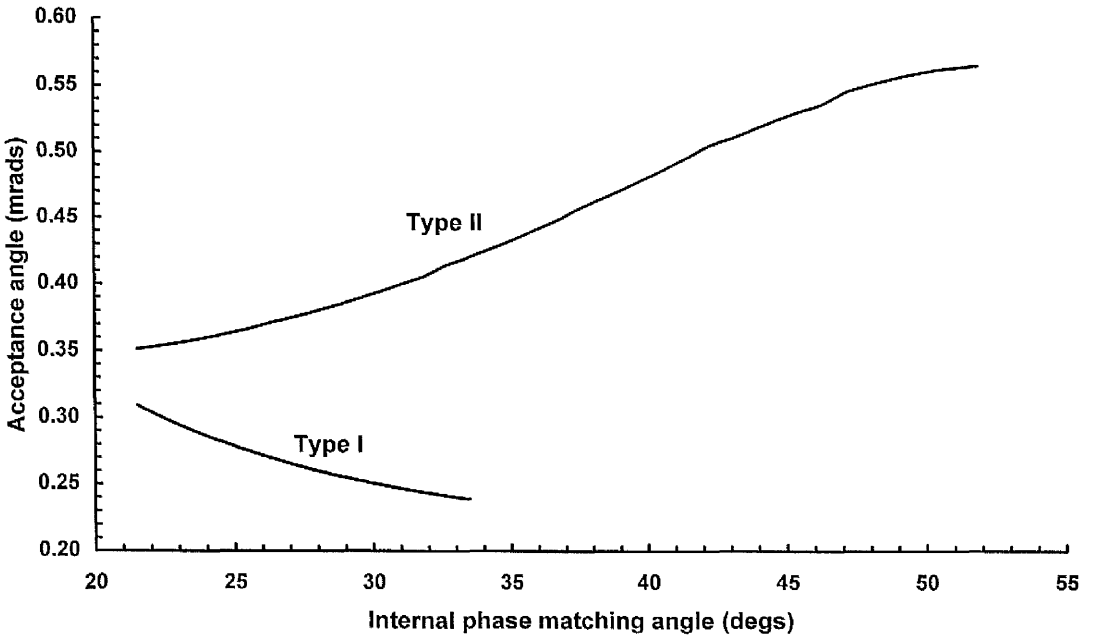

Figure 3.8. Acceptance angles for BBO in both the type I and type II phase matching regimes. The calculation is based on a 12 mm long crystal.

To remain within the limits imposed by the acceptance angle would result in a severe restriction in the length of the BBO to only a few millimetres.

The temperature bandwidth of BBO is not sufficiently narrow for the crystal to require temperature stabilisation in a simple cavity oscillator. Type I and type II phase matching bandwidths are shown in figure 3.9 and both indicate that a crystal temperature change of >50°C would be needed before a significant fall in efficiency is observed.

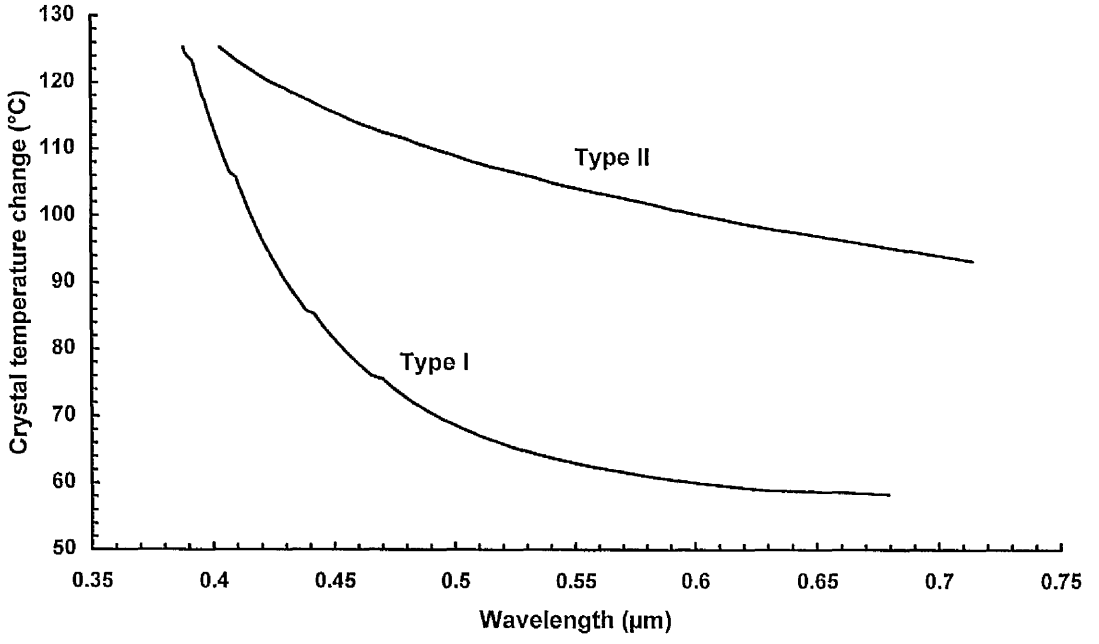

Figure 3.9 Temperature bandwidth of BBO in both the type I and type II phase matching regimes. A crystal length of 12 mm was used in the computation.

The observed temperature insensitivity not only means that stabilisation is not necessary, but also that temperature increases caused by pump energy absorbed by the crystal will not significantly detune the oscillator. This is a positive attribute for high power pumping.

The effects of Poynting vector walk-off can severely limit the conversion efficiency of the oscillator and this is an important parameter to consider when selecting a crystal for a given application. The walk-off angles for both type I and type II phase matching have been calculated and are shown in figure 3.10.

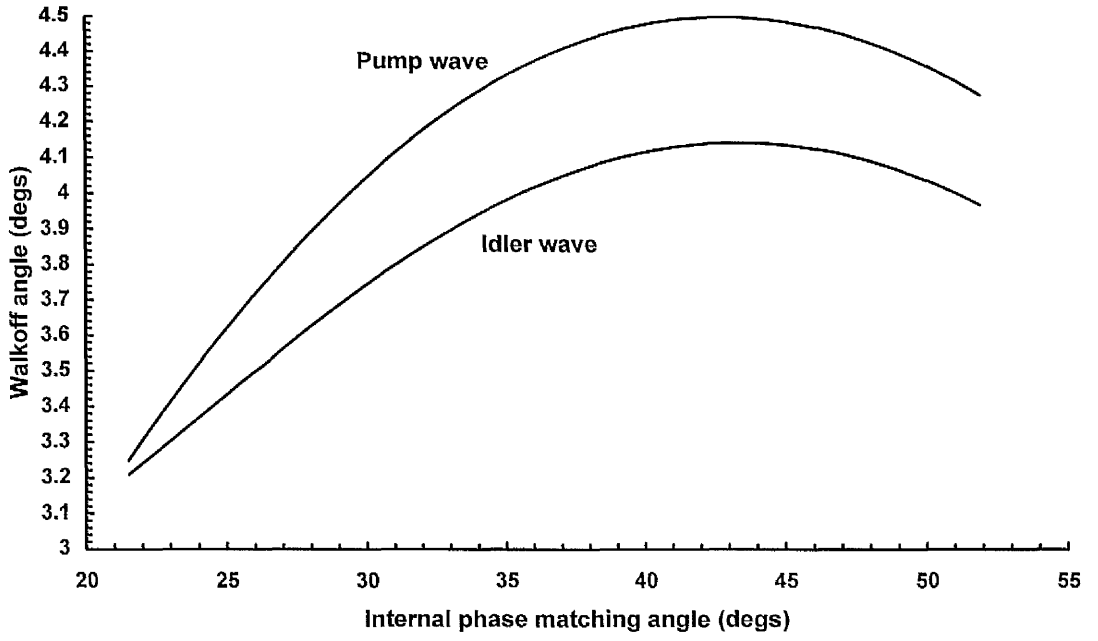

Figure 3.10 Double refraction angles(walk-off angles) for pump (type I and type II) and idler (type II) rays in BBO over the range of phase matched angles.

In the case of type II phase matching, both the pump and the idler waves are polarised as e-rays and so both experience Poynting vector walk-off. The walk-off angle (or double refraction angle) varies over the phase matching angle and peaks at 4.2° and 4.5° for the idler and pump, respectively. This dual walk-off can be exploited in a type II phase matched oscillator by allowing the idler wave to be resonant in the cavity and the signal to be free or non-resonant. The idler, as a result of its walk-off, more closely shadows the pump during its passage through the crystal and this ensures a lower oscillation threshold than a similar set-up with the signal resonant. Such a comparison has been demonstrated by Bosenberg *et al* [6] where the authors reported a 2.4 fold

decrease in the oscillation threshold of the idler-resonant OPO over an otherwise identical signal-resonant device.

The walk-off of the extraordinary pump ray in the type I phase matched regime is the same as that for the type II pump wave, but limited to the type I phase matching angle range of ~21° to ~33°. The large double refraction angle of ~4° is a result of the large birefringence of BBO. In the collinear phase matching configuration, it can severely limit the crystal length available for interaction. Noncollinear phase matching, however, can significantly reduce these effects This is discussed in greater detail in chapter four.

Finally, the signal linewidth of each type of phase matching have been modelled according to equations 2.38 and 2.39. Results are shown in figure 3.11 for a 12 mm long crystal. Signal linewidths of the type I oscillator are shown to vary from 1 nm at the blue end of the tuning range to more than 12 nm when the interaction nears degeneracy.

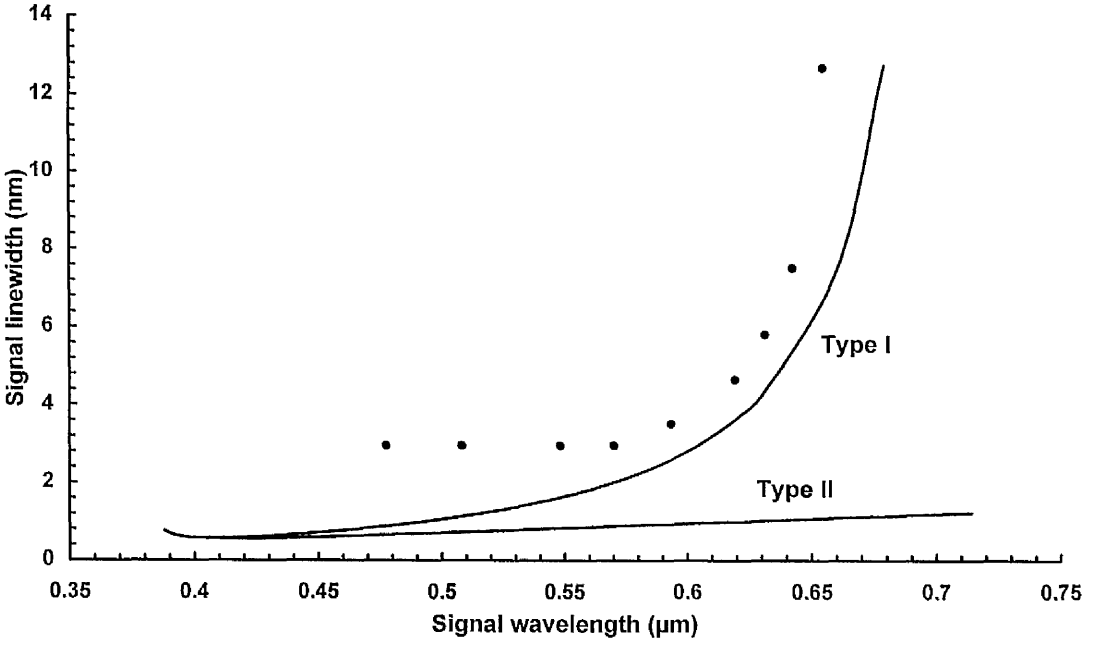

Figure 3.11. Theoretical signal linewidths of a type I and type II OPO using a 12 mm long BBO crystal pumped at 355 nm. The experimental data points are taken from a simple cavity BBO OPO under the same conditions as stated in the theory.

Type II phase matched signal linewidths, on the other hand, remain almost constant at ~1 nm over the tuning range. Experimental data are also shown for a type I, 355 nm pumped 12 mm long BBO OPO. These points were measured using an optical multichannel analyser (OMA) and are shown to be slightly greater than the theoretical values, which could be a result of an underestimation of the pump beam divergence of 2 mrad used in the calculation. The experimental points are also seen to level off at 550 nm with a linewidth of 3 nm which is the resolution limit of the OMA.

The increased difference in the response of the signal linewidth for the two phase matching regimes near degeneracy can be explained in terms of the rate of tuning of each oscillator which is known to govern the output linewidth of the device [10]; the greater the rate of tuning, the broader the linewidth is expected to be. From the tuning response (figure 3.6), the rate of tuning is clearly greater in the type I oscillator as degeneracy is approached.

3.3 Lithium Triborate

Lithium triborate (LiB_3O_5, LBO) was developed in China at the Fujian Institute on Structure of Matter and first reported by Chen *et al* in 1989 [11]. The aim was to improve on the properties of BBO. To some extent, this has been achieved since LBO has an extremely high damage threshold of 25 $GWcm^{-2}$ [11], a large transparency range comparable to that of BBO, a smaller walk-off angle, larger acceptance angles and moderate temperature sensitivity allowing for non-critical phase matching. However, the effective non-linear coefficient is lower in LBO than in BBO and this can lead to higher oscillation thresholds. The properties of LBO are now discussed in more detail.

LBO is an inorganic, biaxial crystal belonging to the point group mm2 whose piezoelectric axes X, Y and Z are parallel to the crystallographic axes a, b and c such that X→a, Y→b and Z→c. When the axes of the index ellipsoid are ordered so that $n_X<n_Y<n_Z$, the principal axes map to the crystallographic axes according to x→a, y→c and z→b. Hence, the three orthogonal axes systems are grouped as (b, Y, z), (c, Z, y) and (a, X, x).

Despite the large transparency range of 160 nm-2600 nm [9], phase matched second harmonic generation in LBO is only possible for fundamental wavelengths greater than 554 nm [12]. However, the generation of UV radiation down to the UV cut-off at 160 nm is possible by sum-frequency mixing of infrared radiation with UV light [12].

LBO has temperature-sensitive indices of refraction and can be temperature tuned. The first parametric oscillator based on LBO was demonstrated with 532 nm pumping by Kato [13] in 1990. The oscillator was type II noncritically phase matched and temperature tuned, generating tunable radiation from 950 nm-1.006 μm. Since then, LBO has risen to be a front-runner for parametric generation of radiation from the UV [14], through the visible [15]-[16] and into the near infrared region [17]-[19]. As a biaxial crystal, LBO offers more phase matching possibilities than BBO since phase matching can be accommodated in any of the three principal planes xy, yz and xz without the non-linear coefficients vanishing.

The principal refractive indices for LBO have been determined by different researchers and a collection are tabulated below in Table 3.2 in order of publication.

The form of the Sellmeier equations is

$$n_x^2 = ax + \frac{bx}{\lambda^2 - cx} - dx \cdot \lambda^2 \qquad (3.5)$$

	na	nb	nc	nd
n_x^2 [11]	2.4517	0.01177	0.00921	0.00960
n_y^2 †	2.5279	0.01652	0.005459	0.01137
n_z^2	2.5818	0.01414	0.01186	0.01457
n_x^2 [20]	2.4542	0.01125	0.01135	0.01388
n_y^2	2.5390	0.01277	0.01189	0.01848
n_z^2	2.5865	0.01310	0.01223	0.01861
n_x^2 [21]	2.45316	0.01150	0.01058	0.01123
n_y^2	2.5369	0.01249	0.01339	0.02029
n_z^2	2.58515	0.01412	0.00467	0.01850

Table 3.2 A collection of published Sellmeier data for LBO.

and two similar expressions for n_y^2 and n_z^2, except for n_y^2 †, whose denominator terms are added instead of subtracted in equation 3.5. LBO has three non vanishing non-linear coefficients, namely d_{33}, d_{32} and d_{31}. The d_{33} coefficient is small (~0.2 pm/V) and may be ignored. The other coefficients, d_{32} and d_{31}, have been reported as 1.46 pm/V and 1.1 pm/V [11] and more recently as 1.24 pm/V and 1.15 pm/V [22]. In the analysis presented here, the first reported set by Chen *et al* are used.

LBO can be critically (CPM) and noncritically phase matched (NCPM). Noncritical phase matching can take place along the x and z axes of the crystal, but not along the y axis, as the effective non-linear coefficient is zero here. At 355 nm pumping, type II NCPM is possible along the z axis, but infrared absorption at the idler wavelength prevents both type I and II NCPM along the x axis at room temperature. CPM in a type I geometry in the xy plane can take place, when pumped by the third harmonic of a Nd:YAG laser, and a similar tuning range to that of BBO can be observed. Type II

CPM also exists in both the xz and yz planes. A brief analysis of these phase matching schemes is now carried out.

3.3.1 xy plane

The type I critical phase matched tuning curve for LBO pumped at 355 nm is shown in figure 3.12. The full tuning range spans more than 20° of rotation and is shown to exceed the infrared cut-off at the extreme end of the curve. The corresponding effective non-linear coefficient is also depicted and is seen to fall off more rapidly approaching degeneracy.

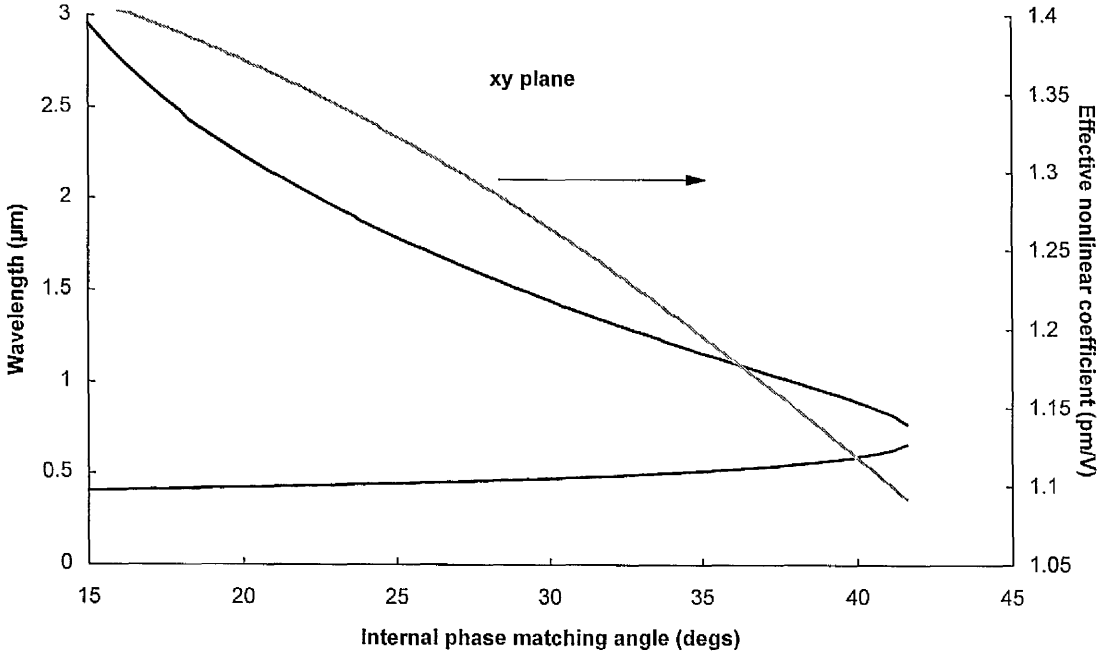

Figure 3.12 Type I phase matching in LBO pumped at 355 nm in the xy plane of the crystal, with the corresponding variation of the effective non-linear coefficient.

Under certain pumping conditions, type I noncritical phase matching (NCPM) can take place along the x axis (ϕ=0). An optical parametric amplifier has been demonstrated under such conditions [23], where the effective non-linear coefficient is a maximum.

In the case of 355 nm pumping, the infrared absorption edge at 2.6 μm is reached at about ϕ=17°, thus preventing further tuning down to the x axis and NCPM. The effective non-linear coefficient for this interaction is given by $d_{eff} = d_{32}\cos\phi$ and reaches its maximum in the type I regime. The critical phase matched tuning range in this plane covers much of the visible part of the spectrum, and is similar to type I phase matching in BBO.

As a result of a smaller birefringence, LBO exhibits a smaller walk-off angle than BBO which again has its maximum in the xy plane. This is seen in figure 3.13 which shows the double refraction angle reaching a maximum as the internal phase matching angle nears the degenerate condition.

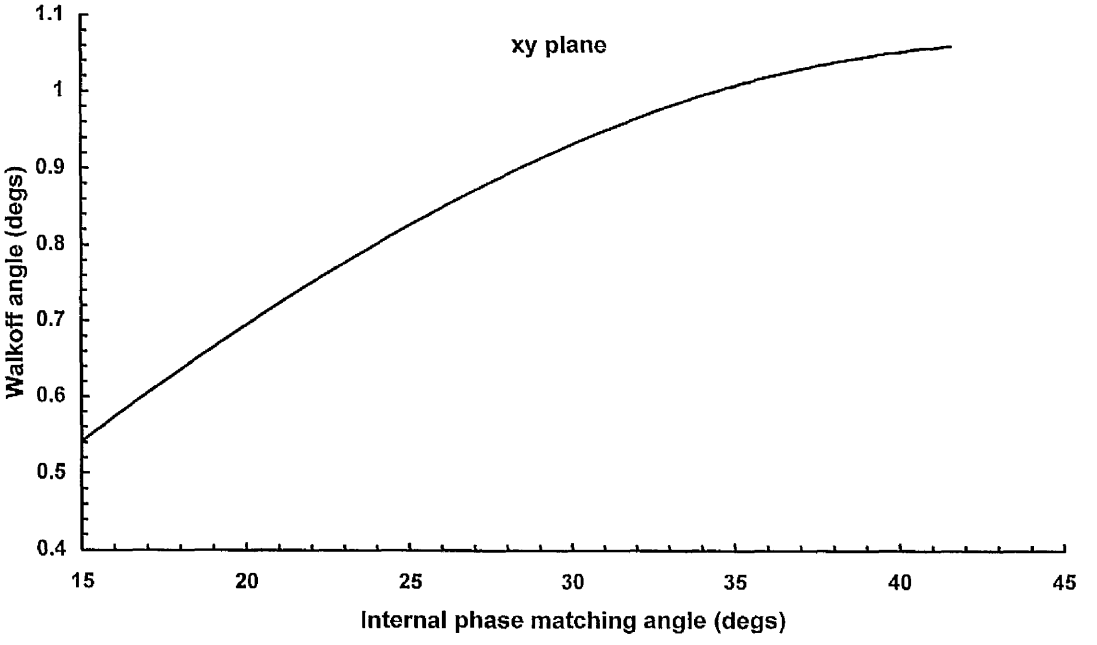

Figure 3.13 Variation of the double refraction angle of the extraordinary pump wave in LBO, in the xy plane, with phase matching angle. The pump wavelength used in the calculation was 355 nm.

Figures 3.12 and 3.13 indicate that near-degenerate oscillation in LBO in the xy plane may become increasingly inefficient, resulting from the combined effect of an increase in the double refraction angle and a decrease in the effective non-linear coefficient.

3.3.2 xz and yz planes

Noncritical phase matching presents an attractive option in any material since the frequency conversion efficiency may be improved in the absence of Poynting vector walk-off, and with an increase in the angle of acceptance. LBO exhibits phase matching in the xz and yz planes. Noncritical phase matching has been demonstrated for type I phase matching along the principal x axis [16], [19] for which the effective non-linear coefficient $d_{eff} = d_{32}\cos\phi$ is a maximum. Type II NCPM has also been demonstrated using an excimer laser at 308 nm along the z axis of the crystal [14]. In this work, critical phase matching was further explored by rotating the crystal away from the noncritical condition to probe into both the xz and yz planes. An example of phase matching in this geometry is shown in figure 3.14 with the third harmonic of a Nd:YAG laser as the pump source.

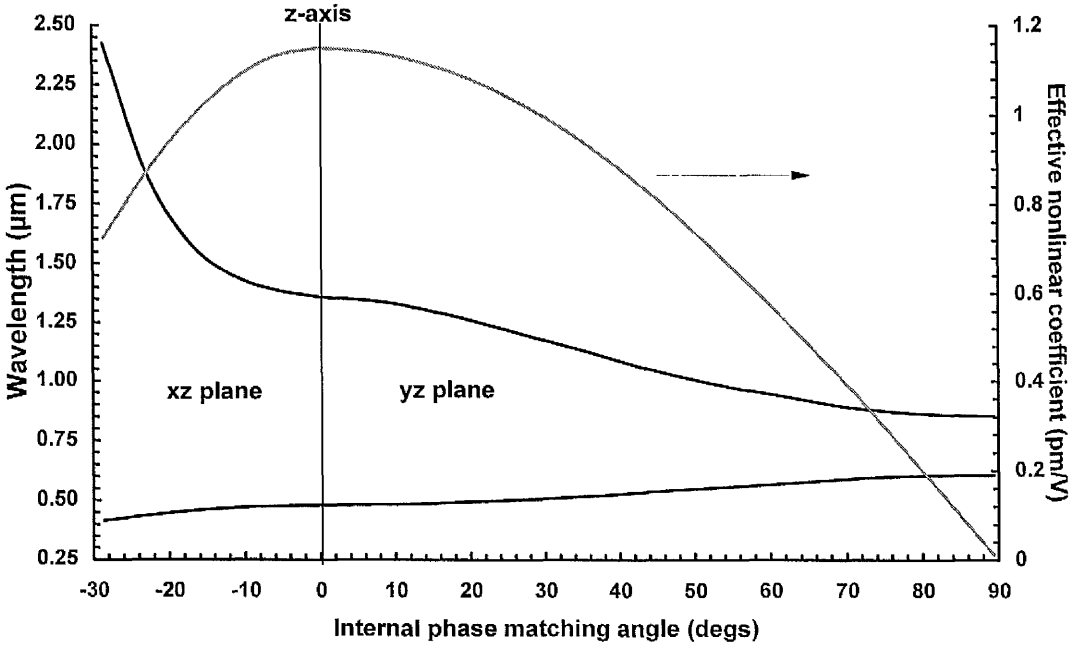

Figure 3.14 Type II phase matching in LBO pumped at 355 nm in the xz and yz planes.

In this case, the effective non-linear coefficient is again a maximum in the noncritical geometry. It is observed that noncritical phase matching along the y axis is not possible as a result of the vanishing non-linear coefficient. The effective non-linear coefficient for each plane is $d_{31}\cos^2\theta + d_{32}\sin^2\theta$ and $d_{31}\cos\theta$ for type II phase matching in the xz and yz planes, respectively.

The double refraction angle associated with both these interactions is shown in figure 3.15. As expected, the double refraction angle ρ is zero at θ=0° and initially increases smoothly as the angle increases into the respective planes.

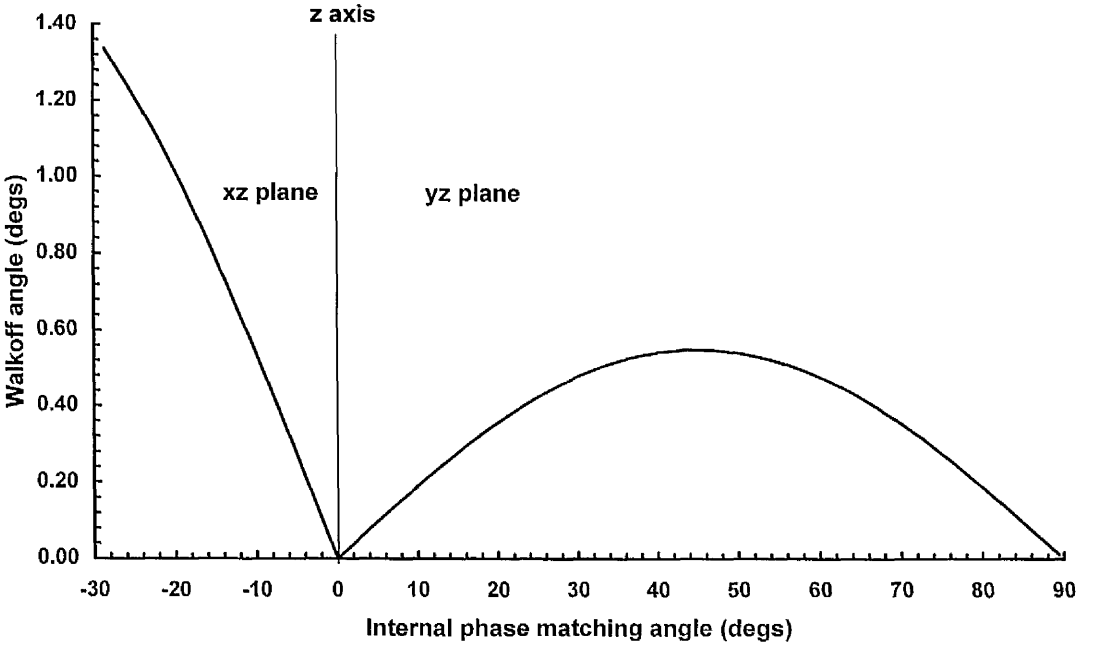

Figure 3.15 Double refraction angle in xz and yz planes in LBO

In the xz plane, ρ increases monotonically to a maximum of 1.3°, at which point the idler reaches the infrared cut-off of LBO. In the yz plane, on the other hand, ρ rises and falls to zero at the principal axes. Unfortunately, however, NCPM using UV pump sources in this plane is impractical for large tuning ranges since it has been reported

that even small tuning ranges of 10 nm require temperature changes of several hundred degrees [24].

3.4 Criteria for Crystal Selection

The previous two sections have reviewed some of the properties of BBO and LBO in an attempt to assess which material best lends itself to line-narrowing in a potentially high threshold cavity, whilst maintaining a broad tuning capability. The main advantages of LBO are that it exhibits noncritical phase matching and possesses a high damage threshold. However, in order to generate a broad visible tuning range the most favourable option in LBO is critical type I phase matching in the xy plane, which also has the highest non-linear coefficient of interaction. The non-hygroscopic nature of LBO must not be underestimated, as this property facilitates easy sample handling.

BBO, by comparison, has a superior effective non-linear coefficient, a potentially larger tuning range and a lower damage threshold. Although type II phase matching is possible, we believe that its low non-linear coefficient rules it out for highly frequency-selective cavities. The principal detrimental feature of BBO is its large double refraction angle which limits the three wave interaction length.

Table 3.3 below summarises some of the main properties of BBO and LBO, including the theoretical oscillation threshold of each oscillator calculated from equation 2.31 for the crystal lengths given in the table.

	BBO Type I	LBO Type I	LBO (NCPM)
Walk-off angle, ρ	4.2°	1.1°	0°
Walk-off length	1.4 cm	5.0 cm	N/A
Acceptance angle, Δθ	0.25 mrad	0.9 mrad	40 mrad
Oscillation threshold	0.55 J/cm^2	1.2 J/cm^2	0.8 J/cm^2
Crystal length	1.4 cm	1.5 cm	1.5 cm

Table 3.3 A summary of features of BBO and LBO calculated from the Sellmeier data presented in sections 4.3 and 4.4 and the crystal lengths in the table.

From the calculations set out in this chapter, and the data summarised in Table 3.3, type I phase matching in both BBO and LBO offer the desired combination of a broad tuning range and modest non-linear coefficient. BBO has been selected as the most suitable for use in a frequency selective cavity because of its high temperature bandwidth and higher effective non-linear coefficient which make it particularly suited to high threshold fluence cavities. Although the oscillation thresholds shown in table 3.3 are high (in chapter five the threshold for a similar cavity using BBO is measured to be ~0.3 J/cm^2), the threshold for type I LBO is still potentially close to the damage threshold of generally available cavity optics at ~1 J/cm^2.

3.5 Conclusions

LBO and BBO have been characterised with reference to their FOM, effective non-linear coefficients, tuning ranges, acceptance angles, temperature bandwidth and walk-off angles. BBO has accordingly been selected as the most suitable material for a highly tunable, narrow linewidth, high threshold device. In the following chapter, noncollinear phase matching is explored as a phase matching technique which reduces the effects of Poynting vector walk-off, and increases the overall performance of the oscillator.

References

[1] K. Kato "Second-harmonic generation to 2048 Å in β-BaB_2O_4" IEEE J. of Quantum Electron., 22, 1013, (1986)

[2] Y. Ishida and T. Yajima "Characteristics of a new type of SHG crystal beta barium borate in the femtosecond region" Opt. Commun., 62, 197, (1987)

[3] D. Eimerl, L. Davis, S. Velsko, E. K. Graham and A. Zalkin "Optical, mechanical and thermal properties of barium borate" J. Appl. Phys., 62, 1968, (1987)

[4] C. Chen, B. Wu and A. Jiang "A new type of ultraviolet SHG crystal-beta-BaB_2O_4" Sci. Sin. Ser. B., 28, 235, (1985)

[5] Y. X. Fan, R. C. Eckardt, R. C. Byer, C. Chen and A. Jiang "Barium borate optical parametric oscillator" IEEE J. Quantum Electron., 25, 1196, (1989)

[6] W. R. Bosenberg and C. L. Tang "Type II phase matching in a β-barium borate optical parametric oscillator" Appl. Phys. Lett., 56, 1819, (1990)

[7] W. Mückenheim, P. Lokai, B. Burghardt and D. Basting "Attaining the wavelength range 189 nm-197 nm by frequency mixing in β-barium borate" Appl. Phys. B., 45, 259, (1988)

[8] D. N. Nikogosyan "Beta barium borate (BBO): A review of its properties and applications" Appl. Phys A., 52, 359, (1991)

[9] G. C. Bhar, S. Das and U. Chatterjee "Evaluation of beta barium borate crystal for non-linear devices" Appl. Opt., 28, 202, (1989)

[10] S. E. Harris "Tunable optical parametric oscillators" Proc. IEEE J. Quantum Electron., 2096, (1969)

[11] C. Chen, Y. Wu, A. Jiang, B. Wu, G. You, R. Li and S. Lin "New non-linear-optical crystal: LiB_3O_5" J. Opt. Soc. Am. B., 6, 616, (1989)

[12] A. Borsutzky, R. Brünger, Ch. Huang and R. Wallenstein "Harmonic and sum-frequency generation of pulsed laser radiation in BBO, LBO and KD*P" Appl. Phys., B., 52, 55, (1991)

[13] K. Kato "Parametric oscillation in LiB_3O_5 pumped at 0.532 μm" IEEE J. Quantum Electron., 26, 2042, (1990)

[14] M. Ebrahimzadeh, G. Robertson and M. H. Dunn "Efficient ultraviolet LiB_3O_5 optical parametric oscillator" Opt. Lett., 16, 767, (1991)

[15] Y. Chi, M. H. Dunn, C. J. Norrie, W. Sibbett, B. D. Sinclair, Y. Tang and J. A. C. Terry "All-solid-state optical parametric oscillator for the visible" Opt. Lett., 17, 646, (1992)

[16] Y. Wang, Z. Xu, D. Deng, W. Zheng, B. Wu and C. Chen "Visible optical parametric oscillation in LiB_3O_5" Appl. Phys. Lett., 59, 531, (1991)

[17] M. Ebrahimzadeh, G. J. Hall and A. I. Ferguson "Temperature-tuned noncritically phase-matched picosecond LiB_3O_5 optical parametric oscillator" Appl. Phys. Lett., 60, 1421, (1992)

[18] S. Lin, J. Y. Huang, J. Ling, C. Chen and Y. R. Shen "Optical parametric amplification in a lithium triborate crystal tunable from 0.65 to 2.6 μm" Appl. Phys. Lett., 59, 2805, (1991)

[19] M. Ebrahimzadeh, G. J. Hall and A. I. Ferguson "Singly resonant, all-solid-state, mode-locked LiB_3O_5 optical parametric oscillator tunable from 652 nm to 2.65 μm" Opt. Lett., 17, 652, (1991)

[20] K. Kato "Tunable UV generation to 0.2325 μm in LiB_3O_5" IEEE J. of Quantum Electron., 26, 1173, (1990)

[21] S. Lin, B. Wu, F. Xie, C. Chen "Phase-matching retracing behavior: New features in LiB_3O_5" Appl. Phys. Lett., 59, 1541, (1991)

[22] J. T. Lin, J. L. Montgomery and K. Kato "Temperature-tuned noncritically phase matched frequency conversion in LiB_3O_5 crystal" Opt. Commun., 80, 159, (1990)

[23] J. Y. Huang, Y. R. Shen, C. Chen and B. Wu "Noncritically phase-matched second-harmonic generation and optical parametric amplification in a lithium triborate crystal" Appl. Phys. Lett., 58, 1579, (1991)

[24] Y. Tang, Y. Cui and M. H. Dunn "Lithium triborate optical parametric oscillator pumped at 266 nm" Opt. Lett., 17, 192, (1992)

Chapter 4

Noncollinear Phase Matching

Phase matching in non-linear optical processes takes advantage of the different refractive indices that orthogonally polarised light experiences as a result of crystal birefringence. With appropriately polarised fields, waves of different optical frequency propagate through the material at the same velocity, remaining in phase with one another. This permits the pump wave to interact with the generated electromagnetic waves throughout the interaction length of the gain medium. This assumes, however, that the waves remain spatially aligned during their passage through the crystal. In collinear critically phase matched interactions, spatial separation of the waves is observed as a result of double refraction of the extraordinary wave. Methods to counter this effect can cause dramatic increases in the conversion efficiency and reduce the operational threshold of the parametric oscillator. One such technique is noncollinear phase matching, which is explored in this chapter.

4.1 Extraordinary Ray Walk-off Compensation

An inherent phenomenon associated with critically phase matched (CPM) interaction processes is the effect of extraordinary ray Poynting vector walk-off. This results from the birefringence of the non-linear material and is characterised by the gradual separation of the extraordinary wave (e-ray) from the ordinary wave (o-ray). This effect is only experienced by the e-ray, as discussed in section 2.7. The greater the birefringence of the non-linear material, the greater the degree of walk-off observed.

Since the effect of Poynting vector walk-off can impose serious restrictions on the actual interaction length of the parametric process, the technique of noncritical phase matching (NCPM) has been widely used in certain non-linear crystals whose indices of refraction are sensitive to changes in temperature, particularly more recently in lithium

triborate (LBO) [1]-[3]. Other techniques include increasing the pump beam spot size which causes an increase in the interaction length [4]. Another strategy is noncollinear phase matching.

Noncollinear phase matching was first reported in optical parametric oscillators by Falk and Murray in 1969 using a $LiNbO_3$ crystal pumped with a ruby laser [5]. Since then, however, this phase matching technique has received relatively little attention. Dou *et al* have investigated noncollinear phase matching in parametric amplification [6] and sum-frequency generation in 3-methyl-4-nitropyridine-1-oxide (POM) [7]. Also, Piskarskas *et al* have used this approach to improve the overall efficiency of their barium borate parametric oscillator [8]-[9], and a similar arrangement was incorporated by Wachman *et al* in their KTP oscillator [10]. In references [9] and [10], the authors report a significant increase in the conversion efficiency of the OPO when noncollinear phase matching is incorporated. In particular, Bhar *et al* [11] have employed noncollinear phase matching in difference-frequency mixing in BBO and have demonstrated more than an order of magnitude increase in the conversion efficiency compared with CPM.

To illustrate noncollinear phase matching, a negative uniaxial crystal is first considered in a type I *critical* phase matching regime. Here, an extraordinary pump wave is required to pump the crystal and two ordinary waves are generated (e→o+o). The e→ o+o interaction in a negative uniaxial is shown in figure 4.1 using one quadrant of the wave vector loci of the three waves. The figure is constructed from the normal surfaces discussed in chapter two, section 2.3.1 and has been converted from the variation of refractive index with propagation angle to momentum variation. The pump k vector $\mathbf{k_p}$, therefore, is shown as a quadrant of an ellipse and shows the angular dependence of the variation of the photon momentum within the crystal. The o-ray signal and idler k vectors, $\mathbf{k_s}$ and $\mathbf{k_i}$, have loci which broadly vary as parts of circles. Plotting the exact momentum loci of the o-rays is complicated by the change in radii of

the circle resulting from the consequent change in frequency as the propagation angle varies.

The vector $\mathbf{k_p}$ lies at an angle θ_p to the optic axis, which shall be called the phase matching angle. This represents a critically phase matched OPO with the resonant axis parallel to $\mathbf{k_p}$, $\mathbf{k_s}$ and $\mathbf{k_i}$. The *direction* of the Poynting vector of the pump, $\mathbf{S_p}$, is also shown and is non-parallel to the resonant axis of the OPO, which is in the direction of $\mathbf{k_p}$. The Poynting vectors of the signal and idler are coincident with their respective k vectors, as they are both ordinary waves. Since the Poynting vector is the direction of the energy flow of the wave, the interaction between the pump wave and the resonant wave diminishes as the separation continues to develop through the crystal.

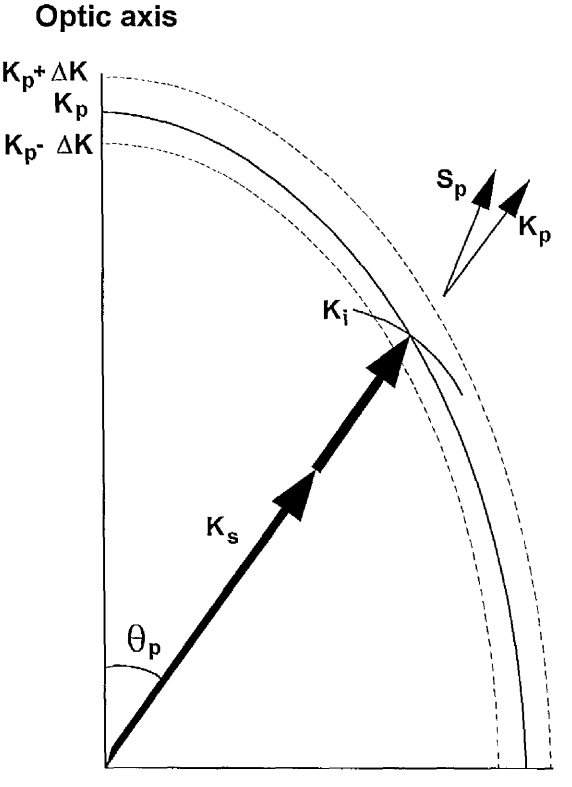

Figure 4.1. Locus of the wave vector of the pump, signal and idler for a type I critically phase matched interaction in a negative uniaxial.

It is apparent from the figure that for an e-ray, there exists only two positions along the surface of the ellipse where $\mathbf{S_p}$ is collinear with $\mathbf{k_p}$ and the walk-off is zero; the first is along the optic axis where the anisotropic medium exhibits no birefringence, and the second is perpendicular to the optic axis. It is here that noncritical phase matching can take place in an appropriate material, as discussed in section 2.3.1. Explanation of the parameters $\mathbf{k_p}\pm\Delta\mathbf{k_p}$ in figure 4.1 will be given in the next section.

The noncollinear phase matching geometry can partially or wholly compensate for the extraordinary ray walk-off of the Poynting vector from the resonant axis. Figure 4.2 illustrates how the three waves of a noncollinearly phase matched OPO might be oriented.

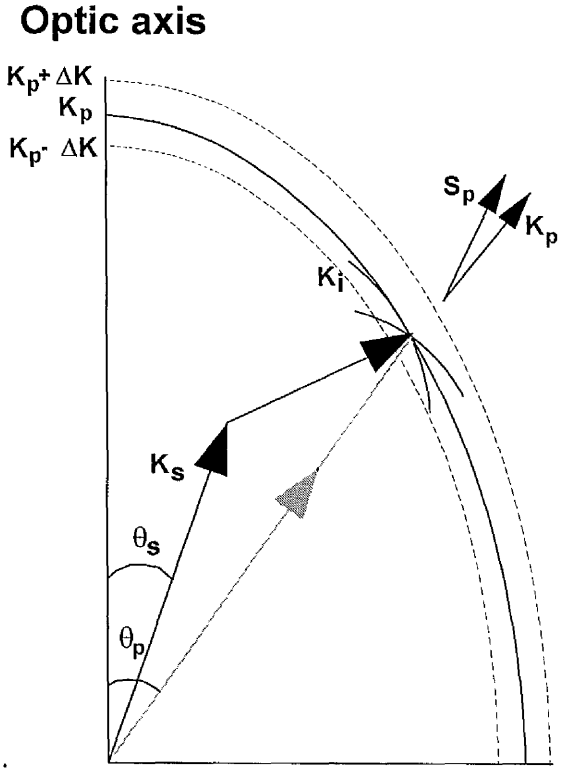

Figure 4.2. Wave vector locus for the three waves in a noncollinear phase matched geometry. The signal Poynting vector (coincident with $\mathbf{k_s}$*) is aligned parallel to that of the pump,* $\mathbf{S_p}$.

Here, the arrangement of the collinear signal and idler k vectors, shown in grey, represents the position of the pump k vector, and the new noncollinear positions of these vectors are shown in black. In this case, the signal is the resonant wave as it is evident that the geometry causes $\mathbf{k_s}$ to align parallel to the Poynting vector of the pump wave, $\mathbf{S_p}$.

In other words, the effect of Poynting vector walk-off has been reduced or even eliminated by the collinear propagation of the Poynting vector of the signal and that of the pump, thereby increasing the parametric interaction length. The degree to which $\mathbf{k_s}$ (and, hence $\mathbf{S_s}$) overlaps with $\mathbf{S_p}$ depends upon the degree of noncollinearity imposed on the OPO cavity and this, in practice, may be limited by the crystal aperture.

The noncollinear phase matching geometry is induced in the OPO either by directing the pump beam into the crystal at an angle to the oscillation axis, or by rotating the cavity mirrors of the oscillator about the crystal of an otherwise collinear arrangement. Both methods result in the oscillation axis lying at an angle to the pump axis. The first method was described by Falk and Murray [5].

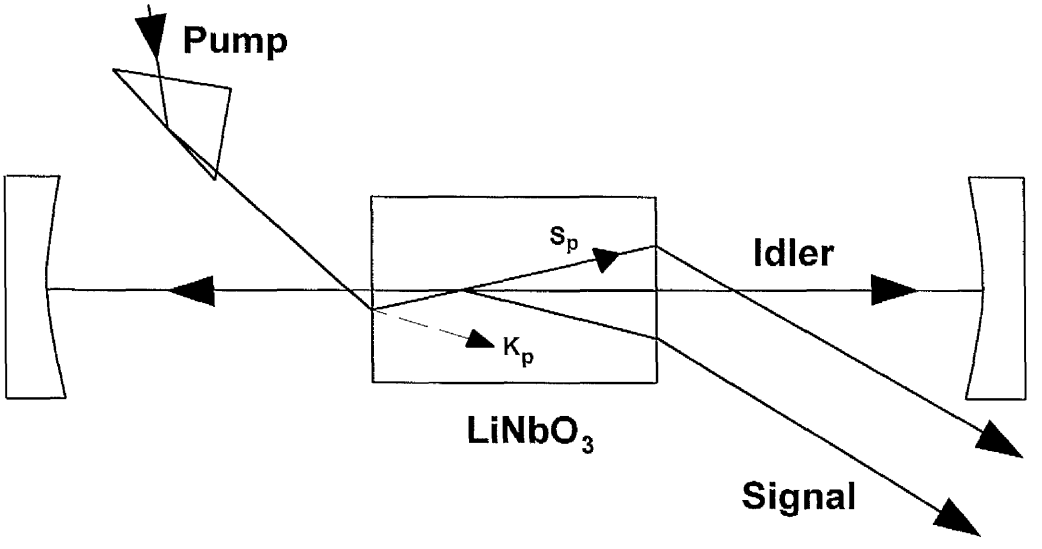

Figure 4.3. Noncollinearly phase matched parametric oscillator as demonstrated by Falk and Murray [5].

Tuning was achieved by varying the angle between the oscillation axis and the pump beam, and was the result of two independent effects: the change in the extraordinary refractive index of the pump and the change in angle between the pump vector and the resonant idler vector. Figure 4.3, adapted from reference [5] shows the cavity designed by Falk and Murray.

Disadvantages of this method are the limitation on cavity length imposed by the steering prism, and the difficulty in varying the degree of noncollinearity. Nevertheless, the effect of Poynting vector walk-off is partially compensated by this geometry as the pump k vector, $\mathbf{k}_p$, is refracted in the normal sense within the crystal whereas the Poynting vector, $\mathbf{S}_p$, is shown crossing the resonant axis.

In the work presented here, the noncollinear geometry is imposed upon the cavity by rotating the two cavity mirrors of the collinearly phase matched oscillator such that the resonant wave tends to reposition itself over the Poynting vector of the pump. The degree of noncollinearity is determined by the extent to which the cavity is rotated relative to the direction of the pump k vector. It is, perhaps, obvious to state that the direction of the cavity rotation is important and must be in the direction of the Poynting vector walk-off, otherwise the detrimental effects of extraordinary ray walk-off are compounded. Typically, a rotation of 10 mrad or less is sufficient to observe a noticeable increase in the efficiency of the OPO. Tuning the OPO takes place by rotation of the crystal relative to the pump k vector, $\mathbf{k}_p$, although the act of twisting the cavity mirrors itself tunes the device.

Figure 4.4 illustrates the OPO in a noncollinear geometry, with BBO as the gain medium. Although the Poynting vector $\mathbf{S}_p$ is shown at an exaggerated angle to the pump k vector, the geometry is seen to partially compensate for the walk-off through the repositioning of the resonant axis.

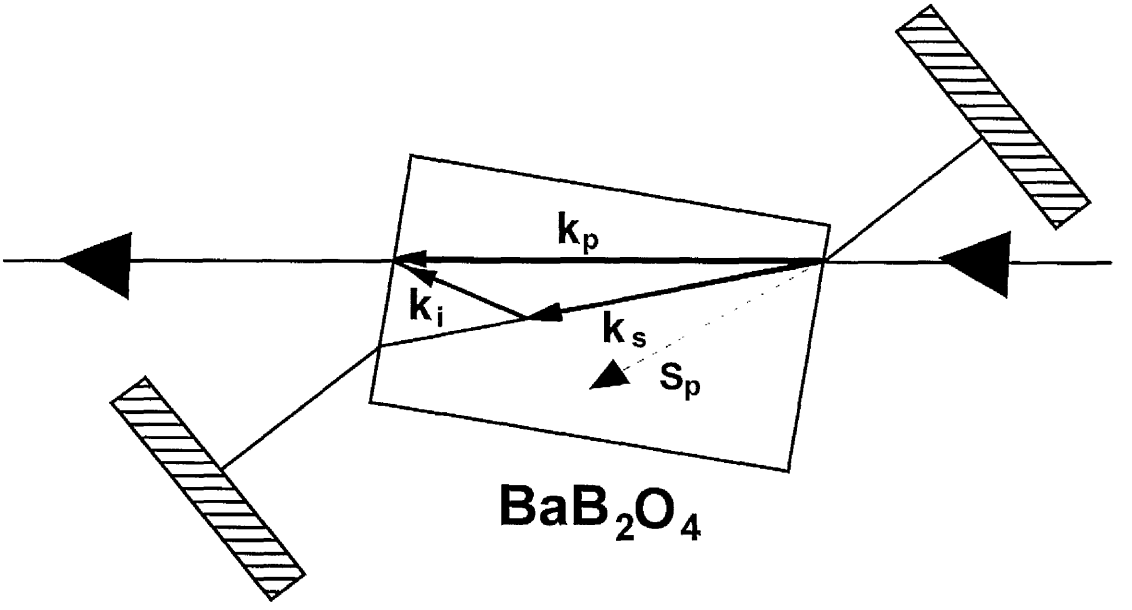

Figure 4.4. Noncollinear geometry used in the work presented here. The twist imposed on the cavity causes the Poynting vector of the resonant wave (in this case, coincident with $\mathbf{k}_s$*) to move towards the Poynting vector of the pump,* $\boldsymbol{S}_p$.

Apart from compensating for the walk-off of the Poynting vector of the extraordinary ray, it is possible for the noncollinear geometry to ease the restriction on the acceptance angle imposed on the pump beam. This is explained in the following section.

4.2 Acceptance Angle

The acceptance angle is defined as the planar angle over which the mis-match of the wave vector for the interaction is not greater than π/l. Critically phase matched, angle-tuned parametric generation is usually characterised by a small acceptance angle. For example, in chapter three, the acceptance angle for a 355 nm pumped BBO parametric oscillator was calculated to be about 0.25 mrad. Although this is considered to be small, acceptance angles of less than 1 mrad in a 1 cm crystal are not uncommon. The

acceptance angle can be determined by means of a Taylor expansion of the phase mis-match which has been described in chapter two.

There are two conditions under which the first order term vanishes and the acceptance angle becomes dependent upon the second term of the Taylor series. The first is NCPM and the second situation arises when the optical beams are propagated noncollinearly so that the tangential phase matching condition applies [12]. NCPM will not be discussed further here. To understand tangential phase matching better, we return to figures 4.1 and 4.2.

Figure 4.1 shows the wave vectors propagating collinearly at an angle θ_p to the optic axis. Here, the phase matching condition relies critically on the angle of propagation in the optic plane, and the exact phase matching condition is satisfied by the discrete intersection of $\mathbf{k_i}$ with $\mathbf{k_p}$. When propagated in a noncollinear geometry, however, the tangential phase matching condition can be reached (figure 4.2) where the intersection between $\mathbf{k_i}$ and $\mathbf{k_p}$ is no longer discrete and the allowable phase mis-match is much greater. Figure 4.2 is designed to illustrate the increase in the allowable deviation from the perfectly phase matched case by showing the idler wave vector loci for both the collinear and noncollinear cases. Where the respective loci intersect the dashed line representing $\mathbf{k_p}$-$\Delta\mathbf{k}$, the lower acceptable mis-match limit is reached. Clearly, the degree of allowable mis-match is greater in the noncollinear phase matched case.

The tangential condition is only reached when the vector propagation of the signal and idler are in the direction shown in figure 4.2; that is when $\theta_s<\theta_p$ in the case of a negative uniaxial. Under the tangential phase matching condition, the maximum tolerable beam divergence becomes dependent upon the second term of the Taylor series for the phase mis-match, and relatively large acceptance angles are obtainable. The exact solution to the second order term is not given here, but it is of the order

$$\Delta\theta_p'' \approx \sqrt{\frac{1}{l}\left[\left(\frac{\partial^2 n_p}{\partial\theta_p^2}\right)\frac{1}{\lambda_p}\right]^{-1}} \qquad (4.1)$$

which has been derived from reference [12] for a type I phase matched interaction in a negative uniaxial crystal. It is shown in the next chapter that the allowable pump beam divergence increases by an order of magnitude relative to the critically phase matched values. Consequently, pump beams of greater divergence can be phase matched by the crystal in a noncollinear geometry.

4.3 Frequency Tuning

The tuning method of the noncollinear OPO is no different to that usually employed for a collinear OPO, and involves rotation of the crystal relative to the pump k vector, $\mathbf{k_p}$. As previously mentioned, the change from collinear to noncollinear geometry also causes the OPO to tune by forcing a change in the propagation direction of $\mathbf{k_s}$ (and consequently, $\mathbf{k_i}$) relative to the optic axis, thereby changing the phase matching condition.

By considering the vectorial triangle made up from the three momentum vectors $\mathbf{k_p}$, $\mathbf{k_s}$ and $\mathbf{k_i}$ in figure 4.5 and resolving the vectors in two orthogonal directions the noncollinear phase matching equation can be calculated. The axes of resolution were chosen to be along $\mathbf{k_s}$ and perpendicular to $\mathbf{k_s}$. The roots of the ensuing equation are then found, and the tuning response of the OPO calculated for a particular degree of noncollinearity. The angle q in figure 4.5 indicates the degree of noncollinearity imposed on the cavity and is defined as the angle subtending $\mathbf{k_p}$ and $\mathbf{k_s}$ in free space.

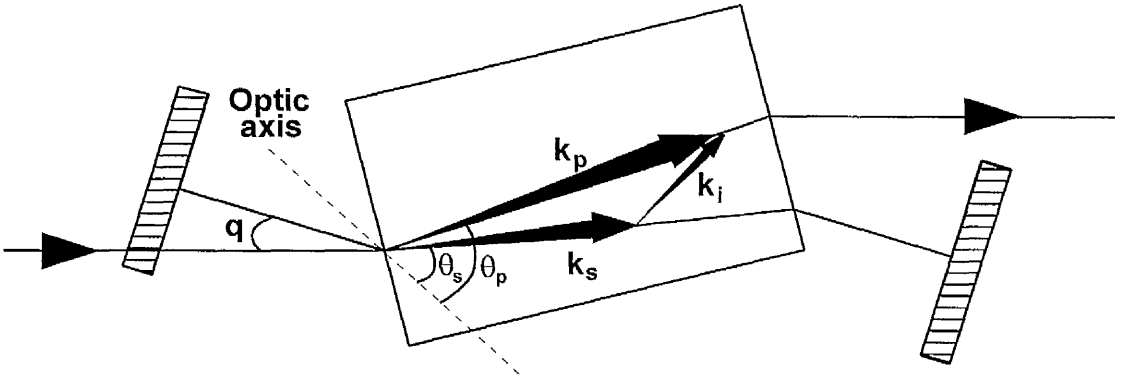

Figure 4.5. Noncollinear geometry characterised by the vectorial triangle of the three k vectors. The degree of noncollinearity is denoted by q, the angle subtending $\mathbf{k_p}$ *and* $\mathbf{k_s}$ *in free space. The angles* θ_p and θ_s *subtend* $\mathbf{k_p}$ *and the optic axis and* $\mathbf{k_s}$ *and the optic axis respectively within the crystal. For the noncollinear process to compensate for Poynting vector walk-off and tend towards the tangential condition,* θ_p *must be greater than* θ_s *in a negative uniaxial.*

Equation (4.2) below can be solved to predict the tuning response of any noncollinearly phase matched OPO. With the appropriate eigenvalues of refractive index, the equation may be applied to both type I and type II phase matching.

$$\left(\frac{n_p}{\lambda_p}\right)^2+\left(\frac{n_s}{\lambda_s}\right)^2-\left(\frac{n_i}{\lambda_i}\right)^2-2\left[\frac{n_p\cdot n_s}{\lambda_p\lambda_s}\right]\cos\left(\theta_p-\theta_s\right)=0 \qquad (4.2)$$

where n is the refractive index and λ is the free space wavelength where p, s and i denote the pump, signal and idler respectively. Equation 4.2 is quadratic in $1/\lambda_s$ (or similarly, $1/\lambda_i$) and has two roots which both have a physical significance. The existence of the two roots arises from the asymmetry of the k-vectors about the resonant axis and, therefore, does not apply to the collinear phase matched geometry. One root denotes the resonant signal and the other represents the resonant idler, both at the same degree of noncollinearity. Later, in chapter five, the equation is solved for both roots and the corresponding tuning response is corroborated experimentally for each case.

4.4 Oscillator Gain Bandwidth

The gain bandwidth of the parametric oscillator increases as a result of the noncollinear geometry. This is broadly explained by an increase in spatial mode coupling of the pump Poynting vector with the resonant wave. To be more specific, it is necessary to return to the coupled amplitude equations for the signal and idler electric fields. Equations 2.7 described the variation of the electric fields of the signal and idler waves as they propagate through the crystal. Similar equations can be derived in the case of noncollinear phase matching. The propagation of the interacting beams is shown in figure 4.6 for type I (e→o+o) phase matching

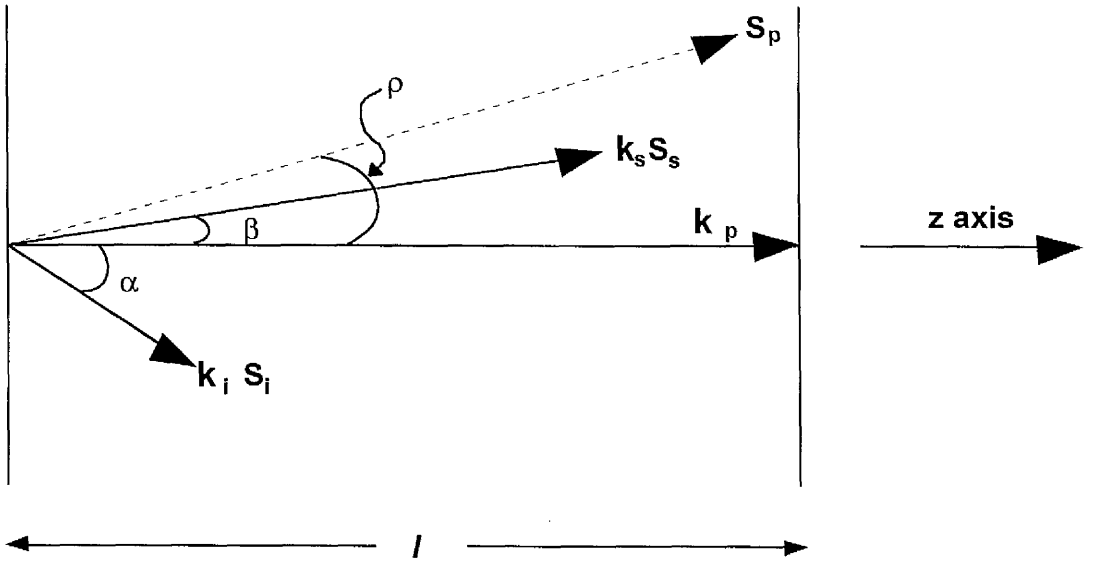

*Figure 4.6. Propagation of the noncollinear waves in the type I e→o+o interaction. **S** and **k** are the Poynting and wave vectors, respectively and p, s and i denote the pump, signal and idler. ρ is the walk-off angle of the pump ray and α and β are the angles subtending the idler and signal Poynting vectors to the z axis. l is the crystal length.*

In figure 4.6, the z axis is not necessarily related to the crystallographic axes but is the variable over which the evolution of the electric fields of the signal and idler is studied. This choice of axis allows the coupled noncollinear propagation equations to be compared directly with those developed in chapter two for the collinear geometry.

The coupled wave equations for the noncollinear interaction describing the directional derivatives of the fields of the signal and idler in the z direction are given by [13]

$$\frac{dE_s}{dz} = -\frac{j\kappa_s E_i^* E_p}{\cos\beta}$$
$$\frac{dE_i^*}{dz} = -\frac{j\kappa_i E_s E_p}{\cos\alpha} \tag{4.3}$$

where κ is defined in the collinear interaction (equation 2.8). The exact solutions to these equations have already been discussed in chapter two of this work, and by various authors (see, for example, [13]) and yield a gain coefficient given by

$$\gamma_{nc}^2 = \frac{2\omega_s\omega_i(deff)^2 I_p}{n_i n_s n_p \varepsilon_o c^3 \cos\alpha\cos\beta} \tag{4.4}$$

It is evident that the parametric gain coefficient increases in the noncollinear phase matching domain as a result of the new denominator in the equation (c.f. equation 2.8), which contains two trigonometric terms. Moreover, when all the other parameters are held constant, the parametric gain coefficient grows as the degree of noncollinearity is increased.

In addition to this increase in the parametric gain coefficient, the effective gain length of the crystal increases with the increased overlap of the pump Poynting vector and that of the resonant wave as a result of the noncollinear geometry. The walk-off length is approximately given by $l_\rho = w_p/\rho$, where w_p is the electric field radius of the pump beam. Brosnan *et al* [14] have defined the parametric gain length of the interaction as

$$L_{nc} = l_\rho erf\left(\frac{\sqrt{\pi}\cdot l}{2l_\rho}\right) \tag{4.5}$$

for Gaussian beams, where l is the actual crystal length. The walk-off length, however, increases with the degree of noncollinearity and can be altered accordingly, such that

$$l_\rho = \frac{w_p}{\rho - \beta} \tag{4.6}$$

where β is defined in figure 4.6. Hence, L_{nc} in equation 4.5 is the effective interaction length of the noncollinear geometry when l_ρ is used as the walk-off length. The gain of the noncollinear OPO has been calculated and compared to that of an otherwise identical collinear OPO. The calculation carried out here is for a BBO OPO pumped at 355 nm with an induced noncollinearity of q=54 mrad, where q is defined in figure 4.5. The data used in the calculation is tabulated below.

$\lambda_i(\mu m)$	$\lambda_s(\mu m)$	$\beta(°)$	$\alpha(°)$	n_p	n_s	n_i	$d_{eff}(pm/V)$	$\rho(°)$
2.376	0.417	1.78	10.20	1.676	1.689	1.633	1.64	3.82

Table 4.1. Pump is 355 nm and q=54 mrad for the noncollinear gain calculation. All other parameters used in the calculation are contained in the table.

Using the line centre gain expression discussed in chapter two (equation 2.10) together with equations 4.4-4.6, the expressions for the collinear and noncollinear gain as a function of length can be compared. It should be noted, however, that the depletion of the pump, resulting from the onset of oscillation, has not been considered.

Figure 4.7 shows the logarithm of the gain as a function of crystal length for both a collinear and a noncollinear OPO based on BBO pumped at 355 nm at two pump radii. Although the calculations are based upon equations which ignore crystal absorption and fail to exploit Gaussian beam intensity propagation, it is clear that the noncollinear geometry can be successfully used to improve significantly the gain of the OPO. When the crystal is thin, the functional dependence of the gain of both types of

geometries is similar. For crystal lengths in excess of 6 mm, however, saturation of the collinear gain begins and enhanced gain is obtained with the noncollinear geometry.

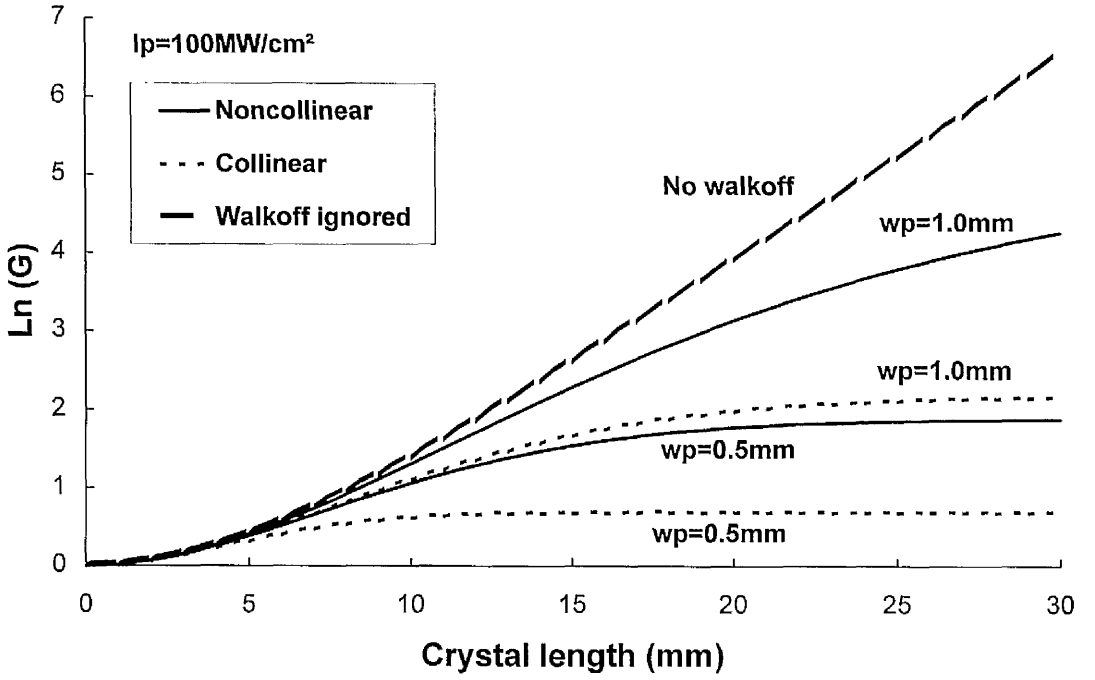

Figure 4.7. Logarithm of gain as a function of crystal length for the pump beam radii of 1.0 mm and 0.5 mm in collinear and noncollinear OPOs. The pump intensity is 100 MW/cm².

This observation has great practical importance, particularly in materials with low damage thresholds or large walk-off angles, or when the pump intensity is limited. In such cases, noncollinear geometry can be used to enhance the resonant wave power and facilitate the use of longer crystal length. Clearly, this is not so for collinear phase matching, where saturation occurs at shorter crystal lengths and further extensions become futile. The reason for the saturation in gain of the collinear OPO is obvious since, as l increases to a point beyond which the signal and pump beams no longer overlap, any further increase in crystal length fails to contribute to the gain of the OPO. Moreover, if crystal absorption and pump depletion are taken into account, the gain would eventually begin to fall with increasing l. Naturally, this is true for both the

collinear and noncollinear OPOs, but the effect is observed at shorter crystal lengths in the collinear case.

The figure also includes the logarithm of the gain of two pump beam radii; 0.5 mm and 1.0 mm. As expected, the gain is greater when the pump spot size is increased as a result of the greater degree of overlap between the pump wave and that of the resonant wave for a constant pump intensity. Such a technique for gain enhancement of the OPO has been studied by Robertson *et al* [4] with successful results and its effectiveness is apparent from the figure here.

The collinear gain has also been calculated under the condition of zero walk-off of the extraordinary pump wave. This is shown as a thick, dashed curve in figure 4.7. Clearly, in the absence of Poynting vector walk-off, the gain continues to increase with crystal length, as expected. This demonstrates the importance of including the effects of Poynting vector walk-off and illustrates the detrimental effect it has on the gain of the OPO.

The search for the optimum gain of an OPO should take into consideration the walk-off angle in addition to the effective non-linear coefficient. The size of the pump beam for a given intensity is also important and influences the walk-off behaviour.

4.5 Oscillation Threshold

It has been demonstrated above that the noncollinear geometry leads to a higher gain in the OPO. This results in a reduction in the oscillation threshold of the device. Using the theoretical model developed by Brosnan and Byer [14], the oscillation threshold fluence of a pulsed OPO can be determined assuming it is singly resonant and coupling only into the TEM_{00} modes of the cavity. The model has been previously discussed in section 2.4. Although the model takes care of the effects of walk-off by a

corresponding reduction in the interaction length, the noncollinear geometry requires an increase in the gain expression K. This is defined as

$$K_{nc} = \frac{\gamma_{nc}^2}{I_p} \tag{4.7}$$

where γ_{nc}^2 is defined in equation 4.4. Moreover, the walk-off length must be altered according to equation 4.6. Therefore, for a given degree of noncollinearity, the threshold fluence of the noncollinear OPO is described by

$$J_o(q) = \frac{2.25\cos\alpha\cos\beta}{Kg_s L_{nc}^2}\tau\left[\frac{l_o}{2\tau c}\ln 33 + 2\alpha_l l + \ln\frac{1}{\sqrt{R}} + \ln 2\right]^2 \tag{4.8}$$

for a type I e→o+o OPO. L_{nc}^2 has been defined previously as the effective walk-off length in the case of noncollinear phase matching, K is defined in equation 2.8 and α and β are shown in figure 4.6. All other terms are explained in reference [14]. Equation 4.8 has been successfully applied to a noncollinearly phase matched OPO and is shown to describe the threshold response as a function of the degree of noncollinearity q well. These and other results are discussed in the next chapter.

4.6 Noncollinear Oscillation Linewidth

The higher gain brought about by the noncollinear geometry causes the linewidth of the parametric oscillator to increase. One of the three contributing terms to the inherent linewidth of an OPO (discussed in section 2.6) is the phase mis-match of the resonant frequency before the fall in gain becomes intolerable. This is actually a definition of the gain bandwidth of the oscillator, and is the major contributing factor to the inherent linewidth of an OPO. It is perhaps not surprising, then, that the linewidth of a noncollinear OPO increases with degree of noncollinear phase matching.

Noncollinear phase matching demonstrates that the gain of the OPO is a variable parameter, which can be increased accordingly.

4.6 Conclusions

The theory of noncollinear phase matching has been described in a negative uniaxial crystal. It has been shown that significant increases in the gain can be attained by noncollinear phase matching by compensating for the Poynting vector walk-off of the extraordinary pump ray. Moreover, when the tangential condition is reached, the angular acceptance of the crystal becomes dependent on the second term of the Taylor series, thereby lifting the otherwise tight restriction on the pump beam divergence. In the following chapter, noncollinear phase matching is applied to BBO at two different pump wavelengths.

It should be noted, however, that the noncollinear phase matching analysis carried out in this chapter does not take account of the displacement of the Poynting vector of the non-resonant idler from the cavity axis as a result of the phase matching geometry. Since the parametric interaction requires all three waves to be present, this action may have a detrimental effect on the parametric gain. The real effect of the increase in the parametric gain may, therefore, result entirely from the opening up of the acceptance angle brought on by the noncollinear geometry. Further analysis is required to fully understand whether the increase in the parametric gain of the noncollinear oscillator results from the increase in crystal acceptance angle or the greater overlap of the resonant wave Poynting vector with that of the pump wave (despite the widely diverging non-resonant Poynting) or a combination of the two effects.

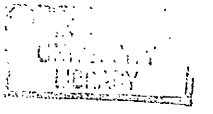

References

[1] J. Y. Huang, Y. R. Shen, C. Chen and B. Wu "Noncritically phase-matched second-harmonic generation and optical parametric amplification in a lithium triborate crystal" Appl. Phys. Lett., 58, 1579, (1991)

[2] J. T. Lin, J. L. Montgomery and K. Kato "Temperature-tuned noncritically phase matched frequency conversion in LiB_3O_5 crystal" Opt. Commun., 80, 159, (1990)

[3] M. Ebrahimzadeh, G. J. Hall and A. I. Ferguson "Temperature-tuned noncritically phase matched picosecond LiB_3O_5 optical parametric oscillator" Appl. Phys. Lett., 60, 1421, (1992)

[4] G. Robertson, A. Henderson and M. Dunn "Attainment of high efficiencies in optical parametric oscillators" Opt. Lett., 16, 1584, (1991)

[5] J. Falk and J. E. Murray "Single-cavity noncollinear parametric oscillation" Appl. Phys. Lett., 14, 245, (1969)

[6] S. X. Dou, D. Josse and J. Zyss " Comparison of a collinear and one-beam noncritical noncollinear phasematching in optical parametric amplification" J. Opt Soc. Am B., 9, 1312, (1992)

[7] S. X. Dou, D. Josse, R. Hierle and J. Zyss " Comparison of a collinear and noncollinear phasematching for second-harmonic and sum frequency generation in 3-methyl-4-nitropyridine-1-oxide" J. Opt Soc. Am B., 9, 687, (1991)

[8] A. Piskarskas, V. Smilgevicius, A. Umbrasas, A. Fix and R. Wallenstein "Parametric oscillation in beta-barium borate synchronously pumped by the third harmonic of a continuously excited mode-locked and Q-switched Nd:YAG laser" Opt. Commun., 77, 335, (1990)

[9] S. Burdulis, R. Grigonis, A. Piskarskas, G. Sinkevicius, V. Sirutkaitis, A. Fix, J. Nolting and R. Wallenstein "Visible optical parametric oscillation in synchronously pumped beta-barium borate" Opt. Commun., 74, 398, (1990)

[10] E. S. Wachman, W. S. Pelouch and C. L. Tang "CW femtosecond pulses tunable in the near- and mid-infrared" J. Appl. Phys., 70, 1893, (1991)

[11] G. C. Bhar, P. K. Datta, A. M. Rudra and U. Chatterjee "Tangentially phase-matched efficient generation in beta barium borate crystal" Opt. Commun., 105, 95, (1994)

[12] N. P. Barnes and V. J. Corcoran "Parametric generation processes: spectral bandwidth and acceptance angles" Appl. Opt., 15, 696, (1976)

[13] J. A. Armstrong, N. Bloembergen, J. Ducuing and P. S. Pershan "Interactions between light waves in a non-linear dielectric" Phys. Rev., 127, 1918, (1962)

[14] S. J. Brosnan and R. L. Byer "Optical parametric oscillator threshold and linewidth studies " IEEE J. Quantum. Electron., 15, 415, (1979)

Chapter 5

Noncollinear Phase Matching in BBO

This chapter describes the experimental design, methodology and results of noncollinear phase matching in barium borate optical parametric oscillators. Two systems have been investigated and are presented here. Both use the harmonics of a Nd:YAG laser; the first is a 355 nm pumped BBO OPO, and the second is a BBO OPO pumped at 532 nm. The first oscillator has a signal wavelength that spans the visible region of the spectrum whilst the second overlaps with the red end of the first and continues into the near infrared. The contents of the previous chapter will be referred to and, in places, expanded upon during the course of the experimental description here.

At this point it seems appropriate to describe the lasers used throughout the work described in this chapter. Two different Nd:YAG systems have been incorporated. The first, a Spectra-Physics DCR 11, with a 6 ns pulse duration and a maximum output energy of ~28 mJ/pulse was used as the pump source for the 355 nm pumped noncollinear OPO. The second, a Spectron SL804 1614 intracavity telescope oscillator-amplifier, was used to pump the 532 nm noncollinear OPO. This had a pulse duration of 19 ns. Both systems were operated at a 10 Hz repetition rate. The second Nd:YAG laser had an improved beam quality over the first. By careful adjustment to an intracavity aperture and the lens separation of the telescope, the beam profile could be configured to fit to a Gaussian intensity distribution to better than 95 %. It is thought that the smoother spatial profile of the Spectron Nd: YAG laser pulse presented less of a hazard to the crystal surfaces compared to the more ragged contour of the Spectra-Physics laser.

As the walk-off angle in BBO pumped at 532 nm is smaller than that pumped by 355 nm, the detrimental effects associated with the walk-off process are less severe at higher wavelengths. However, the 532 nm pumped oscillator is inherently less efficient as a result of the lower frequency pump wave. In such circumstances, it is arguable that attempts to increase the conversion efficiency of the OPO become more important for 532 nm pumping. Both the 355 nm and the 532 nm pumped noncollinearly phase matched OPOs are now presented.

5.1 BBO Pumped at 355 nm

This section describes the performance of type I phase matched BBO OPOs pumped by the third harmonic of an Nd:YAG laser. A single crystal is used with a cut of θ=35° for 355 nm pumping and ϕ=90° to maximise the effective non-linear coefficient. Following the theoretical predictions carried out in the last chapter, the OPO was constructed in collinear and three noncollinear phase matching configurations and the results of the tuning responses, threshold and general gain bandwidth are compared to the theory where appropriate.

5.1.1 Angular Acceptance

In the previous chapter, it was argued that the noncollinear phase matched configuration could extend to the point where the acceptance angle of the crystal depends solely on the second term of the Taylor series since the first term vanishes, or becomes small compared with the second term. This condition is know as tangential phase matching. Although the precise point at which the tangential phase matching condition is reached has not been calculated, the first term becomes small at modest degrees of noncollinearity. This can be shown by considering the first order

acceptance term of the Taylor series for type I noncollinear phase matching in a negative uniaxial crystal [1]

$$\Delta\theta'_p = \frac{1}{l}\left[\frac{dn_p}{d\theta_p}\cdot\frac{1}{\lambda_p}\cos(\alpha-\beta)-\frac{n_p}{\lambda_p}\sin(\alpha-\beta)\right]^{-1} \tag{5.1}$$

where α and β are the internal angles defined in figure 4.6 arising from the noncollinear process. The ratio of $dn_p/d\theta_p$ to n_p is about 0.07 for type I phase matched BBO pumped at 355 nm, with a 5 % variation over the tuning range of the OPO. A consequence of this ratio is that when the argument of the sine and cosine functions is 4° or more, the first order term $\Delta\theta'_p$ vanishes since sin 4°=0.07 whilst cos 4°≈1. This is termed the λ inflection point. With a degree of noncollinearity of 54 mrad induced in the OPO, $\alpha\approx10°$ and $\beta\approx2°$ causing the term in brackets in equation 5.1 to become negative. This in turn makes the first order acceptance angle meaningless, and the second order term must then be used. Evidently, when the phase matching geometry is collinear, the trigonometric arguments are zero and the first order term reduces to equation 2.35 for a type I interaction in a negative uniaxial. In this case, the acceptance angle depends inversely on the crystal length.

Applying the second order term discussed in chapter three to this OPO, the allowable angular acceptance of the crystal can be calculated under the condition of λ inflection. Great simplification in the form of this term can be achieved by assuming $d\beta/d\alpha \approx 1$, when the second order acceptance angle becomes

$$\Delta\theta''_p = \sqrt{\frac{1}{l}\left[\frac{\partial^2 n_p}{\partial\theta_p^2}\frac{1}{\lambda_p}\right]^{-1}} \tag{5.2}$$

The angular acceptance now depends inversely on the square root of the crystal length, leading to greatly enhanced acceptance angles. Applying this to the noncollinear phase

matched BBO OPO pumped at 355 nm in a type I configuration, the acceptance angle increases an order of magnitude to 4.3 mrad compared with the collinear phase matched acceptance angle of 0.3 mrad (figure 5.1). A crystal length used in the calculation is 12 mm.

Easing the acceptance angle restriction can lead to an increase in the conversion efficiency of the OPO. In the collinearly phase matched BBO OPO, the acceptance angle of a 12 mm long crystal is 0.3 mrad which is smaller than the 0.5 mrad full angle divergence of a typical Nd:YAG laser. This result means that the crystal is unable to simultaneously phase match all the spatial frequencies in the pump beam, and the higher spatial frequencies are, in effect, wasted. It is clear that with an acceptance angle of 4 mrad the entire Nd:YAG beam can readily be phase matched, and the use of longer crystals becomes possible.

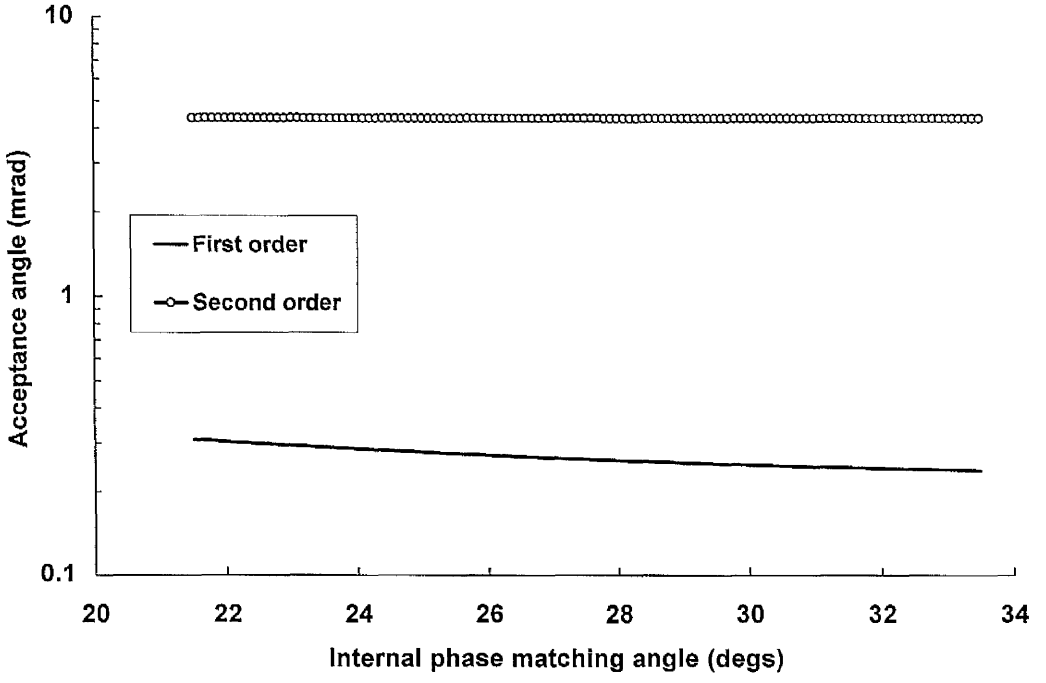

Figure 5.1. First and second order acceptance angles for BBO pumped at 355 nm. The crystal length used in the evaluation is 12 mm.

5.1.2 Phase Matching and Frequency Tuning

Three noncollinearly phase matched OPO configurations have been studied and compared to an otherwise identical collinear system. The β-BBO crystal used in the experiments measured 6x4x12 mm^3 (X, Y, Z) and was grown by the Fujian Institute of Research on the Structure of Matter, People's Republic of China. The three degrees of noncollinearity selected were q=40 mrad, 54 mrad and 90.8 mrad. At all times, the crystal was housed in a windowless oven maintained at 48°C to reduce the effects of water absorption in the crystal. The temperature was controlled to ±1° by a feedback loop varying the current supplied to a Peltier module. Mounted on an automated rotation stage (Newport 495) with a resolution of 0.001°, the crystal was placed between two flat mirrors to form a plane parallel oscillator. A cavity length of 30 mm was maintained throughout all the measurements. Figure 5.2 shows the experimental design of the OPO.

The OPO was aligned with the use of a helium-neon (He-Ne) laser. A pin hole, placed beyond two silvered mirrors used to steer the He-Ne beam, was used as the target point for the pump spot and, later, the signal (or idler) beam of the collinear OPO. By ensuring a spatial overlap of the He-Ne and the pump beams, the crystal face of the OPO was positioned so that it retro-reflected the He-Ne beam back down the pin hole. One OPO cavity mirror at a time was mounted and the retro-reflection process repeated. Providing the pin-hole is positioned sufficiently far from the OPO cavity (typically 1 m) good alignment accuracy is obtained. Furthermore, depending on the reflectivity of the cavity mirrors, the formation of etalon rings were occasionally observed and these were centred on the pin hole for fine alignment. The generated signal/idler waves should also fall onto the pin hole if good alignment is achieved. However, it was usual practice to optimise the output of the OPO once it was oscillating by fine adjustments made to each cavity mirror.

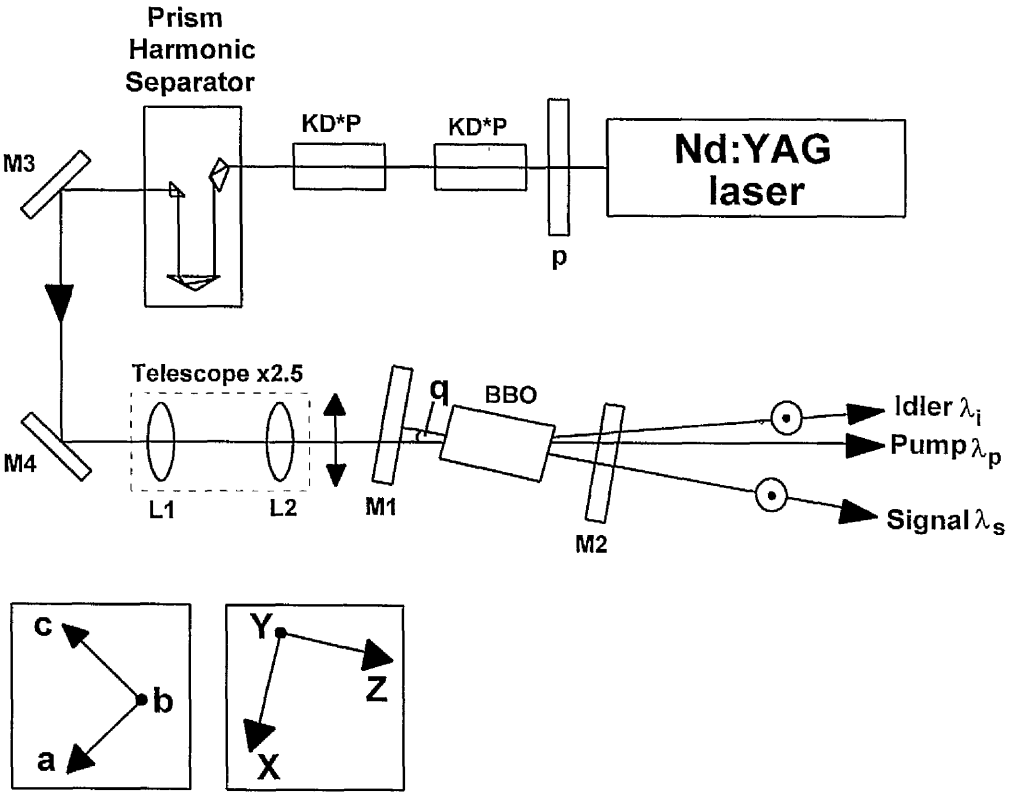

*Figure 5.2. Experimental design of the noncollinear OPO. The fundamental frequency of the Nd:YAG is tripled to 355 nm by two KD*P crystals. The intensity is controlled by a ½-wave plate, P. M3 and M4 are 99.5% R at 355 nm at 45°, L1 and L2 are positive fused silica lenses of focal lengths 100 mm and 40 mm respectively. M1 and M2 are the OPO cavity mirrors for resonant signal or resonant idler. a, b, c indicate the crystallographic axes, where c is the optic axis and X, Y, Z relate to the crystal edges in the laboratory frame. q indicates the degree of noncollinearity.*

The pump spot size was reduced to 2.5 mm diameter using two positive fused silica lenses of 100 mm and 40 mm forming a 2.5 times compression telescope. The $1/e^2$ fall in the peak intensity of the beam was taken to be the radius and this was determined using a silicon photodiode array (Reticon) consisting of 256 elements each of 25 μm in size creating a 6.4 mm length array.

The orientation of the crystal relative to the pump beam $\mathbf{k_p}$ is shown in figure 5.3 with the crystallographic axes a, b, c. The crystal surfaces were polished and uncoated. For the type I interaction, the pump beam enters the crystal as an e-ray. Its electric field is polarised in the plane containing the optic axis and the wave vector $\mathbf{k_p}$.

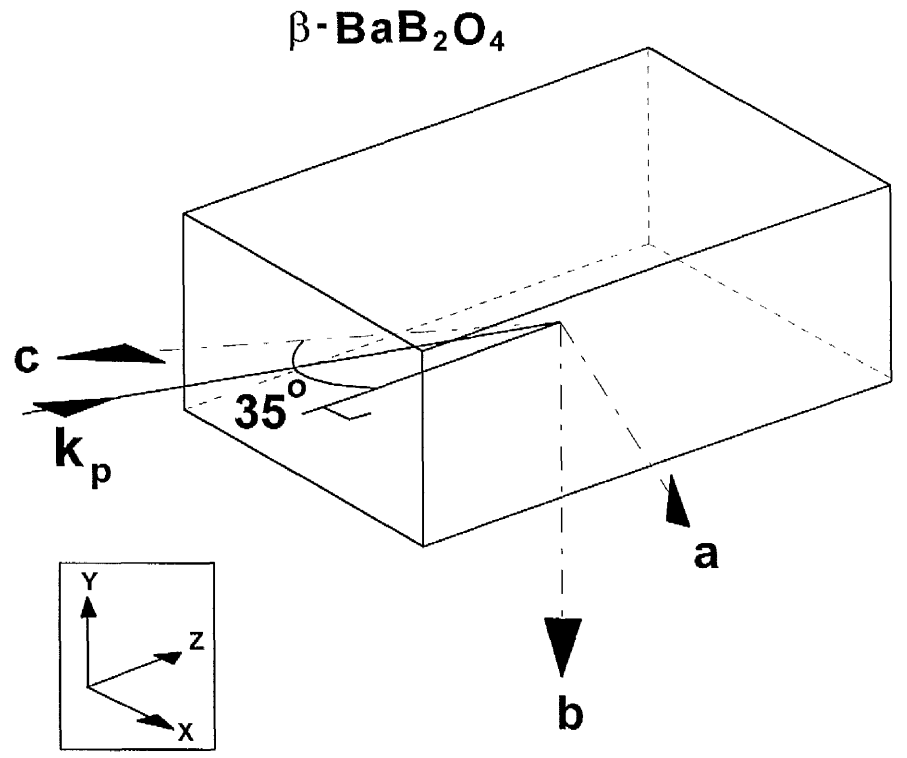

Figure 5.3. Orientation of the BBO crystal cut at θ=35°. Tuning was accomplished by rotation about the crystallographic b axis. As drawn, the projection of $\mathbf{k_p}$ *on the ab-plane is such that it lies at 90° to the b axis.*

The cavity was initially constructed with a set of high reflectivity mirrors in the range of the signal wavelength with reflectivity (R) >97 % at 500 nm-600 nm or 600 nm-700 nm with transmission (T) >85 % at 355 nm. Fewer mirror sets are necessary to cover the tuning range of the OPO for signal resonance compared with a resonant idler device. In fact, two mirror sets were used to cover the tuning range of the resonant-signal OPO, whereas an estimated four sets would have to be incorporated in order to cover the corresponding range of the resonant idler.

With the collinear OPO aligned, the BBO crystal was pumped above threshold at 20 mJ/pulse. The residue pump light was removed from the output signal by means of a UV filter. This was unnecessary for values of q>0 as the three waves become separated by the noncollinear geometry. The output signal wavelength was measured

using a calibrated optical multichannel analyser (OMA, EG&G 1461) via a fibre. For each phase match angle, the signal component was measured and the idler inferred from this value. The degree of noncollinearity, q, was varied by rotating the cavity mirrors about the crystal. The magnitude of q was measured by determining the separation of the output signal spot from that of the pump (at the pin hole) at a known distance from the crystal centre. The cavity length was maintained throughout at 30 mm. Full angle tuning curves were measured for the collinear and three noncollinear geometries of q=40 mrad, 54 mrad and 90.8 mrad. These tuning curves are shown in figure 5.4.

The collinear phase matched OPO tuning response ranges continuously from 450 nm-1.68 μm, with a small gap from 660 nm-768 nm corresponding to the roll-off point of the cavity mirror reflectivity. Similar tuning ranges are shown for q=40 mrad and q=54 mrad. Further tuning into the UV for these three OPOs was hampered by the excessive rotation of the crystal. For q=90.8 mrad, the OPO was only capable of tuning from 535 nm-1.055 μm. This limited tuning range resulted from the signal no longer having a clear aperture through the crystal due to the extreme noncollinear orientation.

The theoretical tuning curves are also shown and these were calculated in each case from the solutions of equation 4.2 for each degree of noncollinearity. The Sellmeier data used in the calculations are after Kato [2] which were found to produce the best fit to the experimental points. The break in the theoretical tuning curves result from an insufficiency in the root-finding method near degeneracy and bears no physical meaning. Single resonant oscillation is guaranteed in the three noncollinear OPOs as a result of the phase matching geometry and continuous tuning was observed.

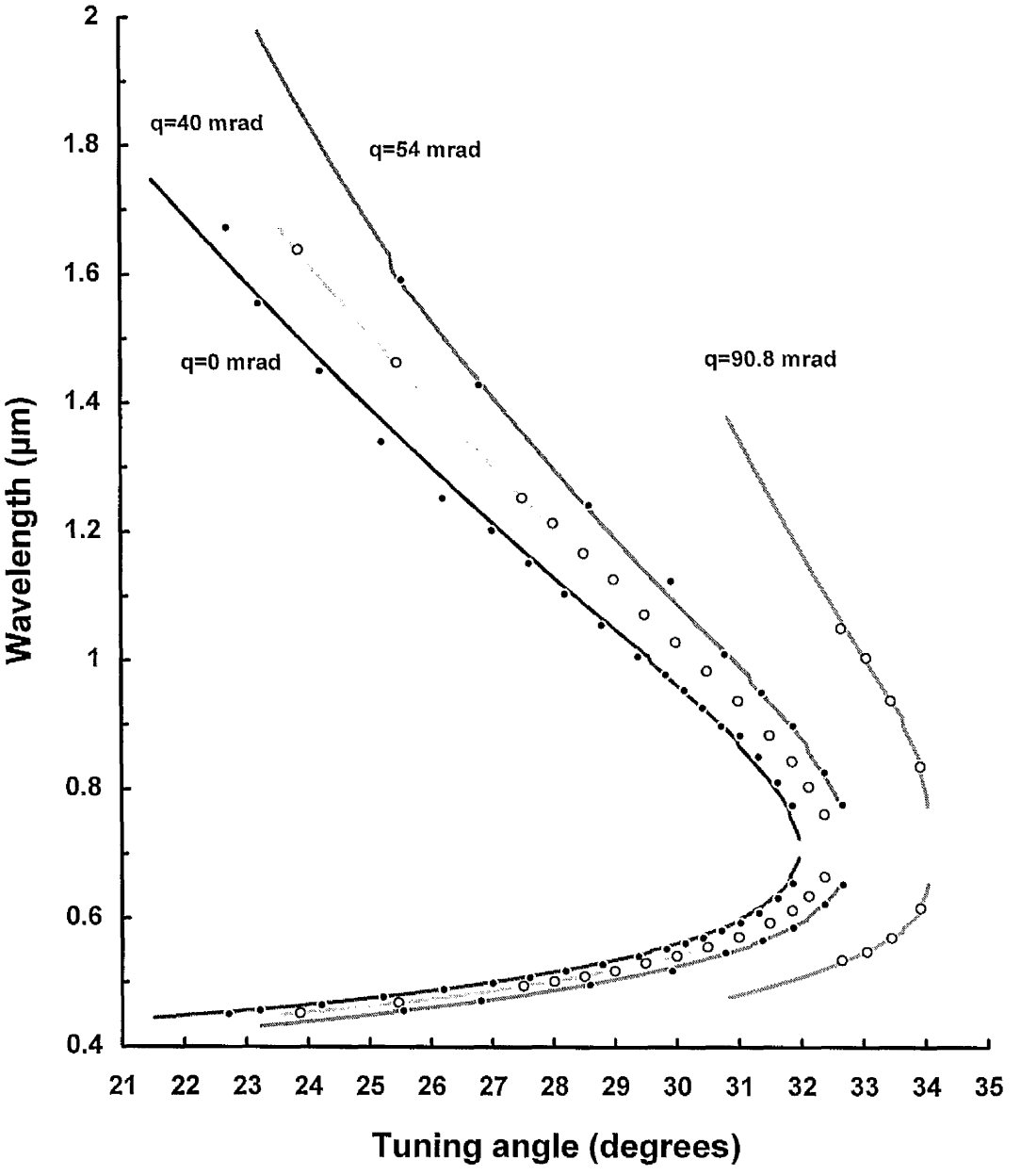

Figure 5.4. Collinear (q=0) and noncollinear (q=40 mrad, 54 mrad and 90.8 mrad) tuning responses in a BBO OPO pumped at 355 nm. Symbols represent experimental data points and the solid lines represent the theoretical tuning curves.

The experimental data points and theoretical tuning responses of each OPO are seen to be in good agreement. For a given tuning angle, the curves become increasingly blue-shifted as the magnitude of q increases. A higher degree of noncollinearity was attempted, specifically chosen to fully compensate the walk-off of the extraordinary ray. Under these conditions, the benefits of walk-off compensation should be

maximised so that a maximum conversion efficiency and a minimum oscillation threshold should be recorded. The calculated value of q for this condition is 130 mrad. The crystal aperture allowed a degree of noncollinearity of 133 mrad, but it was impossible to tune the OPO away from 600 nm. The linewidth was excessive and mode structure was observed. The data point has not been included in the figure.

In the previous chapter, it was stated that the roots obtained from the noncollinear phase matching condition depended upon whether the resonant wave is the signal or the idler. The equation is repeated here for convenience.

$$\left(\frac{n_p}{\lambda_p}\right)^2+\left(\frac{n_{res}}{\lambda_{res}}\right)^2-\left(\frac{n_{free}}{\lambda_{free}}\right)^2=2\left[\frac{n_p\cdot n_{res}}{\lambda_p\cdot\lambda_{res}}\right]\cos\left(\theta_p-\theta_{res}\right) \qquad (5.3)$$

The right hand side of the equation is a cross-term which is dependent upon the resonant wavelength and refractive index, λ_{res} and n_{res}, and not on the properties of the free (or nonresonant) wave. The roots of the equation, therefore, are dependent on the form of the resonant wave when noncollinearly phase matched.

To verify the existence of two roots and to demonstrate their physical meaning, the phase matching equation has been solved for both resonant signal and resonant idler oscillators. In both cases, the degree of noncollinearity was q=40 mrad. The cavity mirrors were R>95 % 500 nm-600 nm (T>80 % 900 nm-1200 nm) for the resonant signal and R>85 % 800 nm-1000 nm (T>90 % 550 nm-640 nm) for the resonant idler. In all other respects, the cavities in both cases were identical. Figure 5.5 shows the tuning curves and theoretical predictions for both the cavities described. As expected, the responses differ from one another with the resonant idler tuning curve slightly red-shifted from that of the resonant signal. The prediction of these tuning ranges illustrates the asymmetry of the noncollinear geometry about the oscillation axis, which is not observed in the collinear case.

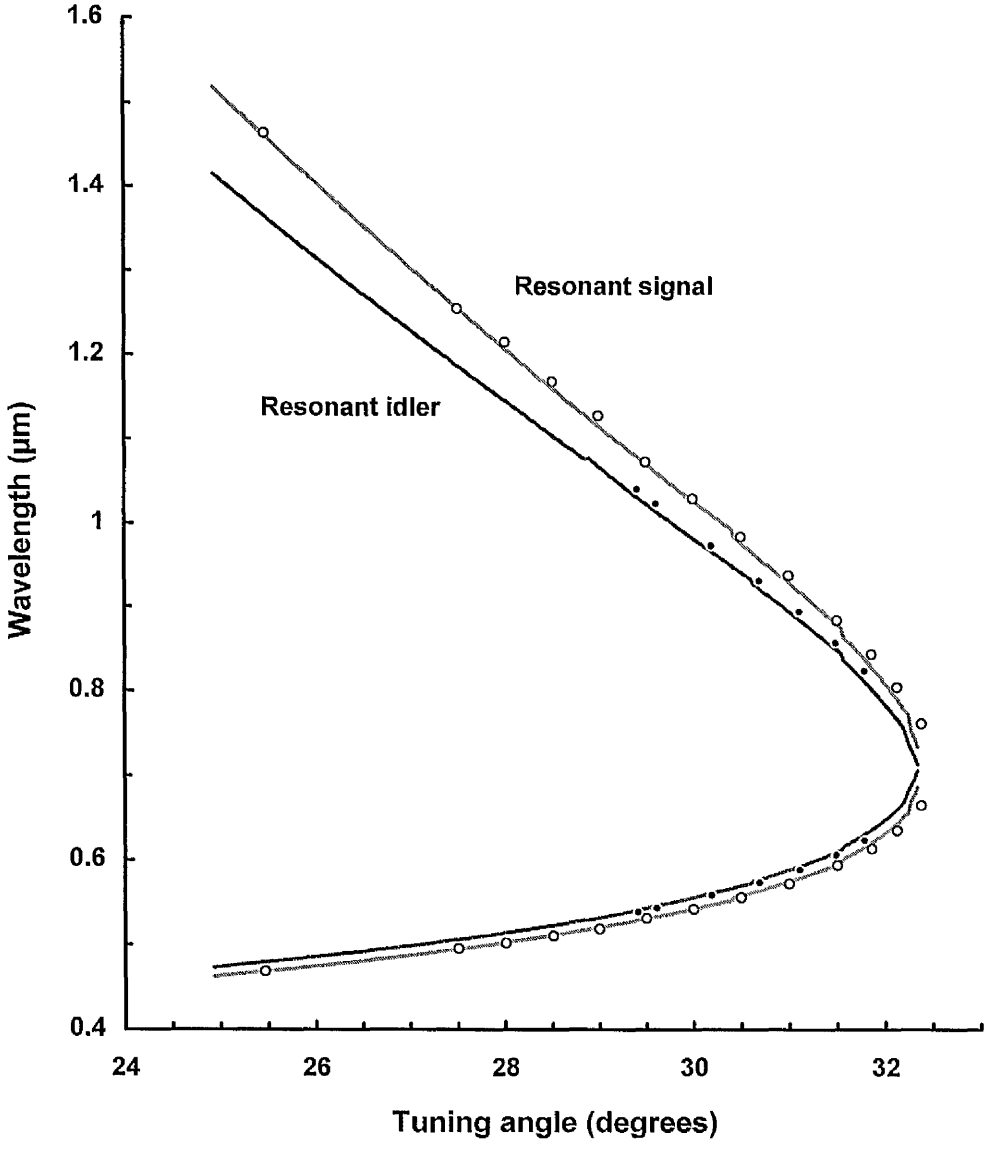

Figure 5.5. Tuning ranges for both resonant-signal and resonant-idler oscillators, both noncollinearly phase matched at q=40 mrad.

5.1.3 Oscillation Threshold

Near threshold, the OPO becomes unstable as a result of pump intensity fluctuations about the threshold point of the OPO. This makes it difficult to take an accurate measurement of the threshold. The threshold of each OPO was determined, however, by reducing the pump beam intensity at 355 nm using a ½-wave plate (or, λ/2 plate) at

the laser head until oscillation is barely maintained. As a guide to standardising the measurement for each OPO, threshold was taken to be the input pump intensity capable of turning the oscillator "on" once in every 10 pump pulses, or every second. The energy of the pump pulse was measured at the laser head. Allowing for the Fresnel reflections at the surfaces of the lenses, the energy at the OPO input mirror surface was deduced.

The noncollinear theoretical model based on the model developed by Brosnan and Byer to predict the threshold of a collinear OPO [3] was applied to each OPO in turn. Equation 4.8, described in chapter four, takes account of the increased effective walk-off length and gain coefficient observed in noncollinear geometries. The equation is repeated here for convenience.

$$J_o(q) = \frac{2.25\cos\alpha\cos\beta}{Kg_s L_{nc}^2}\tau\left[\frac{l_o}{2\tau c}\ln 33 + 2\alpha l + \ln\frac{1}{\sqrt{R}} + \ln 2\right]^2 \qquad (5.4)$$

The values used in equation 5.4 are given in the table below.

Variable	2τ	l_o	αl	R	λ_s	λ_i	d_{eff}	n_s	n_i	n_p	g_s
Value	6	3.8	1	0.97	600	870	1.7	1.66	1.65	1.67	0.9
Units	ns	cm	%	%	nm	nm	pm/V	—	—	—	—

Table 5.1. Symbols, values and units for the variables used to calculate the threshold fluence for the noncollinear OPOs.

The effective gain length L_{nc} of the crystal varies according to the degree of noncollinearity. The variation of the walk-off length as a function of the external tuning angle is shown in figure 5.5 for each of the noncollinear geometries. In the

figure, a dramatic increase in the walk-off length is seen as the degree of noncollinearity increases. The walk-off length is the interaction length within the crystal after which the separation of the waves becomes intolerable. The figure shows, therefore, how sensitively the interaction length depends upon the degree of noncollinearity as well as the useful maximum crystal length for a given geometry.

Using equation 4.5 from the previous chapter and figure 5.5, it is possible to compute the noncollinear parametric gain length for each geometry at any phase matching angle. This is the final variable required in the threshold calculation. The calculated values are tabulated below (table 5.2) for the OPOs under study with a signal wavelength of 600 nm.

q (mrad)	**0**	**40**	**54**	**90.8**
L_{nc} (cm)	1.04	1.13	1.15	1.19

Table 5.2. Values of parametric gain length L_{nc} for corresponding degrees of noncollinearity for a crystal 12 mm in length.

It is clear from the table that at 90.8 mrad, the effective parametric gain length is close to the physical crystal length (1.2 cm), and the effects of walk-off are almost eliminated. At the most extreme degree of noncollinearity reached (133 mrad), the effective parametric gain length is equal to the physical crystal length, as the Poynting vectors of the pump and resonant wave are collinear in the crystal.

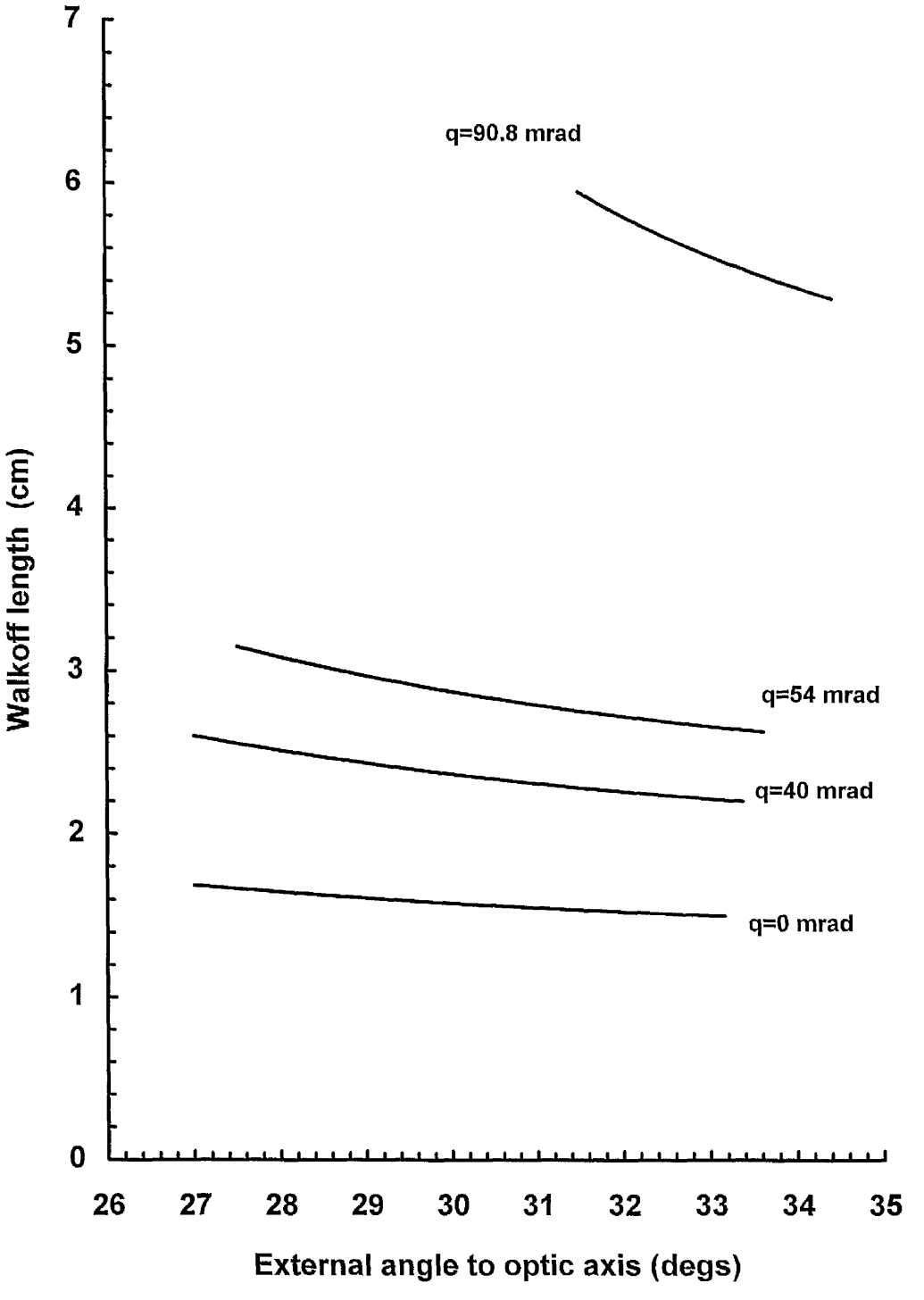

Figure 5.5. Walk-off length in the type I 355 nm pumped OPOs for collinear and the three noncollinear geometries under study, versus the angular tuning range.

Using these values, the threshold for the oscillators has been calculated and compared with the experimental data. These results are shown in figure 5.6 for a signal wavelength of 600 nm.

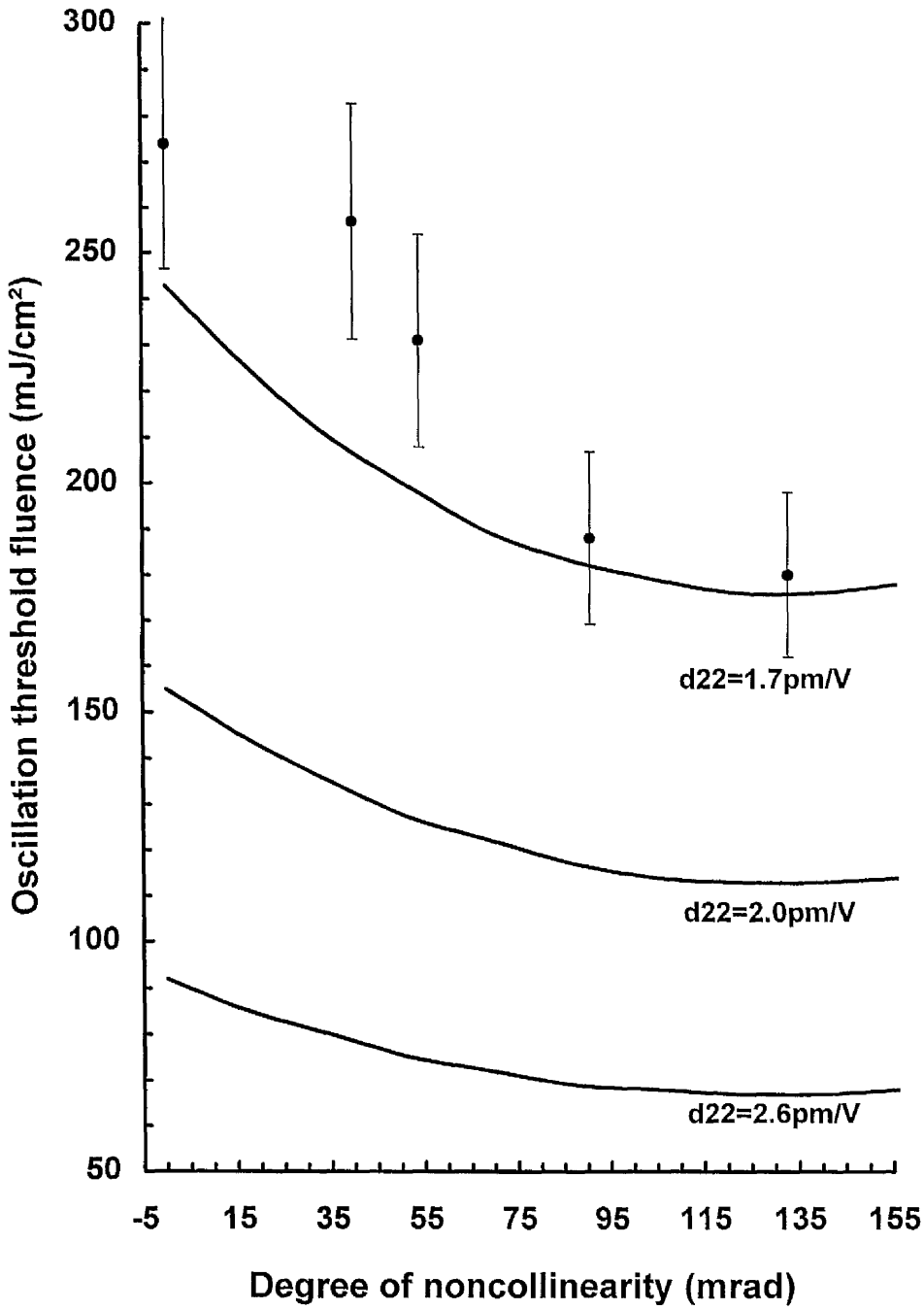

Figure 5.6. Oscillation threshold versus degree of noncollinearity of the OPOs. Different reported values of d_{22} have been used in the calculation.

The threshold is seen to fall with the increasing degree of noncollinearity, as predicted by the theoretical threshold fluence. Three values of d_{22} have been used in calculating the threshold. These have been taken as 1.7 pm/V reported by Chen *et al* [4], 2.0 pm/V [5] and 2.6 pm/V[6]. With d_{22} at 1.7 pm/V, the theoretical oscillation threshold is in fairly good agreement with the measured values. More importantly, perhaps, is the condition of full walk-off compensation which, theoretically, occurs at 130 mrad. Although a minimum threshold was observed at q=130 mrad, further degrees of noncollinearity were not attainable due to the constraints of the crystal aperture. The verification of a true minimum was, therefore, not possible.

5.1.4 Conversion efficiency

The conversion efficiency of each OPO was determined by measuring the input pulse energy of the pump and the corresponding energy of the generated signal and idler pulses. Owing to the symmetry of the cavity mirror reflections, the energy coupled out of one mirror has been doubled. (The pump energy stated was measured at the laser head and Fresnel losses at the four faces of the two lenses making up the telescope have been taken into account). The loss at each surface was ~4 % which amounted to a total loss of 15 % ($1-0.96^4$) at the pump wavelength.

Figure 5.7 shows the OPO output energy against pump laser input energy for the four OPOs under study. The limited power of the Nd:YAG laser meant that none of the OPOs reached saturation. The slope efficiencies for each have been calculated and these increase from 36 % in the collinear case to 62 % in the most extreme noncollinear OPO of q=90.8 mrad. More significantly, perhaps, is an incident pump energy of 15 mJ which brings the collinear OPO to just above threshold, whilst the q=90.8 mrad OPO delivers 5.3 mJ giving an external conversion efficiency of 35 %.

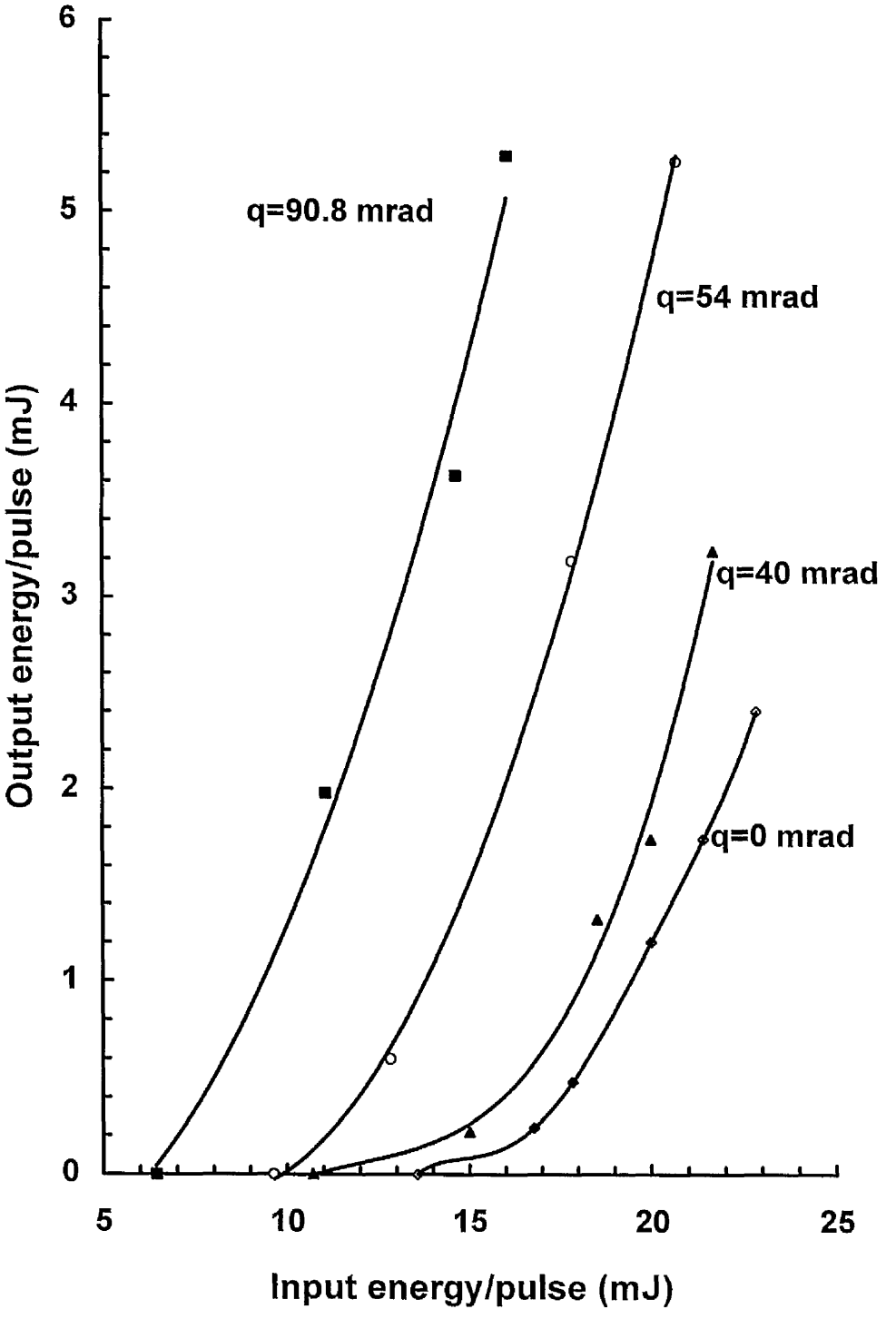

Figure 5.7. Total output energy/pulse of the signal and idler versus input pump energy for the four OPOs under study.

The OPO cavity mirrors in each case were coated to highly reflect the signal and to transmit the idler and the pump waves. The efficiency curves were measured at a

signal wavelength of 600 nm. In practice, the signal made up less than 10 % of the total power of the converted photons. In each case, saturation could not be reached and maximum pumping was limited to ~28 mJ/pulse (0.1 GW/cm^2) at 355 nm from the Nd:YAG laser, a factor of four less than the reported damage threshold of BBO [7].

5.1.5 Oscillator Linewidth

The linewidth of the parametric oscillator is made up from three contributing factors: the gain bandwidth of the OPO, the pump bandwidth and the pump beam divergence. In the case of the four OPOs studied here, the last two contributions remain the same. Any change in the signal (and idler) linewidth, therefore, indicates a corresponding change in the gain bandwidth of the OPO.

Using a calibrated OMA, the signal linewidth of each OPO was measured across the entire tuning range. A resolution limit of 3 nm was measured for the OMA using a single-mode He-Ne laser. Figure 5.8 shows the linewidth variation of all four OPOs over their tuning ranges. The linewidth of the intermediate noncollinear geometries (q=40 mrad and 54 mrad) are presented as datum points only, whilst the collinear (q=0 mrad) and the most extreme (q=90.8 mrad) have best fit curves fitted. This has been done to illustrate the salient points to be made from the figure and to avoid line confusion. It is clear that the greater the degree of noncollinearity, the greater the signal linewidth and, hence, the greater the OPO gain bandwidth. The theoretical linewidth has been determined by considering the two largest contributors to the OPO linewidth, that of the gain bandwidth and the pump beam divergence (see chapter two, section 2.6). This is shown as a dotted line on the figure.

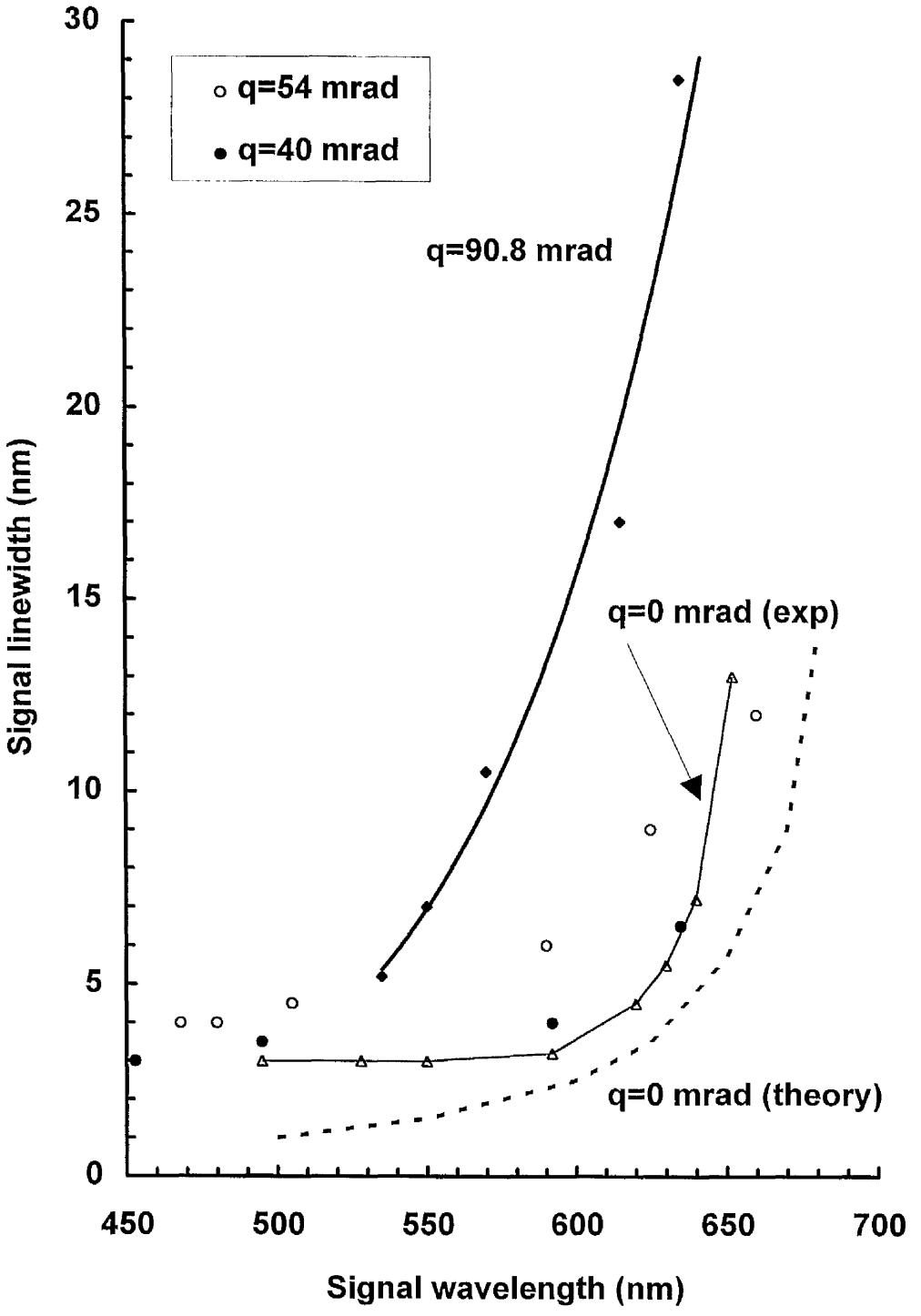

Figure 5.8. Signal linewidth versus tuning range for each OPO. The theoretical linewidth for the collinear OPO is also shown (dotted line).

The collinear linewidth is seen to differ from the theoretical linewidth, although the trend is in good agreement. The reason for the apparent discrepancy may be due to an

underestimation of the pump beam divergence and the resolution limit of the OMA. The linewidth of the q=90.8 mrad OPO increases sharply as the device is tuned towards degeneracy, reaching a maximum value in excess of 25 nm. Linewidths of the intermediate noncollinear geometries fall between those of the collinear and the q=90.8 mrad case, further supporting the theory that the gain bandwidth increases with noncollinearity.

5.1.6 Summary

In summary, noncollinear phase matching has been demonstrated in BBO pumped at 355 nm using the third harmonic of a Nd:YAG laser. The tuning responses of the collinear phase matched OPO of 450 nm-1.68 μm can be matched by noncollinear geometries up to at least q=54 mrad with a corresponding increase in external optical efficiency from 6 % to 27 % (at 20 mJ/pulse pump energy). A reduction in the operating threshold from 0.27 J/cm^2 to 0.18 J/cm^2 is also observed for the same two oscillators. In all cases, the tuning response has been predicted accurately by modelling the noncollinear phase matching condition. The full benefits of exact walk-off compensation can be attained through the use of larger aperture crystals.

The requirements of the pump beam quality have been discussed for efficient phase matching and the restriction placed upon the pump beam divergence in the collinear geometry appears to ease in the noncollinear cases. Full spatial walk-off compensation has been calculated to be at q=130 mrad and the lowest threshold was observed under these conditions. Unfortunately, further degrees of noncollinearity were not possible to determine the existence of a true minimum. Table 5.3 summarises the experimental results for the OPOs.

Property	q=0 mrad	q=40 mrad	q=54 mrad	q=90.8 mrad
Slope efficiency (%)	35.5	42.1	58.4	62.4
Peak efficiency (%)*	<0.2	1.8	12.2	34.0
Threshold (J/cm^2)	0.27	0.25	0.23	0.18
Tuning range (nm)	450-1680	450-1680	450-1680	535-1055

Table 5.3. Summary of some of the experimental data for the collinear and three noncollinear OPOs (measured at 15.5 mJ/pulse pump input energy).*

5.2 BBO Pumped at 532 nm

This section details noncollinear phase matching in 532 nm pumped BBO optical parametric oscillators. The lower pump photon energy means that these oscillators are inherently less efficient compared with the UV pumped devices. It is likely, therefore, that if OPOs based on this pump/crystal combination are to become contenders for frequency selective cavities, the external conversion efficiency will need to be improved. It is shown here that noncollinear phase matching does significantly improve the conversion efficiency, whilst still maintaining a prolific tuning capability.

Areas of analysis in section 5.1 for BBO pumped at 355 nm which are directly applicable to this section will not be discussed in further detail, but they will be alluded to where necessary.

5.2.1 Acceptance Angle

For the reasons discussed in section 5.1.1, the acceptance angle of the BBO crystal can be dramatically increased by implementing a noncollinear geometry so that the

tangential phase matching condition is reached. Under such conditions, the second order term of the Taylor series describing the acceptance angle is used.

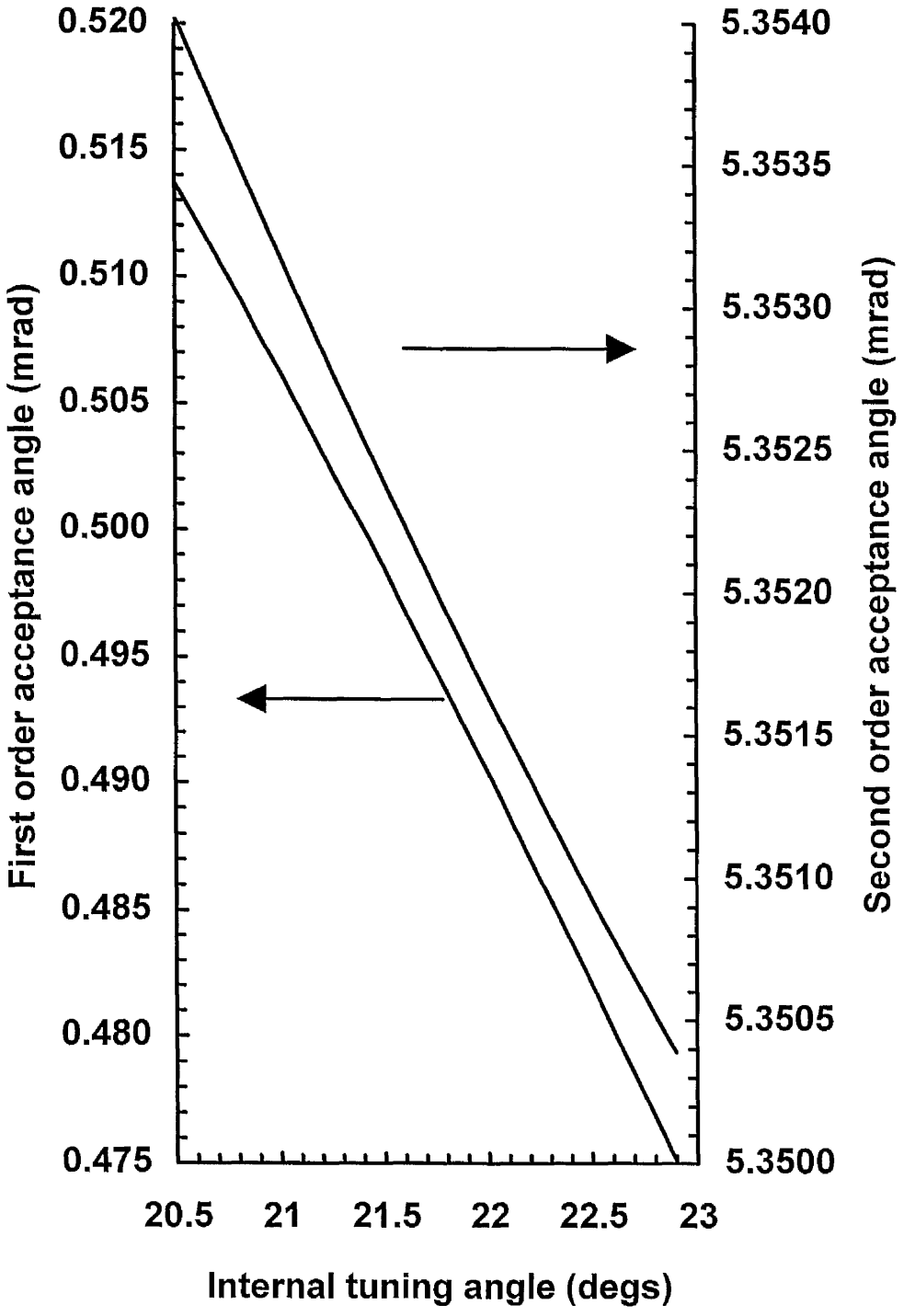

Figure 5.9. First and second order acceptance angles for BBO pumped at 532 nm using a 12 mm crystal.

Figure 5.9 shows the first and second order acceptance angles derived from the first two terms of the Taylor series of the allowable phase mis-match with respect to angular divergence of the pump beam. The first order acceptance angle for critical phase matching is equal to ~0.5 mrad, which is greater than that experienced by BBO pumped in the UV. However, since the full angle divergence of Nd:YAG laser is typically 0.5 mrad any beam compression is likely to affect the efficiency of the OPO. As expected, the tangential phase matching condition has an associated acceptance angle which is an order of magnitude larger than the critical condition and whose limit is well in excess of the compressed pump beam divergence. As previously discussed, this should contribute to a more efficient device.

5.2.2 The Pump Laser

The laser pump source used in the experiments described in this section is a commercially available Spectron SL804 1614 Q-switched telescopic Nd:YAG system. The pulse duration is 20 ns at 532 nm and the repetition rate is variable although maintained at 10 Hz. Contraction of the second harmonic beam waist to a diameter of 1.5 mm is carried out using a Galilean telescope before the OPO. The Galilean telescope was chosen to avoid a real focus in the pump beam which is liable to cause dielectric break-down of the air, and a possible loss of peak power from the beam through plasma absorption. However, focused back-reflections from the curved surface of the negative lens caused breakdown at high pump fluences.

5.2.3 Phase Matching and Frequency Tuning

The OPO cavity is constructed in a similar way to that described for the UV pumped oscillators. Two identical flat mirrors separated by 30 mm constitute the cavity, allowing for ~100 round trips of the resonant wave. Two mirror sets are sufficient to

cover the observed tuning range of the OPOs. The sets are coated to transmit >95 % at 532 nm and have dielectric coatings of R>95 % over 600 nm-800 nm and 800 nm-1000 nm, respectively, allowing resonance of the signal wave only. Figure 5.10 shows the experimental arrangement.

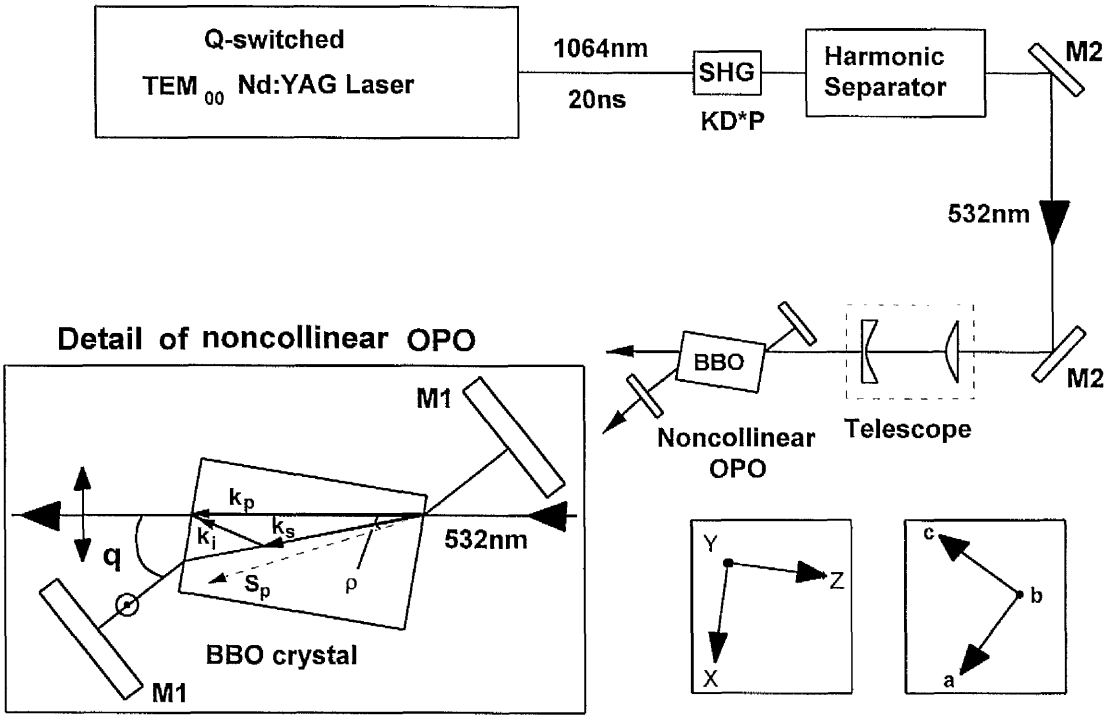

*Figure 5.10. Experimental arrangement of the noncollinear OPO. The fundamental Q-switched radiation is doubled to 532 nm using KD*P. A telescope made up of lenses of focal lengths of +100 mm and -50 mm compresses the beam before being launched into the OPO. M2: Pump steering mirrors with R>98 % at 532 nm at 45°. M1: R>95 % over 600 nm-800 nm and 800 nm-1000 nm with >95 % transmission at 532 nm. DETAIL: pump is polarised parallel to the bench and becomes an e-ray in the crystal. Signal and idler are generated as o-rays. ρ is the Poynting vector walk-off of the e-ray, and q indicates the degree of noncollinearity. [a, b, c] are the crystallographic axes and [X, Y, Z] are the laboratory axes.*

The BBO crystal was grown by the Fujian Institute and measured 4x4x12 mm^3 (X, Y, Z). It had a cut of 21.75° between the normal to the uncoated entrance faces and the optic axis c for type I (e→o+o) phase matching at 532 nm. The crystal was mounted in the same windowless oven used in the UV pumped OPOs which was held at 48°C and mounted in the same fashion on the automated stage. Tuning was accomplished by

rotation of the BBO crystal about the crystallographic b axis. As in the previous nomenclature, the angle q subtending the wave vectors $\mathbf{k_p}$ and $\mathbf{k_s}$ (the resonant wave) in free space denotes the degree of noncollinearity.

In BBO pumped at 532 nm, the condition of full spatial walk-off is satisfied at a noncollinearity of q=98 mrad, corresponding to an internal angle of 3.5°, approximately the walk-off angle of green light in BBO. Owing to the dimensions of the crystal aperture of 4x4 mm, it was not possible to obtain oscillation at q=98 mrad. This meant that full walk-off compensation was not possible with this crystal. Significant walk-off compensation was, however, observed using noncollinearities of q=14.8 mrad, q=28.4 mrad and q=47 mrad, as well as the collinear case (q=0 mrad).

As in the UV pumped noncollinear OPOs, the profile of the noncollinear tuning curves depends upon whether the signal or the idler wave is resonant in the cavity for a given degree of noncollinearity. In keeping with the experimental arrangement here, the noncollinear phase matching condition (equation 5.3) has been solved for type I phase matching in a BBO OPO pumped at 532 nm with the signal as the resonant wave.

The resulting theoretical tuning curves for q=14.8 mrad, q=28.4 mrad and q=47.0 mrad which arise from the roots of the phase matching equation are shown in figure 5.11 with the corresponding experimental data. In each case, the degree of noncollinearity was set by the twist in the cavity, as described in section 4.1. The tuning curves were then determined by rotating the crystal about the b-axis and measuring the wavelength using an OMA. Experimental results are seen to be in good agreement with the theoretical tuning response, and the profiles are similar to those observed with the UV pumped OPOs. For comparison, the collinear phase matching tuning curve is also shown. More extreme degrees of noncollinearity were unobtainable as a result of the limited crystal aperture. All the oscillators were able to generate signal wavelengths

down to 700 nm, although reaching degeneracy ($\lambda_s=\lambda_i$) became increasingly difficult at more extreme angles of noncollinearity.

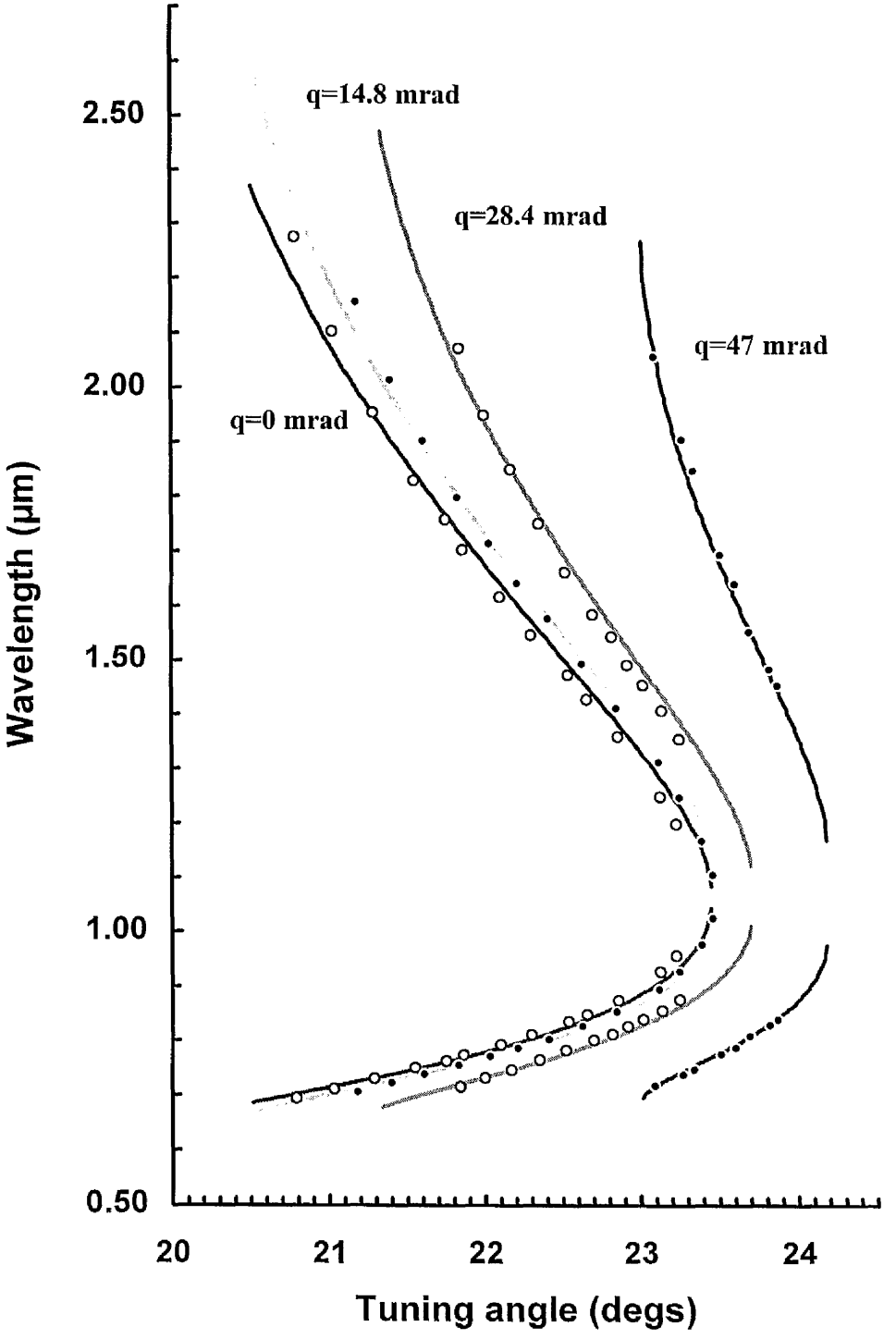

Figure 5.11. Tuning responses of collinear and three noncollinear OPOs pumped at 532 nm. Solid lines are the theoretical responses and datum points are experimental.

As observed in the UV pumping solutions, the theoretical tuning curves do not reach degeneracy as a result of a shortcoming of the root-finding method employed. The observed reduction in the tuning range with increasing q is an inevitable consequence of the diminished oscillation aperture arising from the phase matching geometry and the crystal cut. With careful choice of these parameters, full tuning ranges should be realisable at extreme values of q, and it should then be possible to accomplish the condition of exact walk-off compensation at q=98 mrad.

For a given tuning angle, the curves are seen to blue-shift as q increases. A similar response was also observed with the UV pumped OPOs.

5.2.4 Oscillator Linewidth

It is clear from figure 5.11 that the gradients of the tuning profiles (that is, $d\lambda/d\theta$) are greater with higher degrees of noncollinearity. The rate of change of tuning in the parametric interaction is a measure of the gain bandwidth and, therefore, the signal linewidth of the OPO. This is described by the following expressions. The gradient of the signal portion of the tuning curve is given by [8]

$$\frac{d\lambda_s}{d\theta} = \frac{-\lambda_s^2}{b \cdot 2\pi c}\left[\frac{\partial K_p}{\partial \theta} - \frac{\partial K_s}{\partial \theta} - \frac{\partial K_i}{\partial \theta}\right] \tag{5.5}$$

where $$b = \frac{\partial K_i}{\partial \omega_i} - \frac{\partial K_s}{\partial \omega_s}$$

In equations 5.5, c is the speed of light and b is a dispersive constant given by [9]. From this, the full width at half maximum in Hz of the gain bandwidth is given by

$$|\Delta \nu_s| \approx \frac{1}{b \cdot l} \tag{5.6}$$

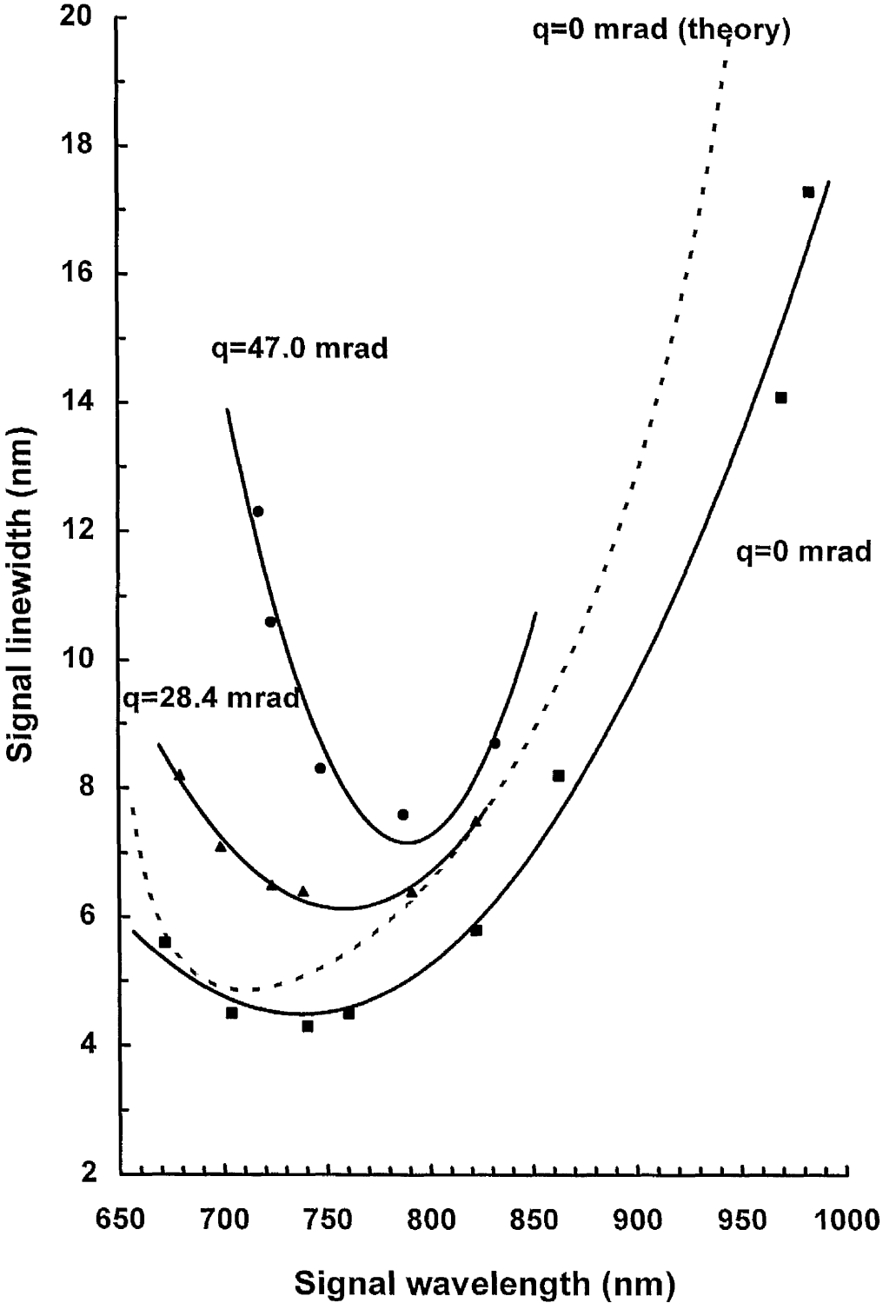

Figure 5.12. Experimental linewidth variation of collinear and noncollinear OPOs. The theoretical linewidth of the collinear OPO is also shown where the characteristic minimum is in evidence.

where l is the crystal length. It is apparent from equations (5.5) that large tuning gradients arise from small values of b and, from (5.6), that these correspond to regions of large linewidths. We can therefore expect to see a signal linewidth increase at the extreme regions of the tuning ranges since the gradient is large both near degeneracy and far from degeneracy. Figure 5.12 shows the signal linewidths of the collinear OPO configuration for both the theory (dashed line) and experimental data. The profiles are similar and both exhibit minima. The theoretical linewidth is derived from equations 2.38 and 2.39 of chapter two; equation 2.38 describes the gain bandwidth of the OPO and 2.39 gives the linewidth contribution from the finite divergence of the pump source. The effects of multiple-passes of the resonant wave have not been taken into account and may explain the off-set between theory and experiment.

The signal linewidths of the noncollinear OPO configurations are also shown, with the exception of q=14.8 mrad which has been omitted as it was found to be experimentally indistinct from the collinear case. Best-fit lines have been added to clarify the trends. Characteristically, all the signal linewidths exhibit minima. Since the only variable contribution to the signal linewidth is the gain bandwidth of the OPO, it is apparent that the increase in the minima is a measure of the increase in parametric gain of the noncollinear OPOs at increasing values of q. The minimum linewidths vary from 4.2 nm at q=0 mrad to 6.1 nm and 7.6 nm at q=28.4 mrad and 47 mrad, respectively. This is a direct result of the partial compensation of the extraordinary pump ray walk-off from the ordinary resonant signal ray arising from the noncollinear geometry.

5.2.5 Conversion Efficiency and Pump Depletion

In accordance with the increase in parametric gain with noncollinearity, an increase in the external conversion efficiency of the OPOs was observed as q increased. The pump energy incident on the OPO cavity was measured using a Laser Instrumentation

power meter, model 5262A, head model 17AN. In all cases, both the signal and idler radiation were measured as the output from the cavity at a resonant signal wavelength of 830 nm. The signal wave, however, made up just 10 % of the overall power measured since the cavity had a high finesse at the signal wavelength. Figure 5.13 shows the efficiency curves for each of the OPOs studied.

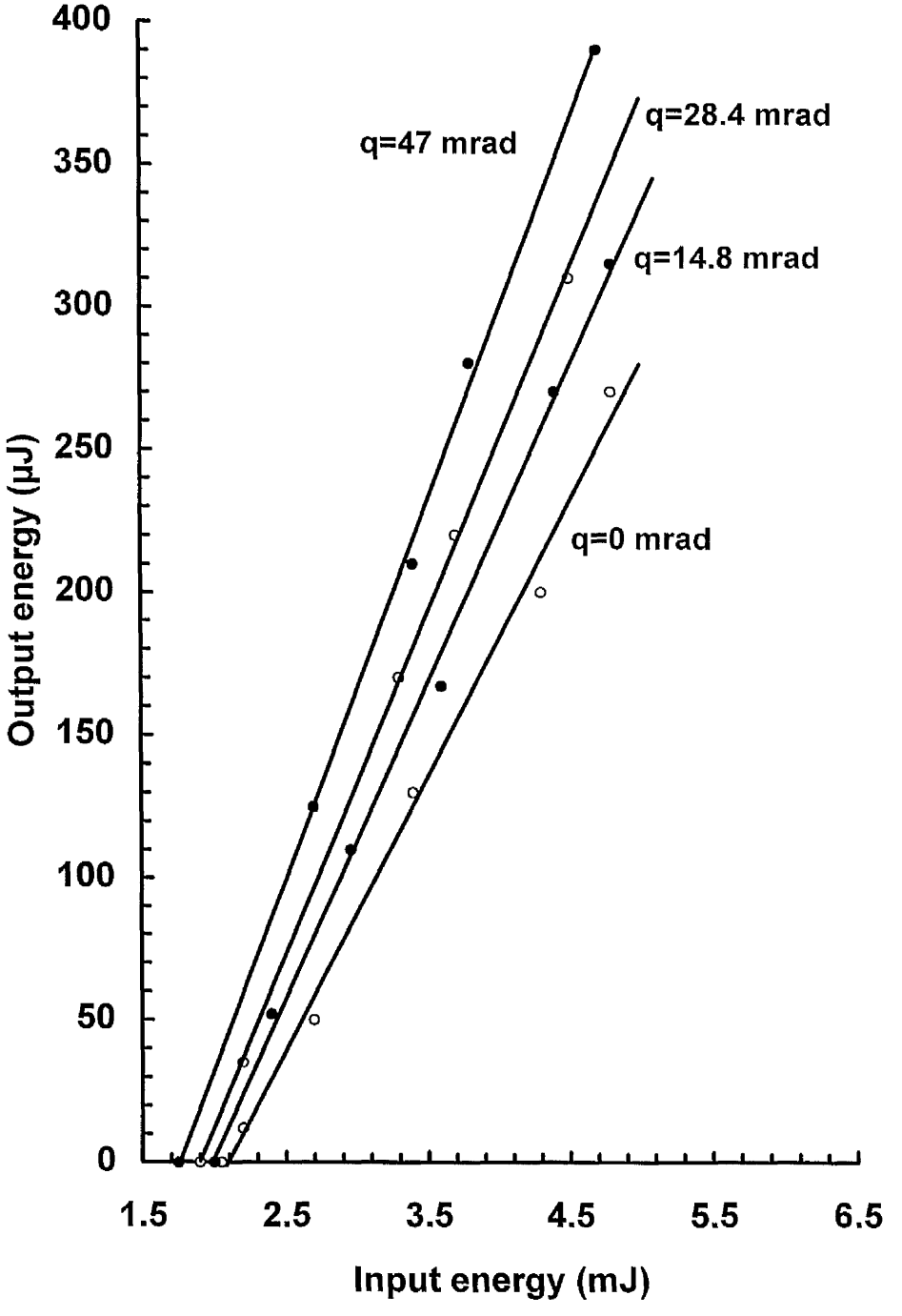

Figure 5.13. Efficiency curves for the collinear and three noncollinear OPOs.

The unsaturated conversion efficiencies increased from 11.3 % at q=0 mrad to 16.6 % at q=47.0 mrad. The conversion efficiency is seen to increase as a result of the noncollinear geometry, although the effect is not as dramatic as that observed in the UV pump OPOs.

The efficiencies are, however, unsaturated and it is clear that greater efficiencies are obtainable at higher pump fluences. A corresponding fall in oscillation threshold of the oscillators from 2.1 mJ to 1.7 mJ per pulse is also observed as predicted for the noncollinear geometry.

To verify the effects of the noncollinear geometry on the cavity efficiency, the pump depletion for each of the configurations under study has also been measured. Two identical EG&G fast risetime (0.5 ns) photodiodes were positioned at the input and output of the OPO. With the OPO crystal detuned from the phase matched condition, both the photodiode responses were observed on a Gould 4096 (200 MHz, 1.6 Gs/s) oscilloscope and the position of the photodiodes adjusted so that the traces became coincident. In this configuration, both photodiodes record the undepleted pump intensity. The crystal was then tuned and optimised and depletion of the pump was seen at the second photodiode. Figure 5.14 shows the four profiles, from (a) through to (d), corresponding to the noncollinear geometries in increasing order of noncollinearity.

For the collinear geometry, figure 5.14(a), the pump was depleted by 19.7 %. Figures 5.14(b) and 5.14(c) have similar depletions of 24.3 % and 28.5 % in line with the energy conversion efficiencies measured at q=14.8 mrad and q=28.4 mrad. Figure 5.14(d) shows a depletion of 39.7 % at q=47.0 mrad confirming the efficiency increases at large q.

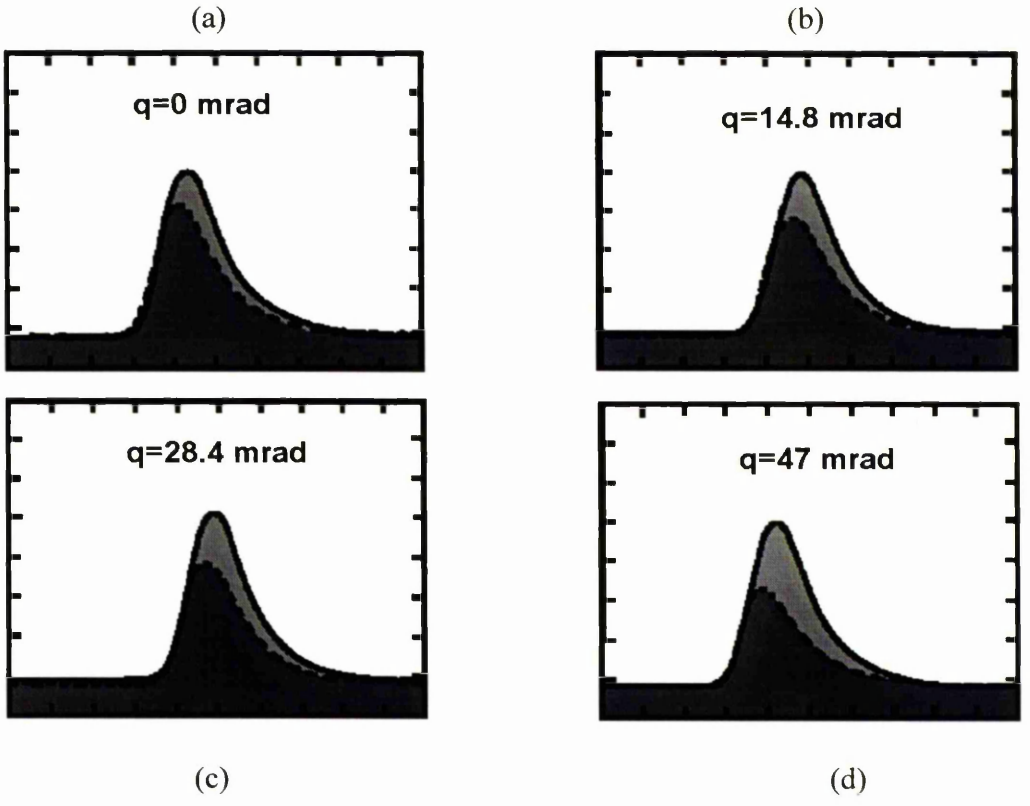

Figure 5.14. Pump depletions of the four OPOs at a signal wavelength of 830 nm. Time base is 10 ns/division.

The apparent discrepancy between the external efficiency and the pump depletion arises from the internal losses of the cavity at the signal and idler wavelengths. The external efficiency is related to the internal efficiency (or pump depletion) by

$$\eta_{ext} = \eta_{\text{int}}\left[\frac{\omega_s}{\omega_p}\cdot\frac{\varepsilon_c}{\varepsilon_c+\varepsilon_l^s}+\frac{\omega_i}{\omega_p}\left(\varepsilon_l^i+R\right)\right] \tag{5.7}$$

using equations 2.46 and 2.47 of chapter two. In equation 5.7, ω denotes the frequency and the subscripts p, s and i are the pump, signal and idler waves where, in this case, the signal is the resonant wave. ε_c is the loss coefficient associated with the mirror coupling of the signal and ε_l is the loss coefficient responsible for Fresnel reflection and crystal absorption at the wavelengths denoted by the superscript. R is the loss to the idler from uncoupled photons from the cavity resulting from less than 100 %

transmitting mirrors. Pump depletion measurements presented here are single shot and, as is often the nature of the OPO, shot-to-shot power fluctuations in the pump intensity cause the pump depletion to vary from shot-to-shot. Snap-shot pump depletion measurements may, therefore, give a distorted picture of the internal efficiency of the OPO. External efficiency measurements, on the other hand, are more stable since the power meter does not respond to single shot fluctuations. The power meter fluctuations in these measurements were <10 %. By estimating the losses at the signal and idler waves associated with the cavity, the pump depletion can be calculated and compared with the measured values. At a signal wavelength of 830 nm and a corresponding idler wavelength of 1480 nm, the Fresnel loss per crystal surface is 5 %. This represents a round-trip loss of the resonant signal of 20 % and a single pass loss to the idler of 10 %. Since the transmission of the cavity mirrors at the idler wavelength is 80 %, R becomes a loss of 20 %. The total loss at the cavity mirrors at the signal wavelength is 15 %. By substituting these values into equation 5.7, the pump depletion can be found. Table 5.4 shows the measured and calculated pump depletion along with the measured external efficiencies taken at the same pump fluence and the peak external efficiencies obtainable from the OPOs.

	η_{ext} (observed)	η_{int} (calculated)	η_{int} (observed)	η_{ext} (peak)
q=0 mrad	9.3 %	**24.3 %**	**19.7 %**	11.3 %
q=14.8 mrad	10.0 %	**26.1 %**	**24.3 %**	13.1 %
q=28.4 mrad	12.0 %	**31.4 %**	**28.3 %**	13.8 %
q=47 mrad	14.7 %	**38.4 %**	**39.7 %**	16.6 %

Table 5.4. Bold percentages show the calculated and observed pump depletions for the OPOs based on the measured external conversion efficiency η_{ext} (observed). The peak external conversion efficiencies are also included.

From table 5.4, it is clear that the calculated pump depletions agree in general with those observed, although they tend to predict higher values. There are a number of factors which could account for this, for example, the calculations are sensitive to the accurate determination of the losses in the cavity, and it is possible that these have been over estimated. The peak external efficiencies are also included in the table. These are measured at the highest pump fluence used in pumping the OPOs. In all cases, the internal and external efficiencies increase as the noncollinearity increases as a result of the spatial walk-off compensation.

5.2.6 Summary

When noncollinear phase matching is applied to 532 nm pumped OPOs, it is clear that a significant increase in the efficiency of the devices can be obtained, with a corresponding fall in the operational threshold. Full spatial walk-off compensation has not been demonstrated due to a limitation of the crystal aperture, however, a doubling in the internal efficiency has been observed at modest angles of noncollinearity. The linewidth of the oscillators is also seen to increase, further demonstrating the increase in the parametric gain bandwidth with noncollinearity. The parametric tuning ranges for all the OPOs have been calculated and shown to be in excellent agreement with the measured ranges.

5.3 Conclusions

This chapter has shown the advantages of noncollinear phase matching in BBO optical parametric oscillators and the ease of inducing the effect on a plane-plane cavity. Such a geometry is seen, in accordance with the theory described in chapter four, to reduce the operational threshold and increase the conversion efficiency of the device. The effectiveness of noncollinear phase matching in countering the effects of extraordinary

ray walk-off is illustrated in the case of the UV pumped OPO. Increases in external efficiencies by a factor of four have been observed, with a modest fall in threshold from 0.27 J/cm^2 to 0.19 J/cm^2. This not only increases the efficiency, but also allows for the use of longer crystal lengths. In addition, the extent of the collinear tuning range is, in most cases, preserved in the noncollinear geometries.

In general, the advantages of noncollinear phase matching can be harnessed for all critically phase matched parametric oscillators and, indeed, any second order critical phase matching process. Further increases in the external conversion efficiency can be attained by pumping past the input mirror to avoid unnecessary reflection losses of the pump beam;: a technique which cannot be applied in the collinear phase matching regime.

In terms of spectroscopic sources, however, narrow linewidths are generally required. Free-running OPOs are not generally considered to be useful spectroscopic sources because of their broad linewidth, and the results of this chapter show that noncollinear phase matching causes a further linewidth increase. The following chapters detail the work carried out on line narrowing the OPO based on BBO whilst endeavouring to maintain a broad tuning range.

References

[1] N. P. Barnes and V. J. Corcoran, "Parametric generation processes: spectral bandwidth and acceptance angles" Appl. Opt., 15, 696, (1976)

[2] K. Kato "Second-harmonic generation to 2048 Å in β-BaB_2O_4" IEEE J. of Quantum Electron., 22, 1013, (1986)

[3] R. L. Byer and S. J. Brosnan "Optical parametric oscillator threshold and linewidth studies" IEEE J. of Quantum Electron., 15, 145, (1979)

[4] C. Chen, B. Wu, A. Jiang, G. You "A new type of ultraviolet SHG crystal-beta-BaB_2O_4" Sci. Sin. Ser B., 28, 235, (1985)

[5] Y. X. Fan, R. C. Eckardt, R. L. Byer, C. Chen, A. D. Jiang "Barium borate optical parametric oscillator" IEEE J. Quantum Electron., 25, 1196, (1989)

[6] Y. X. Fan, R. C. Eckardt, R. L. Byer, J. Nolting and R. Wallenstein "Visible BaB_2O_4 optical parametric oscillator pumped at 355 nm by a single-axial-mode pulsed source" Appl. Phys. Lett., 53, 2014, (1989)

[7] L. K. Cheng, W. R. Bosenberg, C. L. Tang "Broadly tunable optical parametric oscillator in β-barium borate" Appl. Phys. Lett., 53, 175, (1988)

[8] S. E. Harris "Tunable optical parametric oscillators" Proc. IEEE, 57, 2096, (1969)

[9] R. L. Byer and S. E. Harris "Power and bandwidth of spontaneous parametric emission" Phys. Rev., 168, 1064, (1968)

Chapter 6

Narrow Linewidth Oscillators

The historical development of line-narrowing in optical parametric oscillators is summarised, in this chapter. Building on the brief discussion in section 1.5, methods of linewidth control such as intracavity elements and injection seeding are discussed and key relevant experimental results are quoted to provide a back-drop to the narrow-linewidth work contained in this chapter and the next. Of particular interest to this thesis is the grazing incidence cavity. Previous work with grazing incidence lasers and optical parametric oscillators is discussed.

The grazing incidence optical parametric oscillator (GIOPO) was developed as a source of highly tunable, narrow linewidth radiation predominately in the visible region of the spectrum. The ultimate aim was to develop a stable, single-longitudinal mode source. However, the relationship between the bandwidth of the pump laser and the subsequent linewidth of the OPO is not well documented. Single-frequency OPOs have been reported using single-frequency pump sources, but whether a multi-mode pump source could produce the same result is not clear. In order to explore the relationship between the pump bandwidth and the OPO linewidth, the linewidth of the OPO in a grazing incidence configuration is studied using two different pump bandwidths. Finally, a broad tuning range, narrow linewidth grazing incidence OPO is discussed at the close of the chapter to demonstrate the potential of the OPO as a spectroscopic tool.

6.1 A Brief History of Narrow Linewidth OPOs

In 1969, Kreuzer presented a theoretical analysis showing that in steady-state operation, gain saturation will prevent more than one mode oscillating in a singly resonant OPO (SRO) providing the pump power is less than 4.6 times above threshold. Longitudinal

mode competition within the gain profile of the device results in the threshold being exceeded for only one mode. This single-mode grows at the expense of the others and saturates the gain. The resonant mode is usually the one nearest to the wavelength where the phase mis-match is at a minimum or zero. Using intracavity dispersive elements, the linewidth of the resonant wave can be made to narrow, but the non-resonant wave reflects the axial mode spectrum of the pump field. For example, using a pump source of >4 cm^{-1} linewidths of <1 cm^{-1} were demonstrated in the steady state operation of a $LiNbO_3$ OPO for the resonant idler, whilst the corresponding signal wave had a linewidth of 5.8 cm^{-1} [2]. In this case, the steady-state condition was reached using a 400 ns pump pulse duration. The steady-state assumption is not, however, applicable to pulse durations in the 6 ns to 20 ns regime. Under these conditions, unless special precautions are taken, many modes are excited and the OPO linewidth can be as broad as the OPO gain bandwidth. At degeneracy, the linewidth of angle-tuned OPOs can easily reach 10 nm so the need for line narrowing is apparent for spectroscopic applications.

Factors affecting the OPO linewidth include the pump beam divergence. In chapter three, the bandwidth of the pump laser was dismissed as having little influence on the overall free-running OPO linewidth since it is it typically an order of magnitude less than the total linewidth of the OPO. In practice, however, it has been reported that a single-longitudinal mode (SLM) pump source leads to greater conversion efficiency and improved OPO amplitude stability, and can reduce the linewidth [3]. Finally, the linewidth of the OPO may also be affected by the cavity geometry and the pump energy in relation to the threshold energy.

In general, there are three techniques that are widely used for reducing the linewidth of OPOs: dispersive elements (such as gratings and prisms), injection seeding and etalons. Intracavity etalons and injection seeding were employed in the first two reported SLM

OPO devices. In the first, reported by Kreuzer in 1969 [4], mode-selecting etalons were inserted inside the OPO cavity. This method, widely used in laser resonators for the same purpose, produced SLM in the singly resonant OPO and has since been used by other researchers [5]. In the second, Bjorkholm and Danielmeyer [6] seeded a CW single-mode Nd:YAG laser into a ruby laser pumped $LiNbO_3$ OPO to produce a SLM output. The non-tunable Nd:YAG laser line meant that the SLM OPO was not tunable. Since then, injection seeding of OPOs has been widely demonstrated by many researchers and, in general, it has been reported that this method readily produces SLM in the OPO whilst enhancing the conversion efficiency and lowering the threshold of the device. Moreover, such effects can be seen at remarkably low seed energies. Abdullin *et al* [7] reported saturation of the OPO gain at injection signals of just 0.1 μJ. Hovde *et al* [8] have reported near-transform limited 120 MHz bandwidth 10 ns pulses by seeding with a few micro-Watts in a $LiNbO_3$ crystal, whilst Haub *et al* [9] demonstrated the spectroscopic potential of a BBO OPO by seeding the oscillator with 2 GHz bandwidth dye laser radiation.

One disadvantage associated with injection seeding is that the tuning range of the narrow linewidth OPO is limited to the tuning range of the seed source. In some cases, the seed source is a fixed frequency but even with a single-frequency diode laser, the tuning range can be as little as a few tens of nanometres. In a system reported by Fix *et al* [10], however, tunability is maintained throughout the single-mode operation of the OPO. This is achieved by constructing a very short plane-plane cavity using BBO which causes a relatively large cavity mode spacing of 1 cm^{-1}. A single-frequency is isolated from the OPO using a Fabry-Perot etalon and this then becomes the seed source for a second BBO parametric oscillator.

The third method employs the use of intracavity dispersive elements and the techniques involved are varied. Brosnan and Byer [11] used a diffraction grating preceded by

expansion prisms and a tilted etalon and stable SLM was demonstrated from their $LiNbO_3$ OPO. The intracavity prisms expand the light in the cavity on to the diffraction grating causing the resonant radiation to "see" more of the grating grooves. This maximises the resolution of the grating and, therefore, causes it to feed back spectrally narrower radiation. A similar result can be obtained by positioning the grating so that the intracavity radiation grazes the grating surface, thereby illuminating most of its length. High spectral resolution can be sought in this way, which is considered in more detail in the following section.

Similar devices have been constructed using one order of a diffraction grating as the output coupler and feeding back another order on axis providing cavity resonance. This is known as a Littrow configuration. Using a similar technique, Burdulis *et al* [12] reported a linewidth of 0.24 nm from a 502 nm pumped BBO OPO whilst Piskarskas *et al* [13] reported a linewidth of 72 GHz in a synchronously pumped BBO OPO, by allowing the first order of the grating to feed back into the cavity. In all of these cases where the pump laser is specified, an injection seeded pump source was used.

Finally, it is well known that a high angular rate of tuning in an OPO leads to large linewidths and, by inference, the reverse is also true. It was shown in chapter three that the rate of tuning is smaller in type II critically phase matched BBO compared with type I and the linewidth, therefore, is narrower. Experimentally, type II phase matching has been demonstrated in BBO pumped at 355 nm [14] and linewidths of 0.05 nm to 0.3 nm have been reported over the tuning range of the OPO which extended from 480 nm-630 nm (810 nm-1360 nm in the idler). Although this shows a dramatic improvement of two orders of magnitude in linewidth over type I phase matching, type II phase matching in BBO is inherently less efficient compared with type I phase matching and in this instance two crystals were used in the cavity.

6.2 The Grazing Incidence Cavity

The grazing incidence cavity was first reported for a dye laser by Littman and Metcalf [15] and, independently, by Shoshan, Danon and Oppenheim [16]. Generally, the cavity can be configured to provide enough spectral selectivity to generate narrow linewidth in a single-longitudinal mode without the use of intracavity etalons or beam expansion optics. Sufficient dispersion can be obtained by positioning the grating at a high degree of incidence where its dispersive properties are maximised. This makes the oscillator inexpensive to build and keeps the number of cavity elements to a minimum which, in turn, reduces the number of surfaces in the cavity producing loss. The simplicity of the cavity means that, in general, it can be made short, increasing the number of round trips experienced by the resonant wave and maximising the longitudinal mode spacing.

By positioning the grating in a grazing configuration, the resolution is maximised. This is shown by considering the resolving power of a grating, R, defined as

$$R = \frac{\lambda}{\Delta\lambda_{min}} \tag{6.1}$$

where $\Delta\lambda_{min}$ is the minimum resolvable bandwidth or the limit of resolution and λ is the mean wavelength of light impinging on the grating. Using the Rayleigh criterion for a diffraction grating [17] we find

$$R = \frac{Nd(\sin\theta_d - \sin\theta_i)}{\lambda} \tag{6.2}$$

where N is the total number of grating grooves illuminated, θ_d is the angle of diffraction and θ_i the angle of incidence of light of wavelength λ on the grating of period d. Evidently, the resolving power of the grating is a function of the grating length Nd and

this is maximised when the light grazing the surface illuminates the greatest number of grooves.

In the Littman and Metcalf cavity, light incident on the grating from the dye cell is diffracted towards the tuning mirror in first order (figure 6.1). The tuning mirror then reflects the light back into the cavity which then impinges on the output coupler. During each cavity round trip, the light strikes the grating twice. Only light of a specific wavelength range will be fed normally onto the tuning mirror and subsequently reflected back on axis in the cavity. The laser is tuned by rotating the tuning mirror and hence changing the wavelength range which is fed back into the cavity.

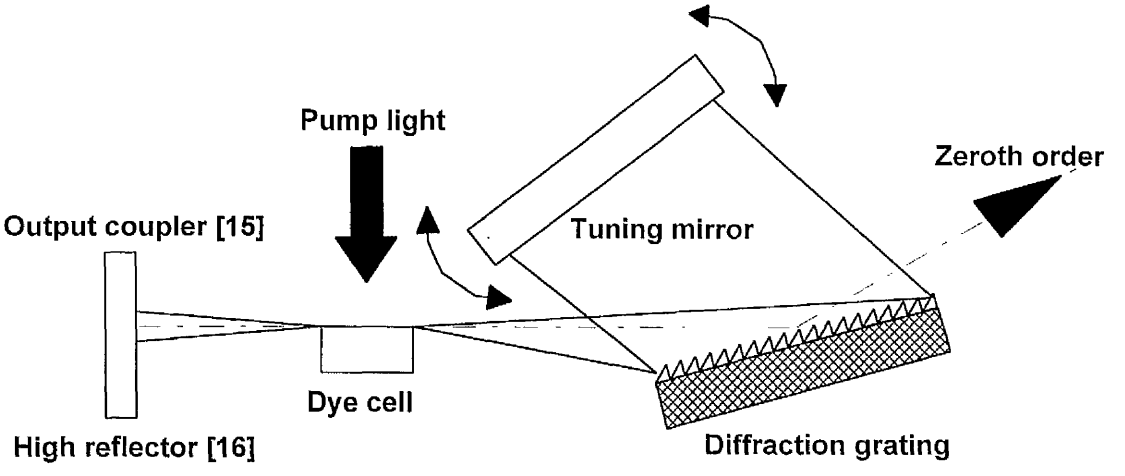

Figure 6.1. Transversely-pumped grazing incidence dye laser cavity based on the designs of Littman and Metcalf [15] and Shoshan, Danon and Oppenheim [16].

A significant loss associated with this cavity design is the zeroth order of the grating being coupled out during each round trip. Shoshan *et al* overcame this problem by replacing the output coupler of Littman's cavity with a high reflector and used the zeroth order of the grating as the useful output of the laser. This is also incorporated in figure 6.1. The system adopted by Shoshan *et al* is similar to that used in the OPO described in this chapter, where the output coupling is from the zeroth order of the grating.

Since the simultaneous publication of the grazing incidence dye laser cavity, much work has been carried out on this cavity using various designs and gain media. An estimation

of the line narrowing capability of the cavity can be sought from the single pass linewidth model detailed here.

6.3 Single Pass Linewidth Model

The first order angle of diffraction θ_d of light of wavelength λ incident on a holographic grating of period d at an angle θ_i is given by

$$\lambda = d(\sin\theta_i - \sin\theta_d) \tag{6.3}$$

where angles θ_i and θ_d are measured on opposite sides of the normal to the grating. In the case of grazing incidence, equation 6.3 is simplified since $\theta_i \approx 90°$ and both angles are measured on the same side of the normal. Equation 6.3 can be rewritten as

$$\lambda = d(1 + \sin\theta_d) \tag{6.4}$$

The angular dispersion of the grating is given by the differential, $d\theta/d\lambda$. For the grazing incidence configuration, this is given by

$$\frac{d\theta}{d\lambda} = \frac{2}{d\cos\theta} \tag{6.5}$$

The factor of two arises because the light undergoes diffraction twice before returning to the gain medium. Using equation 6.5, Shoshan *et al* [16] were able to estimate the single-pass bandwidth of a grazing incidence dye laser to be 6.5 GHz. Experimentally, they found the linewidth to be 3 GHz. It is not unexpected that the calculated single-pass bandwidth is high since the resonant light is likely to undergo more than a single-pass during the pump laser pulse duration. For this reason, the model can be regarded as an upper limit on the laser linewidth.

Later, both Littman [18] and Shoshan and Oppenheim [19] were able to achieve reliable single-axial mode operation by substituting the tuning mirror with a second diffraction grating used in Littrow mode, thereby increasing the resolving power of the cavity. Using rhodamine 6G dye pumped at 532 nm with a pulse duration of 7 ns, Littman was able to produce a single shot linewidth of 300 MHz which increased to 750 MHz when the pulses were time-averaged to take account of the shot-to-shot jitter. In 1984, Littman was able to reduce the linewidth further, by means of improved cavity stability, to <150 MHz [20] by reverting back to just one grating and a silvered tuning mirror. Apart from greater cavity stability, the cavity length was made as short as possible (4-5 cm) to maximise the longitudinal mode spacing, and the dye cell was longitudinally pumped to better define the optical path. Since then, the grazing incidence laser cavity has been used with titanium doped sapphire as the gain medium [21] and much work has been spent stabilising the cavity length for stable single-axial mode operation (see, for example, [22]).

Recently, the optical parametric oscillator has been demonstrated in a grazing incidence cavity by Bosenberg, Pelouch and Tang [23] using two BBO crystals pumped at 355 nm. At an angle of incidence of 87°, linewidths of 0.03 nm (~30 GHz in the visible) were reported. However, owing to poor grating efficiency, the authors reported a high oscillation threshold and low conversion efficiency of the grazing incidence cavity compared with a grating mounted in a Littrow configuration. They concluded that the order of magnitude improvement in linewidth, nevertheless, made the grazing incidence cavity ideal for lower efficiency, high resolution applications.

In 1992, Bosenberg, Guyer and Moody [24] reported a single-longitudinal mode grazing incidence KTP OPO capable of tuning from 700 nm to 900 nm (1.3 μm to 2.2 μm) with a linewidth of 600 MHz and an external conversion efficiency of 12 %. It was during

this time that work independently began on the visible grazing incidence OPO based on BBO which makes up the work presented in this chapter and the next of this thesis. At the Conference on Lasers and Electro-Optics (CLEO 1993), Spectra-Physics Lasers launched a series of grazing incidence oscillator/amplifier OPOs based on BBO (known as the MOPO-700 series) for narrow linewidth operation in the visible region of the spectrum. Since then, other commercial systems have become available which variously use BBO as the oscillator (e.g. Continuum's Mirage), to reach the visible region of the spectrum, and the same material or other gain media, such as KTP, as the amplifier. Generating stable, single-longitudinal mode in the visible using BBO, however, has been difficult to achieve in the grazing incidence OPO and even some commercial systems have experienced problems in this respect [25]. In the following sections, a grazing incidence OPO based on BBO is fully investigated using multi-mode pump sources and in chapter seven single-longitudinal mode operation of the OPO is achieved using an injection-seeded pump source.

6.4 Grazing Incidence Optical Parametric Oscillator

It is apparent that single-mode operation in a grazing incidence OPO is less easily reached without the combination of a single-mode pump source and frequency-selective elements in the OPO cavity. In their grazing incidence OPO, Bosenberg *et al* were unable to observe single-longitudinal mode operation in the OPO when the pump source was operating multi-mode. The OPO, however, "snapped" to single-mode on the action of the pump source being seeded [26]. Unlike a laser, the parametric process is not an energy storing process and the spectral quality of the generated radiation tends to reflect that of the pump source. The correlation between the bandwidth of the pump source and the linewidth of the generated OPO radiation is not well understood. The remaining sections of this chapter seek to explore the effects on the linewidth of the OPO in the grazing incidence cavity when the bandwidth of the pump source is altered from 28 GHz

to 7.5 GHz, and to assess the feasibility of single-longitudinal mode operation of the OPO with a multi-mode pump source.

For the purposes of this work, two 355 nm Nd:YAG laser sources were used and two grazing incidence cavities were designed. Our first demonstration of the grazing incidence OPO used a 20 ns, 10 Hz repetition rate Spectron SL804 1614 with a bandwidth of 28 GHz at 355 nm and a single BBO crystal grazing incidence cavity. However, subsequent work carried out at 28 GHz pumping took place at the Vrije Universiteit, Amsterdam, utilising a 6 ns, 10 Hz repetition rate Spectra-Physics GCR-3 and a *dual-crystal* grazing incidence OPO.

The inclusion of the second crystal in the cavity was simply to yield a higher OPO gain, which was required as the bandwidth of the pump laser was reduced. Under this new cavity design, some results were repeated at 28 GHz and it is shown that the inclusion of the second crystal had little bearing on the linewidth of the OPO. However, caution must be exercised when comparing the threshold and efficiency results of the 20 ns Spectron laser and the single BBO crystal with similar measurements taken using the 6 ns Spectra-Physics GCR-3 and two BBO crystals because of the different number of cavity round-trips and crystal lengths.

Section headings in this chapter are ordered according to the bandwidth of the pump source and not the number of BBO crystals in the cavity. As a consequence, some results are presented for the 28 GHz pumped dual-crystal OPO before the dual-crystal cavity is formally described in the text.

6.5 Single-Crystal Grazing Incidence OPO Design

A short cavity grazing incidence OPO (GIOPO) has been constructed for the initial investigation based upon a single BBO crystal (Cleveland Crystals Inc.) measuring 4x6x14 mm^3. The pump source was the 28 GHz Q-switched, tripled Spectron Nd:YAG laser described in chapter five. A schematic diagram of the single-crystal GIOPO cavity design used in the initial work is shown in figure 6.2. In order to maximise the diffraction efficiency of the grating in first order it was necessary for the resonant intracavity wave to be p-polarised with respect to the grating surface.

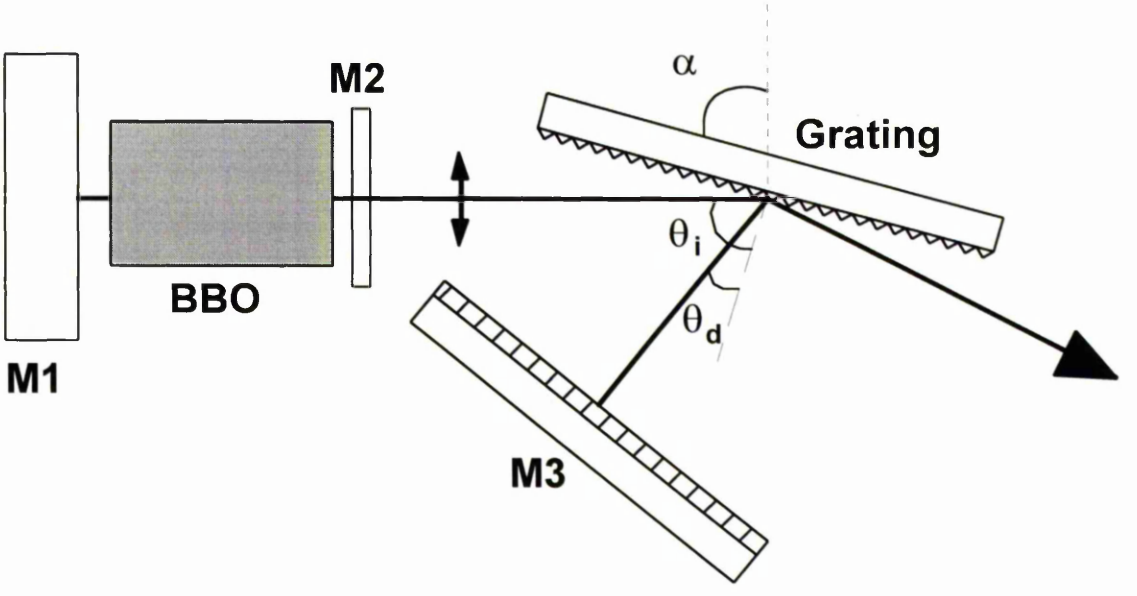

Figure 6.2. Schematic diagram of the grazing incidence OPO cavity. The cavity output is the zeroth order from the grating.

In the type I phase matching process, the e-ray pump beam generates the signal and idler as o-rays. The pump beam was, accordingly, polarised perpendicular to the plane of the optical table and the generated signal and idler were polarised parallel to the table making them perpendicular to the grooves of the grating. A sinusoidal, holographic grating was chosen since problems can arise from a blazed grating in a grazing incidence cavity. The main concern is unwanted direct feedback into the gain medium

from a grating order higher than the one being used. Under these circumstances, the grating behaves as if it were in a Littrow configuration and it is possible that this can occur simultaneously with the grazing incidence condition. These problems are avoided with the use of a holographic grating. Moreover, the greater degree of groove regularity in a sinusoidal grating make it more efficient at high angles of incidence. A 2400 lines/mm diffraction grating was chosen for its high dispersion, with dimensions of 50 mm in length by 16 mm by 6 mm.

The incident angle θ_i and the first order diffraction angle θ_d are shown in the figure and described by the grating equation (equation 6.3). In addition, the grazing angle, α, is shown which is a measure of the degree of grazing incidence and subtends the normal to the incoming ray and the grating surface. From the grating equation for a grazing incidence configuration, with a 2400 lines/mm grating, λ spans the visible region of the spectrum from 450 nm to 700 nm when the diffraction angle varies from 4.5° to 43°. From the cavity geometry, the diffraction angle is also the angle subtending the plane of the grating surface and the tuning mirror surface. In our case, the angular variation of 40° required to cover most of the visible region of the spectrum is made just possible by the mechanical motion of the tuning mirror. However, the reflectivity of the cavity optics may ultimately limit the tuning capability of the OPO.

Figure 6.3 shows a plan view of the grazing incidence cavity used in the initial work. The rotation stage for the tuning mirror of the grazing incidence cavity was a Newport M471 with a resolution of 0.3 arc-sec when used with a DM-13 differential micrometer. The back mirror, tuning mirror and grating were mounted on Photon Control Micropoint 25D holders. The Micropoint holder of the back mirror was then mounted on a Micro-Controle translation stage. This allowed the mirror to be retracted and the optic changed without upsetting the alignment of the OPO. A further development included mounting

the diffraction grating on a translation stage. This enabled the incident angle of the cavity to be varied without further alignment of the system.

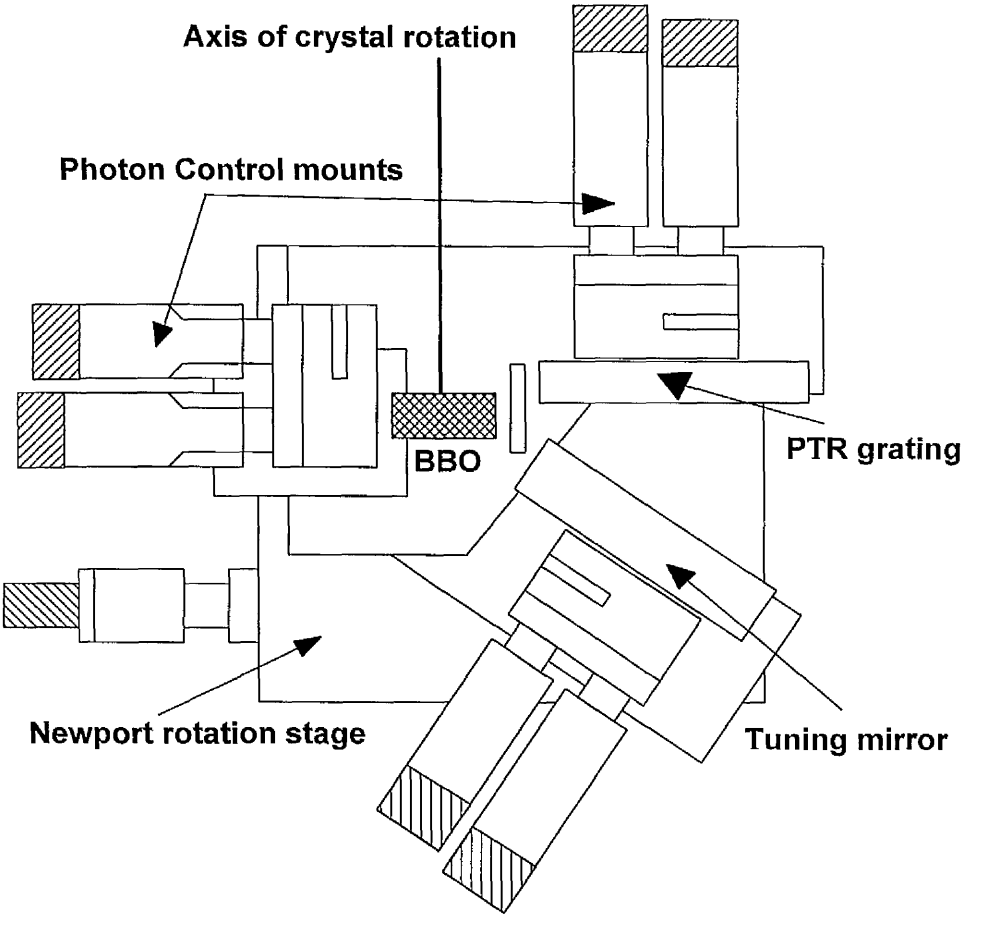

Figure 6.3. Detailed plan view of the short cavity grazing incidence OPO used in the initial work. The rotation stage for the crystal is omitted for clarity. The axis of rotation of the crystal is in the plane of the paper.

The grating, which was held in a home-machined mount, was mounted on a Micro-Controle translation stage which was attached to the base plate of the cavity above the tuning mirror rotation stage. The tuning mirror was an aluminium coated glass substrate measuring 45 mm by 12 mm by 10 mm. This was housed in a home-made mount and attached to the edge of the plate, which was mounted on the moveable section of the rotation stage.

The back mirror, M1, was coated for high reflectivity centred at 633 nm, with a reflectivity range extending to ± 10 % of this value. It transmitted 85 % of the pump power at 355 nm. M2 was a 355 nm filter designed to reflect most of the residual pump light to protect the grating surface and pass the visible and near infrared.

6.6 Diffraction Grating Efficiency

The greatest source of loss to the resonant wave in the grazing incidence cavity is provided by the diffraction grating and whether oscillation threshold is reached in the OPO depends strongly on the efficiency of the grating in first order. The proportion of light which the grating is able to diffract into the first order, as a percentage of that incident on its surface, is strongly related to the angle the incident light makes with the plane of the grating surface, the grating period and the condition of the element itself.

There was a choice of five 2400 lines/mm gratings in the laboratory from two sources: NPL (National Physical Laboratories) and Optometrics. The efficiency of each grating was measured by reflecting a polarised He-Ne at an angle of 88° to the grating normal from the grating surface. The incident power, reflected power and that diffracted into the first order of the grating were measured using a Spectra-Physics 404 continuous wave power meter. The polarisation state of the He-Ne was perpendicular to the direction of the grating grooves to reproduce the conditions in the cavity. The grating efficiency was defined as the ratio of power diffracted into first order and the difference of the incident power and that scattered. The scattered light is the part of the beam which passes parallel to the surface of the grating and is undeviated. This gives a measure of the absolute grating efficiency.

The efficiency results are tabulated below in table 6.1 for the five gratings.

Grating identification	Ist order efficiency %
NPL #1	11.4
NPL #2	10.5
NPL #3	7.8
Optometrics #1	3.2
Optometrics #2	6.1

Table 6.1. First order diffraction efficiencies for five holographic 2400 lines/mm gratings.

From the measurements presented here, the NPL #1 grating is seen to have the greatest first order efficiency and was subsequently used throughout the experiments detailed in this chapter.

6.7 Alignment of the GIOPO

A diagram of the pumping scheme for the grazing incidence OPO (GIOPO) is shown in figure 6.4. Since accurate alignment of the tuning mirror M3 is imperative for successful operation of the GIOPO, a low-power helium-neon laser (He-Ne) at 633 nm was used to position this optic correctly. The He-Ne beam passed through a pin hole and was positioned to illuminate the diffraction grating at a high incident angle (typically 88°). A good criterion for this alignment was to adjust the angle of incidence until a long, symmetrical first order was observed falling on the tuning mirror. The grating was then adjusted in the vertical plane to ensure the optical height of the beam was maintained after reflection from the grating surface. The back mirror M1 was then installed. The reflection from M1 was then retro-reflected onto the grating surface and back onto the pin hole. It is important that the reflected light from the back mirror strikes the grating on its return to the pin hole. At this stage in the alignment, the filter M2 is positioned. This has high reflectivity at the pump wavelength, but transmits the

visible, thus preventing laser damage to the grating face. It is important to locate this optic in a position so that is it unable to form a short cavity around the BBO crystal with the back mirror. This unwanted short cavity has a lower threshold than the grazing incidence cavity. Its operation, therefore, obscures the narrow linewidth operation of the GIOPO.

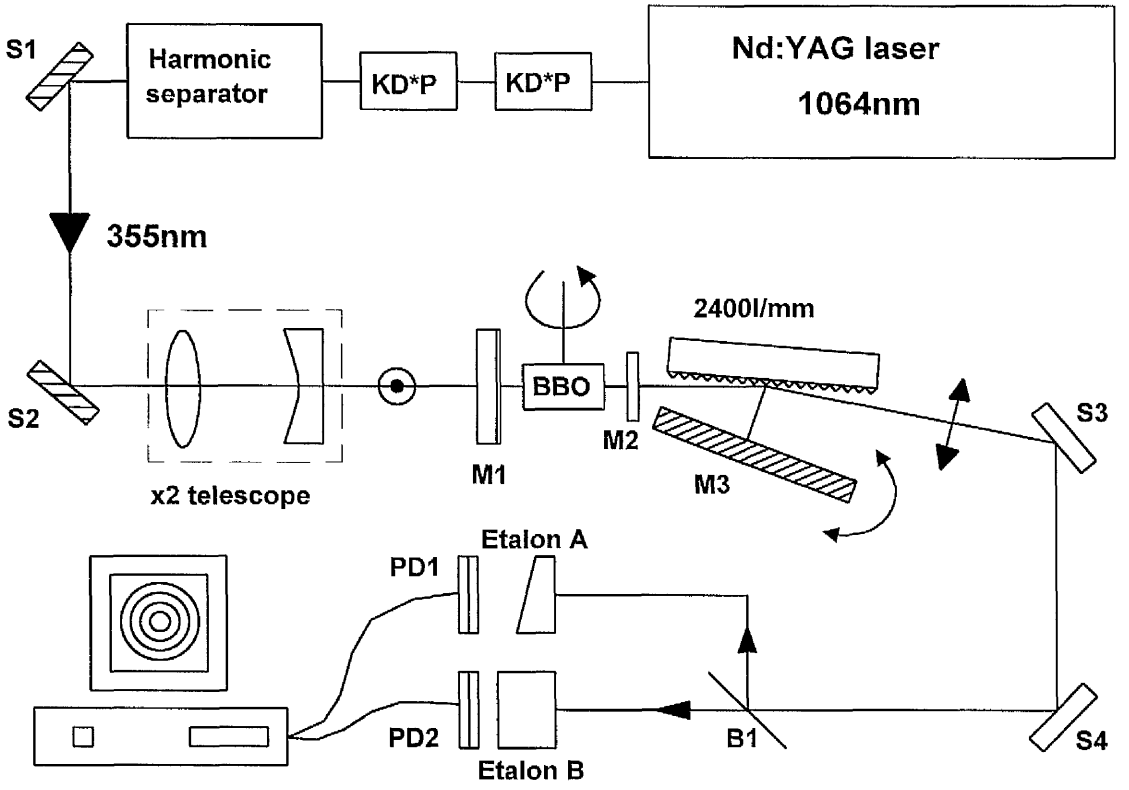

Figure 6.4. A schematic diagram of the GIOPO pumping scheme. S1 and S2 are steering mirrors for the 355 nm pump beam. The beam is compressed using a x2 telescope before being launched into the GIOPO. M1 is HR at 570 nm-700 nm and transmits the pump at >85 %. M2 is HR at 355 nm and has a broad visible AR coating. M3 is a silvered tuning mirror. S3 and S4 are silvered steering mirrors for the signal wave. B1 splits the signal radiation into etalons A and B for diagnostics in conjunction with photodiodes (PD1 and PD2) and the computer interface.

With these optics in place, the BBO crystal is then inserted such that it too retro-reflects the He-Ne beam. The tuning mirror M3 is rotated until a faint spot is seen travelling in a counter direction to the rotation direction of the mirror. This spot has been diffracted twice by the grating and has passed out of the cavity by zero order reflection from the

grating. The vertical adjustment is made with the M3 mirror mount where necessary so that the spot is incident with the pin hole. The pump beam is then introduced through the back mirror and is aligned collinearly with the residue He-Ne light transmitted through the back mirror M1. When good alignment is achieved, the pump beam lies in line with and just below the pin hole of the He-Ne. It is lower than the pin hole as a result of Poynting vector walk-off as it passes through the crystal.

The position of the tuning mirror means that the cavity is aligned to resonate at 633 nm. The rotational position of the crystal, therefore, must similarly be set for generation of a signal wavelength of 633 nm. A simple method used to introduce the correct rotational position of the crystal was to place a temporary output coupler (usually a glass slide) to couple back some of the zero order radiation. The effect of this additional coupling was to create a simple cavity between the glass slide and the back mirror M1 via a reflection from the grating surface The OPO was able to oscillate without the frequency constraints of the grazing incidence cavity. Positioning the crystal so that the generated signal was approximately 630 nm became greatly simplified since the glass slide/M1 cavity had a low threshold of oscillation relative to the grazing incidence cavity. With the glass slide removed, the tuning mirror was then carefully rotated until grazing incidence oscillation took place. Once the cavity was optimised, further tuning no longer required the incidental use of the glass slide since progressive small rotations of the crystal followed by a corresponding rotating of the tuning mirror to the required wavelength allowed unhindered tuning.

Analysis of the OPO spectra has been carried out using a Burleigh Pulsed Laser Spectrum Analyser (PLSA) interfaced to a computer. The PLSA consists of two broad-band coated etalons which are referred to as etalons A and B, respectively. Etalon A is a Fizeau with a free spectral range (FSR) of ~250 GHz. Etalon B is a Fabry-Perot with a FSR of ~10 GHz. Both have a finesse of 50 giving a resolution of ~3 GHz and

~200 MHz, respectively. Single-shot spectra can be analysed using a photodiode array positioned through the centre of the fringe pattern and interfaced to a computer. The detection range of the PLSA is 400 nm to 1100 nm.

6.8 28 GHz Pump Bandwidth and the Single-crystal GIOPO

The initial investigation into the grazing incidence OPO involved the use of a broadband Nd:YAG laser. The fundamental frequency of the Q-switched Spectron SL804 1614 laser was tripled to 355 nm using two KD*P crystals. The pump bandwidth of the fundamental wavelength was measured using a PLSA to be 13.5 GHz. Although the PLSA etalons were not coated for 355 nm, by measuring the doubled frequency (24.0 GHz) it is possible to estimate the bandwidth of the tripled light by the interaction of Gaussian beams. This was found to be about 28 GHz.

With the pump beam polarised perpendicular to the plane of the optical table, a 2 times Galilean telescope consisting of lenses of focal length f=100 mm and f=-50 mm contracted the diameter of the beam to 1.4 mm at the $1/e^2$ point of the intensity profile prior to being launched into the GIOPO. In order to benefit from the improved spatial profile of the pump beam in the far field, the OPO was placed more than a metre from the negative lens. The pulse duration and the pulse repetition rate were 6 ns and 10 Hz, respectively.

6.8.1 The Single-crystal GIOPO

The pump beam was directed through the back mirror of the cavity, M1. This optic measured 25 mm in diameter by 6 mm in width with a custom CVI coating of reflectivity 570 nm-700 nm, and a damage threshold of 300 MW/cm^2 and transmission of 90 % at 355 nm. The perpendicularly polarised pump beam enters the BBO crystal as

an e-ray necessary for the type I interaction with the crystal mounted on its side and rotated about an axis parallel to the plane of the optical bench. This geometry is required to maximise the efficiency of the grazing incidence cavity since the generated o-ray is polarised horizontally to the optical bench and, therefore, perpendicular to the grooves of the grating. This maximises the first order diffraction efficiency of the grating. In order to protect the grating surface from the residual pump light, a filter M2 is placed between the BBO crystal and the grating. M2 (Technical Optics Ltd) measured 10 mm in diameter by 3 mm thick, with high reflectivity at 355 nm and high transmission in the visible (480 nm-700 nm). The overall physical cavity length is 7.5 cm.

6.8.2 Tuning the GIOPO

In the grazing incidence cavity, the position of the tuning mirror determines the frequency which oscillates in the cavity. Similarly, the orientation of the BBO crystal is frequency dependent. Tuning of the two aspects of the cavity, therefore, must be coincident. Once the crystal has been detuned from the frequency required by the cavity, the GIOPO switches 'off', since there is no longer any feedback from the tuning mirror M3. Steady rotation of the tuning mirror M3 turns the GIOPO back 'on' at the new wavelength. The degree of rotation of the tuning mirror is determined by the grating equation in grazing incidence configuration (equation 6.4) although, in practice, finding the resonance condition again is usually a simple process.

The tuning range of the GIOPO was limited to the reflectivity of the back mirror, M1, of 570 nm to 700 nm. At these limits, the reflectivity fell dramatically. Tuning towards the degenerate point at 710 nm can be carried out using the technique described above, with the crystal always rotating towards the 'red' direction, and the tuning mirror angle θ_d increasing. Tuning beyond the degenerate point, so that the idler becomes resonant

rather than the signal, involves reversing the direction of rotation of the crystal towards the 'blue', whilst maintaining the same direction of rotation of the tuning mirror. Using this technique, the GIOPO tuned from 580 nm-700 nm with the CVI optic, and a further 66 nm into the red with the idler resonant using a (Technical Optics Ltd) mirror of HT at 355 nm and HR at 600 nm-800 nm, giving an overall tuning range of 580 nm-766 nm. The tuning was limited to 766 nm by the restricted movement of the tuning mirror M3, which made an angle of 53° with the surface of the grating.

6.8.3 Oscillation Threshold and Conversion Efficiency

The oscillation threshold of the GIOPO was mainly determined by the efficiency of the grating in first order and, therefore, by the degree of grazing incidence. We found, however, that there was little correlation between the wavelength of the GIOPO and the operational threshold. This is contrary to what is observed in a simple cavity BBO OPO where the gain bandwidth of the parametric process increases as the device tunes towards degeneracy and the threshold for oscillation consequently falls. The contrary result observed with the GIOPO may be explained by the gain bandwidth of the cavity being less than the inherent OPO gain bandwidth even at tuning positions far from degeneracy, resulting in the profile of the gain having a reduced effect on the threshold. The threshold, however, was critically dependent on the grazing angle of the grating. The degree of grazing incidence could be determined by measuring the separation between the output of the GIOPO and a low energy portion of the signal light passing undeflected across the grating surface at a known distance from the cavity. Using a Laser Instrumentation power meter model 5262A, the threshold of the GIOPO was determined by reducing the pump energy/pulse until oscillation could just be maintained in the OPO. The nominal definition used here is when GIOPO oscillation could be observed about once in ten pump pulses.

The external conversion efficiency of the GIOPO was also sensitive to the grazing angle of the grating. The output energy of the oscillator was measured and the external efficiency deduced from an input pump energy/pulse of 18 mJ. Table 6.2 below shows the variation of the oscillation threshold and conversion efficiency of the GIOPO for different grazing incidence angles.

Grazing incidence angle	**Threshold mJ (MW/ cm^2)**	**Conversion efficiency %**
86 °	10 (34)	3.7
87 °	12 (41)	1.0
88 °	15 (53)	<0.1

Table 6.2. Threshold and external efficiency measurements for the single-crystal GIOPO pumped at 355 nm with a bandwidth of 28 GHz at three angles of grazing incidence. Numbers in parentheses are in units of MW/cm^2.

Pumping the GIOPO above 20 mJ (70 MW/ cm^2) risked laser damage to the back mirror M1 despite assurances from CVI that the mirror could withstand incident energies of 300 MW/ cm^2 at 355 nm. Therefore, we were unable to safely pump the GIOPO harder and determine the saturated external conversion efficiency.

The pump depletion of the GIOPO was measured using two fast-risetime (<0.5 ns) photodiodes positioned before and after the GIOPO in conjunction with a 600 MHz LeCroy 9360 oscilloscope. The first photodiode detects the temporal profile of the undepleted pump and the second detects a small amount of residue pump exiting the GIOPO cavity. The specific method has been described earlier in section 5.2.5. The pump depletion results are shown in figure 6.5 for three grazing angles of (a) α=87.1°, (b) 88.7° and (c) 89.2°. The pump depletion of the GIOPO is seen to fall as the incidence angle is increased from 7.5 % to 1.4 %. It should be noted that these results

were recorded using the dual-crystal GIOPO pumped with the 28 GHz, 6 ns Spectra-Physics Nd:YAG laser and so cannot be compared with the external efficiency results in table 6.2.

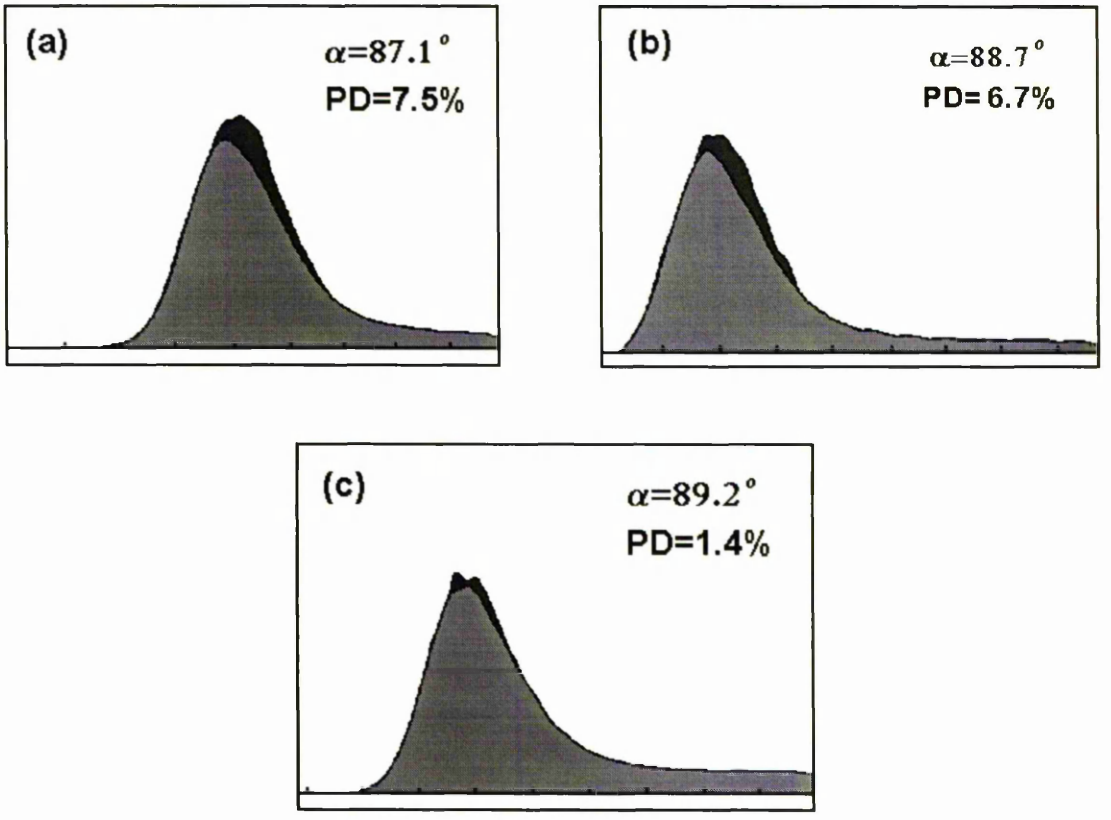

Figure 6.5. Pump depletion results for the 28 GHz pumped, dual-crystal GIOPO at three grazing angles.

6.8.4 Spectral Characteristics

The spectral characteristics of the GIOPO were determined using the PLSA. With etalon A (FSR ~250 GHz, resolution of ~3 GHz) we recorded a linewidth of 11.0 GHz at a resonant signal wavelength of 618 nm at a grazing angle of 88.5°. The spectral profile is shown in figure 6.6, which shows the intensity of the etalon peaks recorded by the photodiode array. Since the resolution of the etalon is less than the full-width half-maximum (FWHM) linewidth measured, the width of a single peak provides a measure

of the GIOPO linewidth. The y-axis of figure 6.6 indicates the intensity of the recorded output and the x-axis is a relative frequency scale in GHz.

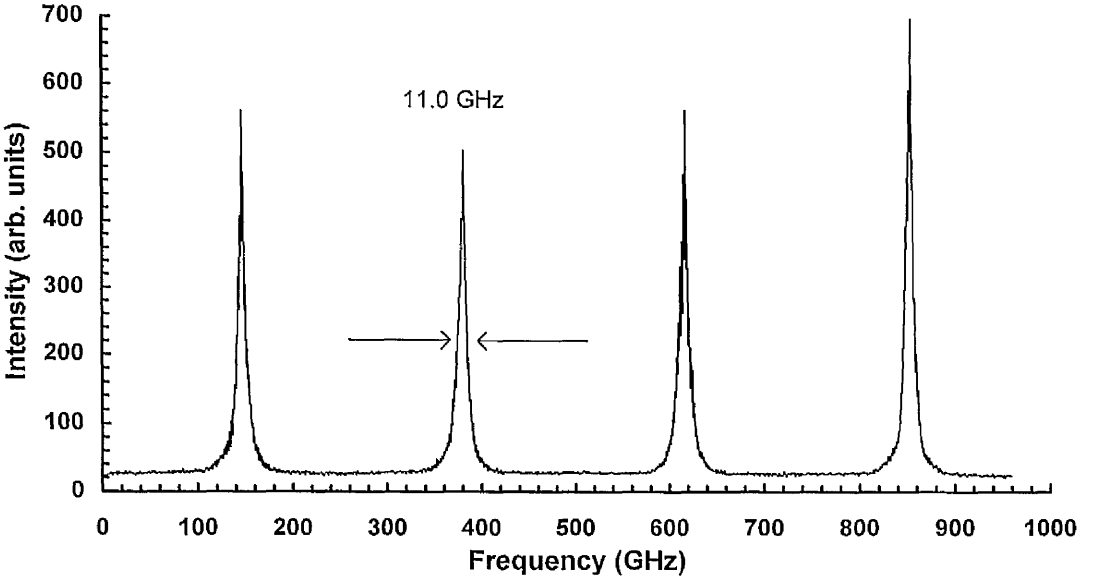

Figure 6.6. Spectral profile of the signal from the GIOPO pumped at 355 nm with a bandwidth of 28 GHz using etalon A.

Using etalon B (FSR ~10 GHz and a resolution of ~200 MHz), the signal was found to have a multimode structure with too many modes for satisfactory analysis by the etalon. This is shown in figure 6.7, where the cavity modes are seen to form a continuum. Figure 6.8 shows the spectral characteristics of the corresponding non-resonant idler at 836 nm measured with etalon A. A linewidth of 19 GHz was recorded.

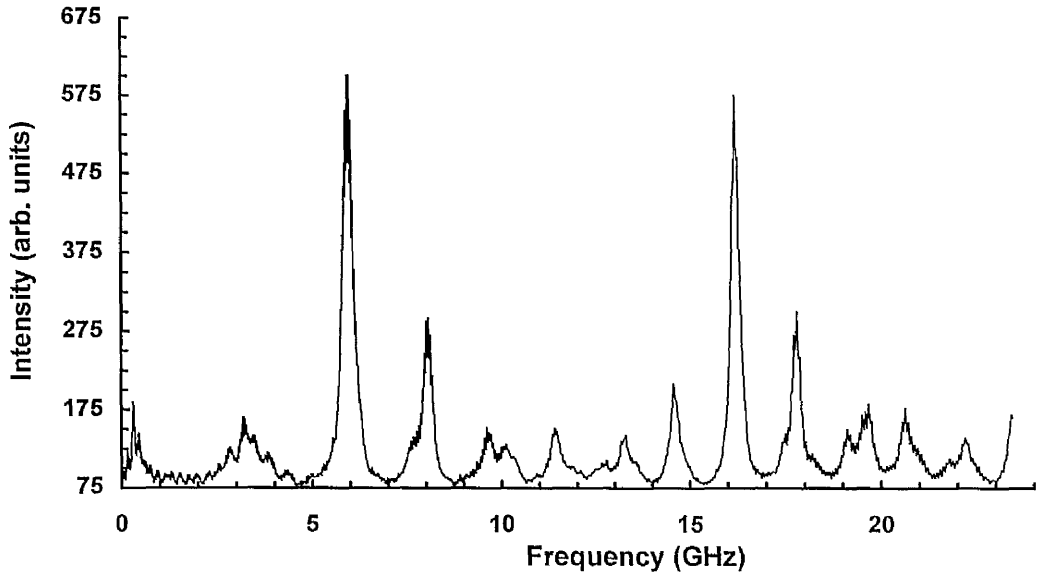

Figure 6.7. Spectral structure of the resonant signal of the single-crystal GIOPO using etalon B. The pump bandwidth is 28 GHz. The figure clearly indicates multimode operation.

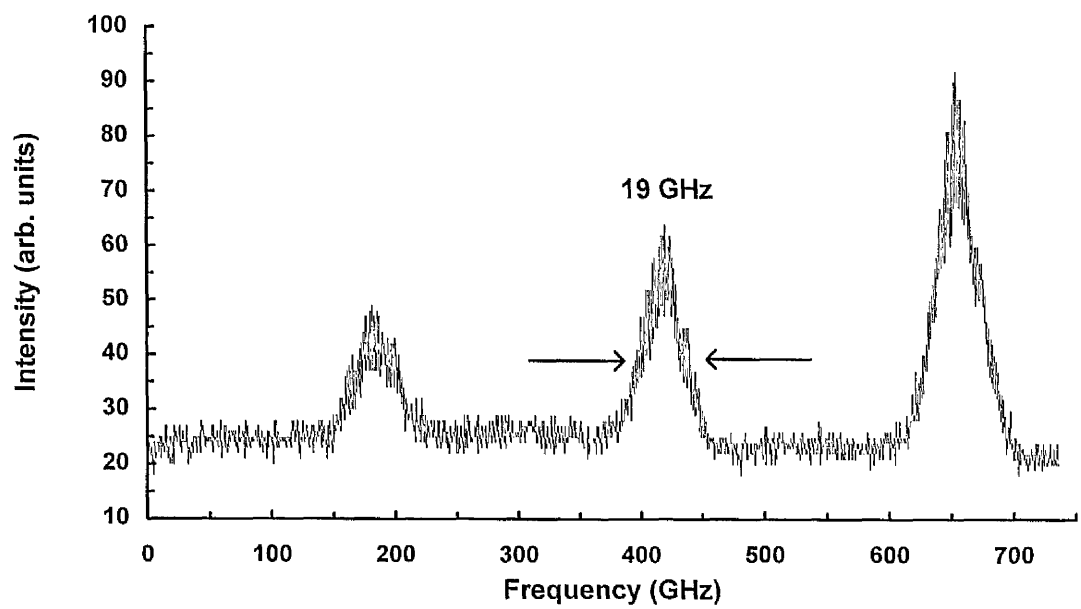

Figure 6.8. Spectral structure of the non-resonant idler using etalon A. The pump bandwidth is 28 GHz.

As the grazing angle was changed, the resonant signal linewidth remained unchanged within the error caused by the linewidth jitter of the signal, despite a grating angle greater than 89°. This is shown in figure 6.9, where the signal linewidth, measured over many tens of single-shots, is seen to remain at about 12 GHz for all angles of α. The corresponding idler linewidth was found to be 19 GHz.

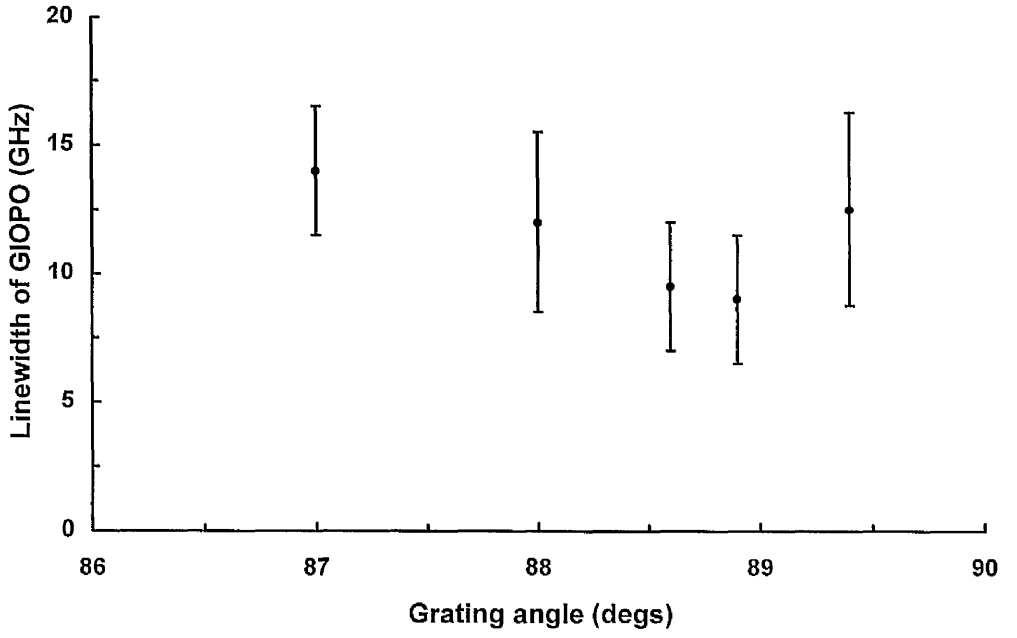

Figure 6.9. Signal linewidth variation with grating angle, α, for the 28 GHz pumped GIOPO.

6.8.5 Summary

A 28 GHz bandwidth pumped GIOPO has been demonstrated and shown to have a threshold and conversion efficiency which vary significantly with the degree of grazing incidence imposed on the cavity. The spectral linewidth of the resonant signal and non-resonant idler have been observed to be insensitive to the grating angle and the smallest possible signal linewidth obtainable from the device was 9 ± 2.5 GHz at a grating angle of 88.9°. However, the shot-to-shot linewidth jitter of the GIOPO means that the

linewidth is not seen to vary between 88° and 89.4°, but a significant improvement in the efficiency is observed at 88°.

6.9 7.5 GHz Pump Bandwidth and the Single-crystal GIOPO

In order to investigate the dependence of the GIOPO linewidth on the pump bandwidth, two intracavity etalons were fitted to the Spectron Nd:YAG laser. The fundamental bandwidth of the Nd:YAG laser reduced to 3.5 GHz. From this, the third harmonic has been estimated to be 7.5 GHz, a reduction of almost four times in the spectral bandwidth of the pump beam at 355 nm. No modifications have been made to the design of the single-crystal GIOPO, so that a direct comparison can be made between the signal linewidths.

With the reduced pump bandwidth and with the cavity aligned at 88°, no oscillation occurred at a 20 mJ/pulse input pump energy. This was not perceived to be a cavity alignment error and the grating was subsequently repositioned to 85.3° to increase the amount of light diffracted into the first order of the grating, and hence increase the cavity coupling at which point oscillation was observed. The insertion of the cavity etalons into the pump laser cavity resulted in an increased intensity instability at 355 nm which could be observed with the eye when the pump illuminated a paper screen. This jitter was amplified in the OPO causing considerable stability problems which, when added to the increase in oscillation threshold, caused the OPO to switch on and off repeatedly.

6.9.1 Spectral Characteristics

The linewidth of the resonant signal was measured using etalon A of the PLSA. The intensity profile of the etalon fringes are shown in figure 6.10. This yielded a signal

spectral linewidth of 4.8 GHz which is near the resolution limit of etalon A and may be instrument-limited. The energy output of the GIOPO, however, was too low to detect using a power meter. Consequently, a consistent and reliable response on etalon B could not be obtained, although two to three cavity modes were observed occasionally.

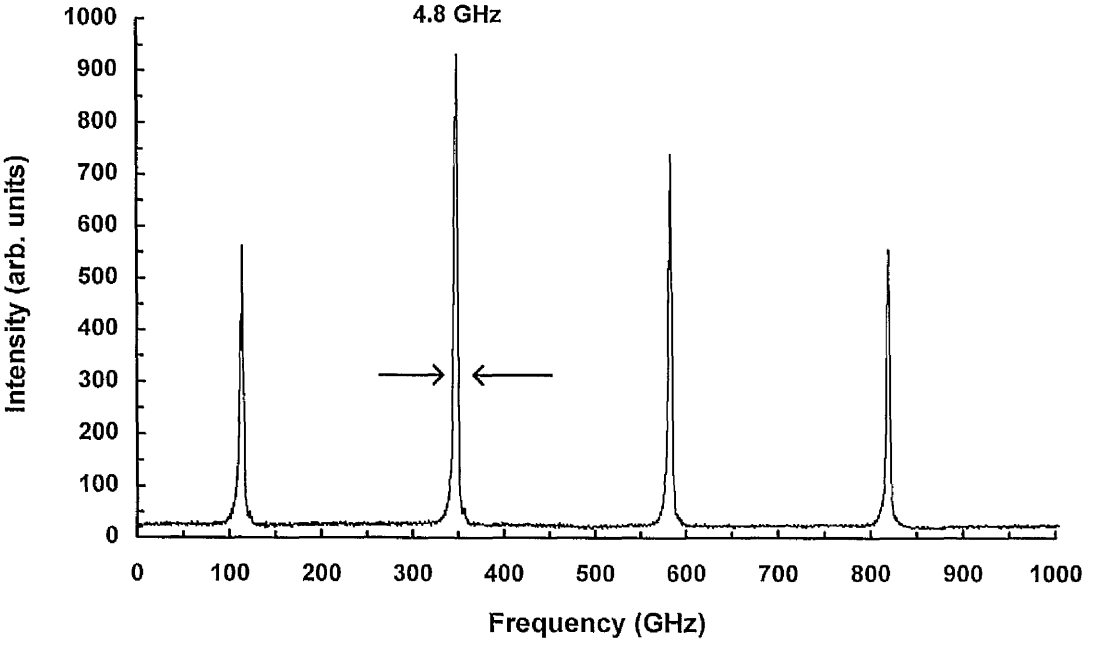

Figure 6.10. Intensity profile of fringes of etalon A indicating a signal linewidth of 4.8 GHz when pumped by a 7.5 GHz pump bandwidth.

The threshold was found to be 18 mJ, just 2 mJ below the damage limit of the back mirror of the cavity.

6.9.2 Summary

Reducing the bandwidth of the pump laser from 28 GHz to 7.5 GHz caused a narrowing of the GIOPO linewidth from ~11 GHz to 4.8 GHz. However, this was accompanied by an increase in oscillation threshold of the single-crystal GIOPO from 10 mJ (at 86°) to 18 mJ (at 85.3°). This initial investigation has show that the linewidth of the GIOPO is partially determined and possibly limited by the pump bandwidth. However, caution

should be exercised when comparing the two cases since the 7.5 GHz pumped GIOPO was at threshold whilst the other was not and pumping just above threshold is known to cause fewer modes to resonate. The insertion of the intracavity etalons in the pump laser resulted in a considerable decrease in amplitude stability at 355 nm, visible to the naked eye. This effect was amplified in the OPO, which, when added to the threshold operation, resulted in difficulties in securing repeatable spectral data.

The threshold of oscillation for the single-crystal GIOPO with the narrowed pump source is close to the damage threshold of the back mirror M1. For further reduction of the pump bandwidth to be carried out, it was first necessary to decrease the oscillation threshold of the GIOPO. Reducing the losses experienced at the resonant wavelength by improving the coatings on any intracavity optics will reduce the threshold. Indeed, the intracavity high reflector used in the GIOPO has no anti-reflection coating for the resonant signal wavelength. Since the resonant wave passes through this mirror three times per cavity round trip, a Fresnel loss of about 12 % is experienced. Increasing the crystal length in an attempt to increase the single pass gain will also reduce the threshold, although the effects of Poynting vector walk-off mean that significant length increases are futile. The solution opted for here is to introduce a second crystal into the cavity, in a walk-off compensated geometry, so that the crystal length could be increased without the concern of walk-off effects. In addition, the intracavity reflector was anti-reflection coated on one side.

6.10 The Dual-crystal GIOPO

The dual crystal GIOPO was constructed in a walk-off compensated configuration. The positioning of the crystals in this configuration is usually credited to Bosenberg, Pelouch and Tang who demonstrated a simple cavity BBO OPO based on such a system [23], although the method had been reported some ten years previously and used frequently

by Soviet scientists [27]-[28]. This simple technique, by positioning the crystals so that one is the mirror image of the other, minimises the effect of Poynting vector walk-off of the extraordinary pump ray in the two crystals by causing the displaced pump in the first crystal to recombine with the resonant axis in the second. A decrease in operation threshold by a factor of two or more compared with that of two crystals in a non-walk-off compensated regime has been reported by Bosenberg *et al.* The following sections explore more closely the design of the dual-crystal GIOPO and the effects of pumping such a system with a narrow bandwidth pump laser.

6.10.1 Walk-off Compensation

The inherent displacement of the Poynting vector of the pump wave from that of the ordinary resonant wave in the type I phase matching regime limits the crystal length available in the parametric interaction, as discussed in sections 2.7, 3.1 and chapter four. Two crystals, however, can be arranged on separate rotation stages in a manner causing the angle between their respective optic axes to be the sum of their respective cuts. A detail is shown in figure 6.11.

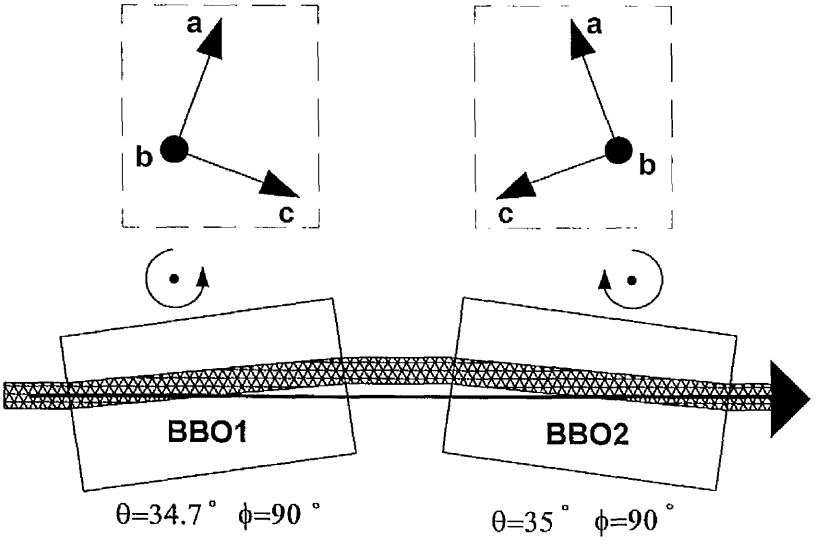

Figure 6.11. Walk-off compensation configuration in BBO. The e-ray pump (cross-hatched) departs from the o-ray signal/idler (heavy line) in BBO1, but they become coincident again in BBO2.

The cross hatched line represents the Poynting vector of the extraordinary pump ray decoupling from the signal and idler Poynting vectors in the first crystal BBO1, and then walking back in the second BBO2. The device is easily tuned by rotation of each crystal about their respective b-axes in an opposite direction to maintain the phase matching condition of each.

6.10.2 The Performance of the Dual-crystal GIOPO

The first crystal in the dual-crystal cavity (BBO1) has a 4x6 mm^2 aperture with an interaction length of 14 mm, and was grown by Cleveland Crystals Inc. It was cut for type I phase matching with an angle of 34.7° subtending the optic axis c and the normal to the crystal entrance face. The second crystal (BBO2) was grown by JTT International Inc., and had the same dimensions with a cut of 35°. Identical crystal lengths ensure the degree of pump beam walk-off is the same in each crystal which causes the pump beam to emerge from the crystals at the same optical height as it entered. This makes the alignment of the oscillator easier. Both crystals were cut with an azimuthal angle of ϕ= 90,° to maximise the effective non-linear coefficient and both had uncoated surfaces. Each crystal was mounted on a separate rotation stage with a resolution of 5 arc seconds (0.001°). During periods of inoperation of the GIOPO, both the crystals were held at a temperature of 48°C by two Peltier modules positioned at the base of each rotation stage to help protect the BBO crystals from water absorption. However, the crystals had to be returned to room temperature during the operation of the oscillator as the ±1°C temperature fluctuations of the crystals caused the OPO to switch on and off. The fact that a small change in temperature of the crystals causes the OPO to detune results from the temperature sensitivity of type I phase matching in BBO pumped at 355 nm which is about 0.45 cm^{-1}/°C [29]. A change in temperature of 1°C consequently tunes the OPO 13 GHz, which is sufficient to detune the grazing incidence cavity away from resonance.

The dual-crystal grazing incidence cavity, shown in photograph 6.1, is similar to that discussed in section 6.7 and shown in figure 6.4. The two crystals have necessarily increased the length of the cavity to 13.6 cm which results in a cavity free spectral range of about 1 GHz.

6.10.3 Efficiency and Threshold

A dramatic decrease in the threshold of the oscillator was observed with the addition of the second crystal in the cavity. Generally, for each grazing angle, the threshold fell by more than a factor of two compared to the single crystal GIOPO under identical pumping conditions. The corresponding rise in output energy from the GIOPO enabled a consistent and repeatable pattern of results to be taken, without the need for cavity re-adjustment. Table 6.3 below shows the efficiency and threshold results for the dual-crystal GIOPO at different degrees of grazing incidence.

Grazing Angle (°)	Threshold (mJ)	Signal Energy (mJ)	Efficiency (%)
85.0	<<5.0	1.20	7.0
86.0	<5.0	1.10	6.5
87.0	5.0	0.78	4.5
88.0	6.2	0.4	2.1
88.7	8.0	0.03	0.15
One crystal	**Threshold(mJ)**	**Signal Energy (mJ)**	**Efficiency (%)**
85.3	19.0	<0.02	<0.1

Table 6.3. Results of the dual-crystal GIOPO as a function of grating angle. Also included are the performance results of the single-crystal GIOPO. Both are pumped with the 7.5 GHz source.

Photograph 6.1

Dual-crystal grazing incidence optical parametric oscillator. Two BBO crystals are positioned in a walk-off compensated configuration and are controlled independently on two separate rotation stages.

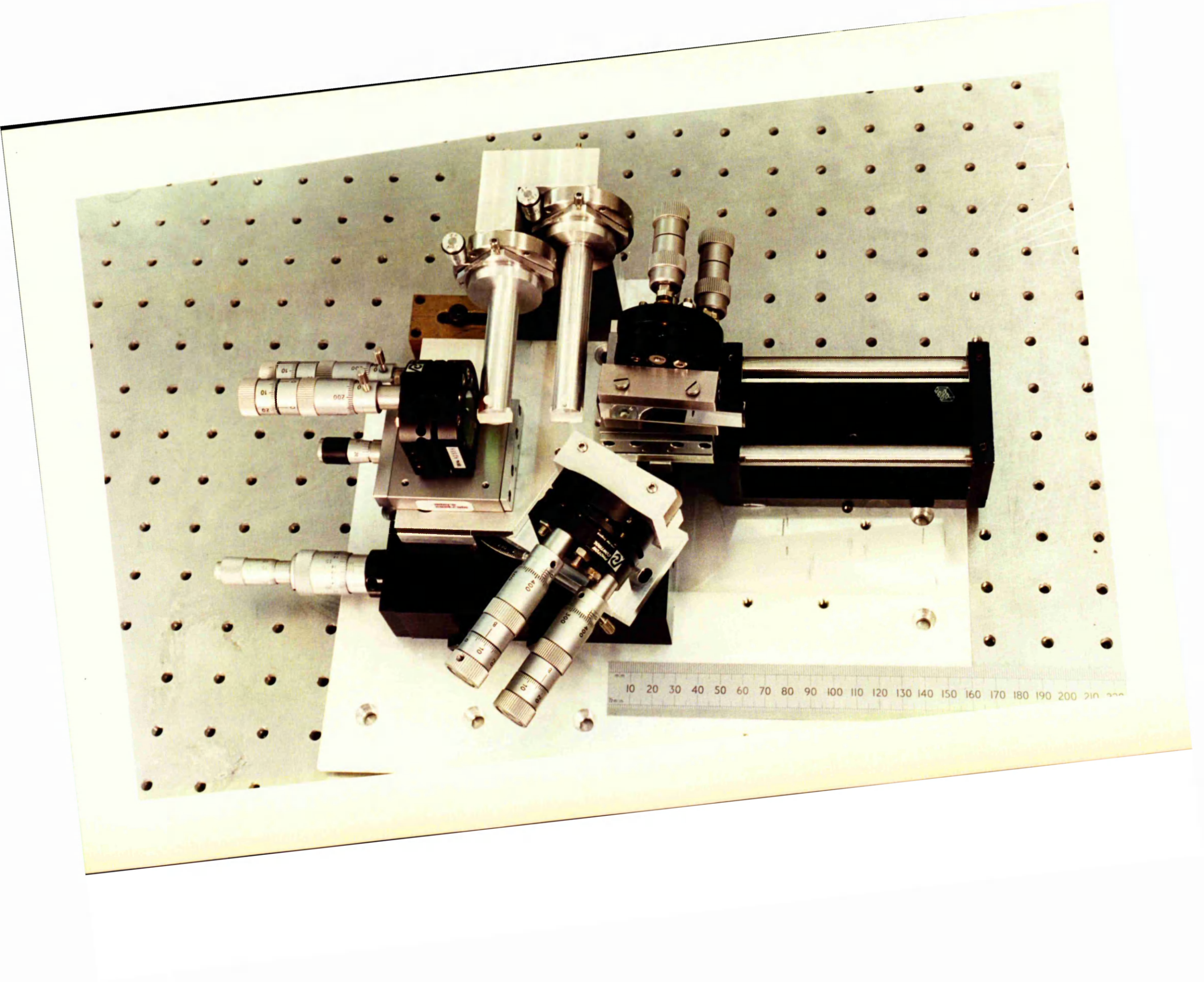
10 20 30 40 50 60 70 80 90 100 110 120 130 140 150 160 170 180 190 200

Also included in the table are the characteristics of the single crystal GIOPO for comparison. The threshold of the OPO was determined in the same way as described in section 6.8.3 for the single-crystal GIOPO and the signal energy was measured at the zeroth order of the grating. A Perspex filter placed in front of the power meter prevented the meter recording any residue pump light from the GIOPO. The 10 % loss introduced by the filter at the signal wavelength has been taken into account for the results recorded in the table. Clearly, the inclusion of the second BBO crystal in the cavity improves the operation of the GIOPO in terms of threshold and efficiency. Pump intensity fluctuations mentioned earlier caused the output of the GIOPO to jitter from pulse to pulse. The output energies in table 6.3 are averaged over several pulses since the power meter cannot respond to each pulse individually.

6.10.4 Spectral Analysis

The resonant signal linewidth and the non-resonant idler linewidth were measured for each grazing angle selected using both etalons A and B of the PLSA. The results are tabulated below in table 6.4.

Grazing Angle (°)	$\Delta\lambda_s$(GHz)	$\Delta\lambda_i$ (GHz)
85.0	8.7	9.0
86.0	7.6	8.7
87.0	7.5	10.2
88.0	7.8	10.4
88.7	5.8	8.1
One crystal	$\Delta\lambda_s$(GHz)	$\Delta\lambda_i$(GHz)
85.3	4.8	/

Table 6.4. Spectral data for the dual-crystal GIOPO pumped at 7.5 GHz bandwidth.

Each linewidth measurement was the average of several single shots (typically 40). The dependence of the signal linewidth on the grazing angle has increased by reducing the pump bandwidth to 7.5 GHz, so that at high degrees of grazing incidence (large α) the signal linewidth is seen to reduce. This dependence was not observed when the GIOPO was pumped with the 28 GHz source. To clarify this observation, the variation of the signal linewidth is shown as a function of the grating angle, α in figure 6.12.

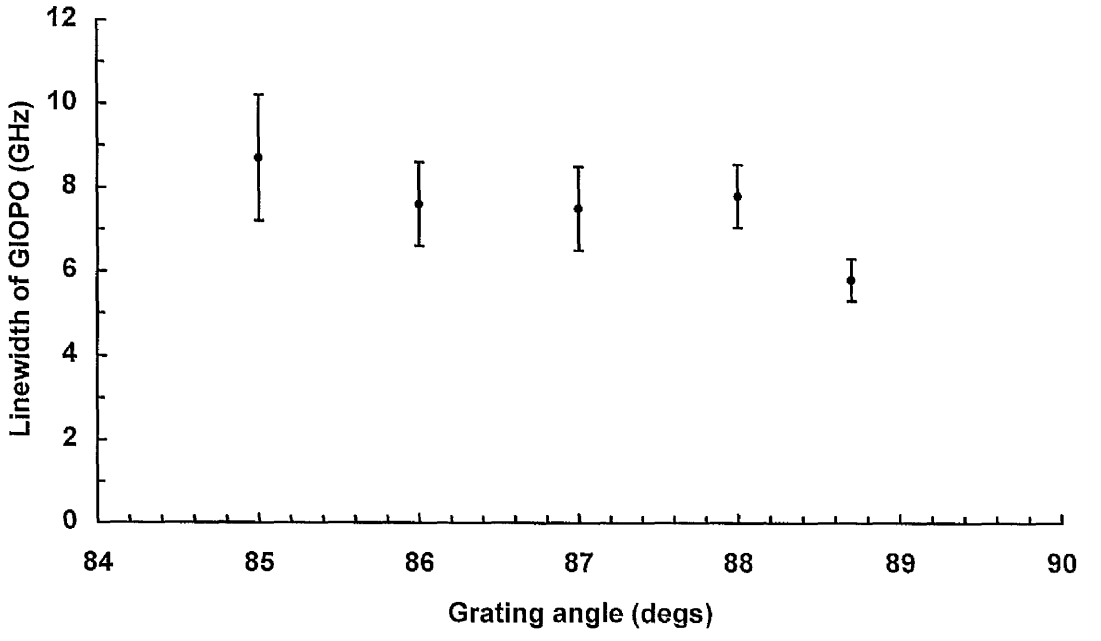

Figure 6.12. Dependence of the linewidth of the GIOPO pumped with a 7.5 GHz source on the grating angle, α.

In addition to the overall reduction in signal (and idler) linewidth with the 7.5 GHz bandwidth pump compared with the 28 GHz source, the shot-to-shot repeatability of the linewidth has improved, leading to a much reduced error on the measurements shown in figure 6.12. A 5.8 GHz linewidth of the signal at a grazing incidence angle of 88.7° is shown in figure 6.13.

The number of longitudinal modes supported by the cavity at a grazing angle of 88.7° was determined using the 10 GHz etalon (etalon B). In figure 6.14, the cavity is seen to support about eight cavity modes separated by ~1 GHz, commensurate with a physical

cavity length of 13.6 cm and an optical length of about 15 cm. These spectral measurements were taken at a signal wavelength of 612 nm. Photograph 6.2 shows a close-up view of the two BBO crystals with the GIOPO operating at 612 nm.

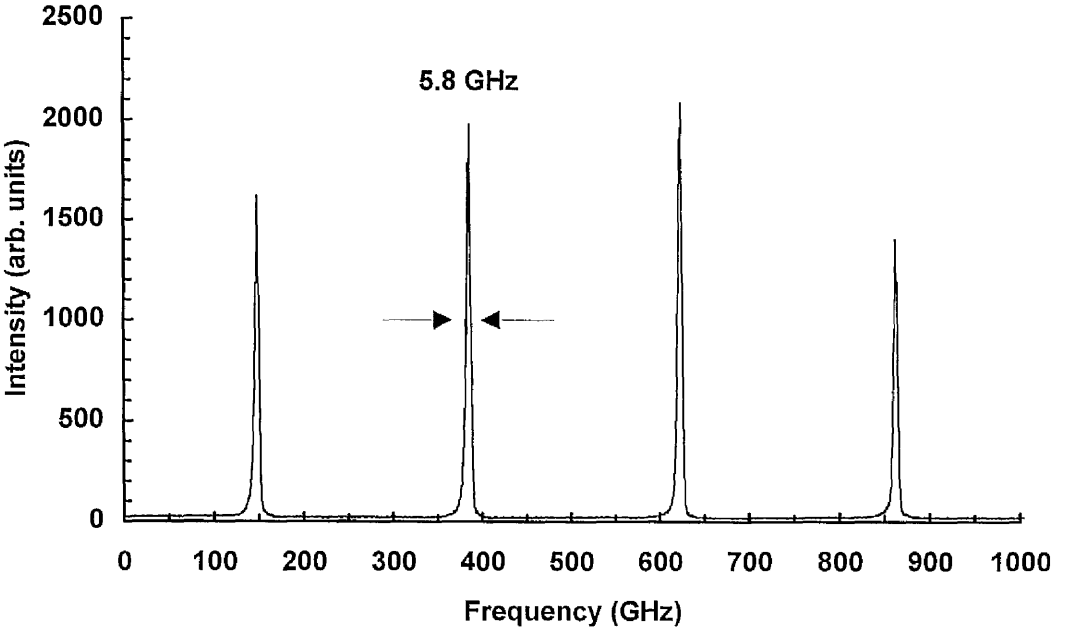

Figure 6.13. Signal linewidth of the dual-crystal GIOPO pumped with a 7.5 GHz source at a grazing angle of 88.7°.

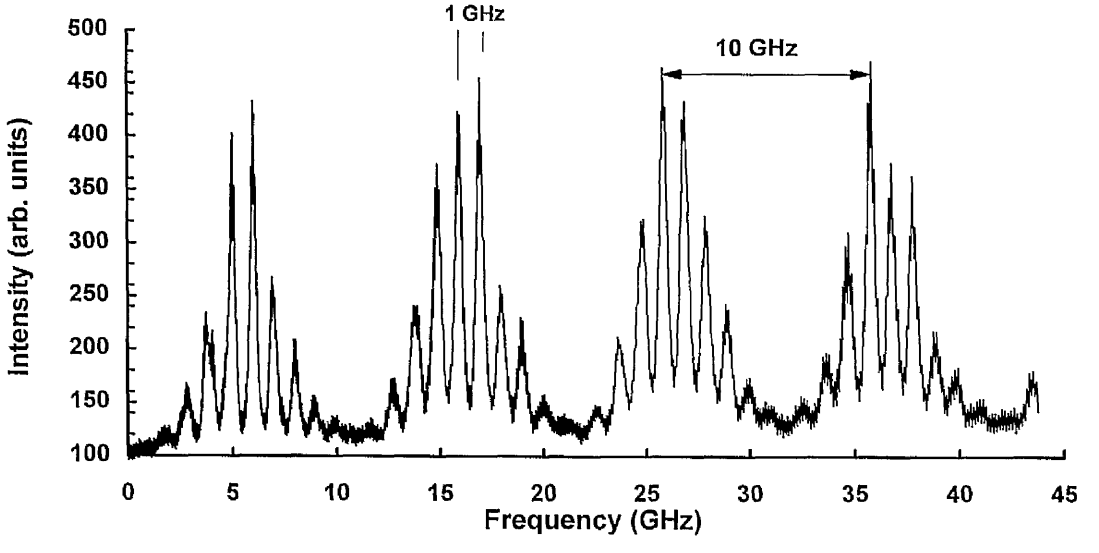

Figure 6.14. Longitudinal cavity modes resolved by etalon B. The cavity is seen to support about 8 modes.

Photograph 6.2

Dual-crystal GIOPO operating at 612 nm.

The corresponding non-resonant idler linewidth is shown in figure 6.15 using etalon A and has a linewidth of 8.1 GHz. We were unable to resolve reliably the mode-structure of the idler using etalon B.

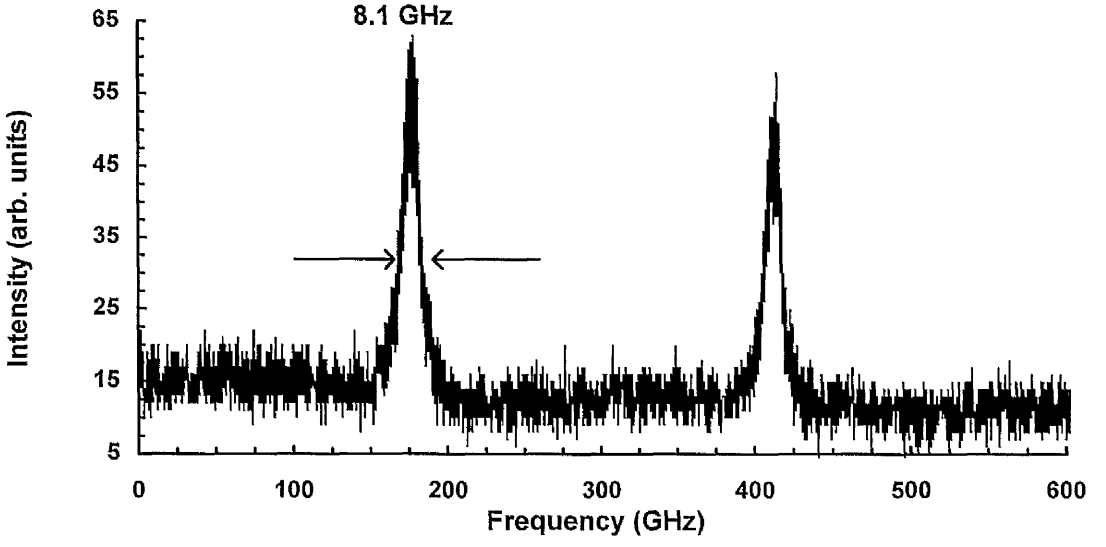

Figure 6.15. Linewidth of the non-resonant idler resolved by etalon A is 8.1 GHz at a grazing angle of 88.7°.

Individual spectral data similar to the figures above for the smaller degrees of grazing incidence studied can be found in appendix II. What these data, and that presented in figure 6.12, show is that the resonant signal linewidth broadens as the grazing incidence angle is reduced, since the increase in output coupling associated with smaller incidence angles increases the gain of the OPO, thus allowing more cavity modes to reach threshold. This is supported by the data in appendix II of the etalon B transmission responses for each grazing angle, which show the presence of more cavity modes supported by the cavity when the angle is decreased. In fact, at only small angular deviations from 88.7°, the cavity modes extend beyond the FSR of the etalon, causing an almost continuous spread of modes.

6.10.5 Summary

Two crystals in a walk-off compensated configuration have been successfully operated in a grazing incidence OPO, with a resonant signal linewidth of 5.8 GHz using a 7.5 GHz pump source. The threshold has been dramatically reduced by more than a factor of two compared with that of the single crystal GIOPO under the same pumping conditions, with an increase in linewidth from 4.8 GHz to 5.8 GHz. However, when the signal linewidths resulting from the same grazing angles are compared for both cavity designs, the linewidth of the dual-crystal GIOPO is 8.7 GHz whilst that of the single-crystal GIOPO is 4.8 GHz. The reason for the increase may arise from the dual-crystal GIOPO being pumped well above threshold.

The dual-crystal design greatly improved the efficiency of the GIOPO. The inclusion of the second crystal allowed grazing incidence oscillation at 88.7°. However, the increase in cavity length shortened the free spectral range of the cavity from 2 GHz to 1 GHz, making it more difficult to isolate a single-longitudinal mode. The tuning range of the dual-crystal GIOPO was limited to the reflectivity of the back mirror coating in the cavity, whose range was 570 nm-700 nm. In principle, the GIOPO should be capable of tuning the signal from degeneracy to 450 nm, at which point the tuning mirror rotation range becomes the limiting factor on the wavelength. Idler oscillation has already been demonstrated from degeneracy to 766 nm, however, by replacing the back mirror with one having high reflectivity in this range.

6.11 Highly Tunable GIOPO

To increase the tuning range of the GIOPO, an ideal would be to use a broad-band high reflective coating optic with a high damage threshold as the back mirror. Such coatings

are currently unavailable and typical reflective coatings range from 10 % each side of a central wavelength, resulting in shorter reflectivity ranges in the blue.

In order to demonstrate a highly tunable grazing incidence OPO, the cavity was redesigned to allow for a low damage threshold, low cost silvered mirror to replace the high damage threshold reflector as the back mirror. The result was to produce a narrow linewidth source of radiation tunable throughout the visible spectrum. The constraint on the tuning range of the OPO in the blue resulted from the excessive rotation of the crystals and the diminishing angle θ_d causing the tuning mirror almost to touch the grating surface. In the red, the tuning limit resulting from the mechanical range of the tuning mirror was θ_d=53°.

The introduction of a low cost silvered mirror as the back mirror of the oscillator has removed completely the constraint of the back mirror reflectivity limiting the tuning range of the GIOPO. However, since the silver coating had a low damage threshold, it was necessary to direct the pump light into the cavity by a route other than through the back mirror. This was achieved by introducing an intracavity 355 nm high reflector at Brewster's angle to minimise the loss of the p-polarised resonant wave at the surface of the optic.

Photograph 6.3 shows the OPO operating at 470 nm, and figure 6.16 shows a schematic diagram of the GIOPO. The 25 mm diameter 355 nm steering mirror in the foreground of the photograph reflects the pump light onto the small, intracavity Brewster mirror which is clearly visible. The intracavity 355 nm high reflector is also seen immediately after the second BBO crystal.

Photograph 6.3

Highly tunable GIOPO operating at 470 nm

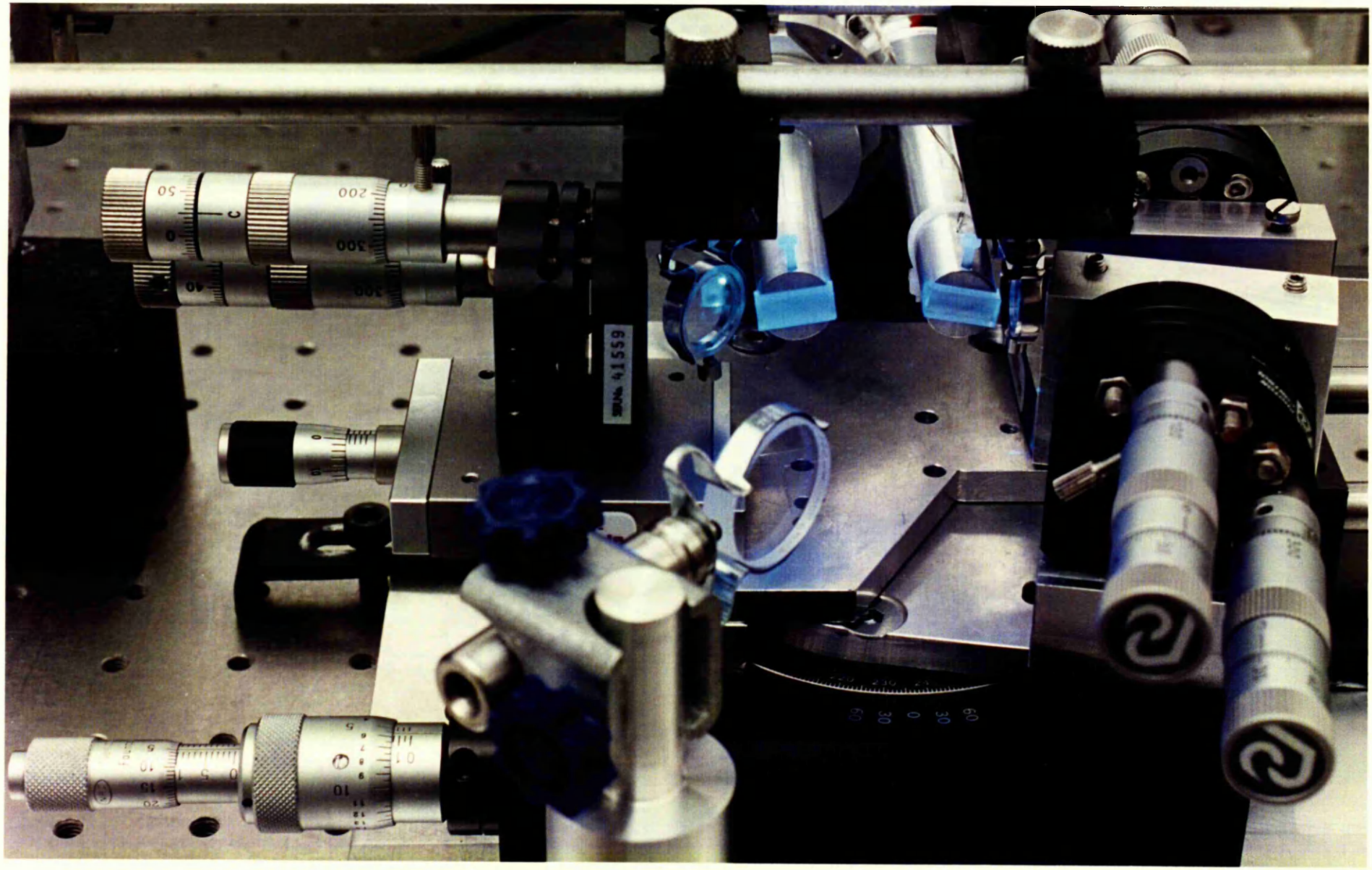
SN 41559

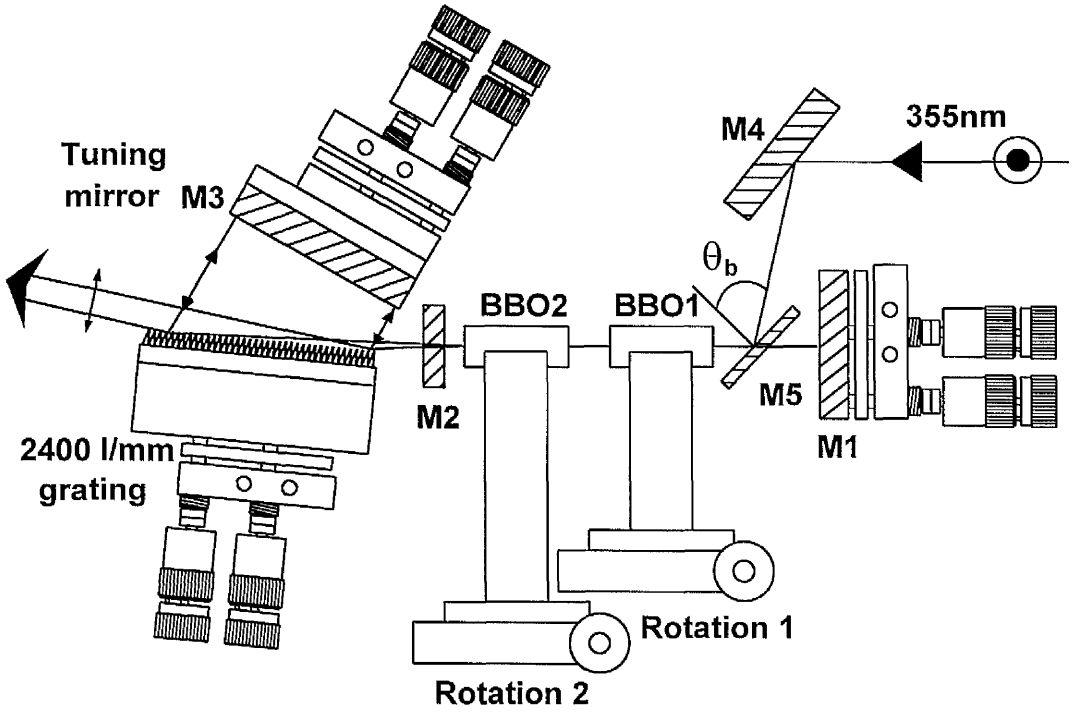

Figure 6.16. Layout of the highly tunable GIOPO. M2: HR at 355 nm and broad visible AR coated. M1: silvered mirror. M5: HR at 355 nm and positioned at Brewster's angle θ_b. M4: 355 nm steering mirror. M3: Silvered tuning mirror. Rotation stages 1 and 2 individually control BBO crystals 1 and 2. The grating periodicity is 2400 l/mm.

The Brewster steering optic (15 mm diameter, 1 mm thick CVI mirror) was coated for 99 % reflection for s-polarised light at 355 nm. For type I phase matching, the generated signal light is p-polarised. Positioning the reflector at Brewster's angle resulted in the resonant wave experiencing minimum loss at the surface of the optic. Other aspects of the cavity are the same as that described in section 6.7. Alignment of the cavity is similar to the procedure described earlier, except the low power He-Ne laser light is weakly reflected by the Brewster optic to provide guidance for the pump light. The silvered back mirror, M1, is aligned in the same manner described previously.

6.11.1 Efficiency and Tuning Range

The inclusion of the Brewster mirror increased the threshold of the OPO to 7.0 mJ at a grazing angle of 85°. Thus, with a grazing incidence angle of 85°, the tuning range for the resonant signal ranged continuously from 710 nm to 470 nm. Further tuning in the blue was limited by the tuning mirror (M3) almost touching the grating surface, although we believe that a higher degree of grazing incidence would allow for M3 to rotate further towards the grating and yield shorter wavelengths. No attempt was made to generate linewidths down to 5.8 GHz similar to that observed in the dual-crystal GIOPO. Tuning the GIOPO was carried out in the same way as that described earlier, with the rotation of BBO1 to the desired angle followed by a counter-rotation of BBO2 until strong parametric fluorescence was observed. The subsequent rotation of the tuning mirror resulted in the GIOPO switching on.

When resonant in the red (at 612 nm) the efficiency was 2.6 % whilst in the blue the efficiency was found to be 1 %. Both efficiency measurements were taken at a pumping energy of 17 mJ/pulse. Spectrally, the Brewster GIOPO linewidth varied only slightly from the shorter dual-crystal GIOPO for the grazing angle used, and only slightly from the red to the blue. Regrettably, a comprehensive study of the linewidth variation of the signal across the tuning range was prevented by surface damage to the second crystal (BBO2) caused by a back reflection of pump light from the high reflector M2. However, prior to the damage, the linewidth at 605 nm and 473 nm was measured using etalon A. Photograph 6.4 shows the two BBO crystals operating in the blue. The walk-off compensated geometry is apparent from the opposite rotations of the crystals. The Brewster optic and the 355 nm high reflector are clearly visible. Figure 6.17 shows the spectral data for the signal at 605 nm. Over several single shots (typically 30) the linewidth was found to be 9.2±1.8 GHz.

Photograph 6.4

GIOPO operating at 470 nm. The two BBO crystals, in a walk-off configuration, lie between the 355 nm HR at Brewster's angle and the 355 nm reflector.

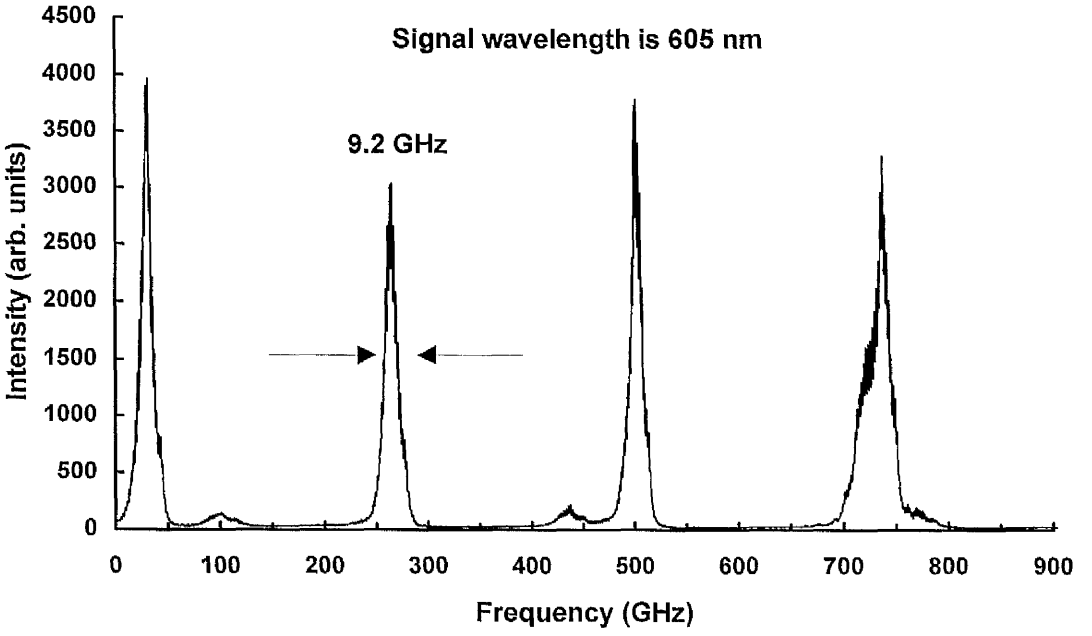

Figure 6.17. Spectral data for the signal in the Brewster GIOPO pumped at 7.5 GHz. The linewidth measured 9.2±1.8 GHz.

The linewidth of the signal at 473 nm averaged over 30 single shot measurements was 10.5±3.2 GHz.

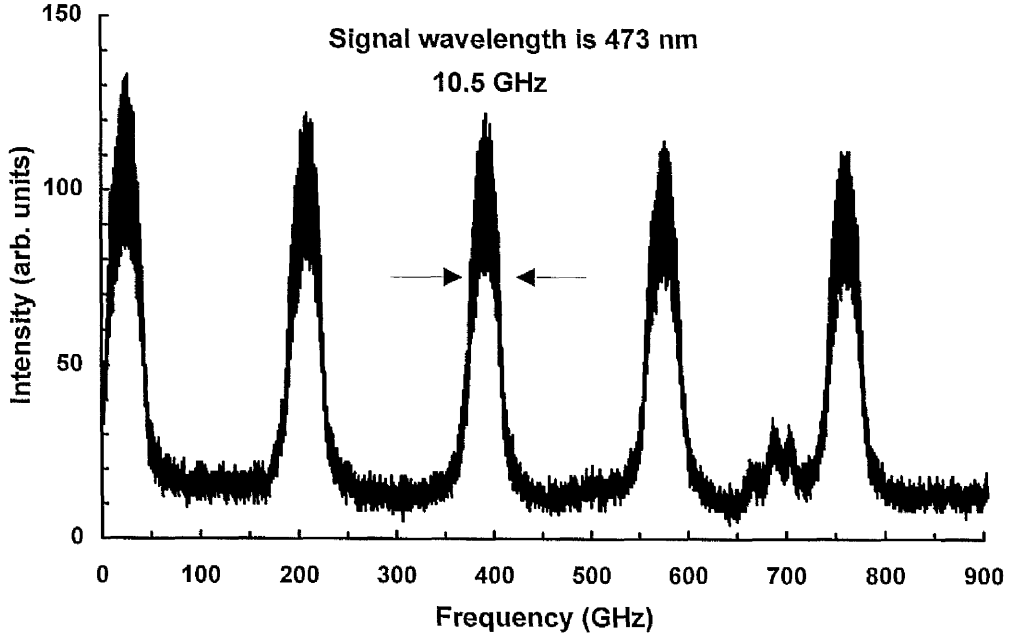

Figure 6.18. Spectral data for the signal in the Brewster GIOPO pumped at 7.5 GHz. The linewidth measured 10.5±3.2 GHz.

The spectral data for a single shot is shown in figure 6.18 on the previous page. At both wavelengths, the oscillator was multimode.

The tuning range was from 710 nm to 470 nm. This range was limited by the rotation constraints imposed by the tuning mirror. Figure 6.19 below shows the OPO tuning calculated from the phase matching relationship and the first order tuning response of the tuning mirror for a 2400 lines/mm grating at grazing incidence as a function of crystal angle.

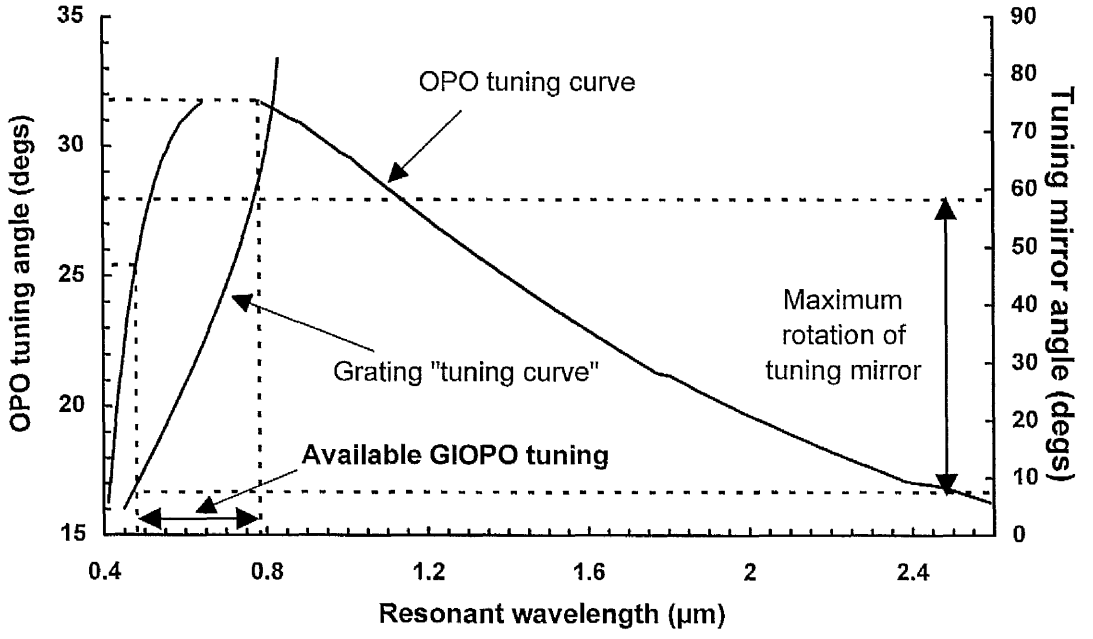

Figure 6.19. Free-running BBO OPO tuning range as a function of crystal angle (left hand axis). The tuning range of the grating is also shown as a function of tuning mirror angle (right hand axis). The dotted lines indicate the tuning range of the GIOPO.

From the figure, the tuning range of the mirror is shown on the right hand axis and is limited between 6° and 58°. This is then shown to correspond to a GIOPO tuning of 470 nm to 700 nm. On the left hand axis, the crystal angular change required for such a tuning range is shown. At the blue end, the angle is about 25°. With a BBO crystal cut of ~35°, the crystal was turned through an angle of 10° from its horizontal position. It

was this excessive rotation that caused a back reflection of the residual pump light to damage the crystal surface. From the figure, the tuning response of the grating/mirror asymptotes at an idler wavelength of about 800 nm. Wavelengths up to this value are possible if the constraint of the tuning mirror is lifted.

6.11.2 Summary

A highly tunable GIOPO has been demonstrated with a tuning range of 240 nm from 710 nm to 470 nm. The linewidth of the radiation was found to vary from 9.2 GHz in the red to 10.5 GHz in the blue with an external efficiency of a few percent. No attempt was made to further narrow the output of the GIOPO but, clearly, increasing the grazing angle from 85° would increase the spectral-selectivity of the cavity.

6.12 Summary of the GIOPO

The grazing incidence optical parametric oscillator (GIOPO) has been demonstrated using type I phase matched BBO to generate narrow linewidth light throughout the visible spectrum. It has been shown that the linewidth of the OPO is strongly dependent upon the linewidth of the pump laser and that this parameter tends to limit the linewidth emitted by the GIOPO cavity. Using 28 GHz and 7.5 GHz bandwidth pump sources, the linewidths of both the signal and idler of the GIOPO have been studied as a function of grazing angle. Linewidths were shown to be insensitive to the grating angle with the broad source, but showed significant dependence with the narrower source. Despite this, however, repeatable signal linewidths of less than 5.8 GHz were not possible.

The introduction of a second crystal in the cavity in a walk-off compensated configuration was necessary and this resulted in a fall in threshold by a factor of four which was accompanied by an increase in the linewidth of the signal from 4.8 to

8.7 GHz at a grazing angle of 85°. However, the fall in threshold allowed for high degrees of grazing incidence to be used and linewidths down to 5.8 GHz have been observed with a tuning range of 580 nm-766 nm limited only by the reflectivity of the back mirror. At a grazing incidence angle of 88.7°, the OPO oscillated on 8 cavity modes when pumped at 2.2 times threshold.

Finally, a broad-tuning range, narrow-linewidth OPO has been demonstrated by placing a Brewster reflector into the GIOPO cavity. The tuning range spanned from degeneracy at 710 nm to 470 nm in the blue whilst maintaining a linewidth of about 10 GHz and an external efficiency of a few percent.

6.13 Discussion

Since single-longitudinal mode operation is readily seen in solid state and liquid dye grazing incidence lasers irrespective of the pump bandwidth, one might expect the same to be true for the GIOPO, provided that sufficient linewidth control of the resonant wave is provided. However, we conclude from the studies carried out in this chapter that single-longitudinal mode operation of the GIOPO is not possible without a single-mode pump source (or a significantly narrower source than that used), and this has also been noted by other authors. Clearly, the bandwidth of the pump source plays an important role in determining the linewidth of the OPO, particularly when the linewidth is much smaller than the gain bandwidth. This is not the case in a laser where the nature of the stimulated photons do not, on the whole, have any of the properties of the absorbed pump energy. Furthermore, the linewidth of the OPO is also determined by the temporal nature of the pump source. Young et al [2] demonstrated a 473 nm Nd:YAG pumped $LiNbO_3$ OPO, with a pump bandwidth of 120 GHz and pulse duration of 400 ns. Although details of the cavity are not presented in the paper, the resonant idler is reported to be 8 GHz, and the non-resonant wave to be ~80 GHz. The authors state

that, whilst the pump is multi-mode, it is possible to generate a spectrally narrow output from the OPO. They consider a single frequency fixed by the optical resonator interacting with a broad band pump to generate a broad band non-resonant wave. In other words, provided the cavity is sufficiently frequency-selective at the resonant wave, the non-resonant wave will 'carry off' the residual pump frequencies. These results, however, contrast with those reported by Burdulis et al [12] who have studied line narrowed BBO OPOs using a passively mode-locked Nd:YAP laser generating 30 ps pulses. They state that, in their experiment, when the time-bandwidth product of the OPO is comparable to that of the pump, further narrowing of the OPO is not possible unless the pump is narrowed. The implication being that the spectral linewidth of the OPO is limited by the bandwidth of the pump source, assuming there is little change between the durations of the OPO and pump pulses.

Of course, the long pulse of 400 ns used in Young's work provides a much lower peak power and, hence, a lower gain in the OPO. It is probable that the steady state condition applies in this case, where the modes of the OPO which experience the least loss become dominant at the expense of the others, and the linewidth of the non-resonant wave duly narrows. This is not true in short pulse systems (a few tens of nanoseconds or less) where many potential modes are excited by the intense pump pulse. Indeed, this forms the basis of our explanation of the dependence of the GIOPO linewidth on the pump bandwidth.

6.14 Conclusions

In contrast with the gain medium of a grazing incidence tunable laser, the resonant signal emission of the non-linear crystal in the GIOPO has not only a broad frequency range caused by the intense pulse, but also an angle range corresponding to a range of wavenumbers. These wavenumbers all fulfil the phase matching condition $\mathbf{k_p}=\mathbf{k_s}+\mathbf{k_i}$ by

varying degrees of noncollinearity in the crystal. This leads to a broadening of the total gain bandwidth in the following manner: a range of components, each with its own wavenumber k_s, are emitted by the crystal at a corresponding range of angles and define a closed path in the cavity. Each component is characterised by a cavity linewidth which is determined by the grating and tuning mirror. The result is that these adjacent bandwidth components, each with a closed path, broaden the spectral output, reducing the resolution of the cavity. The pump bandwidth exerts a large influence on this process, since the range of signal wavenumbers increases with the pump bandwidth [3]. Therefore, a multi-mode pump laser will lead to a broader signal linewidth, whilst single-mode pumping excites fewer wavenumber components, thereby producing the smallest total grating gain bandwidth. Further, we feel confident that the effect on the linewidth of the GIOPO of the different pulse durations of the lasers we used are small, as the 28 GHz 20 ns source yielded the same GIOPO linewidth as the 28 GHz 6 ns source.

6.16 References

[1] L. B. Kreuzer "Single and multimode oscillation of the singly resonant optical parametric oscillator" Proc. Joint Conf. on Lasers and Optoelectronics, University of Southampton, IERE, London, 53, (1969)

[2] J. F. Young, R. B. Miles, S. E. Harris and R. W. Wallace "Pump linewidth requirements for optical parametric oscillators" J. Appl. Phys., 42, 497, (1971)

[3] Y. X. Fan, R. C. Eckardt, R. L. Byer, J. Nolting and R. Wallenstein "Visible BaB_2O_4 optical parametric oscillator pumped at 355 nm by a single-axial-mode pulsed source" Appl. Phys. Lett., 53, 2014, (1988)

[4] L. B. Kreuzer "Single-mode oscillation of a pulsed singly resonant optical parametric oscillator" Appl. Phys. Lett., 15, 263, (1969)

[5] G. Robertson, A. Henderson and M. H. Dunn "Efficient, single-axial mode oscillation of a beta barium borate optical parametric oscillator pumped by an excimer laser" Appl. Phys. Lett., 62, 123, (1993)

[6] J. E. Bjorkholm and H. G. Danielmeyer "Frequency control of a pulsed optical parametric oscillator by radiation injection" Appl. Phys. Lett., 15, 171, (1969)

[7] U. A. Abdullin, G. P. Dzhotyan, Yu. E. D'yakov, B. V. Zhdanov, V. I. Pryalkin, V. B. Sobolev and A. I. Kholodnykh "Investigation of the spectral and energy characteristics of a pulsed optical parametric oscillator operating in the regime of external signal injection" Sov. J. Quantum Electron., 14, 538, (1984)

[8] D. C. Hovde, J. H. Timmermans, G. Scoles and K. K. Lehmann "High power injection seeded optical parametric oscillator" Opt. Commun., 86, 294, (1991)

[9] J. G. Haub, M. J. Johnson, B. J. Orr and R. Wallenstein "Continuously tunable, injection-seeded β-barium borate optical parametric oscillator: spectroscopic applications" Appl. Phys. Lett., 58, 1718, (1991)

[10] A. Fix, G. Goeritz, R. Urschel, D. Wildt, A. Borsutzky and R. Wallenstein "Single-mode optical parametric oscillator system of BBO and $KNbO_3$ tunable from the visible (0.42 μm) to the infrared (4 μm)" OSA Proc. on Advanced Solid State Lasers 20, 458, (1994)

[11] S. J. Brosnan and R. L. Byer "Optical parametric oscillator threshold and linewidth studies" IEEE J. Quantum. Electron., 15, 415, (1979)

[12] S. Burdulis, R. Grigonis, A. Piskarskas, S. Sinkevicius, V. Sirutkaitis, A. Fix, J. Nolting and R. Wallenstein "Visible optical parametric oscillation in synchronously pumped beta barium borate" Opt. Commun., 74, 398, (1990)

[13] A. Piskarskas, V. Smilgevicius, A. Umbravas, A. Fix and R. Wallenstein "Parametric oscillation in beta barium borate synchronously pumped by the third harmonic of a continuously excited mode-locked and Q-switched Nd:YAG laser" Opt. Commun., 77, 335, (1990)

[14] W. R. Bosenberg and C. L. Tang "Type II phase matching in a β-barium borate optical parametric oscillator" Appl. Phys. Lett., 56, 1819, (1990)

[15] M. G. Littman and H. J. Metcalf "Spectrally narrow pulsed dye laser without beam expander" Appl. Opt., 17, 2224, (1978)

[16] I. Shoshan, N. N. Danon and U. P. Oppenheim "Narrowband operation of a pulsed dye laser without intracavity beam expansion" J. Appl. Phys., 48, 4495, (1977)

[17] E. Hecht "Optics" Second edition, Addison-Wesley, 429, (1987)

[18] M. G. Littman "Single-mode operation of a grazing-incidence pulsed dye laser" Opt. Lett., 3, 138, (1978)

[19] I. Shoshan and U. P. Oppenheim "The use of a diffraction grating as a beam expander in a dye laser cavity" Opt. Commun., 25, 375, (1978)

[20] M. G. Littman "Single-mode pulsed tunable dye laser" Appl. Opt., 23, 4465, (1984)

[21] K. W. Kangas, D. D. Lowenthal and C. H. Muller III "Single-longitudinal-mode, tunable, pulsed Ti:sapphire laser oscillator" Opt. Lett., 14, 21, (1989)

[22] T. D. Raymond, P. Esherick and A. V. Smith "Widely tunable single-longitudinal-mode pulsed dye laser" Opt. Lett, 14, 1116, (1989)

[23] W. R. Bosenberg, W. S. Pelouch and C. L. Tang "High-efficiency and narrow-linewidth operation of a two-crystal β-BaB_2O_4 optical parametric oscillator" Appl. Phys. Lett., 55, 1953, (1989)

[24] W. R. Bosenberg, D. R. Guyer and S. E. Moody "Single-frequency optical parametric oscillator" OSA Proc. on Advanced Solid State Lasers, 13, 343, (1992) and Appl. Phys. Lett., 61, 387, (1992)

[25] Private communication with Professor Wim Hogervorst, consultant to Spectra-Physics Lasers Ltd, 1994

[26] Private communication with Dr. Walter Bosenberg, August 1994

[27] V. D. Volosov, A. G. Kalintsev, V. N. Krylov "Degenerate parametric processes during three-wave interactions in crystals arranged in series" Pis'ma. Zh. Tekh. Fiz., 2, 85, (1976)

[28] P. G. Kryukov, Yu. A. Matveets, D. N. Nikogosyan and A. V. Sharkkov "Tunable double-channel ultra-short pulse optical oscillator" Sov. J. Quantum Electron., 8, 1319, (1978)

[29] D. Eimerl, L. Davis, S. Velsko, E. K. Graham and A. Zalkin "Optical, mechanical, and thermal properties of barium borate" J. Appl. Phys., 62, 1968, (1987)

Chapter 7

Single-mode Grazing Incidence OPO

This chapter is divided into two parts. The first part investigates the grazing incidence OPO (GIOPO) pumped with an injection seeded, single-axial mode Nd:YAG laser in an attempt to secure single-mode operation in the OPO. Owing to the absence of such a laser in our laboratories, the GIOPO was dispatched and reconstructed at the Vrije Universiteit, Amsterdam where a Spectra-Physics GCR-3 injection-seeded Nd:YAG laser was available with a 90 MHz single-longitudinal mode (SLM). Using the dual-crystal configuration, the mode structure of the OPO is studied as a function of grating angle. Single-longitudinal mode is demonstrated in the OPO at visible wavelengths at a high degree of grazing incidence, although mode-hopping was observed.

In the second part, a new cavity design is presented which is based on the grazing incidence technique but involves an additional mirror, forming a coupled cavity. The extra constraints imposed by the mirror ensure reliable, single-longitudinal mode operation without any cavity length control for several minutes. The results of this cavity are presented, including a mathematical prediction of the coupled cavity mode spacing.

7.1 Experimental Configuration of the GIOPO

As reducing the pump bandwidth from 28 GHz to 7.5 GHz increased the operational threshold of the GIOPO, so the threshold rose again when the device was pumped with a single-axial mode pump source. The threshold, in fact, doubled, under identical operating conditions, from 27 MW/cm^2 at 28 GHz to 53 MW/cm^2 at 90 MHz SLM. As a result, rather than pumping the GIOPO harder to the extent of risking damage to the back mirror of the cavity, a dye amplifier was constructed to increase the power of the OPO signal so that spectral diagnostics could be reliably performed. Our intention

was not, however, to investigate the performance of the amplifier but simply the characteristics of the oscillator. A schematic of the oscillator/amplifier is found in figure 7.1.

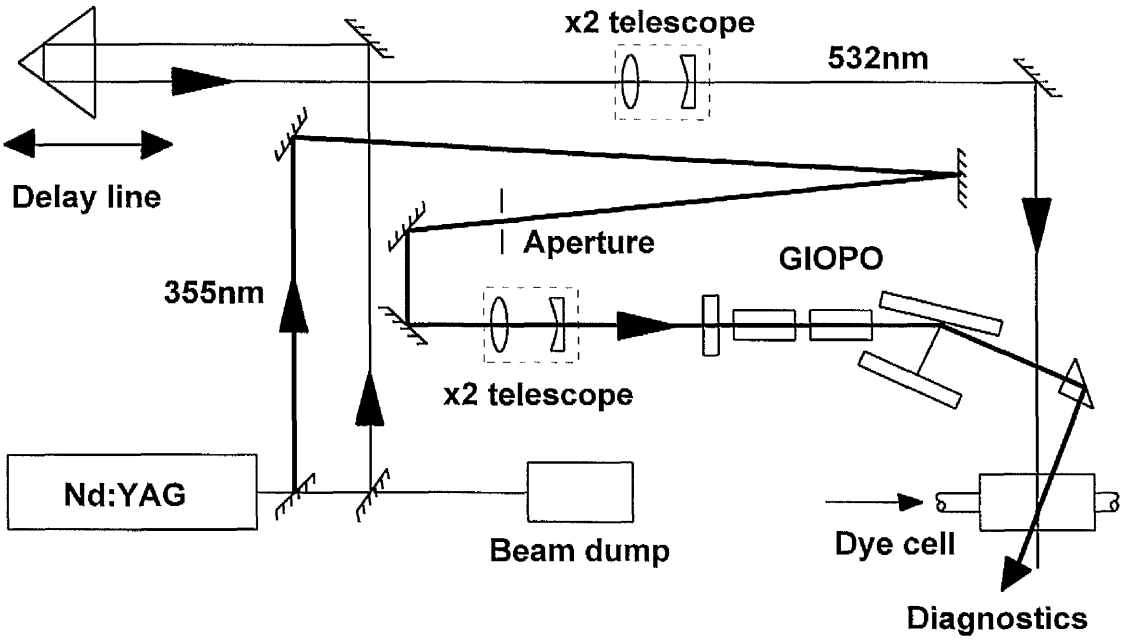

Figure 7.1. Schematic diagram of the grazing incidence OPO pumped with an injection-seeded Nd:YAG laser at 355 nm with the signal energy enhanced using a dye amplifier.

Beyond the laser head, the second and third harmonics of the Nd:YAG laser were separated using a dichroic mirror and the fundamental was directed into a beam dump. The third harmonic underwent several reflections to maximise its path length before being directed into the GIOPO. Over a distance of four and a half metres, the beam diameter had expanded sufficiently to allow an unwanted portion of the beam, separate from the main Gaussian lobe and clearly visible to the eye, to be removed by spatial aperturing. This strategy prevented the beam from forming two hot-spots when brought to a focus (one from the Gaussian lobe and one from the unwanted portion) and reduced the chances of crystal or mirror surface damage. Using a x2 telescope (described in the previous chapter), the beam was contracted to 2.5 mm in diameter at the $1/e^2$ points before being directed into the GIOPO. The second harmonic (532 nm)

was used to longitudinally pump a dye cell of DCM 640, having been contracted using a x2 telescope and temporally delayed by a 90° prism delay line to ensure the OPO signal and the 532 nm pulses arrived at the cell simultaneously. DCM 640 has a fluorescence range spanning 600 nm to 680 nm when pumped at 532 nm. The DCM dye amplifier increased the output energy of the OPO by an order of magnitude, which was ample for diagnostic measurements. The grazing incident OPO was identical in every way to the dual-crystal cavity described in the previous chapter.

7.1.1 Threshold and Efficiency

At a grazing angle of α=88°, the threshold of the GIOPO was 15.5 mJ/pulse (53 MW/cm^2). This result can be compared directly with the threshold measurement for the 28 GHz-pumped dual-crystal GIOPO of 8 mJ/pulse (27 MW/cm^2). Explanation of the observed decrease in threshold when the laser is in unseeded operation may lie with the increase in laser amplitude instability observed, leading to the occurrence of high peak intensities from time to time.

As the grazing angle was increased, the threshold rose as observed in the broadband-pumped GIOPOs. In figure 7.2, the threshold of the 90 MHz pump grazing incidence OPO is shown as a function of grazing angle, α. The threshold is seen to increase dramatically at grazing angles greater than 89.2°, corresponding with the sharp fall in diffraction efficiency of the grating at high angles of incidence. This presented a potential problem, since it became apparent that very high degrees of incidence were required to obtain a single-longitudinal mode in the OPO, thus requiring high pump fluences near the damage threshold of the back mirror. Additionally, the internal conversion efficiency became correspondingly low at such high degrees of incidence. The pump depletion is shown in figure 7.3 at three grating angles.

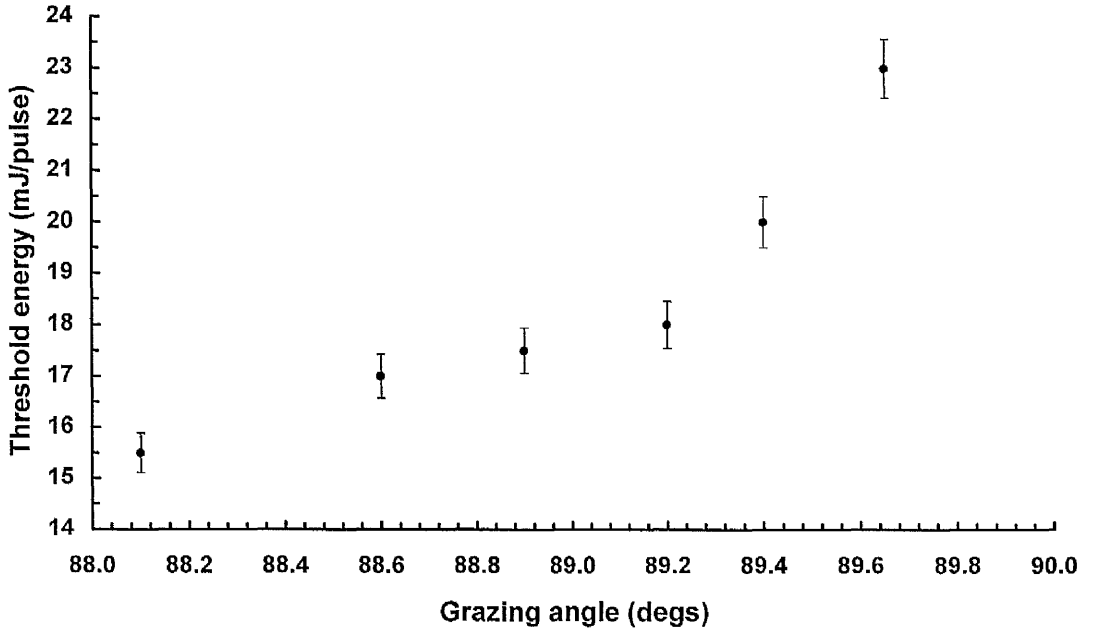

Figure 7.2. Threshold fluence as a function of grazing angle, α, for the GIOPO pumped with the 90 MHz source.

The pump depletion measurements were carried out using two fast-risetime (0.5 ns) photodiodes positioned before and after the GIOPO. The first photodiode detected part of the pump light incident on the OPO and the second detected the depleted pump light when the OPO was operational.

The temporal traces from both the photodiodes were recorded simultaneously and observed on a LeCroy 9360 600 MHz oscilloscope. Each figure in 7.3 shows the trace of both the photodiodes superimposed, at different grazing angles. The dark region is the depleted portion of the pump pulse and is a measure of the internal efficiency of the GIOPO.

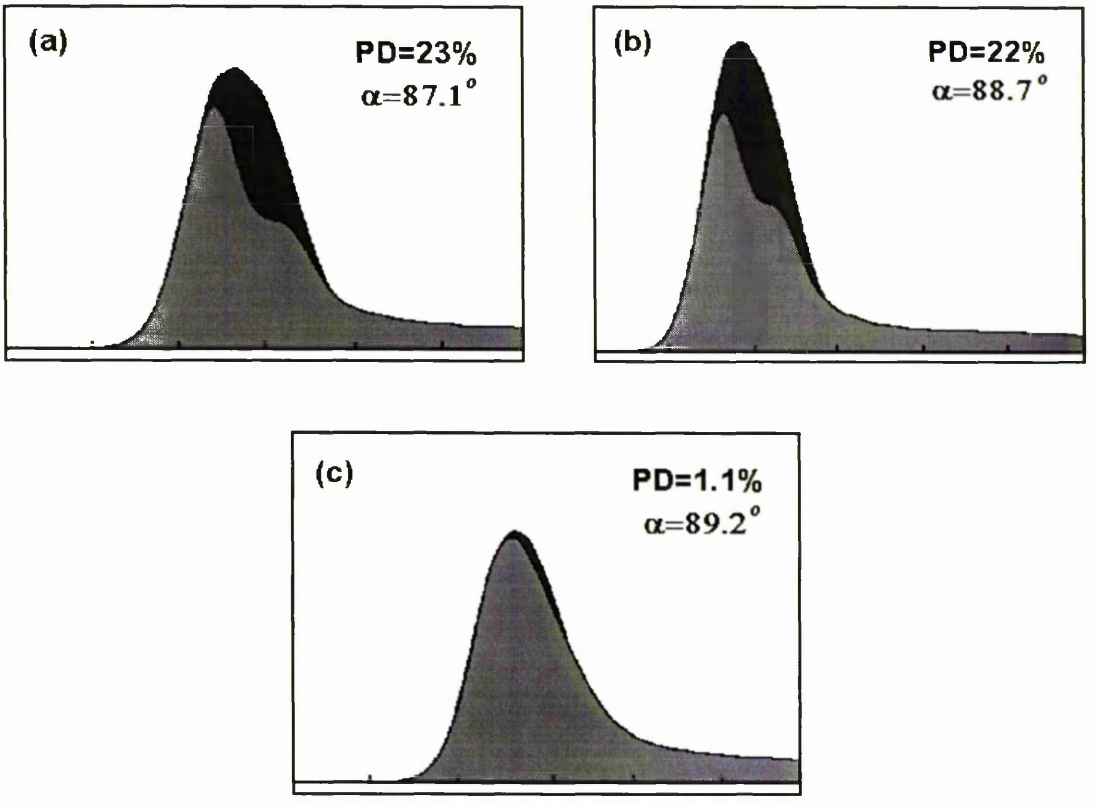

Figure 7.3. Pump depletion traces from the 90 MHz-pumped GIOPO at grazing angle α of (a) 87.1° with a pump depletion of 23 %, (b) 88.7° with a pump depletion of 22 % and (c) 89.2° with a pump depletion of 1.1 %. Time base is 2.5 ns/division.

The percentage pump depletion is calculated by taking the quotient of the depleted area (dark portion) and the total area under the undepleted trace (light and dark areas together). Each trace is averaged over 100 shots. Clearly, the efficiency of the GIOPO decreases rapidly as the grazing angle reaches 89.2°, which results from the fall in grating diffraction efficiency. These results can be compared directly with those of the 28 GHz-pumped GIOPO present in figure 6.2 of the previous chapter. Greater pump depletion was observed with the seeded pump laser, in general, although at 89.2° the broad band pumped OPO is slightly more efficient. However, at such high degrees of grazing incidence, the efficiency of the GIOPO was found to be critically dependent on the cavity alignment and crystal positioning. Thus, a degree of error is inevitable in such a lossy cavity configuration and a direct comparison must be treated with some

caution. Certainly, the pump pulse is more heavily depleted at smaller grazing angles when the pump source is seeded.

The reason for this may result from the relative bandwidths of the sources and the linewidths they generate from the GIOPO: in the case of the 90 MHz source, the generated GIOPO linewidth is greater than that of the pump source and is limited mainly by the cavity bandpass, whereas in the case of the 28 GHz source, the reverse is true and the linewidth is limited by the bandwidth of the pump source. For a given grazing angle, therefore, the seeded source produces a narrower range of signal frequencies, a high proportion of which are able to resonate in the cavity. In the unseeded case, on the other hand, a greater spread of signal frequencies are generated by virtue of the large pump bandwidth, but a significant proportion are outside the bandpass of the cavity. This leaves fewer resonant photons available to deplete the pump pulse.

7.1.2 Spectral Analysis

The analysis of the spectral output of the signal from the grazing incidence OPO was carried out at 620 nm using etalon B of the PLSA, previously described in section 6.7. This etalon had a free spectral range of 10 GHz and finesse of 50, giving a resolution of 200 MHz. This resolution enabled the number of resonant cavity modes in the GIOPO to be resolved as a function of the grazing angle α.

The following figures show the intensity pattern through the centre of the ring pattern of etalon B. At a grazing angle of 88.1°, the number of GIOPO cavity modes was found to vary between 5 and 7. Figure 7.4 shows a typical single shot of the mode structure.

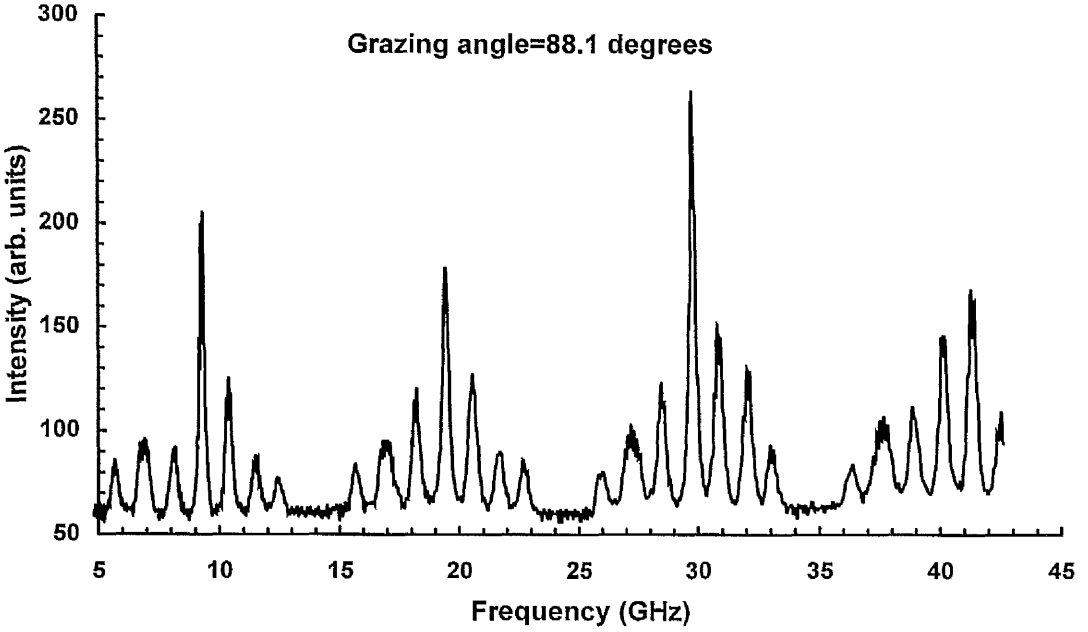

Figure 7.4. Intensity pattern through the centre of the etalon ring pattern for the grazing angle of 88.1°. Seven longitudinal modes are resonant.

Figures 7.5 to 7.8 show the number of modes resonant in the GIOPO cavity as the grazing angle is increased.

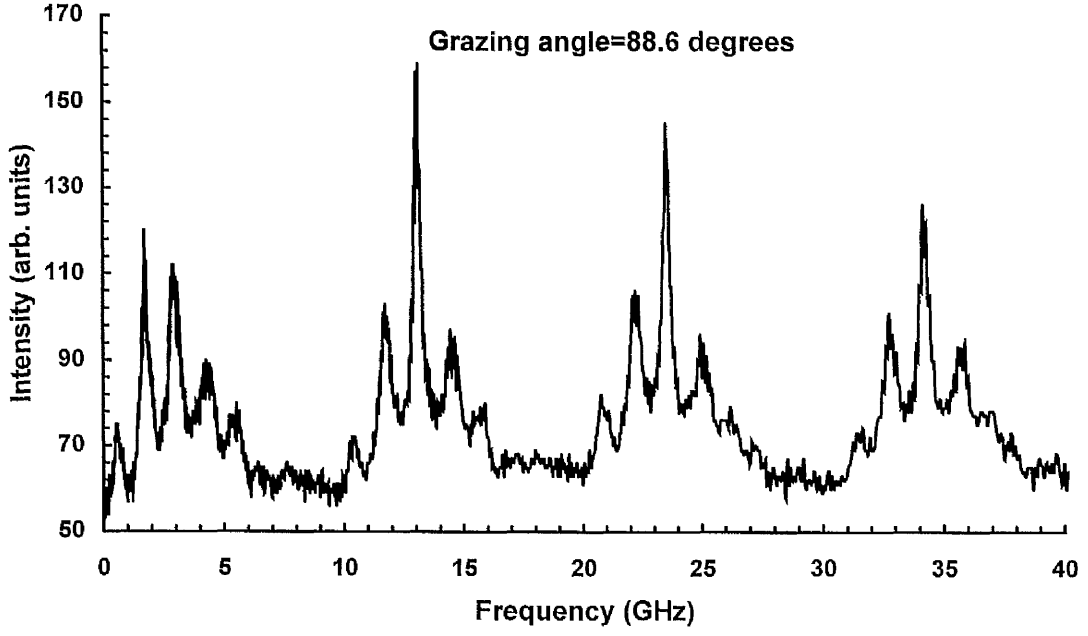

Figure 7.5. Intensity pattern through the centre of the etalon rings for the grazing angle of 88.6°.

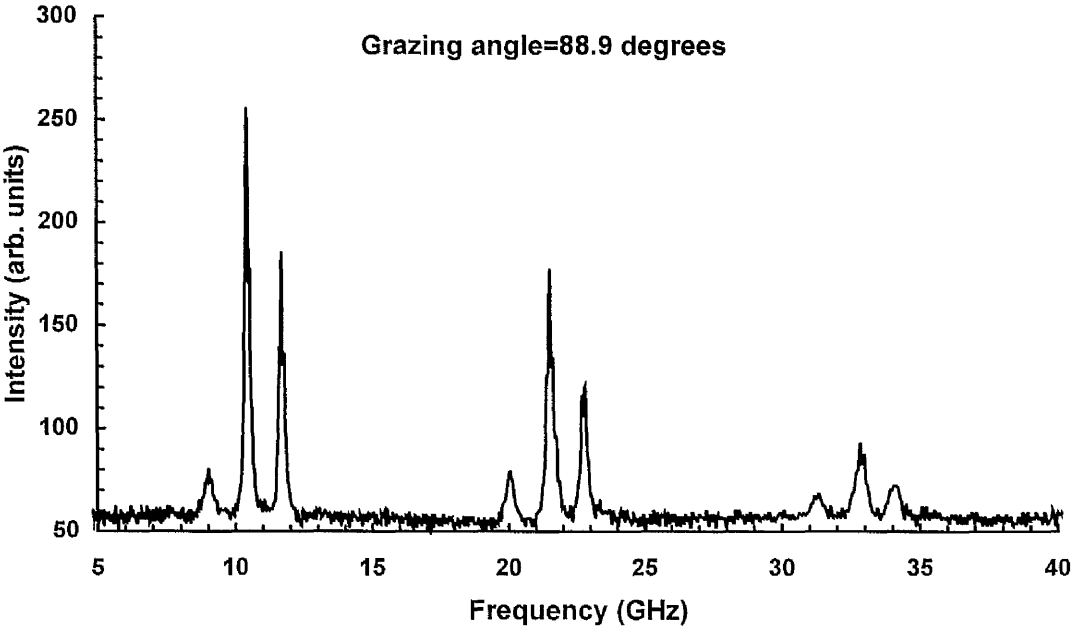

Figure 7.6. Intensity pattern through the centre of the etalon rings for the grazing angle of 88.9°. Two to three longitudinal modes are present.

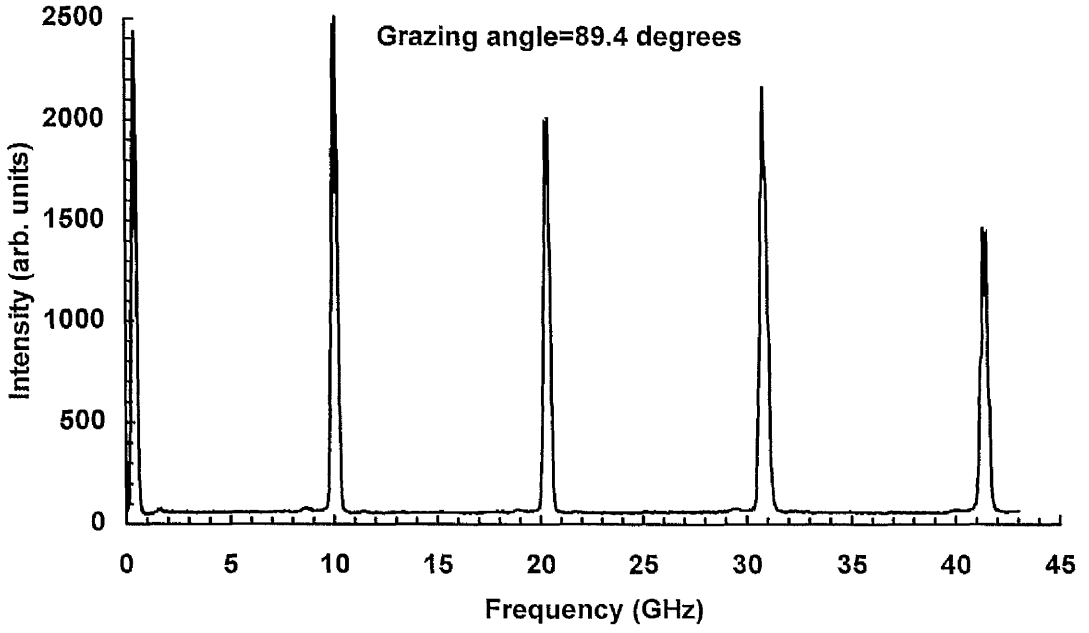

Figure 7.7. Intensity pattern through the centre of the etalon rings for the grazing angle of 89.4°. Single-longitudinal mode operation.

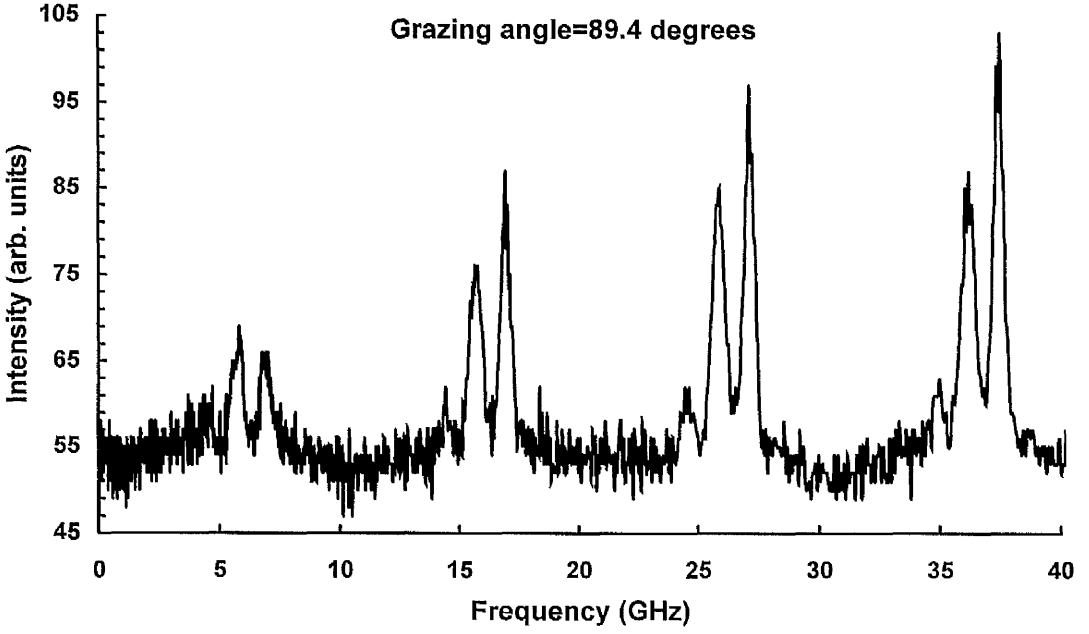

Figure 7.8. Intensity pattern through the centre of the etalon rings for the grazing angle of 89.4°. Two longitudinal modes are present.

The number of modes decreased, as the grazing angle increased from 3 to 4 at 88.6°, to 2 to 3 at 88.9° to a single-longitudinal mode, at 89.4°. The single-mode was not stable although a single-mode could be maintained for a period of several seconds. However, mode-hopping between two adjacent modes was observed during this period. After this period, two modes were frequently seen (see figure 7.8) for a similar duration before returning to a single-mode. This behaviour would occur with no alteration to the cavity or crystals. A further increase in the grazing angle was made to 89.7°, at which point the GIOPO was almost at threshold. No improvement to the mode stability was observed and the near-threshold operation worsened the amplitude stability of the GIOPO. From figures 7.7 and 7.8, it is seen that the high intensity pulses are single-mode in nature, whilst the low intensity pulses are dual mode.

The observed instability of the mode is thought to be a result of a combination of small fluctuations of the intensity of the laser, a long cavity length resulting in a narrow mode spacing and mechanical instability of the GIOPO cavity. The first two, we

believe, were dominant for the following reasons; the 1 GHz longitudinal-mode spacing of the GIOPO was small enough to allow two modes to fall under the gain profile when a small increase in pump pulse intensity was observed. However, a reduction of more than 10 % the cavity length was not possible because of the physical length of the cavity components and the manner in which they were mounted. To this end, another strategy was sought, which is presented in the next part of this chapter.

7.1.3 Summary

The grazing incidence BBO OPO has been pumped using a single-longitudinal mode, injection seeded Nd:YAG laser and the signal output amplified using a single dye power amplifier. Pump depletion and the number of resonant longitudinal modes in the cavity have been studied as a function of grazing angle, α. At high values of α (89.4°), unstable, single-longitudinal mode operation was observed in the GIOPO. Table 7.1 summarises the dependence of the number of modes on α.

Angle (°)	88.1	88.6	88.9	89.4	89.7
N⁰. of modes	5-7	3-4	2-3	1-2	1-2

Table 7.1. Summary of the dependence of the number of cavity modes on the grazing angle α.

Pump depletion measurements shown an internal efficiency of 1.1 % at high grazing angles of 89.2°, increasing to >20 % at angles of 88.7°.

7.2 1800 lines/mm Diffraction Grating GIOPO

Although single-longitudinal mode operation has been achieved in a passive OPO cavity, the grazing angle is so large that the threshold is unacceptably high. Moreover, it was felt that the cavity mode spacing was too small making stable, SLM operation unlikely. It was felt, therefore, that rather than taking further steps to try to reduce the threshold and stabilise the mode, the cavity length would need to be reduced considerably to ensure that only one mode fell under the gain profile of the OPO. Reverting back to the single-crystal design with the injection-seeded laser was not an option, since the OPO was already at threshold with the 7.5 GHz source. The new strategy adopted was to replace the 2400 lines/mm grating with an 1800 lines/mm holographic element, whose diffraction efficiency is known to be higher, and to return to the single-crystal design. The hope was that the increase in the diffraction efficiency of the 1800 l/mm grating would compensate, to some extent, for the reduced gain of the single-crystal configuration, sufficiently for the device to reach threshold.

The 1800 lines/mm, single crystal cavity was constructed from the dual-crystal OPO by simply replacing the grating and making a slight design change to the crystal holders so that only one crystal was incorporated in the cavity. The efficiency measurements are shown below in table 7.2.

Grating identification	Ist order efficiency %
NPL	14.5
Optometrics #1	9.4
Optometrics #2	10.0
Optometrics #3	8.9

Table 7.2. First order diffraction efficiencies for four holographic 1800 lines/mm gratings at an 88° grazing angle.

The first order diffraction efficiency of the 1800 lines/mm gratings available in the laboratory were determined in the same manner as has been previously described in section 6.6 using a low power He-Ne laser. The NPL grating, having the greatest first order diffraction efficiency, was selected and installed in the cavity. It had a zero order reflection coefficient of 60 % at 88° grazing angle at 633 nm. The potential tuning range of the 1800 l/mm grazing incidence cavity spans a different range to the 2400 l/mm, as a result of the higher periodicity. At grazing incidence, the tuning range varies from 633 nm to 1 μm limited by the rotation range of the tuning mirror.

7.2.1 Coupled Grazing Incidence Cavity

In chapter six, the alignment of the GIOPO was described and the technique included the use of a glass-slide as an intermediate output coupler to enable the crystal to be correctly positioned before the tuning mirror was introduced. The glass-slide was subsequently removed. It was noticed†, however, that the 1800 lines/mm grazing incidence OPO had significantly fewer modes when the glass-slide was left in its alignment position, forming a coupled cavity. Further adjustment to its position lead to single-mode operation of the OPO. This phenomenon resulted from the longitudinal modes having to satisfy the resonant conditions of both the original grazing incidence and the new linear cavities. The linear cavity consisted of the back mirror and the glass slide, via a reflection from the grating. The additional constraints imposed on the cavity modes meant that one mode would be resonant under the coupled cavity whereas, under otherwise identical conditions, two or more were resonant in the conventional GIOPO.

A schematic diagram of the coupled cavity is presented in figure 7.9. It consists of a single BBO crystal cut for type I phase matching (e→o+o) with dimensions of 4x6x14 mm^3.

† by J. M. Boon-Engering

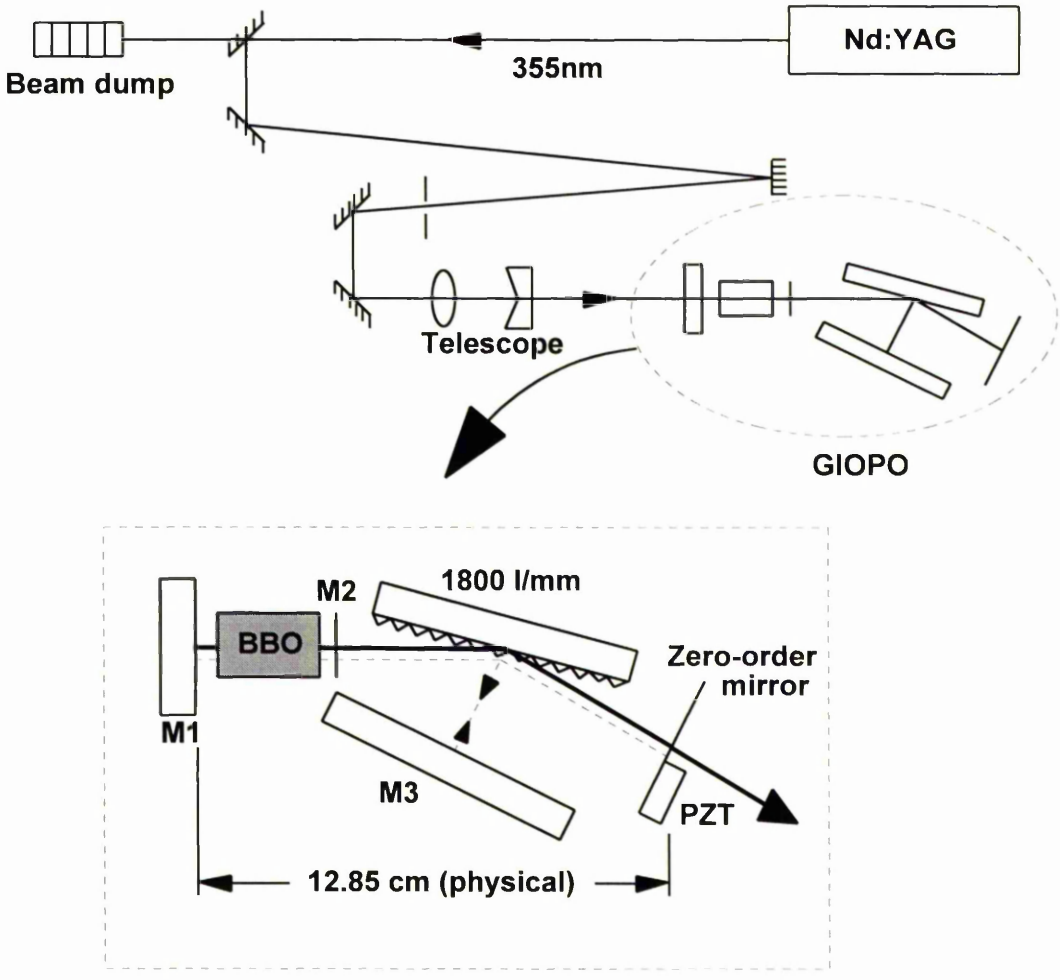

Figure 7.9. Schematic diagram of the coupled cavity OPO. 355 nm pump light is directed into the OPO after beam contraction and aperturing. In the detail: M1 is HR at 570 nm-700 nm, M2 is HR at 355 nm and is AR coated in the visible, M3 is the tuning mirror and the zero-order mirror is mounted on a PZT and forms the coupled cavity.

The pump beam is apertured to remove a spatial defect (as described in section 7.1) and is telescoped to a ($1/e^2$) diameter of 2.5 mm before being launched into the GIOPO. The cavity optics forming the GIOPO were the same elements used in the experiments described earlier in this chapter and chapter six, with a back mirror of reflectivity 570 nm to 700 nm. The additional mirror, a glass-slide, was positioned to couple back a proportion of the zero order output and was mounted on a piezoelectric transducer normal to the cavity output to allow for small adjustments to be made to the

cavity length. The glass-slide had a reflectivity of 4 % at the resonant signal wavelength. The coupled cavity was pumped at 355 nm using a 10 Hz repetition rate, 6 ns pulse duration injection seeded Nd:YAG laser with a single-axial mode linewidth of 90 MHz (Spectra-Physics GCR-4).

7.2.2 The Performance of the Coupled Cavity

For the relatively small grazing angle of 88.6°, the coupled cavity OPO was found to operate SLM with a linewidth of 210±70 MHz, as shown in figure 7.10, and was able to remain in this condition for several minutes without any cavity detuning. After, typically, 5 minutes had elapsed, a second mode would begin to appear, although it took several more minutes before two modes of comparable intensity were observed. By adjusting the cavity length using the piezoelectric transducer on the zero-order mirror, the cavity could easily be returned to SLM operation.

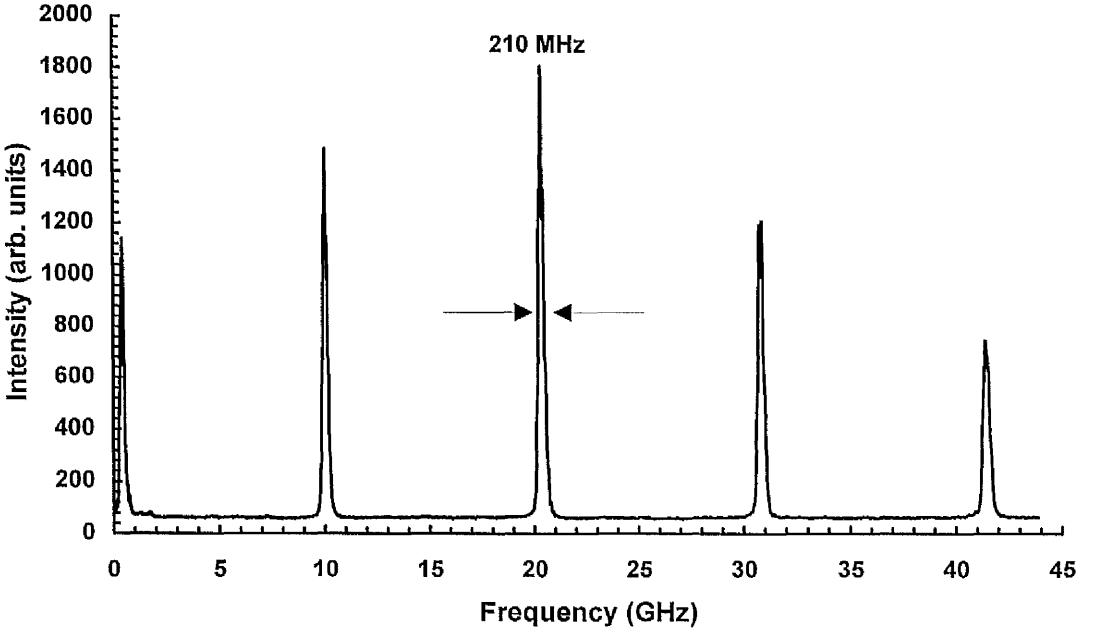

Figure 7.10. Transmission peaks through the centre of the ring pattern of a 5 mm thick etalon capable of resolving 200 MHz. Single-longitudinal mode is recorded with a (FWHM) linewidth of 210 MHz.

Without the constraints imposed on the cavity by the zero order mirror, the OPO operated at all times on two cavity modes. Moreover, with the zero order mirror in position, the external efficiency of the device dramatically improved and the operational threshold reduced as a result of the additional coupling. A threshold of 32 mJ was recorded (Scientech AC 2501) without the coupled cavity mirror, which fell to 25.5 mJ when the mirror was introduced. A corresponding increase in the signal output was observed from 0.07 mJ to 0.5 mJ (Scientech 360001) at a pumping intensity of 39 mJ. This accords with an increase in the external efficiency from 0.18 % to 1.3 %.

Experimentally, it was found that in order for SLM operation to be observed, the reflectivity of the zero order mirror needed to be chosen with some care. When zero-order optics with reflectivities of >10 % where used, the coupled cavity became increasingly less frequency-selective as the linear cavity became dominant. With a 20 % reflectivity, the coupled cavity became consistently multimode. Clearly, the linear cavity loss needs to be controlled by the reflectivity of the zero-order mirror so that its resonance does not overwhelm that of the lossy GIOPO cavity. The coupled cavity OPO was tunable from 580 nm to 690 nm (measured using an Optometrics digital mini-chrom monochromator DMC 1-03), which was predominantly limited by the reflectivity of the back mirror.

7.2.3 The Resonance Condition

The coupled cavity cannot be thought of as a linear cavity seeded by the retro-reflected first order diffraction of the grating. If this were the case, the mode spacing would be determined by the optical length between M1 and the zero-order mirror (see figure 7.9). This is not what is observed experimentally. Nor can the mode spacing be predicted by the conventional GIOPO cavity alone. The mode spacing can be found

accurately by considering the coupled cavity OPO as a Michelson-mirror cavity [1], where a Michelson interferometer is used as a complex reflector. A mathematical description has been developed here using a similar procedure employed by Smith [2] in which the mode spacing for a Fox-Smith cavity is presented. To maintain the generality of the model, the calculation presented here assumes the use of a beam-splitter in a Michelson-mirror cavity whose transmission and reflection properties are later changed to represent the features of the diffraction grating in the GIOPO.

Figure 7.11 shows a schematic of a Michelson-mirror cavity. A wave $e^{i\omega t}$ incident from the left in figure 7.11 on to the beam-splitter M2 will divide into the Michelson arms towards mirrors M3 and M4 with an intensity ratio determined by the reflectivity of M2.

The waves returning to the mirror M2 following subsequent reflections from M3 and M4 will recombine to form

$$e^{i\omega t}\left[\tau_2^2\rho_3 e^{\frac{4\pi i L_2}{\lambda}} + \rho_2^2\rho_4 e^{\frac{4\pi i L_3}{\lambda}}\right] \qquad (7.1)$$

where ρ_i and τ_i are, respectively, the electric field reflection and transmission coefficients of the mirror M_i and λ is the wavelength of the wave. If the gain medium in arm L_1 has a round trip electric field gain g, then the wave *returning* to mirror M_2 will be given by the left-hand side of equation 7.2. For self-consistency, this wave must be equal to the initial wave considered. Hence

$$e^{i\omega t}\left[\tau_2^2\rho_3 e^{\frac{4\pi i L_2}{\lambda}} + \rho_2^2\rho_4 e^{\frac{4\pi i L_3}{\lambda}}\right]\rho_1 e^{\frac{4\pi i L_1}{\lambda}} g = e^{i\omega t} \qquad (7.2)$$

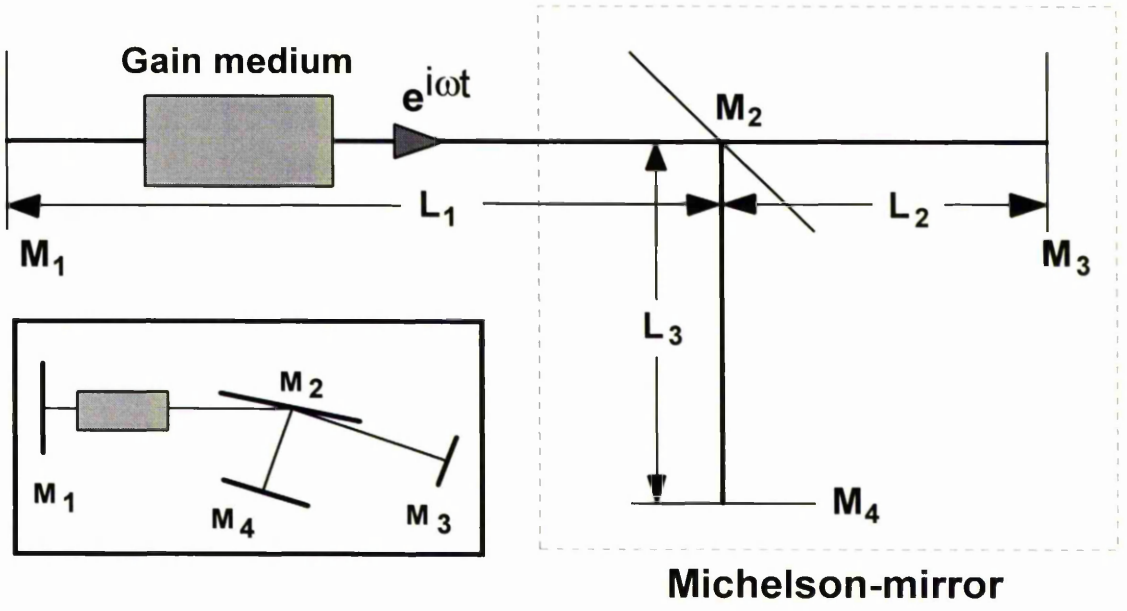

Figure 7.11. A schematic of a Michelson-mirror cavity. The lengths of each arm from their respective mirrors to the beam-splitter M2 are indicated. The inset shows how the Michelson cavity can be related to the GIOPO coupled oscillator.

The requirement that the gain be real gives the resonance condition of the cavity. From equation 7.2 then, we state that the imaginary part of the gain must be zero. To simplify the calculation, the various parts of equation 7.2 have been re-assigned letters as follows:

$$g = \left[\tau_2^2 \rho_3 e^{\frac{4\pi i l_2}{\lambda}} + \rho_2^2 \rho_4 e^{\frac{4\pi i l_3}{\lambda}} \right]^{-1} \rho_1^{-1} e^{-\frac{4\pi i l_1}{\lambda}} \qquad (7.3)$$

a b c d f h

where b, d and h are the exponents positioned directly above the letters and a, c and f are the electric field reflectivity expressions. By multiplying the top and bottom of equation 7.3 by e^{-ih}, the following expression for the gain is formed

$$g = \frac{e^{-ih}\left(a \cdot e^{-ib} + c \cdot e^{-id}\right)}{f\left(a^2 + c^2 + ac \cdot e^{i(b-d)} + ac \cdot e^{-i(b-d)}\right)} \qquad (7.4a)$$

where the real part, Re(g), is given by

$$\mathrm{Re}(g) = \frac{\tau_2^2\rho_3\cos\frac{4\pi}{\lambda}(L_2+L_1) + \rho_2^2\rho_4\cos\frac{4\pi}{\lambda}(L_3+L_1)}{\rho_1\left(\tau_2^4\rho_3^2 + \rho_2^4\rho_4^2 + 2\rho_2^2\rho_4\tau_2^2\rho_3\cos\frac{4\pi}{\lambda}(L_2-L_3)\right)} \qquad (7.4b)$$

The denominator of equation 7.4 a is real. Therefore, in order for the imaginary part to be zero, the imaginary part of the numerator must be zero. Setting the imaginary part to zero yields

$$a\sin(b+h) + c\sin(d+h) = 0 \qquad (7.5)$$

re-substituting $$\tau_2^2\rho_3\sin\left[\frac{4\pi}{\lambda}(L_1+L_2)\right] = -\rho_2^2\rho_4\sin\left[\frac{4\pi}{\lambda}(L_1+L_3)\right]$$

This is the resonance condition of the cavity. To find the resonances of the coupled cavity OPO, the beam-splitter is "replaced" by the grating, taking the transmission of the beam-splitter as the zeroth order reflection of the grating and its reflection as the first order diffraction. The inset of figure 7.11 shows how the model relates the arms created by the beam-splitter to those of the grating. The measured reflection and transmission properties of the grating are substituted into equation 7.5 along with the lengths of the coupled cavity arms. The power reflection and transmission coefficients of the variables required for equation 7.5 are shown in table 7.3, with a description of the cavity optic and the variable symbols.

Description of optic	**1st order diffraction**	**Zero order reflection**	**"Zero-order" mirror reflection**	**Tuning mirror reflection**
Variable	ρ_2	τ_2	ρ_3	ρ_4
Power reflect./trans.	10 %	60 %	4 %	98 %
Value for equation 7.5	0.1	0.6	0.04	~1

Table 7.3. Variable values required for equation 7.5 are shown in the last row. The power reflection/transmission of the coupled cavity optics are also shown (these have been measured and discussed in the text) and the variable symbol and the optic to which it refers are included for clarity.

The arms of the coupled cavity OPO were measured using a vernier calliper and were found to be L_1= 4.50 cm (physical length), L_2 = 8.35 cm and L_3= 1.00 cm. By plotting the two sides of the resonance condition as a function of frequency, υ, the solutions to equation 7.5 can be found by the intersections of the two functions, as shown in figure 7.12 by the *solid* lines. The x-axis is not the actual frequency of the OPO, but a relative frequency scale. We can consider the zero frequency as the "single-mode" frequency, and the next solution as the mode spacing if the OPO is operating multimode. However, finding the next solution requires further steps to be taken.

Half of the solutions to equation 7.5 can be rejected as they have negative electric field gain. To determine which have negative electric field gain, the real part of the gain, g, is evaluated (equation 7.4b) and plotted against frequency shown in figure 7.13. By considering the frequency associated with each solution in figure 7.12, the sign of the gain at that frequency can be found.

It is seen that the first intersection has positive gain (at υ=0), the next solution has negative gain, the following positive and so on. Each positive-gain solution is indicated in the figure by a filled circle. Clearly, there are still several possible solutions. To determine which of the positive-gain solutions predicts the coupled cavity mode spacing, the fractional loss L for each solution has been calculated using equation 7.6 below. The solution whose loss is at a minimum can be expected to be the resonant mode in the cavity. The fractional loss, L [2], is given by

$$L = 1 - \frac{1}{G} \tag{7.6}$$

where the power gain, $G = gg^*$ and is given by

$$G = \frac{1}{\rho_1^2\left(\tau_2^4\rho_3^2 + \rho_2^4\rho_4^2 + 2\rho_2^2\rho_4\tau_2^2\rho_3\cos\frac{4\pi}{\lambda}\left(L_2 - L_3\right)\right)} \tag{7.7}$$

The loss as a function of frequency is also included in figure 7.12 (dotted line) and the loss associated with each solution can be read-off the right-hand axis.

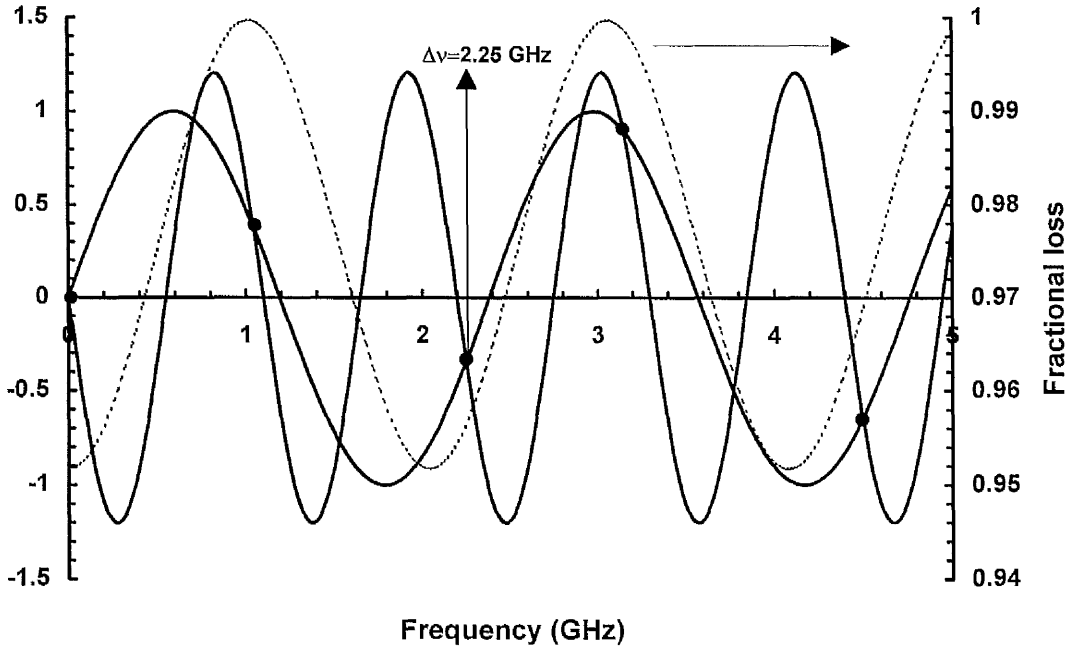

Figure 7.12. Solid lines are the functions shown in equation 7.5. The intersections are solutions to the equation. The intersections marked with a filled circle are those solutions which correspond to positive gain (see next figure). From the dotted line, the loss associated with each solution can be found.

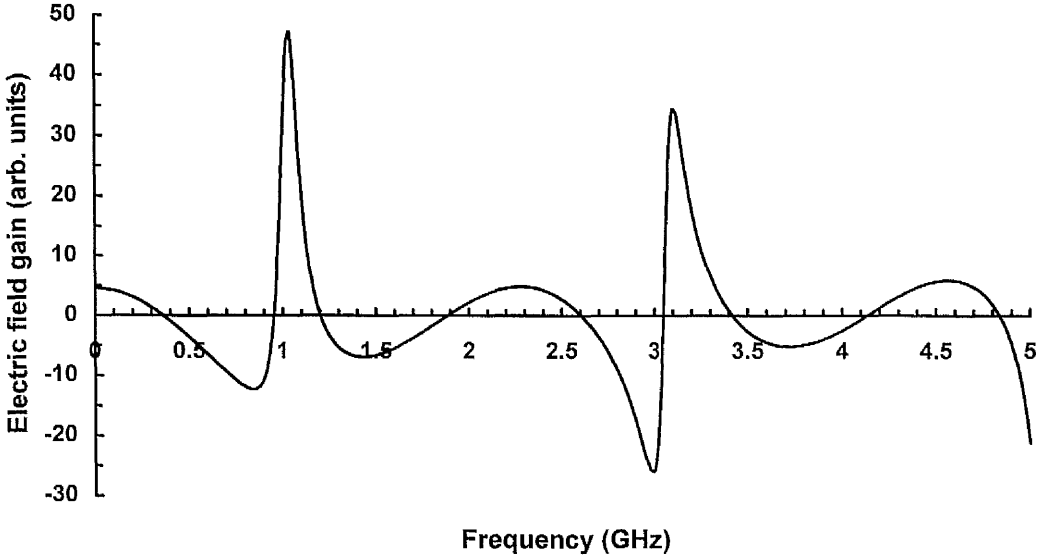

Figure 7.13. The gain, g, as a function of frequency. Only solutions to the resonance condition with positive gain can resonate in the cavity. At Δν=2.25 GHz, the gain is real.

The least-lossy solution is given by 2.25 GHz. The next solution is at 4.5 GHz, precisely double the first solution's frequency. The model, therefore, predicts a mode spacing of 2.25 GHz when the coupled cavity OPO is multi-mode. Experimentally, by changing the grating angle to 87°, multimode operation was seen with a mode spacing of 2.25 GHz, precisely as predicted by the model. Figure 7.14 shows the multimode spectrum of the signal, with a longitudinal mode spacing of 2.25 GHz. A similar analysis was carried out at a different linear cavity length, and the theory predicted the mode spacing to within 5%.

On removal of the zeroth order mirror, the mode spacing of the grazing incidence cavity alone was found to be 2.4 GHz, which further demonstrates the existence of cavity coupling. Furthermore, by varying the lengths of the different arms of the cavity, the mathematical description presented here is able to predict the change in mode spacing observed.

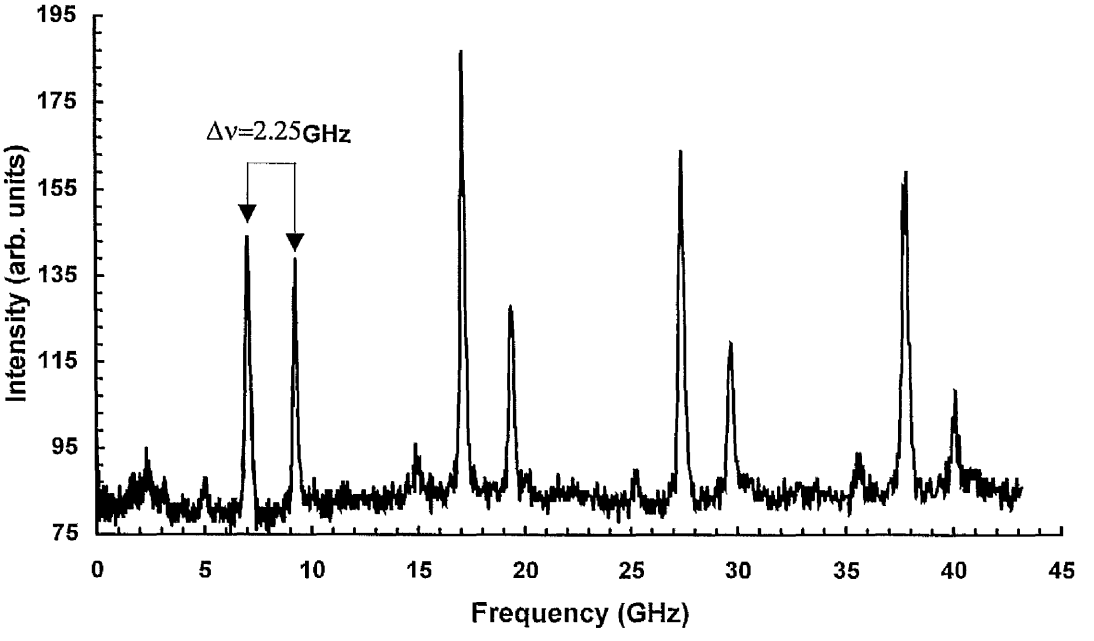

Figure 7.14. Coupled cavity grazing incidence OPO in multimode operation at a grazing angle of 87°. The mode separation is 2.25 GHz.

This cavity geometry differs considerably from the more general case where the reflectivities of the mirrors are $\rho_1=\rho_3=\rho_4=1$ and the beam splitter divides the incident light equally so that $\tau_2^2 = \rho_2^2 = 0.5$. In these circumstances, the solutions of the resonance condition experiencing the lowest loss coincide with the x-axis in figure 7.12. The mode spacing is then expressed in the general form of $c/2(L_2-L_3)$ and the lengths L_2 and L_3 are usually chosen to be almost equal to give a large mode spacing.

In the coupled cavity GIOPO, however, a general form of the mode spacing cannot be given since there are a number of solutions lying between the zero solutions which may also be above threshold, and the largest mode spacing does not necessarily result from L_2 and L_3 being made almost equal.

7.3 Conclusions

The grazing incidence OPO has been pumped with a single-longitudinal mode Nd:YAG laser. The number of resonant cavity modes was found to be greatly dependent on the grazing angle and at high angles single-longitudinal mode was observed with an internal efficiency of 1.1 %. The SLM operation was unstable, however, with the occasional weak pulse generating a second mode. By removing one of the OPO crystals and replacing the 2400 l/mm grating with an 1800 l/mm element and including an additional optic, a new coupled cavity design has been demonstrated.

The new OPO cavity design is capable of single-axial mode operation with a linewidth of 210 MHz and a tuning range of 580 nm to 690 nm at higher external efficiencies compared with a conventional grazing incidence cavity. The design is based on a grazing incidence cavity and includes an additional mirror to form a coupled cavity. A mathematical description has been discussed, capable of predicting the mode spacing of this type of coupled cavity by considering the geometry of an equivalent Michelson-

mirror interferometer. The additional mirror must have a low reflectivity comparable to the first order diffraction efficiency of the grating to ensure that the linear cavity has a similar loss to the grazing incidence cavity. Without the additional mirror, two modes were seen at all times. Moreover, the efficiency rose by a factor of seven and the threshold fell by 20 % when the cavity was coupled.

This coupled cavity design can also be applied to other OPO gain media and laser systems based on, for example, liquid dye and Ti:sapphire. Indeed, the use of this cavity with a commercial Ti:sapphire laser and a dual-crystal BBO GIOPO has been explored and it was found that a significant reduction in the threshold, a corresponding increase in output power and a reduction in the number of resonant modes was observed.

References

[1] A. E. Siegman "Lasers" University Science Books, California, 524, (1986)

[2] P. W. Smith "Stabilized, single-frequency output from a long laser cavity" IEEE J. Quantum. Electron., 1, 343 (1965)

Chapter 8

Summary and Conclusions

8.1 Summary

In this thesis, noncollinear phase matching and line narrowing have been studied in barium borate (β-BaB_2O_4, BBO) pulsed, optical parametric oscillators (OPOs) in the nanosecond time domain. The objectives of the work were to assess the potential of the optical parametric oscillator as a source of efficient frequency generation and to determine its suitability as a narrow-frequency source for potential spectroscopic applications.

After chapters one and two, which introduce the background and theory of the OPO, chapter three compares the FOMs and performance characteristics of BBO and LBO. Following this analysis, BBO was selected for further investigation. In chapter four, spatial walk-off compensation has been discussed and, by re-evaluating the coupled amplitude equations of the three wave interaction in the noncollinear regime, the noncollinear gain coefficient has been found. The parametric gain length has been calculated for a general degree of noncollinearity and this was shown to increase as the noncollinearity increased. The parametric gain was shown to be significantly greater in a BBO OPO with a modest degree of noncollinearity of 54 mrad compared with the collinear OPO. By evaluating the Brosnan and Byer [1] expression for the operational threshold of the OPO, it was shown that the threshold of a type I phase matched 12 mm long BBO OPO pumped at 355 nm can fall by up to 30 %. The phase matching expression for the noncollinear interaction has been evaluated and the tuning curves for both type I and type II phase matching in BBO have been calculated with good experimental agreement shown in the type I phase matching regime.

Noncollinear phase matching has been applied to 355 nm and 532 nm pumped BBO OPOs. In both cases it was shown that when the tangential condition is reached, significant increases in the angular acceptance of the pump beam are observed compared with the collinear case, thus reducing the constraints imposed on the pump beam divergence. Three, type I, noncollinear geometries have been studied in a 12 mm BBO crystal pumped at 355 nm. The degrees of noncollinearity were q = 40 mrad, 54 mrad and 90.8 mrad. The tuning responses have been measured with respect to angle tuning and these were shown to be in good agreement with the theoretical description. It was shown that full spatial walk-off compensation occurs at 130 mrad although a tuning profile at this angle was not possible. The oscillation threshold was found to fall with the degree of noncollinearity in a way which could be predicted from the Brosnan and Byer model. The model predicted a minimum threshold at 130 mrad of 175 mJ/cm^2. A threshold measurement was taken at 130 mrad which was found to be 180 mJ/cm^2 and was the lowest recorded threshold of all the noncollinear geometries, but a true minimum could not be demonstrated as the oscillator was at its noncollinear limit. The conversion efficiency was measured for each geometry and the slope efficiency increased from 36 % for the noncollinear case to 62 % at the most extreme configuration.

Similar results are shown for the type I 532 nm-pumped BBO OPO. In this case, the noncollinear angles were q=14.8 mrad, 28.4 mrad and 47 mrad. The internal efficiencies in this case increased from 19.7 %, for the collinear OPO, to 39.7 % for the 47 mrad OPO with a corresponding fall in threshold from 2.1 to 1.7 mJ/pulse. Greater pump depletion and lower thresholds are expected at full spatial walk-off compensation, which occurs at 98 mrad.

In both the 355 nm and 532 nm pumped OPOs, the linewidth increased with noncollinearity for a given signal wavelength, indicating an increase in the gain bandwidth of the OPO. In the noncollinear regime, the tuning profile depends on

whether the signal or the idler is the resonant wave. The tuning expression has been solved for both conditions, and the experimental results are shown to be in excellent agreement with the theory.

In chapter six, a grazing incidence BBO OPO (GIOPO) is described. Using two Nd:YAG laser pump sources with bandwidths at 355 nm of 28 GHz and 7.5 GHz, respectively, the variation of OPO linewidth with grating angle has been explored. Initially, a single BBO crystal was used in the cavity, but it was found that reducing the pump bandwidth to 7.5 GHz increased the threshold of the GIOPO. To overcome this, two identical BBO crystals were inserted into the cavity in a walk-off compensated configuration [2]. Using the 28 GHz source, the internal efficiency fell from 7.5 % at a grazing angle of 87.1° to 1.4 % at 89.2°. However, the multimode linewidth of the signal wave remained at ~11.0 GHz, with a corresponding idler linewidth of 19.0 GHz, irrespective of the degree of grazing incidence.

When the bandwidth of the pump source was reduced to 7.5 GHz, the signal linewidth fell to 5.8 GHz, corresponding to eight cavity modes, and the linewidth became more dependent on the grazing angle. Single-mode operation, however, was not observed. The tuning range of the GIOPO was limited to 570 nm to 700 nm. The use of a separate back mirror extended this range to 760 nm, where further tuning was limited by the movement of the tuning mirror. The first order diffraction equation in the grazing incidence configuration asymptotes at about 820 nm. This represents the true long-wavelength limit of the GIOPO.

In order to demonstrate the tuning versatility of the grazing incidence OPO, an aluminium coated back mirror was installed and, using a small intracavity optic positioned at Brewster's angle, the pump light was steered into the cavity. Pumped with the 7.5 GHz source, the linewidth was found to be 9.2 GHz at 605 nm and 10.5 GHz at 473 nm at a grazing angle of 85°, with corresponding external efficiencies

of 2.6 % and 1 %. A tuning range of 240 nm in the visible region from the degenerate point at 710 nm to 470 nm was demonstrated. Further linewidth control was not carried out.

From the work presented in chapter six, it became clear that the pump bandwidth exerted a large influence on the linewidth of the OPO. To secure stable, single-longitudinal mode operation, therefore, a single-longitudinal mode pump source was sought.

Chapter seven details the dual-crystal grazing incidence OPO pumped with a single-axial mode Nd:YAG laser. By studying the number of longitudinal modes in the OPO cavity as a function of grazing angle, we were able to show a steady decrease from 5 to 7 modes at 88.1° to a single-longitudinal mode at 89.4°. The single-mode, however, was not stable and was subject to mode-hopping and, occasionally, dual-mode operation was observed. The pump depletion of the OPO was seen to reduce from 23 % at 87.1° to 1.1 % at 89.2°.

The factors which determine the linewidth of the grazing incidence OPO are many. In this thesis, we have demonstrated that the bandwidth of the pump laser plays an important role in this process. It was shown that by altering the position of the grating, the cavity losses can be controlled, causing the linewidth of the oscillator to reduce for 7.5 GHz pumping and 90 MHz pumping, but not for the 28 GHz case. Another factor affecting the linewidth is the number of times the OPO is pumped above threshold. The cavity losses increase as the grazing angle increases, leading to a rise in the threshold of the oscillator. At a constant pump energy, the number of times the OPO is pumped above threshold, therefore, decreases as the grazing angle increases.

The 7.5 GHz dual-crystal GIOPO was pumped between 2 and 4 times above threshold across the range of grazing angles considered, whereas the 28 GHz and 90 MHz

pumped GIOPOs were both pumped at a level between 1 and 2 times the threshold over the same grating angle range. Therefore, although the linewidth of the dual-crystal GIOPO clearly fell when the pump source changed from 28 GHz to 7.5 GHz, fewer modes may have been observed if the OPO had been pumped less hard at 7.5 GHz and the mode structure may have more closely resembled the 90 MHz pumped OPO. However, a comparison can be made between the 28 GHz source and the 90 MHz source, as the pumping factor above threshold in each case was similar. Figure 8.1 shows the linewidth variation of the GIOPO as a function of grazing angle for both the 28 GHz and 90 MHz sources. Above each datum point is the pumping factor above threshold.

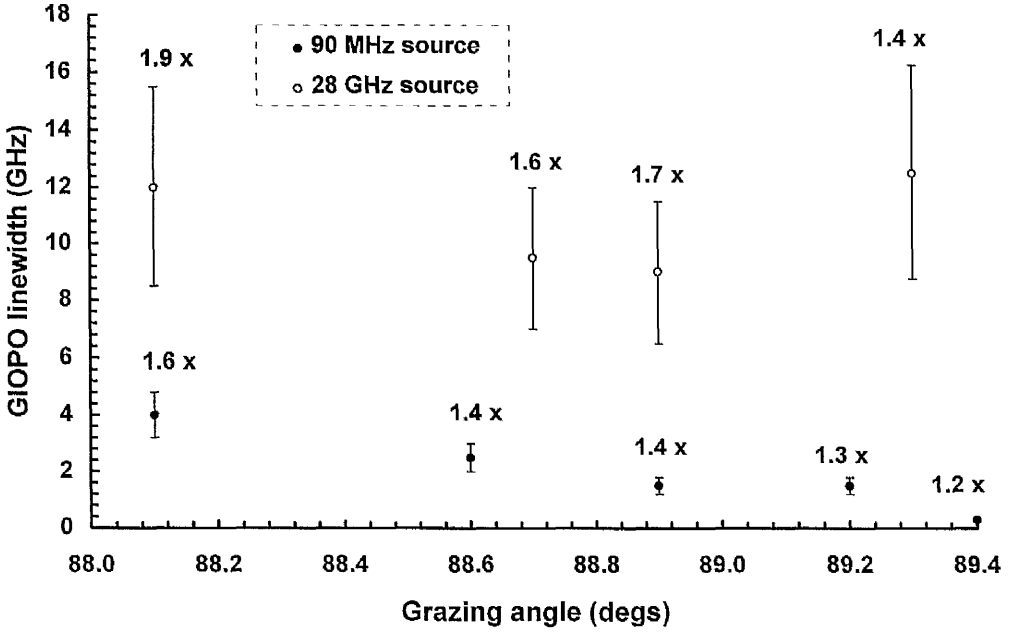

Figure 8.1. Linewidth of the GIOPO as a function of grazing angle for the 28 GHz and 90 MHz bandwidth pump sources. The number above each datum point is a measure of the pump intensity (expressed as the number of times above threshold the OPO was pumped).

The figure shows clearly the effect the bandwidth of the pump laser has on the linewidth of the GIOPO. In the case of the 28 GHz source, the signal linewidth

remains around 10 GHz and is insensitive to the grating angle whereas single-mode operation is possible with the single-mode source at high grazing angles.

Stable, single-longitudinal mode operation in the dual crystal GIOPO, however, was not observed since the device was prone, on occasions, to mode-hopping and to dual-frequency oscillation. Reduction in the cavity length, causing a widening of the cavity mode separation, was considered to be the most secure route to obtaining stable, single-mode operation in the OPO. However, only marginal cavity length reduction was possible without removing one of the BBO crystals, which would prevent the OPO from oscillating at all. The new strategy applied involved replacing the 2400 lines/mm grating with an 1800 lines/mm element, whose diffraction efficiency is greater, and removing one of the BBO crystal from the cavity.

Chapter eight describes the 1800 lines/mm grazing incidence OPO. The introduction of an additional optic, positioned to partially reflect back some of the zero order light reflected from the grating, secured SLM operation for several minutes at a time with no adjustment necessary to the cavity length. Moreover, SLM operation could be achieved at modest grazing angles, as a result of the additional constraint imposed on the cavity modes, allowing for high external efficiencies. A seven-fold decrease in output energy, and multi-mode operation, was observed when the zero-order mirror was removed.

The mode spacing of the coupled cavity GIOPO has been modelled and is shown to agree well with that observed when the oscillator is forced to run multi-mode.

8.2 Conclusions

Noncollinear phase matching has been characterised in BBO at two pump wavelengths for the first time. This phase matching technique has proved to be a highly successful method of countering Poynting vector walk-off in the parametric process, thereby improving the efficiency of the OPO and reducing its threshold whilst still maintaining a broad tuning range. Although demonstrated in this thesis using BBO, noncollinear phase matching may be applied to all critically phase matched systems, in particular in those crystals whose walk-off angle is large. Large aperture BBO crystals are now available with apertures up to 10 mm by 10 mm [3], allowing for full spatial walk-off compensation to be realised, thus maximising the advantages of this phase matching process. Under noncollinear phase matching conditions, the phase matching may become non-critical and the aperture effect limiting the divergence of the pump beam may be alleviated.

The large tuning range, high non-linear coefficient and modest damage threshold of BBO make it ideally suited to high energy applications and lossy cavity configurations. This, coupled with the unquestionable desirability of highly tunable, narrow linewidth radiation from compact, solid state devices, has been the major thrust behind the development of a line-narrowed and single-frequency GIOPO. The creation of a 10 GHz-linewidth (0.3 cm^{-1}) GIOPO capable of tuning from 470 nm to 710 nm (and further into the infrared with idler resonance) has meant that such narrow-band OPOs, have the potential for replacing the dye laser as the spectroscopic tool for medium- to narrow-band spectroscopy. Narrower linewidths of 6 GHz were also demonstrated using a 7.5 GHz bandwidth pump source with the dual crystal GIOPO with a (mirror reflectivity-limited) tuning range of 700 nm to 570 nm and an external conversion efficiency of 1 %.

Single-longitudinal mode, pulsed, OPOs are currently enjoying considerable attention [4], particularly with the emergence of commercial systems [5] and will, no doubt, become a familiar sight in the research laboratory. Since the OPO is not a laser in the classical sense, controlling the pump beam divergence, intensity fluctuations and bandwidth play an important role in the quest for pulsed, SLM OPO. The influence of the bandwidth of the pump laser on the linewidth of the GIOPO has been explored in detail in this work and it has been shown that SLM operation in the GIOPO is difficult to achieve without a single-mode pump source.

Nonetheless, securing a stable, SLM in a grazing incidence OPO in the visible even with a single-mode pump source has been difficult, largely due to the length of the OPO cavity and the finite divergence of pump beam. The cavity length causes a small axial mode separation while the pump divergence causes a broadening of the cavity bandwidth through noncollinear phase matching processes. However, in this thesis it has been shown that the inclusion of an additional optic in the grazing incidence cavity, established a coupled cavity with stable SLM operation for several minutes in the BBO GIOPO with no active cavity length control. Moreover, a 20 % fall in the threshold is observed and a seven fold increase in the external efficiency has been measured. A patent application is currently being sought for this cavity architecture.

A Michelson-mirror cavity model [6] has been adapted to predict the cavity mode separation in the coupled cavity. The theoretical prediction of the cavity mode separation is in excellent agreement with that observed experimentally. The application of this type of coupled cavity to other OPO and laser systems based on grazing incidence cavities is underway, and preliminary results have shown that not only can SLM operation be achieved more easily in these oscillators, but a considerable increase in the efficiency of the oscillator is also observed.

8.3 Future Work

The desirability of single-mode, tunable devices which are compact, efficient, cheap to manufacture and easy to operate is clear. Future work will concentrate on the coupled cavity GIOPO with a view to incorporating active cavity control via a feed-back loop to lock the cavity to a single-mode. Some work has already been carried out to determine whether the second mode of the coupled cavity is spatially distinct from the main, resonant mode. A spatial distinction would allow a split photodiode to monitor the intensities of the adjacent modes and, via simple electronics, correct the cavity length with the piezoelectric transducer.

At the same time, work will focus on scanning the frequency of the mode continuously and without mode-hop to make a highly efficient spectroscopic device. So far, no work has been carried out in this area with this cavity by us, and it is likely that computer control will be required to carry out simultaneous adjustments to the crystal orientation, the tuning mirror and the cavity length. Furthermore, incorporating noncollinear phase matching in a frequency-selective cavity could significantly improve the overall efficiency of the device. Preliminary work is currently underway to design the cavity architecture.

Investigations are underway in our laboratories aimed at using diode-pumped solid state lasers as pump sources for the OPO to reduce the overall size of the composite devices and increase the wall-plug efficiency. Both end-pumped and side-pumped designs are being considered with a view to replacing the flashlamp-pumped laser in the near future. Indeed, the rapid development of both crystal quality and diode laser beam quality has already led to direct diode-pumping of the OPO, and this is likely to become a familiar practice in many laboratories over the next few years. This combination of optical components leads to extremely compact, tunable sources in the

infrared. In the future, tunable light at shorter wavelengths will be possible as the blue/green diode laser develops into a commercial device.

Finally. the significantly higher non-linear coefficients of some organic non-centrosymmetric crystals make them potential candidates for parametric devices. Chemical instability, narrow transmission windows and low damage thresholds have hindered their progress into the parametric field. However, with ever improving crystal growing techniques, these materials may too join the successful optical parametric renaissance.

References

[1] S. J. Brosnan and R. L. Byer "Optical parametric threshold and linewidth studies" IEEE J. Quantum Electron., 15, 168, (1979)

[2] W. R. Bosenberg, W. S. Pelouch and C. L. Tang "High-frequency and narrow-linewidth operation of a two-crystal β-BaB_2O_4 optical parametric oscillator" Appl. Phys. Lett., 55, 1952, (1989)

[3] Private communication with Jean Aitchison, Photox Optical Systems, Headington, Oxford, April, (1995). Suppliers of barium borate from Castech Inc.

[4] see, for example, M. J. T. Milton, T. D. Gardiner and P. T. Woods "A tunable injection-seeded optical parametric oscillator between 1.526 μm and 1.578 μm" OSA proceedings on Advanced Solid State Lasers, 20, 451, (1994), A. Fix, G. Goeritz, R. Urschel, D. Wildt, A. Borsutzky and R. Wallenstein "Single-mode optical parametric oscillator system of BBO and $KNbO_3$ tunable from the visible (0.42 μm) to the infrared (4 μm)" OSA proceedings on Advanced Solid State Lasers, 20, 458, (1994), J. G. Haub, R. M. Hentschel, M. J. Johnson and B. J. Orr "Controlling the performance of a pulsed optical parametric oscillator to suit the spectroscopic application" Submitted to J. Opt. Soc. Am. B., Special Issue on Parametric Devices, (March 1995).

[5] See, for example. Quanta-Ray MOPO-700 Series, Spectra-Physics Lasers and The Sunlite, Continuum.

[6] P. W. Smith "Mode selection in lasers" Proc. IEEE 60, 423, (1972)

Appendix I

Program to Calculate Phase Matching Angles

```
c     To use this program: Create file (e.g. KTPdata.dat) containing the
c     Sellmeier data nx, nx, nz in that order for the biaxial crystal
c     and a pump wavelength in microns. The code assumes the crystal is
c     'well behaved', that is nx<ny<nz. Once the code has been compiled,
c     the values of nx, ny and nz are written to the screen. If the above
c     condition is not met then the Sellmeier data has to be permutated in
c     the file KTP.dat. Four Sellmeier constants can be accepted per Sellmeier
c     equation in the form n=a+b/(w*w-c)-d*w*w, where w is wavelength in
c     microns. If only three constants are required/known then the forth ('d')
c     must be set to zero in KTPdata.dat or the code will use 'a' of the next
c     Sellmeier equation for d of the last.
c     Having loaded dbos, compile using FTN77 biaxial.f/LINK77. Then type
c     'biaxial KTPdata.dat KTP.dat' (KTP.dat is the output file). Whether
c     a type of phase matching exists in a certain plane or not, a file will
c     be created. These files will take the output file name (in this case
c     KTP) and add the plane (e.g. XZ) and the type of phase matching (e.g. I,II)
c     Often, type II and type II phase matching in a given plane are the
c     same.
c
c
      implicit none
c
c...first declare our variables
c
      double precision      p
      character*12          inputfile, outputfile
      character*12          filename
      double precision      t, idler, signal, tmp
      double precision      accuracy, lower, upper
      double precision      thetamin, thetamax, thetastep
      parameter ( thetamin  = 1.0d0 )
      parameter ( thetastep = 0.05d0 )
      parameter ( thetamax  = 90.0d0 )
      integer               i, nsteps, j, jj
      parameter ( nsteps = (thetamax - thetamin)/thetastep + 1)
      double precision      radperdeg, degperrad
      parameter ( degperrad = 57.29577951 )
      parameter ( radperdeg = 0.017453292 )
      integer               ierr
c
c...accuracy is to 0.1 angstroms
c
      parameter ( accuracy = 0.00001 )
```

Appendix I

```
c
c...functions
c
      double precision        rootfind
      integer                 leng
c
c...These two are declared external since they are passed into rootfind
c
      double precision        pm, pm3
      external                pm, pm3
      double precision        nx, ny, nz
      character*60            cmnam    ! gets command line arguments
c                             ! this is not standard F77
c
c...common blocks for sellmeier constants
c
      double precision        ax, bx, cx, dx
      double precision        ay, by, cy, dy
      double precision        az, bz, cz, dz
      common / nx_sellmeier / ax, bx, cx, dx
      common / ny_sellmeier / ay, by, cy, dy
      common / nz_sellmeier / az, bz, cz, dz
c
c...common blocks for data passed into pm etc
c
      integer                 plane, typeI_or_II
      double precision        theta0
      common / conditions /   plane, typeI_or_II, theta0
c
c...parameter statements
c
      integer     TYPEI, TYPEII, TYPEIII
      parameter ( TYPEI=1 , TYPEII=2 , TYPEIII=3)
      integer     XYPLANE, YZPLANE, XZPLANE
      parameter ( XYPLANE = 1, YZPLANE = 2, XZPLANE = 3)
c
      ierr = 0
c
c...open the data file
c
      inputfile = cmnam()
      outputfile = cmnam()
      open ( unit = 4 , file = inputfile, status = 'old', err = 2000)
      write(*,'(2a)')'Reading data from file ',inputfile
c
c...read in the Sellmeier constants
c
cjrh      write(*,*)'Input the Sellmeier constants:'
```

```
      read(4,*) ax
      read(4,*) bx
      read(4,*) cx
      read(4,*) dx
      read(4,*) ay
      read(4,*) by
      read(4,*) cy
      read(4,*) dy
      read(4,*) az
      read(4,*) bz
      read(4,*) cz
      read(4,*) dz
c
c...read in the wavelength of the pump
c
cjrh      write(*,*) 'Input the pump wavelength in microns:'
      read(4,*) p
c
c...close the data file
c
      close ( 4 )
c
c...work out the optic axis of the crystal
c  N.B. We do this at the pump frequency and it should not vary
c  from this value by much for other wavelengths.
c
      write(*,'(1a,f8.5)')'Nx ',nx(p)
      write(*,'(1a,f8.5)')'Ny ',ny(p)
      write(*,'(1a,f8.5)')'Nz ',nz(p)
      tmp = nz(p) * sqrt((ny(p)*ny(p) - nx(p)*nx(p)) /
     >      (nz(p)*nz(p) - ny(p)*ny(p))) / nx(p)
      theta0 = atan ( tmp )
      write(*,'(1a,1f8.3,1a)')
     >         'Optic axis at ',degperrad*theta0,' degrees'
c
c...write out the conditions we have read in
c
      write(*,'(1a,1f9.5,1a)') 'Pump wavelength is :', p, ' microns'
c
c...set up the lower and upper search ranges for the signal frequency
c
      lower = p * 1.15          ! to avoid divide by zero in pm
      upper = 2.0d0 * p         ! only find signal roots
c     upper = .8d0
c     read(*,*) upper
c
c...loop over the two types of phase matching
c
```

```
      do j = 1 , 9
       if (j.eq.1) then
         typeI_or_II = TYPEI
         plane = XYPLANE
         write(filename,'(2a)')outputfile(1:leng(outputfile)),'XYI'
       elseif (j.eq.2) then
         typeI_or_II = TYPEII
         plane = XYPLANE
         write(filename,'(2a)')outputfile(1:leng(outputfile)),'XYII'
       elseif (j.eq.3) then
         typeI_or_II = TYPEIII
         plane = XYPLANE
         write(filename,'(2a)')outputfile(1:leng(outputfile)),'XYIII'
       elseif (j.eq.4) then
         typeI_or_II = TYPEI
         plane = YZPLANE
         write(filename,'(2a)')outputfile(1:leng(outputfile)),'YZI'
       elseif (j.eq.5) then
         typeI_or_II = TYPEII
         plane = YZPLANE
         write(filename,'(2a)')outputfile(1:leng(outputfile)),'YZII'
       elseif (j.eq.6) then
         typeI_or_II = TYPEIII
         plane = YZPLANE
         write(filename,'(2a)')outputfile(1:leng(outputfile)),'YZIII'
       elseif (j.eq.7) then
         typeI_or_II = TYPEI
         plane = XZPLANE
         write(filename,'(2a)')outputfile(1:leng(outputfile)),'XZI'
       elseif (j.eq.8) then
         typeI_or_II = TYPEII
         plane = XZPLANE
         write(filename,'(2a)')outputfile(1:leng(outputfile)),'XZII'
       elseif (j.eq.9) then
         typeI_or_II = TYPEIII
         plane = XZPLANE
         write(filename,'(2a)')outputfile(1:leng(outputfile)),'XZIII'
       endif

c
c...open a file to write the results into
c
      open ( unit = 4 , file = filename, status =
     >'unknown',err=3000)
c
c...write in some header information to the output file
c
      write(4,'(1a)')'# Output from Crystal Solutions code'
```

```
      write(4,'(2a)')'# Input from file: ',inputfile
      if (typeI_or_II .eq. TYPEI) then
        write(4,'(2a)')'# Type is TYPEI'
      elseif(typeI_or_II .eq. TYPEII) then
        write(4,'(2a)')'# Type is TYPEII'
      else
        write(4,'(2a)')'# Type is TYPEIII'
      endif
      write(4,'(1a)')'#'
      write(4,'(1a)')'# Angle        Signal      Idler'
      write(4,'(1a)')'#'
c
c...vary phase matching angle in steps
c
      do i = 1 , nsteps
c
c...theta for this step
c
        t = radperdeg * (thetamin + (i-1) * thetastep)

c
c...for this angle, find the wavelengths which satisfies PM
c
        if (typeI_or_II .ne. TYPEIII) then
c
          signal = rootfind(pm,t,p,lower,upper,accuracy,ierr)
          if ( ierr .eq. 0 ) then
            idler = p * signal / ( signal - p )
            write(4,'(f10.5,1a,f10.5,1a,f10.5)')
     >       (1.57-t)*degperrad, '  ', signal, '  ', idler
          endif
c
        elseif (typeI_or_II .eq. TYPEIII) then
c
          signal = rootfind(pm,t,p,lower,upper,accuracy,ierr)
          if ( ierr .eq. 0 ) then
            idler = p * signal / ( signal - p )
            write(4,'(f10.5,1a,f10.5,1a,f10.5)')
     >       t*degperrad, '  ', signal, '  ', idler
          else
c
c...if we are doing typeIII phase matching and we have not found
c  any roots we will try the alternative pm function pm3.
c
            signal = rootfind(pm3,t,p,lower,upper,accuracy,ierr)
            if ( ierr .eq. 0 ) then
              idler = p * signal / ( signal - p )
              write(4,'(f10.5,1a,f10.5,1a,f10.5)')
```

```
   >        t*degperrad, ' ', signal, ' ', idler
          endif
c
         endif
c
        endif
c
c...go back and do the next angle
c
       enddo
c
c...we've done all of the angles, let's output the results
c
       close ( 4 )
     enddo
     stop
c
2000  continue
     write(*,'(2a)')'ERROR - could not open file ',inputfile
c
3000  continue
     write(*,'(2a)')'ERROR - could not open file ',filename
4000  continue
     write(*,*)'ABORTING - Crystal is not anisotropic'
     end
c
c++++++++++++++++++++++++++++++++++++++++++++++++++++++++++++++++++++++++++++++
c
c This function returns the extraordinary refractive index for a
c given
c wavelength W. Note that the Sellmeier constants are passed via
c the common block nx_sellmeier.
c
     double precision function nx(W)
c
     implicit none
c
     double precision       W
     double precision       ax, bx, cx, dx
     common / nx_sellmeier /  ax, bx, cx, dx
     double precision       tmp
c
     tmp = ax + bx*W*W/(W*W-cx) + dx*W*W
     if ( tmp .le. 0.0d0) then
       write(*,*)'tmp negative in nx'
       stop
     else
       nx = sqrt(tmp)
```

```
      endif
c
      return
c
      end
c
c+++++++++++++++++++++++++++++++++++++++++++++++++++++++++++++++++++++++++++++++
c
c This function returns the extraordinary refractive index for a
c given
c wavelength W. Note that the Sellmeier constants are passed via
c the common block ny_sellmeier.
c
      double precision function ny(W)
c
      implicit none
c
      double precision      W
      double precision      ay, by, cy, dy
      common / ny_sellmeier /  ay, by, cy, dy
      double precision      tmp
c
      tmp = ay + by*W*W/(W*W-cy) + dy*W*W
      if ( tmp .le. 0.0d0) then
        write(*,*)'tmp negative in ny'
        stop
      else
        ny = sqrt(tmp)
      endif
c
      return
c
      end
c
c+++++++++++++++++++++++++++++++++++++++++++++++++++++++++++++++++++++++++++++++
c
c This function returns the ordinary refractive index for a given
c wavelength W. Note that the Sellmeier constants are passed via
c the common block nz_sellmeier.
c
      double precision function nz(W)
c
      implicit none
c
      double precision      W
      double precision      az, bz, cz, dz
      common / nz_sellmeier /  az, bz, cz, dz
      double precision      tmp
```

```
c
      tmp = az + bz*W*W/(W*W-cz) + dz*W*W
      if (tmp .lt. 0.0d0) then
       write(*,*)'tmp negative in nz'
       stop
      else
       nz = sqrt(tmp)
      endif
c
      return
c
      end
c+++++++++++++++++++++++++++++++++++++++++++++++++++++++++++++++++++++++++++++
c
c This function is a quadratic in signal wavelength, the roots of
c which tell us the phase matching wavelength at angle t.
c Note the common block set up in main for whether we are positive or
c negative.
c
      double precision function pm ( t , p , s )
c
      implicit none
c
c...passed variables
c
      double precision      t    ! theta
      double precision      p    ! pump
      double precision      s    ! signal
c
c...local variables
c
      double precision      i    ! idler
      integer               typeI_or_II
      integer               plane
      double precision      theta0
      common / conditions /   plane, typeI_or_II, theta0
      integer               TYPEI, TYPEII
      parameter ( TYPEI = 1 , TYPEII = 2 )
      integer   XYPLANE, YZPLANE, XZPLANE
      parameter (XYPLANE = 1, YZPLANE = 2, XZPLANE = 3)
c
c...functions
c
      double precision      nb, na
c
      i = p * s / ( s - p )
c
c....phase matching for all planes and types
```

```
c
      if ( typeI_or_II .eq. TYPEI ) then
        pm =    na(t,p,plane,theta0)/p
     >        - nb(t,s,plane,theta0)/s
     >        - nb(t,i,plane,theta0)/i
      else !TYPEII
        pm =    na(t,p,plane,theta0)/p
     >        - nb(t,s,plane,theta0)/s
     >        - na(t,i,plane,theta0)/i
c
      endif
c
      return
c
      end
c
c++++++++++++++++++++++++++++++++++++++++++++++++++++++++++++++++++++++++++++++
c
c This function is a quadratic in signal wavelength, the roots of
c which tell us the phase matching wavelength at angle t.
c Note the common block set up in main for whether we are positive or
c negative.
c
      double precision function pm3 ( t , p , s )
c
      implicit none
c
c...passed variables
c
      double precision      t    ! theta
      double precision      p    ! pump
      double precision      s    ! signal
c
c...local variables
c
      double precision      i    ! idler
      integer               typeI_or_II
      integer               plane
      double precision      theta0
      common / conditions /   plane, typeI_or_II, theta0
      integer               TYPEI, TYPEII
      parameter ( TYPEI = 1 , TYPEII = 2 )
      integer   XYPLANE, YZPLANE, XZPLANE
      parameter (XYPLANE = 1, YZPLANE = 2, XZPLANE = 3)
c
c...functions
c
      double precision      nb, na
```

```
c
      i = p * s / ( s - p )
c
c...this is for the xy plane
c
      pm3 =    na(t,p,plane,theta0)/p
     >       - na(t,s,plane,theta0)/s
     >       - nb(t,i,plane,theta0)/i
c
      return
c
      end
c
c++++++++++++++++++++++++++++++++++++++++++++++++++++++++++++++++++++++++++++++
c
      double precision function na ( t, W, plane, theta0 )
c
      implicit none
c
      double precision          t, W, theta0
      integer                   plane
      double precision          tmp
      integer   XYPLANE, YZPLANE, XZPLANE
      parameter (XYPLANE = 1, YZPLANE = 2, XZPLANE = 3)
c
c...functions
c
      double precision          nx, ny, nz
c
      if (plane .eq. XYPLANE) then
        tmp = 1.0d0 / ( (cos(t)/ny(W))**2 + (sin(t)/nx(W))**2 )
        if (tmp .le. 0.0d0) then
          write(*,*)'tmp negative in na'
          stop
        else
          na = sqrt(tmp)
        endif
      elseif (plane .eq. YZPLANE) then
        na = nx(W)
      elseif (plane .eq. XZPLANE) then
c
c...if we are doing the XZPLANE we need to decide whether this
c   angle represents an angle above or below the angle of the
c   optic axis (theta0)
c
        if (t .lt. theta0) then
          tmp = 1.0d0 / ( (cos(t)/nx(W))**2 + (sin(t)/nz(W))**2 )
          if (tmp .le. 0.0d0) then
```

```
          write(*,*)'tmp negative in na'
          stop
        else
          na = sqrt(tmp)
        endif
      else
        na = ny(W)
      endif
    endif
c
    return
    end
c
c++++++++++++++++++++++++++++++++++++++++++++++++++++++++++++++++++++++++++++++
c
c This function returns the ordinary refractive index for a given
c wavelength W. Note that the Sellmeier constants are passed via
c the common block nz_sellmeier.
c
    double precision function nb(t, W, plane, theta0)
c
    implicit none
c
    double precision      t, W, theta0
    integer               plane
    double precision      nx, ny, nz, tmp
    integer   XYPLANE, YZPLANE, XZPLANE
    parameter (XYPLANE = 1, YZPLANE = 2, XZPLANE = 3)
c
    if (plane .eq. XYPLANE) then
      nb = nz(W)
    elseif (plane .eq. YZPLANE) then
      tmp = 1.0d0 / ( (cos(t)/ny(W))**2 + (sin(t)/nz(W))**2 )
      if (tmp .le. 0.0d0) then
        write(*,*)'tmp negative in nb'
        stop
      else
        nb = sqrt(tmp)
      endif
    elseif (plane .eq. XZPLANE) then
c
c...if we are doing the XZPLANE we need to decide whether this
c  angle represents an angle above or below the angle of the
c  optic axis (theta0)
c
      if (t .lt. theta0) then
        nb = ny(W)
      else
```

```
        tmp = 1.0d0 / ( (cos(t)/nx(W))**2 + (sin(t)/nz(W))**2 )
        if (tmp .le. 0.0d0) then
          write(*,*)'tmp negative in nb'
          stop
        else
          nb = sqrt(tmp)
        endif
      endif
    endif
c
    return
c
    end
c
c
c++++++++++++++++++++++++++++++++++++++++++++++++++++++++++++++++++++++++++++++
c
c Finds the roots of the equation
c Uses the bisector method from Numerical Recipes
c Returns an error if there is a problem
c
    double precision function rootfind ( func, t , p , x1 , x2 , xacc,
   >       ierr)
    implicit none
c
c...passed variables
c
    double precision    func, t , p , x1 , x2 , xacc
    integer             ierr
c
c...local variables
c
    integer jmax
    parameter (jmax = 40)
    double precision   fmid, f, dx, xmid
    integer          j
c
    ierr = 0
c
    fmid = func(t,p,x2)
    f    = func(t,p,x1)
    if (f * fmid .gt. 0.0d0) then
      ierr = 1
      return
    endif
    if (f.lt.0) then
      rootfind = x1
      dx = x2 - x1
```

```
      else
        rootfind = x2
        dx = x1 - x2
      endif
      do j = 1 , jmax
        dx = dx * 0.5
        xmid = rootfind + dx
        fmid = func ( t , p , xmid )
        if (fmid .lt. 0.0d0) rootfind = xmid
        if (abs(dx) .lt. xacc .or. fmid .eq. 0.0d0) return
      enddo
c
      write(*,*)'Not enough iterations in bisector'
      ierr = 1
c
      return
      end
c
c+++++++++++++++++++++++++++++++++++++++++++++++++++++++++++++++++++++++++++++++
c
      integer function leng(string)
      character string*(*)
      leng=len(string)
      do while(string(leng:leng).eq.' ')
        leng=leng-1
        if(leng.eq.0)then
          leng=1
          return
        endif
      enddo
      return
      end
```

Appendix II

Spectra of GIOPO Pumped with 7.5 GHz Source

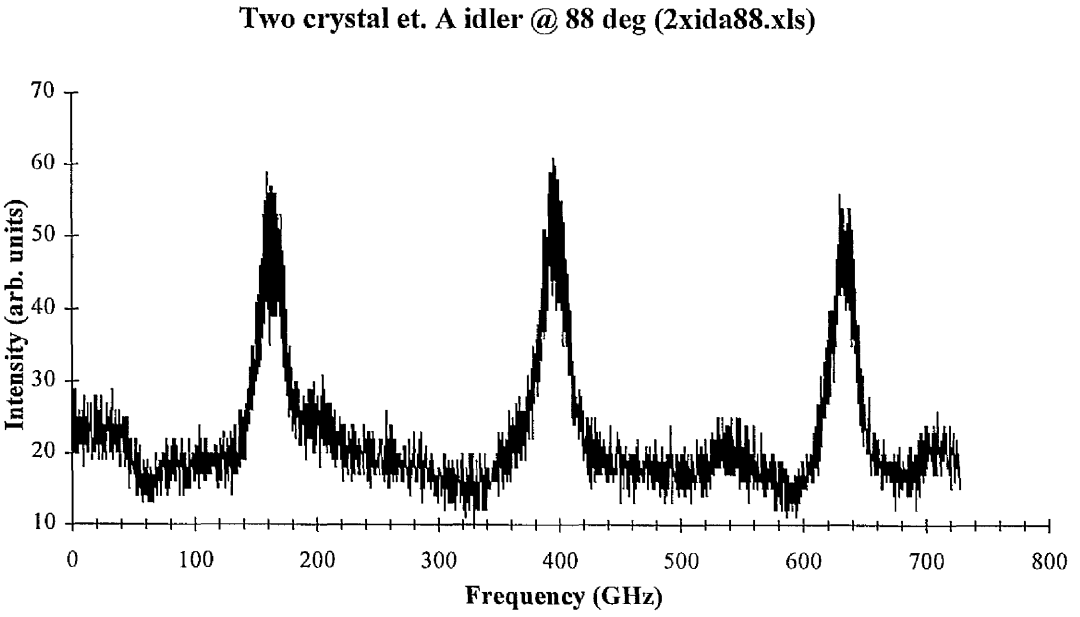

A.II. 1. Spectral profile of idler at a grazing angle of 88 degrees, using etalon A.

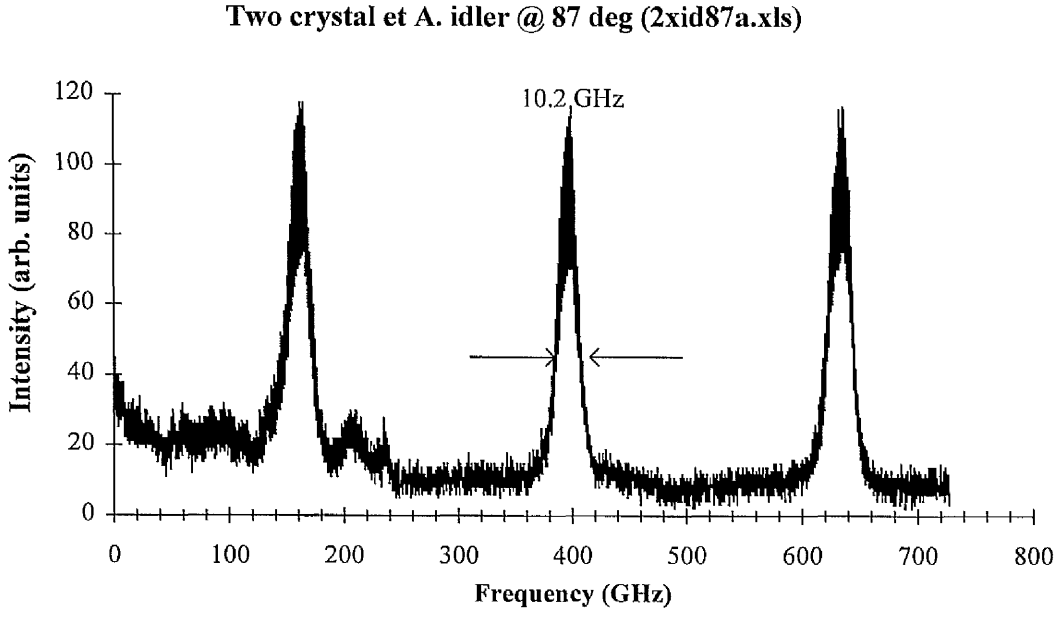

A.II. 2. Spectral profile of idler at a grazing angle of 87 degrees, using etalon A.

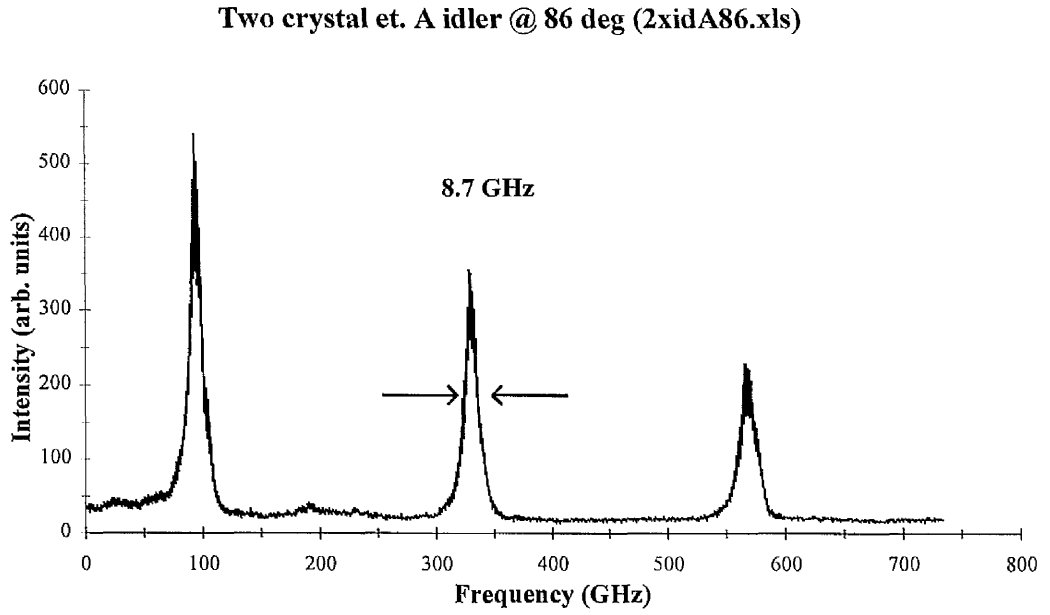

A.II. 3. Spectral profile of idler at a grazing angle of 86 degrees, using etalon A.

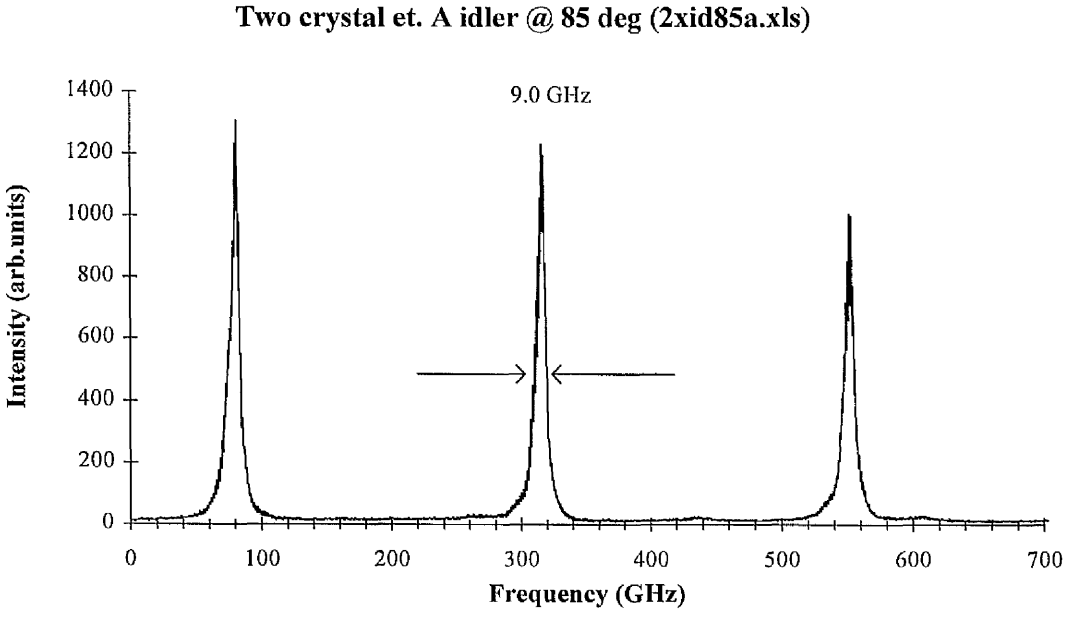

A.II. 4. Spectral profile of idler at a grazing angle of 85 degrees, using etalon A.

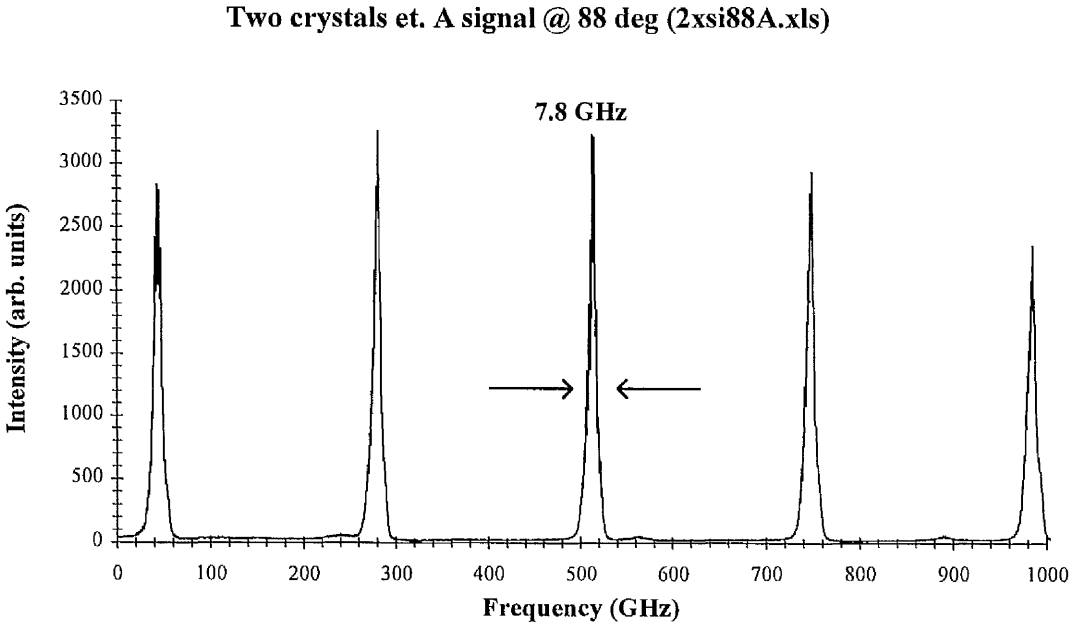

A.II. 5. Spectral profile of signal at a grazing angle of 88 degrees, using etalon A.

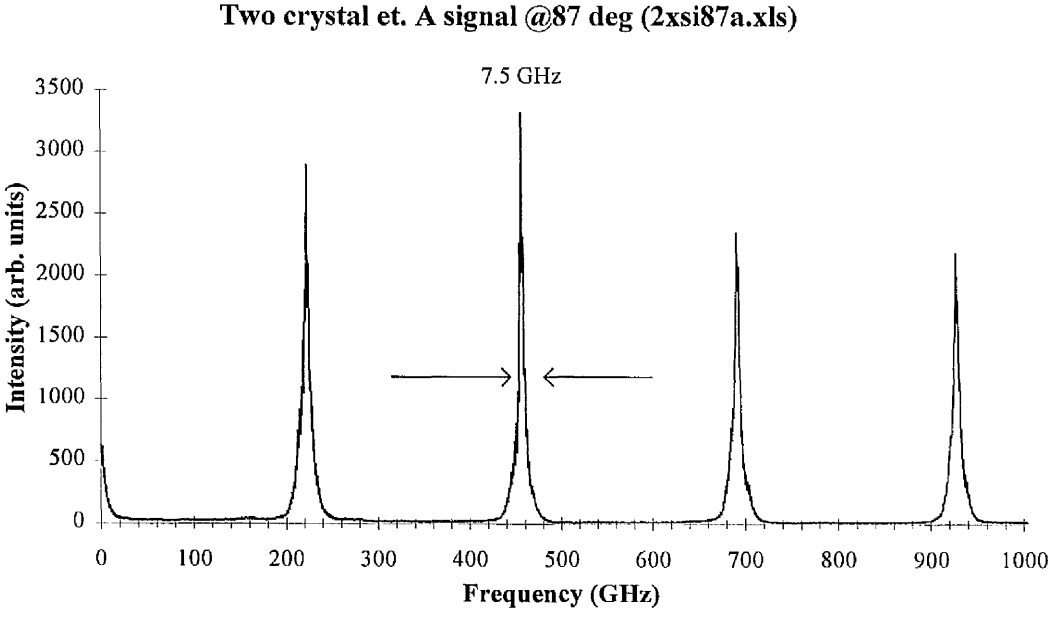

A.II. 6. Spectral profile of signal at a grazing angle of 87 degrees, using etalon A.

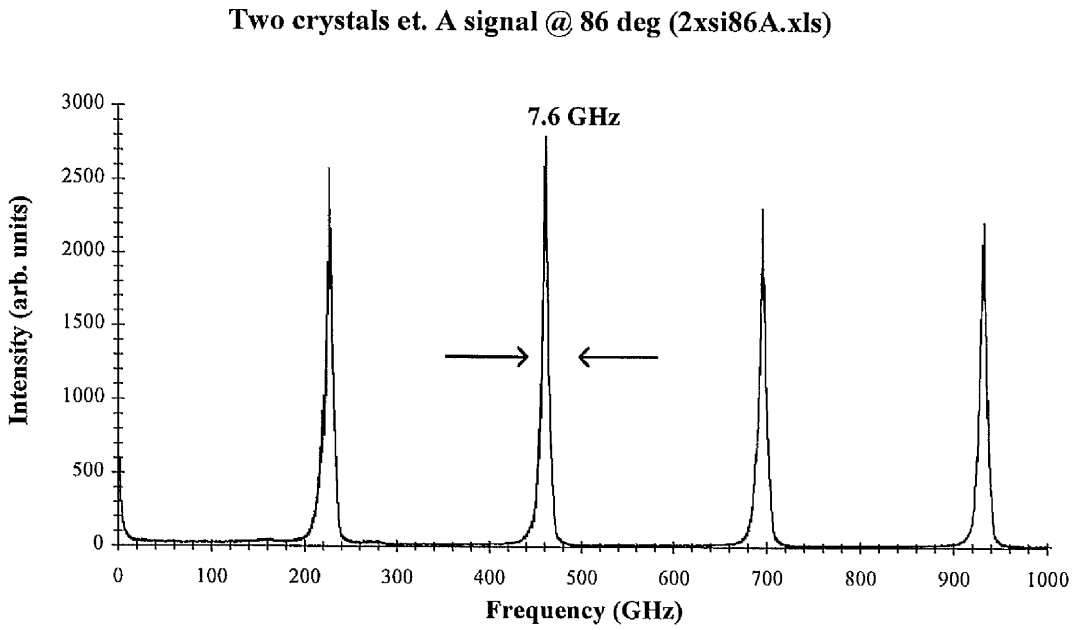

A.II. 7. Spectral profile of signal at a grazing angle of 86 degrees, using etalon A.

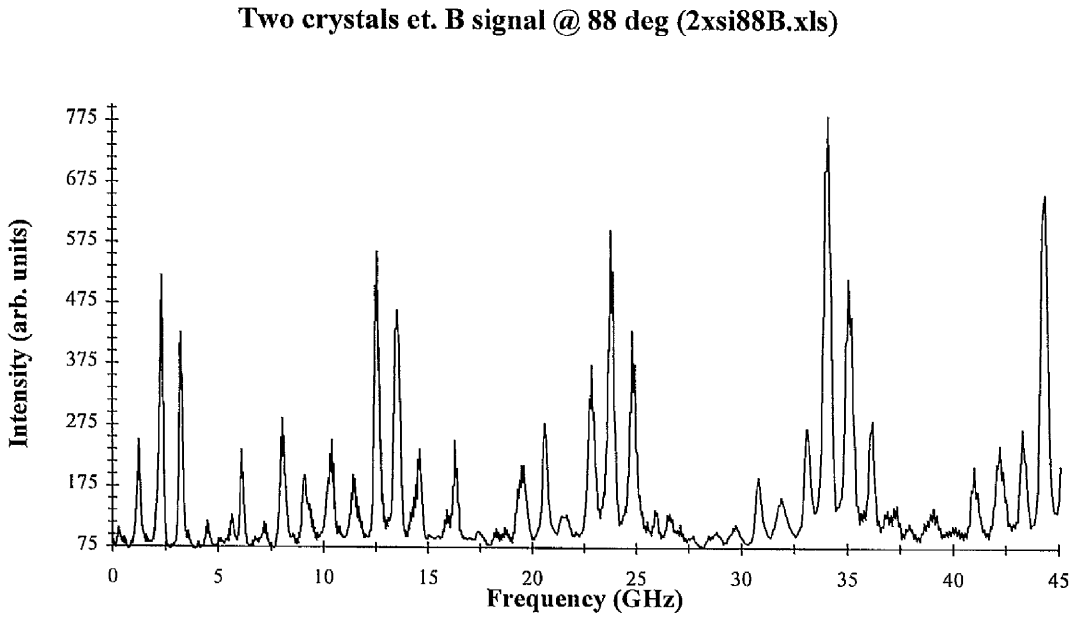

A.II. 8. Spectral profile of signal at a grazing angle of 88 degrees, using etalon B. The cavity modes are resolved.

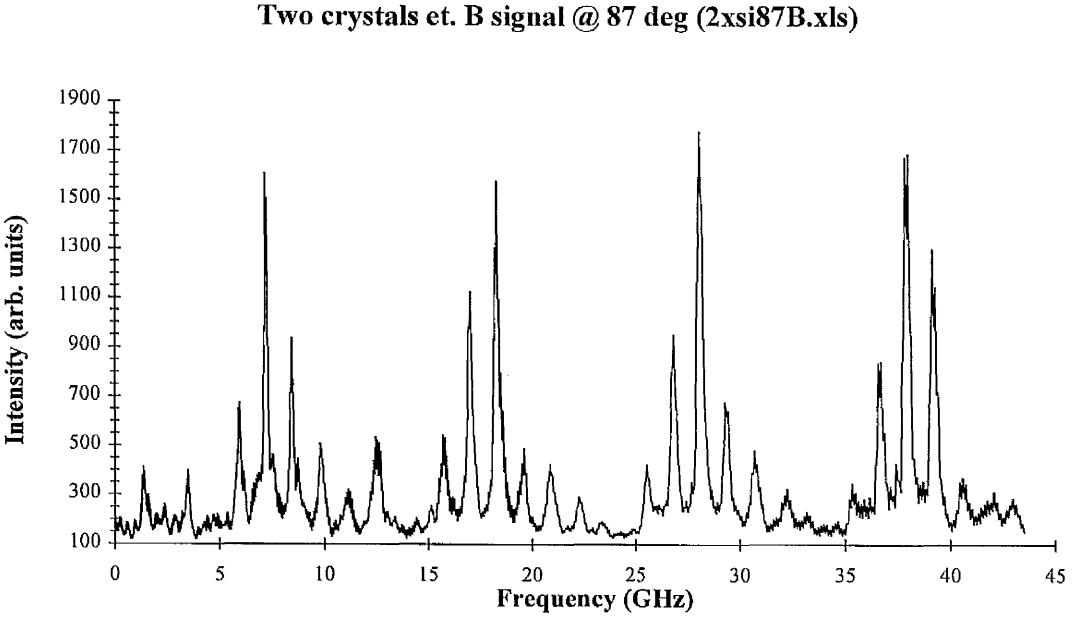

A.II. 9. Spectral profile of signal at a grazing angle of 87 degrees, using etalon B. The cavity modes are resolved.

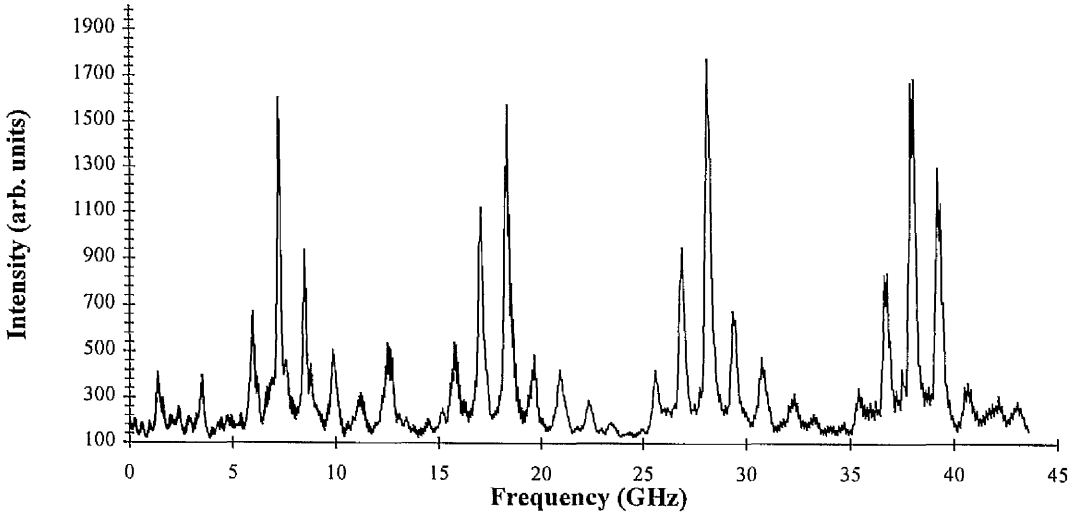

A.II. 10. Spectral profile of signal at a grazing angle of 86 degrees, using etalon B. The cavity modes are resolved.

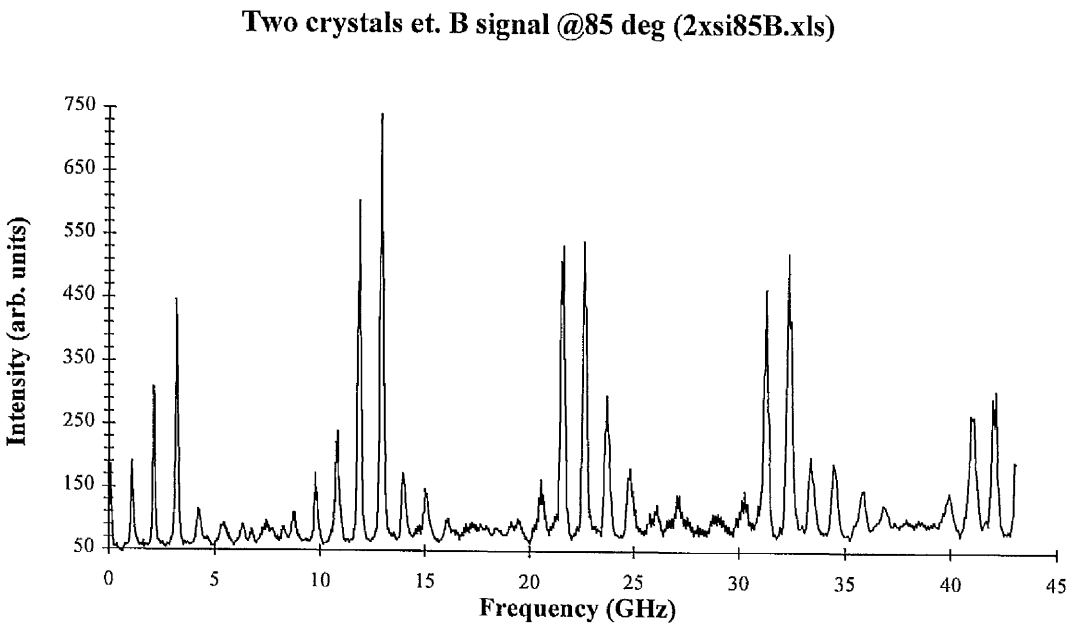

A.II. 11. Spectral profile of signal at a grazing angle of 85 degrees, using etalon B. The cavity modes are resolved.